TAMPEREEN TEKNILLINEN YLIOPISTO
TAMPERE UNIVERSITY OF TECHNOLOGY

Jani Pelto

Applications of Biopolymer Doped Polypyrroles in Biomedical Implants and Electrical Stimulation Devices

Julkaisu 1307 • Publication 1307

Tampere 2015

Tampereen teknillinen yliopisto. Julkaisu 1307
Tampere University of Technology. Publication 1307

Jani Pelto

Applications of Biopolymer Doped Polypyrroles in Biomedical Implants and Electrical Stimulation Devices

Thesis for the degree of Doctor of Science in Technology to be presented with due permission for public examination and criticism in Tietotalo Building, Auditorium TB109, at Tampere University of Technology, on the 9th of July 2015, at 12 noon.

Tampereen teknillinen yliopisto - Tampere University of Technology
Tampere 2015

ISBN 978-952-15-3543-7 (printed)
ISBN 978-952-15-3552-9 (PDF)
ISSN 1459-2045

Abstract

Organic conductive polymers are emerging new materials for biomedical engineering. They offer surface properties which are attractive for many biomedical applications, such as surface coatings on metallic or biodegradable polymeric implants, tissue engineering scaffolds, implantable electronic tissue stimulation devices and microelectromechanical systems for the manipulation of single living cells *in vitro*, for example. Owing to the proven compatibility with tissues and cells, conductive polypyrrole (PPy) has been intensively investigated for bone and neural stimulation applications. A salient feature of PPy is its easy modification with bioactive molecules and macromolecules, such as the extracellular matrix (ECM) components of animal tissues. This work assessed the ECM components hyaluronic acid (HA) and chondrointin sulfate (CS) as dopants, which we incorporated into the PPy during the syntheses by electrochemical and oxidative chemical polymerization.

Biopolymer doped PPys have been earlier reported to be good substrates for cell cultures. Furthermore, preceding implantation studies have shown promising results. However, considering clinical application and registration of PPy as a biomaterial in commercial cell culturing or tissue engineering products, there are still many practical aspects requiring more attention, such as the establishment of feasible synthetic routes, sterilizability, preservation of the electronic properties during storage and during the incubation in physiological conditions, possible biodegradation mechanisms, stability and biological elimination of the degradation products *in vivo,* for example. Mass spectroscopy of the hydrolysis products of polylactide (PLA) fibers coated with layer of PPy, suggested that the PPy was biostable in water at neutral pH. Electrical conductivity measurements and Raman spectroscopy showed that the PPy chain was prone to de-doping, and hence the lost its conductivity under biological conditions, but these effects were partly reversible by acid doping and positively biased electrochemical potential. The electrochemical redox activity and electromechanical actuation property of the biopolymer doped PPys was thoroughly studied. It was shown that the biopolymer doped PPy had significant and reversible redox activity, which could be potentially utilized in microelectromechanical stimulation of cells and implantable microscopic actuators.

Practical and reproducible polymerization protocols were developed during this work. We took novel approaches and suggested a relatively simple “one-pot” chemical polymerization scheme, avoiding the complications of biological functionalization using potentially toxic click-chemistry. The developed methods were successfully applied in the deposition of electrically conductive, biopolymer doped PPy coatings on polylactide (PLA) nonwoven tissue engineering scaffolds and commercial poly(lactide-co-glycolide)-β-tricalcium phosphate (PLGA-β-TCP) bone fixation screws.

The physical properties and cell response of HA and CS doped PPys (PPyHA and PPyCS) electrode coatings were investigated by atomic force microscopy (AFM) and electrochemical methods. Drastically different behaviour of adipose stem cells (hASC) was found on the different electrode coatings, highlighting the sensitity of the hASCs on the nanoscopic and microscopic surface properties of the PPy substrate, such as surface roughness, elasticity and surface potential distribution, factors which could be engineered during the synthesis and affected by external stimuli during incubation in cell culture medium.

In conclusion, the resuls of this thesis supported the use of PPy coatings in bone tissue engineering. The electropolymerized films and also the chemically polymerized PPyHA and PPyCS coatings on bioabsorbable polymer were highly compatible with hASCs, supported cell adhesion and could be utilized in delivering direct electrical stimulation *in vitro*. There is also future potential in designing permanently implantable scaffolds and microstimulation devices, but still further insight into the biodegradation mechanism and biological elimination of PPy *in vivo* is needed.

Table of Contents

Abstract i
Acknowledgements v
List of publications vi
Author's contributions vii
1. Introduction 1
2. Literature survey 4
2.1 Historical perspective 4
2.2 Electronic conduction in PPy 4
2.3 Commercial applications 5
2.4 Biomedical application in the research phase. 6
2.5 Electromechanical microactuation 6
2.6 Motivation for the tissue engineering applications of PPy 7
2.7 Electrochemical synthesis 8
2.8 Polymerization by chemical oxidants in liquid phase 12
2.9 In situ polymerization on material interphases 15
2.10 Alternative routes for conductive polymers 16
2.11 Patterning of PPy microstructures 17
2.12 Degradation of polypyrrole by ionizing radiation 18
2.13 Stability of biopolymer doped polypyrroles in air and in physiological fluid environment 19
2.14 Cell-surface interactions 22
3. Aims of this study 31
4. Experimental procedures 32
4.1 Synthesis of the test materials 32
4.1.1 Electropolymerization of PPyHA and PPyCS 32
4.1.2 Chemical oxidative polymerization of PPy 37
4.2 Fluid AFM 38
4.3 Kelvin force probe microscopy (KFPM) 39
4.4 Raman spectroscopy 39
4.5 Electrospray ionization mass spectroscopy (ESI-MS) 40
4.6 Quartz crystal microbalance under electrochemical control (EC-QCM) 41
4.7 Two and three dimensional cell culturing platforms 41
4.8 Cell culture 44
4.9 Pre-clinical study 44

5. Results 45
5.1 Surface properties of PPyHA and PPyCS 45
5.2 Stability of biopolymer doped PPys 51
5.3 Electro-mechanical actuation in nanometer scale 56
5.4 Cell attachment and viability 58
5.5 Tissue reactions 62
6. Discussion 63
6.1 Electroactivity and the surface properties of biocompatible PPyHA and PPyHA-CNT electropolymerized films 63
6.2 Hydrolytic stability of PPyCS in hASC in vitro 64
6.3 Electrical conductivity in hydrolysed PPyCS and PPyHA 65
6.4 The role of surface charge on early cell attachment 66
6.5 Correlation between surface charge, roughness and cell adhesion 67
6.6 Electrical stimulation in 2D and 3D cell cultures 68
6.7 In vivo biocompatibility of PPyCS 69
7. Conclusions 70
References 71
Publications 1-5 85

Acknowledgements

This thesis work is completing my longish introductory journey to the world of conductive polymers. For me it all started in a project meeting at VTT in the year 2006, when I first met Dr. Edwin Jager from Micromuscle AB. Soon afterwards I found myself as a visiting researcher surrounded by the enthusiastic staff and students at the Intelligent Polymer Research Institute (IPRI) at the University of Wollongong Australia. During that six month period in 2006-07 at UOW I had a unique opportunity to “breathe” organic conductive materials, especially polypyrroles, and the Pacific air, learning and making experiments which were finally reported in the first publication of this thesis work. I would like to thank Professor Geoffrey Spinks for welcoming and hosting me, and to especially express my appreciation to Philip Whitten, Scott MacGovern and Mehrdad Bahrami-Samani for their involvement in the experiments, and their friendship.

Biomedical applications of organic conductors in tissue engineering in 2007 was a new and topical research area for the tissue engineering group at the University of Tampere and the biomedical engineering department at Tampere University of Technology. I would like to thank Professor Riitta Seppänen (UTA), and my supervisors Professors Minna Kellomäki and Jari Hyttinen (TUT) for taking this bull by the horns and starting collaboration in joint projects with VTT. The majority of the work reported in papers II-IV was done during the two joint projects 2009-2012 funded by TEKES, whose financial support is also greatly appreciated. During that time I had a possibility to visit UOW again, this time for AFM work with a wizard, Dr. Michael Higgins, who has contributed a great deal to my work (publication 3) and has continuously worked on the subject. Many thanks also belong to Professor Gordon Wallace, the captain of the crew at UOW.

I would like to address special thanks to my tenacious and enthusiastic collaborator Docent Suvi Haimi from the adult stem cell group at the University of Tampere, who has been the driving force in the research projects. And special thanks belong to the co-workers at UTA, Aliisa Siljander and Miina Björninen, who have done enormous work in culturing cells and tirelessly stimulating them. I want also to acknowledge all the co-authors and my team members at VTT, Dr. Tommi Vuorinen, Hannu Välimäki and Timo Flyktman, how have contributed to the experimental work, and the project co-workers at TUT, Anne Rajala, Maiju Hiltunen and Elina Talvitie, for their great contributions.

I express my gratitude to my former and present superiors at VTT, my team leaders Dr. Mika Paajanen, Dr. Kirsi Tappura, Dr. Outi Härkki, for their support in initiating and completing the work.

Finally, I thank my parents Hannu and Lea Pelto for their continuous encouragement. Most of all, I thank my wife Elina for her endless patience, love and kind support throughout the years, and our beloved little Alisa. You are my inspiration and my haven.

List of publications

(P1) Electroactivity and biocompatibility of polypyrrole-hyaluronic acid multi-walled carbon nanotube composite. **Pelto, Jani**; Haimi, Suvi; Puukilainen, Esa; Whitten, Philip O.; Spinks, Geoffrey M.; Bahrami-Samani, Mehrdad; Ritala, Mikko; Vuorinen, Tommi. *Journal of Biomedical Materials Research Part A*. Vol. 93 (2010) No: 3, 1056 – 1067.

(P2) Novel polypyrrole-coated polylactide scaffolds enhance adipose stem cell proliferation and early osteogenic differentiation. **Pelto, Jani**; Björninen, M.; Pälli, A.; Talvitie, E.; Hyttinen, J.; Mannerström, B.; Suuronen Seppänen, R.; Kellomäki, M.; Miettinen, S.; Haimi, S. *Tissue Engineering - Part A.* Vol. 19 (2013) No: 7 - 8, 882 – 892.

(P3) Surface properties and interaction forces of biopolymer-doped conductive polypyrrole surfaces by atomic force microscopy**. Pelto, Jani;** Haimi, S.P.; Siljander, Aliisa; Miettinen, S.S.; Tappura, Kirsi; Higgins, M.J.; Wallace, G.G. *Langmuir.* American Chemical Society . Vol. 29 (2013) No: 20, 6099 – 6108.

(P4) Comparison of Chondroitin Sulfate and Hyaluronic Acid Doped Conductive Polypyrrole Films for Adipose Stem Cells. Björninen, M; Siljander, A**; Pelto, Jani**; Hyttinen, J; Kellomäki, M; Miettinen, S; Seppänen, R; Haimi, S. A*nnals of Biomedical Engineering*. Biomedical Engineering Society. Vol. 42 (2014) No: 9 , 1889 - 1900.

(P5) Polypyrrole coating enhances new bone formation on polylactic/glycolic acid -β-tricalcium phosphate screws in rabbits. Zhao, M-D.; Björninen, M., Cao, L; Wang H-R., **Pelto J**.; Hyttinen J.; Jiang Y-Q.; Kellomäki M.; Miettinen S.; Haimi S.; Dong J. Polypyrrole coating enhances new bone formation on polylactic/glycolic acid -β-tricalcium phosphate screws in rabbits. *Submitted to Tissue Engineering – Part A*.

Author's contributions

(P1) Conducted the majority of the experimental work excluding the cell work. Synthesized the polypyrrole samples, designed the setup and the measurement for the electrochemical atomic force microscopy (AFM), in situ Raman spectroscopy methods and the quartz crystal microbalance (QCM) measurements. Carried out the analysis and interpretation of the AFM and Raman data. Designed the manuscript and was the first author in Publication 1.

(P2) Developed the in situ polypyrrole polymerization methods and supervised the generation of the polypyrrole coated PLA scaffolds. Conducted the scanning electron microscopy (SEM) and the AFM analyses. Designed the experiments and interpreted the generated electrospray-ionization mass spectroscopy (ESI-MS) data. Designed and set up the 3D electrical stimulation platform. Conducted the impedance measurements for the electrodes and 3D scaffolds. Designed the material characterization parts of the experiments and was the first author in Publication 2.

(P3) Designed and conducted the Kelvin Probe Force Microscopy (KFPM) and fluid AFM force mapping experiments. Analysed the data of the force-distance curves. Carried out the statistical analyses for the cell attachment data. Designed the experiments and was the first author of Publication 3.

(P4) Developed the electrochemical polymerization methods and supervised the syntheses of the biopolymer doped polypyrrole film samples. Designed the setup for the electrical stimulation of cells. Carried out the characterization of the samples by AFM. Interpreted the impedance spectra of the film samples. Partly designed and co-authored the manuscript.

(P5) Developed the polypyrrole-chondroitin sulfate in situ polymerization method utilizing ferric oxidant onto polylactic/glycolic acid -β-tricalcium phosphate screws. Co-author in the manuscript.

1. Introduction

Bioelectrical potentials and currents are fundamental driving forces acting in functional tissues and cells. For example, neural and muscle tissues are built from excitable neural and muscles cells, having their own developed mechanisms for detecting and transporting electrical signals and responding to them appropriately, e.g. by the contraction of the skeletal muscle cells. The transport of electrical signals within all types of cells is mediated by sodium (Na^+), potassium (K^+) and calcium ions (Ca^{2+}), driven by the changes of the intra- and extracellular ionic concentrations. Membrane proteins, such as the Na/K-pump, Ca-channels and other transmembrane receptors actively maintain the balanced concentration of ions and regulate the permeability of the cell membrane. External stimulation of the cells, and the tissue, means actively affecting these protein structures, either by mechanical excitation (Brown, 2000) or by external electromagnetic energy (Adey, 1993). Electrical stimulation is commonly applied in cardiac pacemakers, electrical muscle- and neural stimulators, etc. In the electrical engineering aspect, the extracellular volume and the cell culture medium are inhomogeneous ionic conductors and the cell membranes are highly electrically insulating. Transmembrane proteins, whose permeability to ions and molecules is controllable by transmembrane potential difference, i.e. electrical stimulation, have a key role in regulating the cell behaviour in excitable tissue (Newton *et al.*, 1999).

Bioelectricity is not restricted to excitable tissues. It is widely accepted that bioelectrical phenomena are involved in embryonic development, organogenesis, healing of damaged tissues and remodelling of bone. For example, Fukada and Yasuda (1957) reported the piezoelectric generation of electrical potentials in mineralized bone. Later, it has been well established that constant regeneration of the mineralized bone *in vivo* requires constant loading of the bone mechanically (Carter, 1984), which in effect induces ionic (electrokinetic) currents and, subsequently, stimulation of the osteoblast cells (Carvalho *et al*., 1994). On the cellular level, movement can be linked to the stimulation of the mechano- and voltage sensitive ion channels and signalling proteins in the cell membrane (Spadaro, 1997). Hence, the external stimulation triggers an ongoing cascade of intracellular biochemical reactions producing extracellular matrix (ECM) components and signalling molecules directing the proliferative and the differentiation phases of new, premature and undifferentiated cells.

The fate of undifferentiated cells can be also manipulated by applying electrical current to cells *in vitro*. For example, electrical stimulation (ES) has been successfully utilized in cardiac tissue engineering (TE) in directing the fate of mesenchymal stem cells (MSCs) towards cardiac myocytes in 2-dimensional and 3-dimensional cell cultures (Tandon *et al*., 2009). Furthermore, stimulation of the cells by the application of capacitively coupled external AC and DC electrical fields has been shown to both orient and induce the migration of cells (McGaig *et al.,* 2005). These

early studies have paved the way for the application of ES in the TE of connective tissues, such as bone, cartilage and tendon. Recently, human adipose stems cells (hASCs) have been successfully utilized in the TE of bone (Mesimäki *et al.,* 2009). However, the clinical application of the methods developed would require enhanced proliferation and differentiation phases *in vitro*. Hence, for practical patient treatments there is a rationale for applying external ES to accelerate the *in vitro* culturing of autologous hASCs. Furthermore, in favour of the external ES, the stimulus can be considered a safer and less expensive alternative compared to the bioactive growth factors which are commonly applied in TE.

Stimulation current can be delivered to the cells by microelectrodes, typically made of platinum metal or activated iridium oxide, offering large faradaic charge, and typically applied in the stimulation or localized small volumes of neural tissue. Larger area micro-patterned electrodes of indium tin oxide (McCullen *et al.*, 2010) or macroscopic electrodes made of carbon rods (Tandon *et al.*, 2009) have been utilized in the stimulation of cell cultures. In 2D cultures the cells can be attached directly onto the conductive polymer stimulation electrode (Shi *et al.*, 2004; 2008a; 2008b), or on an insulating substrate, and stimulated through the ionic currents through the cell culture medium (Tandon *et al.*, 2009). In 3D cell culture the cells are attached to a macroscopic porous scaffold biomaterial and the electrical currents are applied from metallic electrodes large enough to deliver current throughout the scaffold. Typically, the stimulation electrodes are isolated from the cell culture medium and the scaffold by salt bridges (Sun *et al.*, 2004; 2006).

It is commonly recognized that the delivery of stimulation current is far more efficient for the microelectrodes in the vicinity of the cells and tissue. This condition is rarely possible in stimulating cells attached to a 3D scaffold by using planar electrode geometry, where the distance between the electrodes and the cells can be millimetres. Hence, larger stimulation potentials are typically utilized, which leads to various complications: In DC stimulation use, high electrode potentials arise, leading to electrochemical reactions, such as electrolysis, degradation of cell culture medium components and cell death (Stevenson *et al*., 2010; Gimsa *et al*., 2005). Therefore, in order to alleviate these, AC- and biphasic pulsed DC currents, electrochemically stable, and low polarizable electrodes have been suggested (Merrill *et al*., 2005). In addition, pulsed stimulation waveforms allow control over the efficacy of electrical energy transfer by matching the frequency dependent electrical properties of the stimulation cell and the tissue (Gimsa et al., 2006).

The cell culture medium itself has significant ionic conductivity, but commonly applied polymeric scaffold materials, e.g. bioabsorbable polylactide (PLA) nonwoven are dielectrics. Hence, the 3D stimulation currents are applied to the cell primarily by the cell culture medium. In contrast, electrically conductive biomaterial will better target the stimulation current to the cells (Shi *et al*. 2004; Zhang *et al*. 2007). Conductive polymers, such as polypyrrole (PPy) containing biological functionalization offer electrical conductivity combined with large faradaic charge capacity for the

delivery of stable stimulation currents and attractive biological properties for the electrode-cell interfacing. A good combination of electrical conductivity and interaction with the cells PPy has been already applied in neural probes and cochlear implants (Richardson *et al.* 2009). These studies pave the way for future application in TE.

Bioactive ECM components, hyaluronic acid (HA) and chondroitin sulfate (CS) have been utilized as dopants for PPy (Collier et al., 2000; Cen *et al*., 2004; Serra Moreno *et al.*, 2008). HA and CS have been recently explored in bone tissue engineering (Wollenweber *et al.*, 2006; Jha *et al.*, 2011). However, the properties of PPyHA and PPyCS biomaterials, such as their surface elastic and electronic properties and surface topography in the nanoscopic scale, the stability of their electronic conductivity in hydrolysis and sterilization, and their biodegradation have not yet been thoroughly examined. The main the target of this thesis is to elucidate the roles of these, especially in the perspectives of clinical TE and long term implantable devices. For example, to date, studies concerning the stimulation of cells on PPy have been limited to cell culturing and electrical stimulation on a single well plate environment (Shi *et al*. 2004; Zhang *et al*. 2007; Lee *et al*., 2009), which is not practical for tissue engineering. Furthermore, potentially toxic reagents and chemistries have been utilized in the chemical synthesis of PPy, which would not allow long term implantation.

Application of electrochemical microactuation by bulk expansion has been well established for PPys containing hydrophobic molecular dopants (Smela and Gadegaard, 2001; Berdichevsky and Lo, 2004; Higgins *et al*., 2009; Svennersten *et al.*, 2011). This work has further explored the actuation properties of biopolymer doped PPys, with the possible application of electromechanical stimulation of cells *in situ*. Such electrochemical actuation property would open up perspectives in the use of the PPy in 2-dimensional cell culturing substrates, or even in the stimulation of 3-dimensional tissue engineering scaffolds.

There are numerous fundamental aspects regarding the practical use of biopolymer doped PPys in tissue engineering on other implantable devices which still require more attention, such as the availability of PPy material, processability, reproducible synthetic routes, sterilizability, stability of the electronic properties during incubation, biostability of the PPy and the dopants, long term toxicity, etc. For example, the chemical and the electrochemical routes for the syntheses of PPyHA and PPyCS are currently not well established. In this work, conductive PPyHA and PPyCS coatings have been electrochemically deposited on various 2D metallic stimulation electrode susbtrates and chemically polymerized onto 3D bio-absorbable nonwoven scaffolds and bone fixation screws. Simple and reproducible laboratory methods for the syntheses of PPyHA and PPyCS, also applicable for production scale, and compatible for tissue engineering techniques utilizing 24- multiwell plate cell cultures, have been developed. The surface properties and the osteogenic differentiation of hASCs have been explored on 3D nonwoven scaffolds *in vitro*. To

demonstrate the performance of the chemically polymerized PPyCS coating, a 26 week preclinical study on New Zealand rabbits has been conducted. Tissue reactions and the stability of PPyCS coated bioabsorbable bone fixation screws were evaluated *in vivo*. The possible alternative synthetic routes and current micro-patterning techniques have also been shortly reviewed.

2. Literature survey

2.1 Historical perspective

PPy is a non-soluble black organic substance, generated by the chemical oxidation of heterocyclic five-membered molecule pyrrole, a naturally occurring oily constituent of coal tar. Polypyrrole in its amorphous and weakly electrically conductive form was first reported by Italian chemists in 1916 (Angeli and Alessandri, 1916), who oxidized pyrrole by hydrogen peroxide. It was reported in 1963 by Weiss and co-workers (McNeill *et al.* 1963) that polypyrrole generated by the pyrolysis of tetraiodopyrrole is highly electrically conductive. Obvious to the researchers of today, the observed high conductivity was due to the reasonably chosen polymerization conditions and the fortunate discovery of iodine doping, but not by serendipity. Since 1963, extensive research on the synthesis, new dopants, conduction mechanisms and characterization of polypyrrole materials has dramatically improved their performance. Numerous applications where the electronic conductivity, electrochemical charge storage or redox activity can be utilized have been proposed, such as electrostatic discharge protection in textiles (ESD) (Pron *et al.*, 1987), conductive textiles (Gregory *et al.*, 1989), supercapacitors (Rudge *et al.*, 1994), lithium ion batteries (Naoi *et al.*,1987) and microactuators for microrobotics and cell clinics (Smela, 1999; Jager *et al.*,1999; Jager *et al.*, 2002).

2.2 Electronic conduction in PPy

Intrinsic electrical conductivity in conjugated polymer is a complex and still debated subject. The mechanisms of charge transport in PPy are not in the focus of this dissertation, but a short introduction on the subject is advantageous in understanding the behaviour of the material in physiological electrolytes. It is widely agreed that intra-chain electronic charge carriers (polarons and bipolaron), i.e. delocalized charged radical cations, are associated with the lattice distortion caused by chain conjugation. The polaron lattice is illustrated in Figure 1. Inter-chain electronic charge transport is likely caused by quantum mechanical hopping, e.g. Mott's variable-range hopping conduction mechanism (Yoon, *et al*., 1995) and/or via chemical crosslinks of PPy chains.

Conceptually, the doped PPy chain is always linked to an anionic dopant molecule (A^{n-}). The positive charge on the PPy chain (PPy^{n+}) is electrically neutralized by the anionic dopant $PPy^{n+}A^{n-}$. The dopants are incorporated into a layered supramolecular structure of polypyrrole during synthesis, rendering the materials both into the properties of the doped polypyrrole chains and the

dopants. Doping can be thought of as intercalation of dopant molecules, unrelated to interstitial atomistic doping if inorganic semiconductors. Furthermore, in fully doped PPy the amount of dopant is high. Up to 30-50% per dry weight of the $PPy^{n+}A^{n}$ complex may consist of dopant molecules. In fully doped polypyrrole, approximately one dopant molecule or anionic group per three monomeric pyrrole units of the conjugated chain is inserted.

Conductivity by ionic charge carriers is possible in PPy swollen by electrolyte solution (such as physiological salt solution) or in the gel state. In weakly doped (neutral) PPy^{0}, the ionic conductivity may be the dominant mechanism of charge transport.

Regardless of the synthetic route, PPys are not highly crystalline solids. However, early diffraction studies (Geiss *et al.*, 1983; Wernet et al., 1985) already showed that atomistically small periodic structures or crystals “islands in an amorphous sea”, or at least local molecular order is present in the solid state. The high electrical conductivity and mechanical properties are predominantly due to the molecular order. It is widely known that the electronic properties of PPy are anisotropic and that they vary in the nanoscopic domain, reflecting the nodular morphology observed in SEM and AFM images, for example. Hence, engineering of the properties is possible by affecting the material in the molecular level, that is by controlling the synthesis conditions affecting the molecular weight and chain branching of PPy, applying substitute pyrrole monomers and by applying functional dopants.

2.3 Commercial applications

*Se*veral industrial companies have developed products based on polypyrrole. Electrostatic discharge control (ESD) coating and composites and electrochemical charge storage are by far the most commonly studied applications. The Milliken Corporation has been a front runner in conductive textile application in introducing polypyrrole coated polyamide, polyester and glass fiber products (Gregory *et al.*, 1989). At present, polypyrrole coated acrylic fibers are available from Sterling Fibers, Inc. (Florida, US).

Polypyrrole lithium ion batteries have been studied by BASF SE (Ludwigshafen am Rhein, Germany) and VARTA AG (Ellwangen, Germany) already in the mid 80’s (Naarman, 1986; Naegele and Bittihn, 1988). Those developments did not result in industrially successful products, but the use of polypyrrole in batteries is still the subject of intensive research. The Matsushita Electric Industrial Company, Ltd. (Osaka, Japan) has been developing from the early 90’s to the present commercial solid electrolyte capacitors utilizing polypyrrole in Aluminium/MnO_2.

A limiting aspect in the widespread industrial use of polypyrrole is the lack of its processability, i.e. the polymer cannot be easily dissolved or processed in melt state. Suppliers of polymerized polypyrrole films, powders or dispersion for research purposes have been scarce. BASF has been the main source of pyrrole and polypyrrole with the brand name Lutamer from 1988. At present,

polypyrrole dispersions and composite powders with titanium dioxide and carbon black are available in research quantities from Sigma-Aldrich.

A recent interesting pre-commercial development in the biomedical materials sector is a block-copolymer of polycaprolactone (PCL), and PPy is currently marketed with the brand name Biotron PP-LM. This material is available in the Sigma-Aldrich catalog (accessed 14.11.2014).

2.4 Biomedical application in the research phase.

Conducting polymers are attracting interest in tissue engineering application as they can deliver electrical and electromechanical stimulation to cells. Of those PPy and poly(3,4-ethylenedioxythiophene) (PEDOT) are the most investigated for biomedical applications owing to their proven compatibility with tissues and cells (Guimard *et al*., 2007; Ravichandran *et al*., 2010; Balint *et al.*, 2014). PPy has been intensively investigated for bone (Serra Moreno *et al.*, 2012; Meng *et al.*, 2011) and neural applications (Richardson *et al*., 2009) due to its easy modification with bioactive molecules, which can be trapped and released by electrical signals (redox cycling) and highly adjustable properties, such as surface charge and topography (Gelmi *et al.*, 2010; Gilmore *et al.*, 2009; Serra Moreno *et al*., 2008). In addition, PPy has been applied as coatings for osseointegration in titanium implants (Di Giglio *et al.*, 2001) owing to the surface properties mimicking more biological surfaces than hard ceramic or metallic ones. Furthermore, there are applications in a vast number of biosensors (Ates, 2013), drug delivery systems (Wang X *et al.*, 2008) and actuators (Liu *et al*., 2009; Jager *et al.,* 2002).

Although an organic polymer surface offers obvious advantages, the inherent biostability of the PPy chain has limited the applications in biodegradable implants. Therefore, bioerodible and potentially biodegradable alternating copolymers of pyrrole and acid-substituted pyrroles (Zelikin *et al*., 2002), pyrryl-thiophene copolymers with trimeric electrically active oligomers linked to hydrolytically degradable ester linkages and aliphatic linkers (Rivers *et al.*, 2002), and more recently, PT quarterthiophene polyesters or adipic acid (Guimard et al., 2009), have been developed and suggested for implantation. However, their electrical properties have not been comparable to high polymeric PPys. Furthermore, the biochemical pathways of potentially toxic degradation products containing trimeric and quatromeric pyrroles and thiophenes may be of concern.

2.5 Electromechanical microactuation

Electromechanical microactuators based on PPy have been extensively studied (Smela, 1999; Jager *et al*., 1999; Temmer, *et al*., 2012; Gaihre *et al.*, 2012). Dimensional changes of electro-polymerized PPyDBS on a metallized polymer film (Au/PET) film have been transferred to the large bending movement of bilayer or trilayer actuators (Smela, 1999; Jager *et al*., 1999). Bending mechanisms have been applied in miniatyrized microfingers, lifting plates, microrobots, closable

microvials and valves operating in biological electrolytes (Jager *et al*., 1999, 2002). Bulk expansion of PPyDBS has been utilized in microvalves (Berdichevsky and Lo, 2004) and recently in electromechanical stimulation of epithelial cells utilizing micropatterned PPyDBS on silicon (Svennersten *et al.*, 2011). Typically, the full range of motion in the devices can be seen in approximately one volt potential range (e.g. -0.8 V vs. +0.2 V vs. Ag/AgCl), where the CV of the PPyDBS shows that the full oxidation and reduction charge has been transferred during the electrochemical cycle.

The biological compatibility of DBS dopant has been well established in short term studies, also in our study where we utilized PPyDBS as a bridging layer underneath a PPyHA-CNT film (P1, 2010). DBS is known to slowly leach out of the PPy film. Furthermore, PPyDBS has a relatively hydrophobic surface with no apparent biological functionality. Therefore, it is anticipated that better response in cell culturing or permanent implantation would be achievable by PPys with biological active dopants, e.g. PPyHA and PPyCS, and other polymeric dopants, such as PSS. However, the electromechanical (bulk) expansion of these materials has not been thoroughly investigated.

The speed of operation of the electrochemically driven actuator is dependent on the diffusion of the charge carriers (see section 1.2) in the PPy chain and the diffusion of the electrolyte ions, alkali metal ions (Na^+), and their hydration water during the redox cycling. Hence, the necessary but not sufficient properties for a material actuating by bulk expansion are as follows (i) moderate redox activity and electronic (polaron) conductivity in the doped state, comparable to highly doped PPys, (ii) bulkiness or total immobility of the anionic dopant, (iii) sufficient hydrophilicity to allow fast ion/water ingress and outgress (Smela and Gadegaard, 2001; Bay *et al.*, 2001; 2002a; 2002b). The sensitivity of the actuation on the choice of hydrophilic and immobile PSS dopant is illustrated in the following study by Higgins *et al.* (2009). They report on visualizing the actuation of ultrathin PPyPSS films in 0.05 M NaPSS electrolyte by electrochemical AFM (EC-AFM). PPyPSS film thickness was varied over 3 orders of magnitude from the micrometer to the nanometer range and actuation height measured as a function of the applied potential and scan rate. They found 100-350% increase in strain and strain rate when the film thickness was reduced below 100 nm. However, the attained strains (2.6% at scan rate 50 mV/s) were quite modest compared to studies concerning PPyDBS (Smela, 1999; Jager *et al*., 1999, 2002). EC-AFM measurements on PPyDBS have yielded different results, showing that an optimal thickness with 36% strain was 1.5 µm. Expansion was significantly reduced either side of this optimal thickness to 15-20% for the studied 150 nm and 3 µm thick films (Smela and Gadegaard, 2001).

2.6 Motivation for the tissue engineering applications of PPy

The range of elastic moduli of synthetic organic polymers can be designed to match with moduli of the biological hard and soft tissues, from the properties of cortical bone (10 GPa range) to

natural soft hydrogels (<1 MPa range). This is to some extent also possible for polypyrrole due to the very distinguishing features of conductive polymer syntheses utilizing anionic polymers, the polymeric dopants. These dopants form ordered supramolecular structures (supramolecular complexes) with the polypyrrole chains (see Figure 1) (Armes *et al*., 1991; Genies *et al*., 1993). Polymeric dopants and surfactants, such as polystyrene sulfonate, typically have significant influence on the microscopic morphology (Fonner *et al*., 2008) and electrochemical charge storage properties (Baker *et al*., 1991) of polypyrrole. The morphology of the solid state material might reflect the micelle structure of the polymerization medium, in generating nanorods, nanospheres or nanofibers (Antony *et al*., 2010). Incorporation of bioactive glycosaminoglycan (GAG) polymers such as hyaluronic acid (HA) and chondroitin sulphate (CS) into the polypyrrole material will result in novel materials having surface properties of both polypyrrole, i.e. intense color and electrical conductivity, and the hydrophilic character and surface biochemical functionality of the two GAGs. CS and HA are the two abundant GAG components in the proteoglycans of the extracellular matrix (ECM) of animal tissues (Mikami and Kitagawa, 2013). The HA and CS polymer structures are depicted in Figure 2A and 2B, respectively.

Both CS and HA have their role in the remodelling and mineralization of bone matrix and they have been reported to support osteogenic differentiation of MSCs in vitro within various scaffolds modified with these GAGs (Wollenweber *et al.*, 2006; Jha *et al.*, 2011).

The possibility of applying the functionality *during* simple synthesis, without applying complicated click-chemistry and potentially toxic reagents, is very attractive for biological applications. It is also a unique feature of conductive polymers. For these reasons the biopolymer doping of polypyrrole is today the subject of active research, including this work.

2.7 Electrochemical synthesis

Basic principle*.* In a traditional three electrode electrochemical cell, pyrrole is readily polymerized and deposited onto the working electrode. The onset of the polymerization is typically seen at oxidizing electrochemical potential above +0.55 to 0.6 V vs. Ag/AgCl reference electrode, which is the oxidation potential of the pyrrole monomer in water. The deposited film has an electrical conductivity in the range 10-10000 S/m, attributable to the electronic conductivity along the conjugated pyrrole units along the 2-5 couplings of the pyrrole ring (see Figure 1). The electropolymerized PPy is a cross-linked (e.g. by 3-4 carbon couplings), insoluble material and the majority of the material has random head-to-tail tacticity (Genies *et al*., 1983).

The exact mechanism of the polymerization has been studied already by Diaz and co-workers. Their proposed mechanism is still currently the most accepted model of the complex reaction scheme. It has eight individual reaction steps and proceeds via a radical-radical coupling mechanism. The deposition of PPy film starts from discrete points, which then begin to fuse into a

coherent film. The resulting film has typically a microscopically nodular “cauliflower” structure which implies that the mechanical and electrical properties vary significantly in the microscopic domain (Genies *et al*., 1983).

Synthetic variables. It is now widely recognized that the properties of conductive films are dependent on the polymerization conditions, for example the substrate material, nucleophilicity of the solvent(s), dopant and/or the surfactant, acidity of the dopant and the pH of the reaction medium (Heinze *et al*., 2010).

For example, the acididity of the dopant anion has an effect on the polymer growth, evidenced by a hallmark study on a series of carboxylate anions doped PPys. Lower conductivity of the PPy was observed for the higher basicity of the anion due to reduced interactions between the positive charges of the PPy chain and the anions. In contrast, anion acidity led to an increase in the conductivity. Secondly, anion nucleophilicity interfered with the reaction by increasing the formation of soluble products (Kuwabata *et al*., 1988).

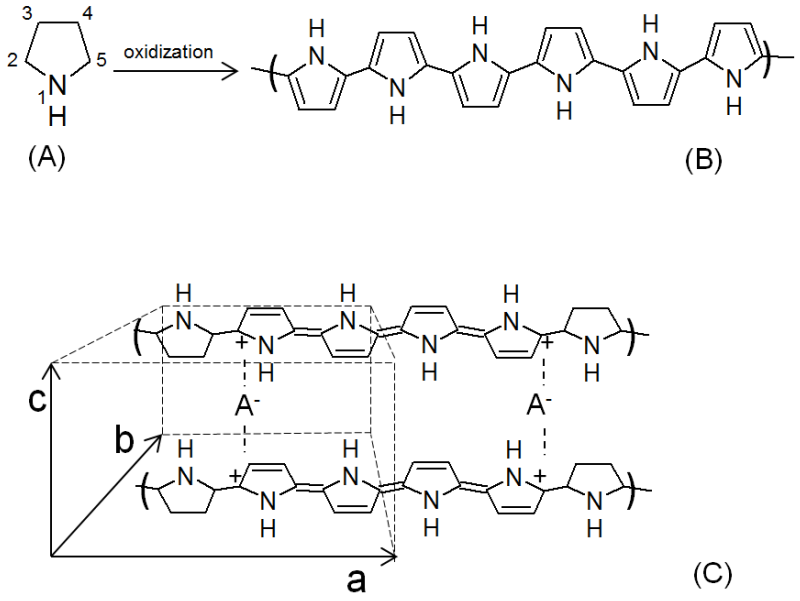

Figure 1. Schematic presentation of the PPy-dopant complex. (A) Pyrrole monomer and indexing of the carbon atoms. (B) Neutral PPy chain. (C) Doped PPy chain. The dopant anion (A-) is located between stacked pyrrole rings in every third position of the conjugated PPy chain. The unit cell and crystallographic axes are marked by a, b and c.

Reproducible syntheses require the purity of the monomer. For example, removal of colored dimeric and oligomeric species from the monomer by vacuum distillation is essential. Due to the monomer oxidation by atmospheric oxygen, colored mers are generated into the monomer reservoir during long term storage. Oxygen should be eliminated from the polymerization reactions as it reacts with the monomer with a similar mechanism as other nucleophiles (Wallace *et al.*, 1997). Optimization of the electrochemical potential applied or the current density on the substrate

should be done as substrates have different polarization overpotential and affinities for the deposited polymers (Zhou *et al*., 2002). In general, choosing the synthesis conditions must be carefully done, as in the two most extreme cases polypyrrole can form a very well adhered, uniform and dense film, or the polymer might not precipitate at all on a given electrode surface. Pyrrole oxidation with non-compatible substrate and/or ill-designed synthesis will result in the generation of low molecular weight soluble oligomers into the polymerization medium, which has been clearly demonstrated in the experiments carried out in the current work.

In a typical setup the polymerization is carried out in water, acetonitrile/water mixture, propylene carbonate or ionic liquid solvents in the presence of organic sulfonic or carboxylic acid dopants and working electrode potential > +0.52 V (vs. Ag/AgCl) (Wallace et al., 1997). Stability of the solvent limits the polymerization potential window, which in the case of aqueous medium is limited to electrolysis of water (+1.26 V vs. Ag/AgCl). The nature of the working electrode surface is largely responsible for the initial rate of monomer oxidation, then subsequently the oligomerization of pyrrole and finally the precipitation of the polymer by the mechanism originically suggested by Diaz *et al*. (1981).

Structure of the electropolymerized PPy. Early electron diffraction studies (Geiss *et al*., 1993) and wide angle/small angle x-ray diffraction (WAXS/SAXS) studies (Wernet *et al*., 1983) implied that electropolymerized polypyrrole films typically have some degree of molecular order, either local order in the atomistic domain (Figure 1C, crystallographic axis c) or more microscopically (observable by WAXS or electron diffraction) preferred orientation of the polypyrrole chains indicated by sharp WAXS peaks and/or SAXS peaks. However, the molecular order is dependent on the size and structure of the dopants. For example, PPys doped by small inorganic anions (chloride, sulphate, etc.) show only very broad diffraction peaks and are generally reported “amorphous”, whereas larger organic anions presenting having cyclic structures (toluene and camphor sulfonates, etc.) may induce significant molecular stacking (crystallographic a-b plane, Fig.1C) in the plane parallel to the electrode surface (Wernet *et al*., 1983). In general, molecular order has a positive impact on the mechanical and electrical properties of the material.

Role of the dopants. Acidity and hydrophilicity and size of the dopant molecules also play a key role in the organization of the materials on the electrode surface and in the bulk, as those factors may contribute to the coordination of the dopant mole on the electrode and the molecular packing of the materials (Figure 1). Protonation (Zhou and Heinze, 1999) and the oxidation potential (Wallace *et al*., 1997) of the pyrrole monomer in the nucleophilic solvents will be important in determining the rate of polymerization, as they directly affect the formation of reactive pyrrole dimers (Zhou and Heinze, 1999). Under efficient polymerization conduction the deposited film thickness can be estimated from the electrical charge Q_{pol} transferred in the electrochemical cell.

For the galvanostatic polymerization of PPyDBS on Au substrate taken as an example, a linear relation has been verified for 0-1000 nm films (53× Q_{pol} – 153) nm, Q_{pol} [mC/cm^2] (Smela, 1999).

Microelectrode substrates. Polymerizing on µ-electrodes the local current densities are typically higher than on larger area electrodes. This is due to the enhancement of the electric field near the edges of the electrodes. The electric filed effects induce enhancement in the rate of the mass transport to and from the electroactive center of the polymerization, which may unexpectedly cause increased difficulty in obtaining a polymeric deposit (Wallace *et al*., 1997). In contrast, on large area substrates, the depletion of the monomers and dopants from the reaction active centers may become important limiting factor for the rate of polymerization.

Engineering the adhesion of the PPy film. Bridging PPyPSS layers has been utilized to improve the surface morphology and better mechanical and electrical properties of PPyHA films on ITO. Bilayer PPyPSS/PPyHA films were found promising as electrically conductive cell culture substrates substrates for vascular tissue engineering. (Collier *et al*., 2000)

Mechanical actuation in electropolymerized PPy. PPy microactuators are unique designs generated by controlled electropolymerization. The devices generate force and movement (linear of bending) by dimensional change of PPy in electrolytes. In these devices the adhesion of the polymer on substrate (typically Au or platinum metal) is critical. Submicron PPyDBS films on Au have been previously applied as bilayer microactuators operated in physiological fluids by oxidation-reduction cycling (Jager *et al*., 1999; Pei and Inganäs, 1992). In electrochemical cycling, delamination of the polypyrrole is often seen because of the large dimensional changes of the PPy film. Up to 30% swelling perpendicular to the plane of the substrate has been certain in four submicron thick electropolymerized films (Jager *et al*., 1999; P1, 2010). The volume change is believed to be mediated by the ingress and outgress of hydrated small ions from electrolyte solutions. The hydrated ions are diffusing in the intra-chain space, inducing swelling perpendicular to the PPy chain (Fig. 1C, crystallographic axis c) (Bay *et al*., 2001). Additionally, the PPy chain will undergo a less significant dimensional change in the conjucated carbon-carbon bonds upon polaron lattice formation (see Figure 1B and 1C, crystallographic axes a).

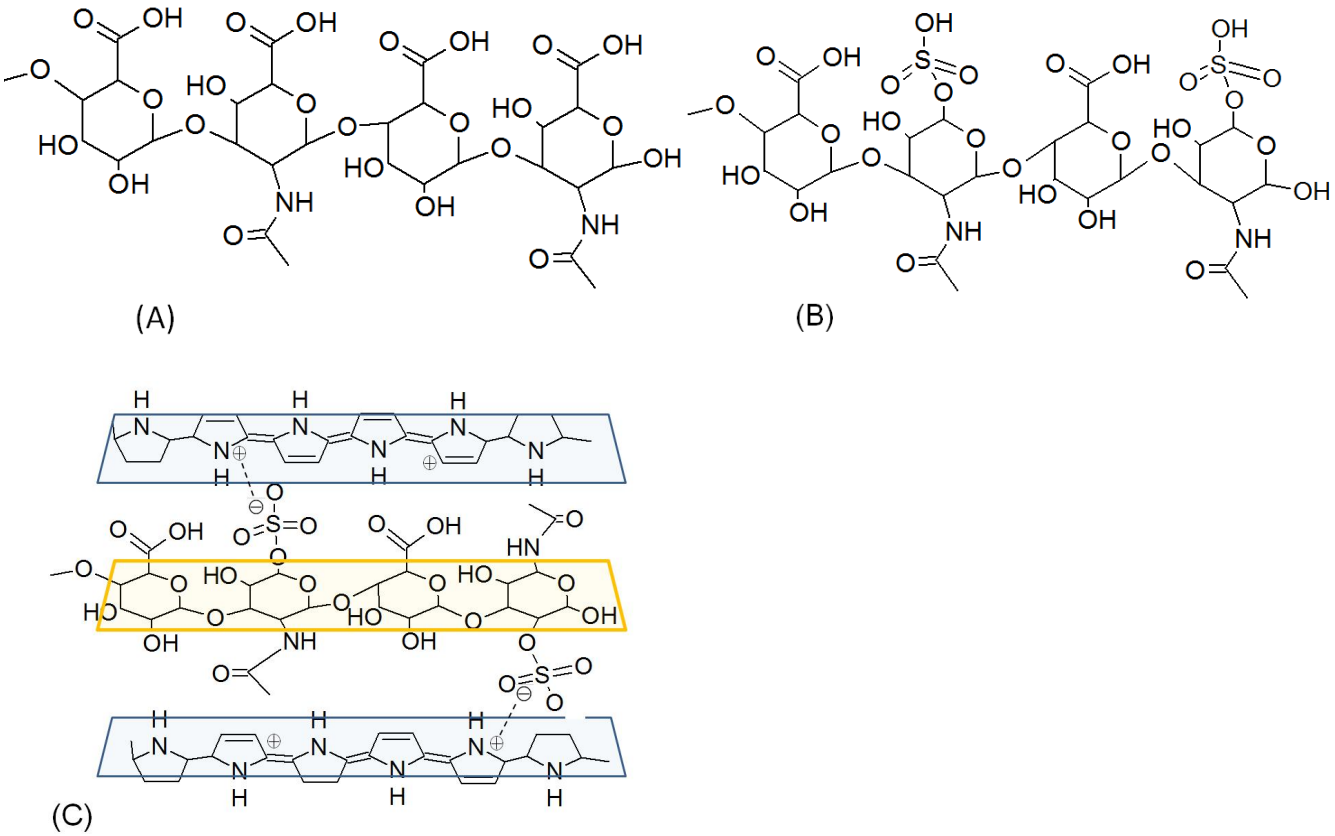

Figure 2. 2D molecular structure of the polymeric dopants (A) HA and (B) CS. (C) 3D schematic presentation of a possible insertion of the polymeric dopant (CS) between PPy chains. The size of the dopants molecule may change the intra-chain interaction in PPy, affecting the mechanical and electrical properties of the material. Furthermore, the surface properties such as hydrophilicity of the dopants are incorporated into the PPy.

The reported Au/PPy microactuator designs have invariably involved hydrophobic dopants carrying sulfonic acid functionality (DBS or trifluorosulfonimide TFSI) (Smela, 1999; Wu Y *et al*., 2006). Mechanical actuation of biopolymer doped PPys is discussed further in section 5.3.

2.8 Polymerization by chemical oxidants in liquid phase

Analogous to electropolymerization, the pyrrole ring is easily oxidized and polymerized by various oxidizing agents, such as Fe^{3+}, Cu^{2+}, $Ce^{4+,}$ Cr^{6+}, Mn^{7+} salts, peroxydisulfates, iodine, organic peroxides, hydrogen peroxide with catalytic amount of Fe^{3+}, quinones and enzymes, for example (Rodriquez *et al*., 1997). The polymerization reactor will only result in highly conductive material when the concentration of the oxidant is in a suitable regime (Blinova et al., 2007). This concentration range is dependent on the oxidation potential of the oxidant, but is typically high compared to the concentration of the monomer. In practice, roughly 2.3:1 oxidant/monomer ratio

for one-electron oxidants is feasible. For example, 0.5 M to 2 M Fe^{3+} ions and 0.1 M to 0.2 M peroxydisulfate are typically utilized in the polymerization of 0.05M to 0.1 M pyrrole monomer in water. Hence, one crucial parameter in designing the syntheses is the solubility of the oxidant(s) in stoichiometric amounts.

Chemically synthesized materials have similar electrical properties to the electropolymerized PPys. However, electron spin resonance (ESR) studies have shown that chemically oxidized polymers are typically highly branched, rather that fully crosslinked (Wallace *et al*., 1997). Nevertheless, the polymers usually do not have true solubility in aqueous solvent. Solubility, or at least "nanoscopic dispersion" or PPy chains in organic solvents have been reported by numerous reseachers, invariably by applying organic sulfonic acids, such as DBS, as dopants. These bulky molecules reduce the intra-chain interactions of PPy chains (Oh *et al*., 2001). An important advance in processability was taken when high molecular PPys soluble in alcohol solvents were reported (Jang *et al*., 2002). 1-2 wt/vol-% solubility was induced by 2-(ethylhexyl sulfosuccinate) sodium salt Na(DEHS) dopant. However, the films cast from ethanol were only moderately conductive (10^{-2} S/m). To underline the successful synthesis of soluble high polymer, they measured the "first world record" molecular weight of PPy (M_w 32500 Da by GPC). In general, reports of the molecular weights of conjugated (doped) PPy chains should be cautiously interpreted, as the doping of the chain renders it highly rigid and the properties are dependent on the environment (e.g. oxygen, ionic strength) of the solvent, for example.

Another important practical difference in chemical and electrochemical polymerization method is that oxidant species are typically associated with the dopant. For example, the Fe^{3+}-ion and the counteranions of the oxidants ($FeCl_3$, FeTSA etc.) will be incorporated as co-dopants or complexed with the dopants (Wallace *et al*., 1997; DeArmitt and Armes, 1993; Li and Pickup, 1999). Based on the author's experiences and discussions with other investigators (Albers, 2010), the residue of ferrous ion is hard, if not impossible, to eliminate completely from the doped polymer. This is an obvious complication in designing a biocompatible material. Hence, to summarize the fundamental practical differences between the chemical and electrochemical, (1) due to the oxidant, the chemical polymerization has fewer free experimental variables compared to electrochemical methods and (2) in contrast to chemical methods, the properties of the electropolymerized material can be tailored by choosing polymerization conditions, but the deposited insoluble film is essentially non-processable after the synthesis.

Polymerizations are typically carried out in low temperatures (0 to +5°C) and in inert atmosphere (Rodriquez *et al*., 1997; Wallace *et al*., 199). By far the most common oxidants applied in aqueous polymerization are $FeCl_3$ and peroxydisulfates. In fact, rather high conductivities, up to 20000 S/m, have been achieved by simple $FeCl_3$ oxidation in aqueous solution (Machida *et al*., 1989). However, the resulting PPyCl powder has inferior mechanical properties, stability in air and stability

against de-doping in physiological salt solution (Fonner *et al*., 2008), due to the mobility and leaching of the chloride ions. Furthermore, better mechanical properties have been attained by bulkier dopants, such as p-toluene sulfonic acid (p-TSA) (Zhao *et al*., 1998; Fonner *et al*., 2008) or dodecylbenzene sulfonic acid (DBSA) (Bay *et al*., 2002). These presumably reduce the inter-chain interactions of the rigid PPy chains, and may induce molecular order by stacking with the pyrrole-ring (Figure 1), in analogy to the well known phenyl-stacking in polyaniline (Ikkala *et al*., 1997). Further improvement in the mechanical properties can be attained by using polymeric dopants and co-dopants (Lee *et al*., 2010), as their macromolecular structure directly contributes with the mechanical properties of the molecular PPy-dopant complex.

Ammonium-, sodium- or potassium peroxydisulfate (APS, NPS and KPS) oxidations in micellar PSS and DBS emulsion result in stabilized colloidal materials (PPyPSS and PPyDBS, respectively). The latter can be readily applied as dispersions in coatings, for example. As hypothesized above, the colloid particles probably consist of PPy particles which are partially doped by the sulfonate anions and partially by the sulphate anion of the oxidant (DeArmitt and Armes, 1993)

The conductivity of dried PPyPSS films is moderate (1-10 S/cm) and the stability in air and in liquids greatly enhanced. Peroxydisulfate oxidants are often preferred over multivalent oxidizing ions (e.g. Fe^{+3}) when polyanions are utilized as dopants or surfactants. This is due to the potential of the multivalent ions to complex with polyanions (DeArmitt and Armes, 1993).

Ferric ions have an appropriately mild reduction potential ($Fe^{3+} \rightarrow Fe^{2+}$ E_0 =0.77 V) to allow some control over the polymerization rate, as compared to peroxydisulfates (e.g. ammonium peroxydisulfate APS) ($S_2O_8^{-2}$- $+2H^+ +2e^-$ $2HSO_4^-$, E_0 =2.1 V). Peroxydisulfates, which are preferred over the ferric oxidants in the dispersion polymerization, are strong oxidants inducing more side reactions and oxidation during the synthesis and hence products with lower conductivity (Wei *et al*., 2011; Han and Armes, 2003).

Templated polymerization has been done successfully also on polymeric colloids, which appear non-functional in doping. Colloids act as steric stabilizers for the PPy chains and stable PPy-nanoparticle dispersions have been generated. Such procedures have been successful with polyvinyl alcohol (PVA) (Armes and Aldissi, 1991a; Jang *et al*., 2002), polyvinyl pyridine PVP (Armes and Aldissi, 1990), polyethylene oxide (PEO) (Armes and Aldissi, 1991b), polymerizations in wood based polysaccharides templates such as xylan, carboxymethyl cellulose (CMC), and nanocellulose fibers (NCF) have also been demonstrated recently (Sasso *et al*., 2008, 2010)

Chemical polymerization is a feasible method for depositing PPy coatings on complex shaped and porous solid substrates. In contrast to electropolymerizations, the substrate material can be also electrically non-conductive, such as a plastic film or a textile fiber. In the simplest approach

the surface is immersed into a polymerization path and some of the PPy will be precipitated on the surface. However, very few substrates have affininity towards the monomer or PPy to achieve good adhesion or mechanical durability of the coating. A better approach is polymerizing the PPy *in situ*. This means the polymerization reaction will be confined or enhanced on the substrate layer, forming a thin composite layer with the substrate polymer (see section 1.9).

Carbon materials such as graphite, glassy carbon, nanotubes, graphene and graphene oxide are good substrates for PPy polymerization. Compatibility stems from the chemical similarity of these material groups. Both carbon and CPs consist of aromatic or heterocyclic rings, which in analogy to naturally occurring graphitic carbon, have a tendency to form molecular stacks with chemically similar molecules such as pyrroles (Chitta and D'Souza, 2008). PPy among other CPs easily form composites with carbon materials. Carbon nanomaterials carrying negatively charged carboxylate groups can be readily incorporated into PPy as dopants or co-dopants with surfactant anions (Chen *et al*., 2000; P1, 2010).

2.9 In situ polymerization on material interphases

Polymerization *in situ* is defined as a process occurring inside a host material or confined to the surface layer of the host material. The difference with template polymerization described in the preceding section is that the substrate or the *host* should be solid, typically slightly swollen by the reagents and/or reaction solvent (De Jesus *et al*., 1997; Shenoy *et al*., 2002).

In situ polymerization of PPy has been successfully done on suspended solid inorganic and polymeric particles, polymer fibers, film, textiles, 3D shaped devices, etc. The host surface may have micro- and nanoporosity, or it can be smooth. *In situ* polymerization offers several benefits over conventional mixing of materials or the coating of a host surface by polymer dispersion, etc. Firstly, the resulting mechanical properties of the in situ composite are superior – typically, most of the properties of the host are preserved and transferred to the composite, for example the surface confined conductive PPy coating. Secondly, the reaction is confined to the composite (surface) where the reagents are concentrated. For example, the monomer and/or the oxidant solution can be sprayed on the surfaces or the coated object can be successively dipped into the solutions. Therefore, it is not necessary to have condition for homogeneous and well mixed polymerization or a large reaction vessel where the solid host was then immersed. This in turn may require fewer reagents and less waste material should be generated during the polymerization. (Shenoy *et al*., 2001a; 2001b; 2002).

Oxidative *in situ* polymerization of PPy within a surface of a polymer host (fiber, film, rod, etc.) leads in many cases to superior properties and enhances the mechanical durability of the PPy coating. In situ polymerization can be realized with different strategies. 1) First impregnate the host with the monomer and a solvent capable of swelling the host. Secondly, introduce the dopant and

the oxidant to initiate the polymerization reaction. 2) Reversing the order of introducing the reagent may be beneficial in certain cases, for example when the oxidant was more easily immobilized on the host surface. However, only with appropriately chosen solvent mixtures and concentration of reagents will the polymerization take place *in situ*. Whether this is possible is also dependent on the substrate polymer. For example, substrates that are swollen by the monomer are good substrates, particularly good examples being polyamide 6 fiber (Harlin *et al*., 2005), polyvinyl chloride (PVC) (Nakata and Kise, 1993) polyvinyl alcohol (PVA) (Pron *et al*., 1987) and polyurethanes (Wang X et *al*., 2008; Sahoo *et al*., 2005). Porous beta-cyclodextrin (CD) host has been demonstrated in the fabrication of core-shell structured PPy nano- and microspheres (Shang *et al*., 2012). It has been suggested that pyrrole monomer could be shielded against air oxygen in the pores and cavities of CD (Braun *et al*. 2005). Hence, synthetic strategies utilizing a separate impregnation step for hydrophobic monomer into a protecting host matrix are justified in many ways.

In situ polymerized biodegradable polyester composites suitable for cell culture applications have been recently demonstrated by several research groups. Polylactic acid /glycolic acid copolymer (PLGA) fiber mesh was coated by PPy doped with para-toluene sulfonic acid (p-TSA) and polymerized in situ onto the electrospun fiber (Lee *et al*., 2009). Yu and co-workers (Yu et al., 2011) fabricated dual multi-porous poly L-lactic acid / PPy (PLLA/PPy) composite micro/nano fiber films by combining electrospinning of microporous PLLA with successive in situ polymerization of PPy doped by sulphuric acid. Hollow sub-micron PPy fibers “fluffy-PPy” were fabricated by electrospinning of a PLLA template and successive in situ polymerization of thin PPyCl layer, followed by solvent extraction (Jin *et al.*, 2012). Mixing of PPy particles polymerized in emulsion or dispersion and successive mixing with the host has been demonstrated (Shi *et al*., 2004). In mixing the PPy and the bulk of the bioabsorbable matrix polymer the percolation for electrical conductivity is high compared to surface coatings: the theoretical loading for electrical percolation is >16 vol-% for spherical particles, whereas 2-10 vol-% of the coating, depending on the dimensions of the host (e.g. fiber, film) being typically sufficient. Hence, the coating by *in situ* polymerization of the PPy is attractive, especially if permanent implantation with bioabsorbable polymers is considered.

The examplified *in situ* polymerized structures could have been very difficult to fabricate by any other strategy. From the application point of view, some improvement in bringing true biological functionality could have been desirable. The functionality brought by biomolecules is precisely in the focus of the current work.

2.10 Alternative routes for conductive polymers

Organic vapor phase deposition (OPVD) or vapor phase polymerization is a potential coating method for reagents that can be vaporized or sublimed. Pyrrole monomer has a boiling point +150 C at normal pressure. Therefore, only moderate heating and reduced pressure are needed for

efficient mass transfer in the vapor phase. In a well-designed reactor it is possible to apply controlled concentrations of pyrrole on surfaces for in situ reactive coatings, for example. A limited number of oxidants are available for polymerization in moderate conditions and vapor phase polymerization typically involves involatile ferric oxidants pre-dispersed in the host matrix (Winter-Jensen *et al*., 2004; Ueno *et al*., 1988; Yin *et al*.,2001) or patterned by ink-jet printing (Cho *et al*., 2010). The use of elemental iodine oxidant has several advantages over ferric oxidants (Shenoy *et al*., 2004). For example, elemental Iodine can be applied in normal pressures (at >100 kPa) as it sublimes and has reactivity and oxidation potential suitable for the generation of high quality PPy films. In addition, iodine is inexpensive and can be completely exchanged by re-doping with other dopant. However, iodine has been only reported as a volatile dopant in plasma assisted deposition (Goktas *et al*., 2009). The major drawback in using vapor phase polymerization is the need for highly sophisticated deposition reactors and the limited number of volatile oxidant precursors.

For biomedical applications, another feasible approach is the use of *supercritical* CO_2 ($scCO_2$) solvent in PPy polymerization. CO_2 is an inert solvent for pyrrole and thus applicable. The solvent itself leaves no residues (it is vaporized upon relieving the pressure), thus potentially improving the microbiological properties and reducing the soluble organic contamination of the host materials.

The processing conditions are above the critical point of CO_2 (T_c=+31.1°C and p_c =7.38 MPa). Hence, pressure vessels and batch operations are utilized. Pyrrole monomer has significant solubility and known phase behaviour in $scCO_2$ (Kulik *et al*., 2008). However, soluble oxidants are scarce, as significant solubility of potential molecules is limited to non-polar (oily) aliphatic, fluorine- or siloxane- containing compounds, carbonyl compounds, or those having volatility. Iodine has been utilized in polymerization in the polystyrene host (Shenoy *et al*., 2004). Thus far the attempts to find alternative well soluble oxidants have been unsuccessful. Compounds having the chemical structure described in the above list combined with high acidity of the dopant anion, such as Ferric salt of trifluoromethane sulfonic acid ($Fe(TFMSI)_3$) have been tested, but an ethanol co-solvent has been necessary to achieve sufficient concentrations of the oxidant (Shenoy, *et al*., 2001b). Complexation of ferric ions with a non-soluble host, such as sulfonated crosslinked polystyrene, is proven to be a feasible approach to overcome oxidant solubility issues (unpublished data, Pelto and Kulik, 2007).

2.11 Patterning of PPy microstructures

Patterning of PPy on electrically insulating and conductive substrates is of great practical interest in cell culturing platform, for example. Micropatterning by radiation assisted polymerization and etching have been demonstrated utilizing several techniques: photochemically initiated polymerization has been reported by Segawa and co-workers. They demonstrated VIS laser light activated deposition of PPyCl, applying ruthenium bipyridine photosensitizer and a cobalt complex

$[Co^{+3}Cl(NH_3)_5]^{2+}$ sacrificial oxidant. However, the electrical properties of the materials produced were inferior to the PPyCl prepared by the standard chemical or electrochemical methods. In another study, a nafion membrane substrate was impregnated with reagents, and it was possible to generate fine 10 µm patterns through a photomask (Segawa *et al*., 1989). The same ideas have been extended to paper and glassy carbon surfaces by the use of a Cu^{2+} -complex and p-nitrobenzyl bromide sacrificial oxidant (Kern and Sauvage, 1989). The biocompatibilities of the photochemically generated materials were not assessed, but the photoinitiators used raise some concern for any application in long term contact with cells and tissues.

Choi and Park (Choi and Park, 2006) introduced a versatile method to fabricate microstructures of conducting PPy. They prepared polymer patterns as an insulating template on ITO glass using PDMS soft-imprint technique, forming templates for polymeric microstructures. In order to expose selectively the bare ITO, the residual layer of polymer patterns on ITO was removed with reactive ion etching (RIE). Electropolymerization of PPy was conducted using the patterned ITO as an electrode. 2D/3D microstructures of PPy were fabricated with 1 µm resolution.

RIE was also applied successfully in the manufacturing of organic field-effect transistors (OFETs) (Cui *et al*., 2003). OFETs were fabricated by spin coating thin films and subsequently reactive ion etching (RIE) of poly(3,4-ethylene dioxythiophene) doped with PSS (PEDOT:PSS). The patterning with RIE technique utilized an aluminum thin film mask. Direct laser ablation of conductive PPy and the laser assisted processing of insulating films of precursor polymers or composites into conducting patterns have been successfully applied by Bargon and Baumann (1993). More recently, the microstructuring of polypyrrole was demonstrated by maskless direct femtosecond laser ablation (Lee K *et al*., 2012).

2.12 Degradation of polypyrrole by ionizing radiation

The behaviour of conductive polymer under ionizing radiation has been a less studied subject, probably due to the limited access of research groups to radiation sources. Sterilization by gamma irradiation has in many cases become a standard for biomedical implants, surpassing chemical sterilization by ethylene oxide (EO) gas and steam autoclaving. Gamma sterilization is a suitable method for materials having reasonable stability under the high radiation doses utilized. Previous preclinical work on a steerable vascular stent and microanatomosis connector devices based on PPy, performed at Micromuscle AB in Sweden (Jager *et al*., 2010) demonstrated good stability of the PPy in EO sterization. However, due to the potential toxicity of EO residues, gamma sterilization should be the preferred method for permanently implantable tissue engineering scaffolds, and polymeric implants in general.

It is well known that most polymeric materials undergo chemical and physical changes, such as chain scission and crosslinking when radiated with high energetic photons. The effects are dose

dependent and the mechanisms are quite different to those observed by attack of reactive chemicals. In the case of electrically conductive polymers the changes of the electronic conjugation length, i.e. the electronic delocalization charge of the polaron lattice, become critical. In the most comprehensive study to date, Kane and co-workers (Kane *et al*., 2010) studied the mechanism of radiation induced decay of electrical conductivity in polyaniline (PANi) and poly(3,4-ethylenedioxythiophene) (PEDOT), which are polymers structurally related to PPy, PAni and PEDOT films when exposed to gamma radiation in both air and deuterium environments. Tritium gas exposures combined with Raman and UV/VIS spectroscopy of gamma irradiated samples were applied to reveal de-protonation, which is known to be a significant mechanism of conductivity loss in PAni. Furthermore, the oxidation of both conductive polymers during gamma irradiation was investigated. They concluded that chain scission via free radical formation and chain cross-linking were most likely the two dominant mechanisms for the measured conductivity changes. Their data showed that 10^5 Gy equivalent total dose of gamma rays in air was the point at which the measured surface conductivity began to gradually decrease, finally reducing by 3-5 orders of magnitude compared to the original.

In earlier studies a far less significant reduction of the conductivity, induced by gamma rays in vacuum, was reported for PAni, polythiophene (PT) and PPy. PPy had retained about 50% of its original conductivity up to doses $5 \cdot 10^5$ Gy. At low $2 \cdot 10^3$ Gy dose the PPy conductivity was two-fold increased compared to the original, suggesting that significant gamma radiation induced doping of PPy (Wolszchak *et al*., 1995; Ercan *et al*., 1995).

2.13 Stability of biopolymer doped polypyrroles in air and in physiological fluid environment

Stability and oxidation of polypyrrole chain in fluids. Reasonable stability properties in a cell culture environment are highly desirable. All materials undergo reversible and irreversible chemical changes when immersed into a biological environment. The rate and extent of those in PPy has been reported by early investigators. The PPy chain is prone to attack by oxygen and nucleophilic attack by –OH radicals. Schlenoff and Xu (1992) highlighted the gradual over-oxidation of the PPy chain upon electrochemical anodic oxidation. The onset of (nearly) reversible insertion of –OH groups to the 4-carbon of the pyrrole ring occurred at electrochemical potential of about +0.5 V vs. saturated calomel electrode (SCE). At potential in excess of +0.7 V vs. SCE the hydroxyl groups were further oxidized to carbonyl groups as evidenced by FTIR spectra. This resulted in irreversible degradation of the electrical conductivity and mechanical properties of PPy. Hence, the +0.7 V vs. SCE oxidation potential is the long term stability limit for PPy chains. Continued electrochemical (over)oxidation will result in breaking of the polymer into oxidized cyclic degradation products such as maleimide and succinimide (Park *et al*., 1993). Both compounds are biologically active, water soluble and reactive, linking covalently with proteins. Hence, the

generation of the compounds is highly undesirable under any conditions during cell culturing or implantation.

***De-doping* of *PP*y.** Loss of electrical conductivity is observed when PPy is immersed into physiological electrolyte solution (Serra Moreno and Panero, 2012; Fonner *et al*. 2008). If the material is kept within the electrochemical stability window (roughly -0.3 V to +0.5 V vs. Ag/AgCl), the anticipated mechanism of losing the electrical conductivity is de-doping by gradual reduction of the PPy chain associated with dopant leaching. Dopant leaching is a process which is driven by the ion concentration differences of the PPy and the surrounding electrolyte solution. As described earlier, the PPy may contain 30-50 wt-% dopant molecules and a few wt-% water, which leads to ion concentrations far exceeding the physiological ion concentration (0.15 M). Hence, there is typically a dramatic concentration gradient of ionic species across the PPy-electrolyte solution interphase. For smaller anions the dopant leaching is faster due to the higher mobility of ions. De-doping is fast in de-ionined water. This is particularly noticeable when washing PPyCl with pure water. It is also largely reversible by re-doping, which can realised simply by rinsing with acidic dopant, hydrochloric acid, for example. Dopant leaching cannot be completely eliminated but is significantly reduced when high concentrations of electrolytes are used to stabilize the dopant in the PPy.

One illustrative example of salt stabilization is the PPy based electrochemical charge storage device based on concentrated 2 M sodium chloride (NaCl) aqueous electrolyte, aka the “salt and paper battery” developed at Ångström laboratory in Uppsala University (Nyström *et al*., 2009). In the construction the PPyCl was polymerized on nanocellulose fibers (NFC) in suspension. The NCF was derived from green algae. The device can be repeatedly charged and recharged in either neutral pH 2-3 M NaCl (aq.), or in salt solution acidified by 0.01 M HCl. This device has a very stable operation for several thousands of cycles in 0 to +0.8 V (vs. Ag/AgCl) potential window.

Dopant leaching is less significant in PPys doped by polymeric immobile dopants, such as PSS. This is manifested also by the more stable electrical conductivity of the PPyPSS compared to PPy-pTS or PPyCl immersed in phosphate buffer solution at pH 7.4 (Fonner *et al*., 2008).

Stability of the HA and CS. HA is scissioned by ionizing radiation during gamma sterilization in solid state (Armand *et al*., 1975). In solution or gel state, chemical cross-linking reactions may dominate. For example, HA hydrogels have been fabricated by applying gamma rays (>15 kGy dose) to HA/CS aqueous solutions (Zhao *et al*., 2015).

Kim *et al*. (2008) reported that 2-90 kGy gamma irradiation resulted in a linear decrease of the MW of HA in water solution. Yellowing of the HA was observed, correlating with UV spectral changes, which indicated the formation of carbon double bonds. FTIR spectral changes in the range 1700–1750 cm^{-1} were associated with the formation of carboxylic acid. Furthermore, some

evidence of the formation of pyrancarboxylic acid was found. It is anticipated that changes in the functional groups will permanently change the specific biological functionality of the HA.

Polymerization of pyrrole by electrochemical or chemical oxidation occurs best in acidic pH around 2. Furthermore, as the chemical polymerization utilizing $FeCl_3$ or peroxydisulfate oxidant progresses, the pH of the medium is constantly decreasing because hydrochloric or sulphuric acid are liberated from the oxidants, respectively. The lowering of pH may occur homogeneously in a stirred reactor, or locally, for example at the positive anode during electropolymerization or at the confined reaction initiated by an oxidant on the surface. The chemical environment in the reactors is both highly oxidizing, acidic and containing abundant reactive molecules and radicals (-OH, oxygen, chloride, etc.). Hence, most biomolecules will undergo degradation in polymerization conditions.

Polysaccharides, such as HA (Figure 3A) are easily hydrolysed in vitro by singlet oxygen, dichloride- and hydroxyl radicals (Stern *et al*., 2007), acid hydrolysis and by mechanical chain scissoning by ultrasonic energy (Gura *et al*., 1998). HA is, in fact, a name for a diverse group of structurally similar polymers (containing D-glucoronic acid and D-N acetylglucosamine, see figure 2A) that typically have giant molecular weight (M_w > 1 MDa) and originate from various biosynthetic routes. In addition, the HA molecule has a secondary structure based on ionic interactions in the physiological environment. For these reasons the characterization of native HAs, e.g. the determination of molecular weight, is complex. Biologically active HA *in vivo* is in the form of degraded and well soluble oligomeric material (Collier *et al.*, 2000).

CS is closely related to HA, having N-acetylgalactosamine and glucuronic acid mono-saccharides, unsulfated, sulfated once, or sulfated twice in the hydroxyls at the 4 and 6 positions of the N-acetyl-galactosamine (Figure 3B). The bio-elimination mechanisms and the stability of CS may be dependent on the degree of sulfonation. However, it is anticipated that the degradation mechanisms of CS by crosslinking and depolymerization are similar to HA.

Collier *et al*. (2000) studied thin PPyHA electropolymerized films and probed the presence of biologically active HA using a HA-binding protein and showed that HA was present at 3-4 days during incubation in the medium. They discussed the mechanisms by which the HA was incorporated into the PPyHA and how it was eliminated during incubation. High viscosity of the polymerization solution and a very slow polymerization rate were observed, which suggest that the HA was indeed incorporated as a high molecular weight polymer and mostly hydrolysed during the incubation. Yet, it was presumed that the MW of HA polymer was decreasing also during the synthesis of PPyHA.

2.14 Cell-surface interactions

Surface roughness. It is widely accepted that the surface roughness of biomaterials, whether metallic, ceramic or polymeric, is one of the key parameters explaining the cell-surface interactions *in vitro* and *in vivo*. Therefore, considerable research effort has been put into the subject. The subject has been traditionally treated from the viewpoint of either nanoscopic or microscopic phenomena. However, it should be appreciated that both aspects are relevant, as the cell-surface interaction is typically mediated by the plasma proteins adsorbed and their interactions with the cell surface adhesion proteins. Individual proteins have sizes in nanometers. Cells have sizes from a few microns to tens of microns. Many functional (protein) structures of adhering cells are confined to the elastic and plastic cell membrane. Hence, both the nanometer and the micrometer domains are relevant for the adhering cell.

Figure 3 illustrates the lateral length scales of a realistic rough surface (PPyHA) compared to the the size of a single hASC (10 to tens of microns) and an AFM probe. The surface roughness of the macrocopiclly smooth biomaterial surface is typically in the range 20-50 nm (RMS). As illustrated, the surface properties of the PPyHA vary significantly within the area covered by a single cell attached.

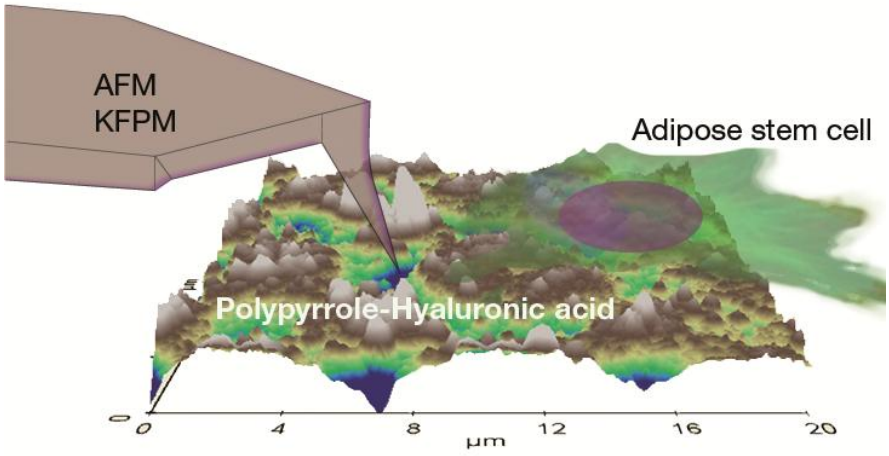

Figure 3. Illustration of the lateral length scale of a realistic rough surface (PPyHA) and an adipose stem cell (hASC) and an AFM cantilever and the tip. Surface properties may vary significantly within the area covered by a single cell. The z-range (50 nm) of the AFM image is greatly magnified in proportion to the AFM tip and the cell. Reprinted with permission from Pelto *et al*., *Langmuir* 29:20: 6099 – 6108. Copyright (2013) American Chemical Society.

The microroughness is due to the surface features that have vertical or lateral dimensions in the micron domain. Such features are typically, but not without exception, observable by optical microscope or SEM. Stylus profilometers are the most commonly applied instruments for

quantitative and fast measurement of the commonly applied roughness parameters, such as R_a and R_q. Stylus profilometers are equipped with a fast scanning tip with adjustable vertical force on the sample. Vertical resolution of the measurement is a few Ångströms. The lateral resolution of any mechanical probe is limited by the shape of the tip; for profilometers the radius of curvature is typically a few microns. Hence, stylus profilometers are best suited for probing the roughness on significantly larger areas (say, 100 times) than AFM.

Fonner *et al*. (2000) have attempted to correlate the surface roughness (measured using a stylus profilometer) of differently doped electropolymerized PPy film polymerized on the ITO and gold substrates, with the choice of the dopant ion, and the resulting PPy film thickness. Cell viability studies using PC-12 and Schwann cells were conducted to elucidate the roles of these factors. They noticed differences in the macroscopic uniformity, but no significant differences in the surface nanoroughness parameters of the coatings (PPyCl, PPyTSA and PPyPSS) were reported. Qualitatively, PPyCl was reported to have the highest microroughness. TSA and PSS doped materials had significantly higher uniformity, lower surface roughness, and also better viability of the cells compared to PPyCl. The differences in the film morphology were explained by the different nucleation and growth mechanisms.

The atomic force microscope (AFM) is also a mechanical probe. However, there are significant differences in the operation and the data generated. The AFM scans very slowly compared to profilometers but it utilizes a sharp probing tip (tip radius of a few nanometers) and a vertical resolution of a few picometers. Hence, AFM is truly capable of detecting roughness in the nano domain. The AFM is normally focused on significantly smaller surface areas (1 μm^2 to a maximum 10000 μm^2) than profilometers. Therefore, roughness parameters derived from Stylus profiler and AFM are poorly comparable, but do complement each other.

The data presented in this thesis work is generated by AFM. Representative AFM data is collected by choosing the analysed areas based on optical microscope images of the sample surface near the probing cantilever/tip.

The AFM images of various PPy surfaces (Barisci *et al*., 2000; Gelmi *et al*., 2010; Silk *et al*., 1998a, 1998b; Mabrouk, 2005; P3, 2013) clearly reveal the “cauliflower” or globular fine surface features which are not as clearly presented by any other surface probing technique. An obvious advantage of AFM over SEM in studying biomaterial surface is that images can be taken and roughness studied on surfaces immersed in liquids such as aqueous buffer solutions mimicking the physiological environment. The observed surface features and properties of PPy, such as roughness and elasticity, are different under ambient air and immersion in electrolyte, particularly soft PPyHA and PPyCS surfaces absorbing significant amounts of water and salt (P4, 2014).

AFM tip condition, i.e. sharpness of the probe or contamination from the surface, may easily convolute with the surface topography, inducing imaging artefacts. This is particularly true for soft samples, e.g. PPyHA films, for which suitable AFM measuring parameters (imaging mode, tip, contact force, etc.) are not easily found. Still, for roughness analysis, conventional contact AFM should be preferred over the non-contact mode (dynamic tip AFM). This can be justified by the simpler feedback system and easy calibration of topographic height data.

The “cauliflower” morphologies seen are generally accepted to be the manifestation of the nucleation and growth mechanism of the PPy deposition (Genies *et al*., 1983; Armes *et al*., 1991a). Analysis of the size distribution of the globular structures of the electropolymerized PPy surface reveals typically two distinct peaks. These typical sizes of the nodules tend to vary as film thickness increases (Silk *et al*., 1998a). Chemical polymerization results in similar appearance of the morphology. In dispersion or emulsion polymerization of pyrrole the primary particle generation is usually nucleated in sub-micron in surfactant stabilized monomer droplets or surfactant micelles (Armes *et al*., 1991b). In chemical surface polymerization (or in situ polymerization) on insulating polymer substrate the nucleation and growth mechanisms are determined by the compatibility of the substrate and the deposited PPy. If the compatibility is poor, the PPy will be deposited on the surface as particles and aggregates resembling those generated in the bulk of the solution. If the polymerization is confined in the swollen surface layer of the substrate, the PPy will form a polymer mixture, even an interpenetrating network of polymeric phases (Harlin *et al*., 2005). In this case the appearance of the very thin outermost PPy surface strongly reflects the surface topography of the substrate (P2, 2012).

Surface roughness on polymer surfaces has a well-established role in cell adhesion on polymers. It is also well known that surface roughness is linked to the surface energy (hydrophilicity) of polymers. A general trend present in the literature is that increased submicron roughness, at least to a certain extent, will promote cell adhesion (Wan Y *et al*., 2005; Hallab *et al*., 2001; Miller *et al*., 2004; Biggs *et al*., 2009), presumably at least partly due to the increased surface area for protein adsorption. On the other hand, microscopic features on the surface offer mechanical cues for the cell attachment and spreading even after the surface has been first covered by the plasma proteins to form the culture medium. This implication is supported by the results of Gittens *et a*l. (2011). A combination of micro-/submicro-scale surface roughness with a high density of nanoscale structures on oxidized titanium resulted in an additive, if not synergistic effect, on cell differentiation evidenced by various osteogenic markers.

On practical biomaterial surfaces is it seldom possible to completely deconvolute the distinct significance or nano- and microroughness. Hence, we are forced to interpret the surface topographical information through averaging parameters (R_a and R_q). We can hypothesize that both the universal nanoroughness and the microscopic protrusions should have their roles in cell

adhesion on the studied PPyHA and PPyCS surfaces. Different cell lines should also have variable responses to specific surface roughness.

Serra Moreno *et al*. have studied the effects of synthesis parameters of CS (CS-4) (2008), HA and Heparin doped PPy (2009), including the effect of their surface roughness, on osteoblast adhesion and proliferation. Their findings suggest that smooth surfaces allow the best adhesion of osteoblasts on electropolymerized films. Molino *et al*. (2012) utilized AFM and EC-QCM to show the adsorption of the model proteins, bovine serum albumin (BSA) and fibronectin (FN), onto PPy doped with dextran sulphate (PPyDS) as a function of DS loading and surface roughness. BSA adsorption was enhanced on rougher surfaces (>40 nm RMS) above what could be explained by the increase in surface area alone. The surface roughness was modulated by the loading of DS in the PPyDS film. Higher surface roughness was observed in PPyDS films polymerized with the least amount (0.2 mg/ml) of DS in the polymerization medium. The study also highlighted the simultaneous role of redox state, i.e. the charging of the PPyDS on the FN adsorption.

Surface roughness is certainly not the single master parameter determining the behaviour of cells on biomaterials. Surface energy, which can be thought to include the combined roles of the density of surface functional groups (hydroxyl, carboxyl, amine etc.), and the specific surface area (through nano/micron topography), have been known to contribute (Wan Y, 2005; Discher *et al*., 2005; Dubiel *et al*., 2011). The processes on biomaterial surfaces are designed to mimick the natural environment of cells *in vivo*. Hence, for a given biomaterial *in vitro* the adhesion is cell specific and strongly dependent on the culture conditions, such as the component of the cell culture medium (serum proteins, growth factors, etc.).

On practical biomaterial surfaces is it seldom possible to completely deconvolute the distinct significance or nano- and micro-roughness. Making an over-simplification, researchers are mostly interpreting the surface topographical information through averaging parameters (R_a and R_q). We can hypothesize that both the universal nanoroughness and the microscopic protrusions should have their convoluted roles in cell adhesion on the studied PPyHA and PPyCS surfaces.

The excess surface charge and surface elasticity have also been considered significant factors in explaining protein adsorption, cell attachment and adhesion on conductive polymer surface (Gelmi et al., 2010; 2012; 2013a, 2013b; Wan *et al*., 2009; Molino *et al*., 2012; P3, 2013). The roles of other factors will be discussed in the next sections.

Surface elasticity. Several studies, as reviewed by Wong *et al*. (2004), have highlighted the capability of cells to probe the (visco)elasticity of the 2D substrate surface or a 3D matrix. This is the intrinsic mechanism by which the cells build tissues. In fact, many primary cells are viable only when attached to a substrate, preferably mimicking their natural host tissue. Cell adhesion proteins anchor to ligands (serum proteins) on the surface. The forces are transmitted from the extracellular

space to the cytoskeleton through focal adhesion protein complexes, which subsequently trigger intracellular responses. The proposed mechanism on how cells probe elasticity is by constantly anchoring and pulling on their surroundings (Engler *et al*., 2006; Discher *et al*., 2005).

Engler and co-workers prepared series of polymer gel samples having slightly different elastic moduli but similar surface chemistry, and study the spreading and adhesion of primary cells and aortic smooth muscle cells (Engler *et al*., 2004). They found significantly enhanced spreading and adhesion on collagen coated crosslinked polyacrylamide (PAAm) gels having their elastic moduli designed to match with the biological tissue samples. Furthermore, layer-by-layer microfilms of poly(L-lysine)/hyaluronic acid showed equivalent trends.

Cell proliferation, surface marker expression and motile phenotype in amniotic fluid-derived stem cells have been recently shown to correlate with substrate elasticity (Skardal *et al*., 2012). In a comprehensive study Engler *et al*. (2006) found that mesenchymal stem cells (MSCs) specified their lineages and committed to phenotypes with extreme sensitivity to tissue level elasticity: for example, soft gel matrices that mimic the brain were found neurogenic, stiffer matrices that mimick muscle tissue were myogenic, and comparatively rigid matrices mimicking collagenous bone were osteogenic. Reprogramming of these lineages was possible during the initial week in culture, with the addition of bioactive factors, but after several weeks in culture, the cells committed to the lineage specified by matrix elasticity.

Hence, the elasticity of the substrate may partly override the biochemical cues from the medium, especially during the later phases of cell culture. For any cell attachment to occur, the substrate should contain suitable ligands for serum proteins (if present during the incubation). Protein adsorption processes do not generally require only certain surface elasticity, but rather the combination of elastic properties with suitable surface chemistry and surface charge (Dubiel *et al*., 2011). Therefore, an optimized substrate for cell culture should have well balanced elasticity and surface functionality, such as recently demonstrated by Kumar *et al*. (2013) for hematopoietic stem and progenitor cells on polyvinyl alcohol (PVA) and itaconic acid (IA) (PVA-IA) dopolymer hydrogels, grafted with fibronectin (FN) and the hematopoetic connecting segment-1 motif or the FN.

Surface elasticity mapping done with nanometer lateral resolution of AFM tip is a well-established method (Engler *et al*., 2006; Domke and Radmacher, 1998). The mapping comprises the collection of individual AFM force-distance (F-D) curves on each pixel of the image and subsequent fitting of the compliant part of F-D data to elastic contact model. The simple Hertz contact model (Hertz, 1882) has been used to characterize the elastic moduli of various PPy surfaces (Gelmi et al., 2012; P3, 2013). Several more advanced viscoelastic contact models have been developed (Butt *et al*., 2005), and they are used for characterization of very soft structures, down to the elastic moduli of a

single cell membrane (Helenius *et al*., 2008). Additional information on tip-sample adhesion energy and indentation of the tip to the sample is automatically collected by the AFM software during the elasticity mapping. The elasticity and adhesion data can be superimposed on the scanned AFM images or fluorescence microscope images of the sample, such as a biomaterial or a single cell. These features are provided in commercial AFM systems (Ludwig *et al*., 2008).

Surface charge and potential. Electrical double layer forces, strong van der Waals interactions and steric forces are present in colloidal aqueous systems, including biomaterial surfaces. Hence, the physical interactions between the biomaterial, plasma proteins and surface receptors of living cells are clearly attributable to the electrostatic charges and/or hydrated polymers on their surfaces. The importance of the electrostatic forces on adhesion of proteins has been well-stated in the the literature (Lubarsky *et al*., 2005; Hartvig *et al*., 2011; Takahashi *et al*., 2000; Asthagiri and Lenhoff, 1997; Zhou *et al*., 2003). Lubarsky *et al*. (2005) have shown that electrical double layer forces drive human serum albumin adsorption more efficiently onto non-oxidized and less negatively charged tissue culture polystyrene plates in PBS. The charge distribution within the protein molecules has been linked to adsorption (Hartvig *et al*., 2011; Takahashi *et al*., 2000; Asthagiri and Lenhoff, 1997). Most negatively charged segments in polysaccharide molecules have been linked to adsorption by Etteleie *et al*. (2012), who highlighted the electrostatic attraction/repulsion forces. Furthermore, ionic interactions between the electrolyte and the solvated proteins (Takahashi *et al*., 2000) and the pH (Zhou *et al*., 2003) of the biological systems have been suggested to contribute to the adsorption.

Some previous studies have addressed the surface charge and surface potential of PPy and correlated the charge with protein adsorption. Zhang and Bai (2003) reported strong dependence of the surface ξ-potentials of chloride-doped polypyrrole (PPyCl) particles on the solution pH. They also noted that the point of zero ξ-potential was dependent on the previous acid/based treatments of the PPyCl sample. Some authors (Salto *et al*., 2008; Wan *et al*., 2005; Gumus *et al*., 2010) have investigated the adsorption of model proteins on charged conductive polymer surfaces. Few studies have addressed the adsorption of plasma proteins on PPy surfaces (Smith and Knowles, 1991; Molino *et al*. 2012). Molino *et al*. (2012) reported that the electrochemical state of the PPyDS was affecting the FN adsorption, with the application of an oxidizing (+300 mV vs. “Dry-Ref, World Precision, standard potential not reported) or reducing (-300 mV) potential impacting both the mass and viscoelasticity of the surface-bound protein layer. The indication of the study was that increased hydrophilicity of PPyDS, associated with DS loading and positive electrochemical potential was both enhancing the FN adsorption and changing the viscoelastic properties of the FN ad-layer, presumably changing the FN conformation towards a more biologically active open conformation. Although the role of the surface charge has been well established, there are no

studies attempting to correlate the distribution of surface charge density on the PPy surface to the adsorption of plasma proteins and the attachment of cells.

Scanning probe techniques have been utilized in the imaging of the surface potential distribution of dense polythiobiphene films (PBT) using AFM and Kelvin force probe microscopy (KFPM) (O'Neil *et al*., 2007; Semenikin *et al*., 1997) and of dense PPyTS films using AFM and electrostatic force microscopy (EFM) (Barisci *et al*., 2000). It has been observed that the nanoscale nodular morphology correlated with the inhomogeneties of the surface potential (Barisci *et al*., 2000) and the viscoelastic properties (Gelmi *et al*., 2013) of the conductive polymers.

However, the surface charge information from the AFM and KFPM is representative of the surface charge condition in air. Surface charge measurements in fluid are by far more complicated than electrostatic measurements conducted in air. Furthermore, the interpretation of data acquired in the fluid phase may be further complicated simply because the numerical results given by different analytical techniques are simply not comparable. Force-distance curve measurements using AFM fluid yield local information on the effective surface charges/potentials between the electrical potential of the AFM tip and of the solid surface under investigation. The information is in nanoscale, as the AFM tip radius of curvature is a few nanometers.

Ions from the electrolyte solution form electrical double layers on the sample and on the AFM tip spontaneously. The thicknesses of the double layers are functions of the ionic concentration of the electrolyte solution, described by the Debye-Hückel law (Figure 4, equation 3). For example, in physiological NaCl (aq.) with concentration 0.15 M the Debye length ($1/\kappa$) characterizing the thickness is about 0.76 nm, which is in the same range as the possible steric forces experienced by the AFM in the vicinity of soft polymeric surface. Therefore, we have used a low concentration of salt (0.005M) applied in order to be able to project the electrostatic interactions to long distances where they can be distinguished from hydration and steric forces.

As there is no universally applicable theory available linking the electrochemical charge and the effective surface charge and potential (Wang and Bard, 2001), relevant information should be extracted using a probe extending to the solid surface, i.e. penetrating the double layer, such as an AFM tip of a colloid probe. Subsequently, fitting the data into a double layer interaction model (DLVO model, named after Derjaguin, Landau, Verdey and Overbeek) will give insight into the surface electrostatic interactions.

Surface potentials are typically calculated from approximated solutions of nonlinear Poisson equation describing the (screened) electrostatics of the electrical double layer repulsion. The principle of measurement is very different compared to the commonly applied measurements of ξ-potential, the potential difference between the double-layer at the location of the ionic slipping plane relative to a point in the bulk fluid away from the interface. Traditionally, ξ-potential has been

effective in explaining the stability of colloid dispersions, but give very little insight into the charge at the solid surfaces.

Both parameters have been used to describe the attachment of charged biopolymers and cells on biomaterials. However, neither parameter can be directly deduced from the electrochemical (bulk or surface) charge injected into the biomaterial (e.g. potential of the PPyHA in an electrochemical cell) and/or the properties of the electrolyte. The picture is even more complicated for polyelectrolyte surfaces, which may absorb significant amounts of the ions and water, making the definition of the solid surface elusive. This is problematic in the analysis of the AFM F-D data, as the fitting of the data is based on setting the surface to "zero distance", either automatically by software, or manually, as illustrated in Figure 4, which presents the approaching F-D curve of a AFM tip on PPyHA. In the Publication 3 we have tested two DLVO models suggested by Onshima (1998) (equation 1) and Hull and Kitchener (1969) (equation 2) in nonlinear data fitting the AFM force curves.

In the calculation of surface potential, R is the AFM tip radius, κ is the inverse if the Debye screening length of the electrolyte, e is the electronic charge, $\varepsilon\varepsilon_0$is the electrical permittivity of the electrolyte, k_T is the Boltzmann coefficient, c_i is the concentration of component i the solution, Z_i is the valence of the component i, D is the shortest distance between the tip and the surface , ψ_T and ψ_S are the potential of the tip and the sample, respectively.

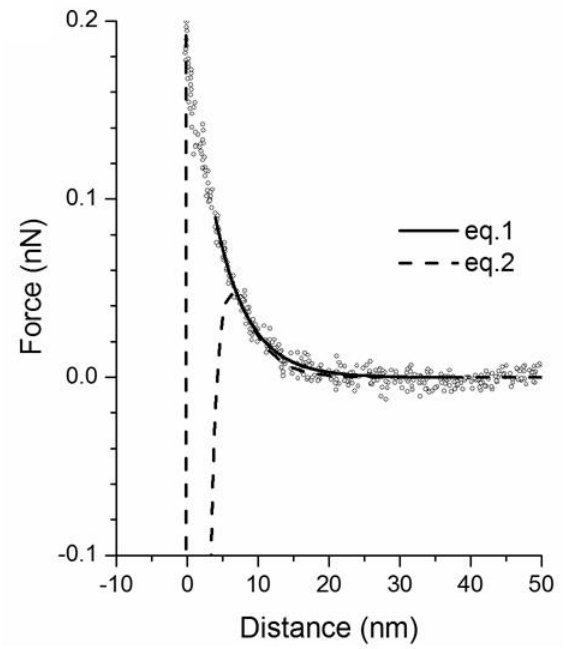

$$F(D) = 4\pi R\varepsilon\kappa \exp(-\kappa D) \qquad \text{(eq.1)}$$

$$F(D) = \pi R\varepsilon\kappa\left(\left(\psi_T^2 + \psi_S^2\right)\left(1 - \coth(\kappa D)\right) + \frac{2\psi_T\psi_S}{\cosh(\kappa D)}\right) \qquad \text{(eq.3)}$$

$$\frac{1}{\kappa} = \sqrt{\frac{e^2}{\varepsilon\varepsilon_0 k_T T}\sum c_i Z_i^2} \qquad \text{(eq. 3)}$$

Figure 4. Data fitting (equations 1 and 2) of the approaching part of the AFM force-distance curve. PPyHA surface. Solid line: a single exponential model (Ohshima, 1998). Dashed line: nonlinear model presenting the breaking of the double layer repulsion (Hull and Kitchener, 1969). Tip potential -200 mV. Electrolyte NaCl 0.005 M (aq.). Debye length 4.3 nm (eq.3). Reprinted with permission from Pelto *et al*., *Langmuir* 29:20:6099–6108. Copyright (2013) American Chemical Society.

3. Aims of this study

The evolution of the research of this dissertation can be reasoned by the progress in the field during the time of study and the generation of important new results. The starting point of the thesis work was Publication 1, aiming to demonstrate the reversible electroactivity of the materials, in which we discovered that the electropolymerized composites of PPy, HA and multi-walled carbon nanotubes (CNT), i.e. PPyHA-CNT biomaterial on titanium substrate showed equal or better cell attachment, viability and proliferation of human derived adipose stem cells (hASC) compared to the reference polylactide (PLA) disk. The early results suggested that the PPyHA-CNT showed much potential as a 2D cell culturing substrate for hASC. Since the material was also found reasonably conductive and showed marked redox electroactivity, it could be potentially utilized in the direct electrical and mechanical stimulation of cells, either in 3D tissue engineering scaffolds or AC microstimulation electrodes. Our first findings were also supported by related reports from other academic research groups currently working on the biological applications of conductive polymers, such as PPy, polyaniline (PANI) and polythiophenes (PT).

However, there were important practical aspects requiring more attention, such as the availability of the reproducible synthetic routes, sterilizability, electronic properties during incubation, biostability of the PPy and the dopants, in vitro stability and performance. For example, the chemical and the electrochemical routes for the syntheses of PPyHA and PPyCS surfaces had to be established for each study. Gaining more insight into these specific issues has been the leading guideline of the progression of the laboratory experiments, publications and the target of this thesis work.

In the series of publications 1-4 we have developed practical and reproducible PPy synthesis protocols for bone tissue engineering. We have taken novel approaches in suggesting a relatively simple chemical polymerization scheme for biopolymer doped PPy. The second aim has been to develop direct “one-pot” deposition of thin electrically conductive coatings on PLA nonwoven tissue engineering scaffold material [P2], avoiding the complication of biological functionalization using click chemistry, for example. The potential of different PPyHA and PPyCS electrode coatings on large area metallic 2D electro-stimulation electrodes for cell cultures have been investigated. The third aim of the work, as reported in Publication 4, was to find practical ways to apply the 2D PPy substrates in electrical stimulation of hASCs in the standard 24 well-plate cell culturing environment in the adult stem cell group, led by Dr. Susanna Miettinen at the University of Tampere.

Fundamental understanding of the surface physicochemical properties relevant to biological application was quite limited at the time of the first publication (2010). Our collaborator, Professor Gordon Wallace’s group in Wollongong Australia, has been active in this field. Since 2010, several

important journal articles related to cell biological applications PPy have been published, for example Higgins *et al*. (2012), Gelmi *et al*. (2010), (2012), (2013) and Molino *et al*. (2012). Elucidation of the role of the surface properties, such as surface charges, elasticity and nanotopography on the hASC attachment has been the most ambitious scientific, fourth objective of this dissertation. Joint research reported in Publication 3 has been devoted to this subject.

Ultimately, in Publication 5 we have extended the developed PPy coating strategies to a commercial bioabsorbable bone polymer-ceramic composite fixation screw (ActivaScrew™ TCP, Bioretec, Tampere, Finland) and implanted PPy-coated screws in New Zealand rabbits. Our 6 month preclinical study (P5, submitted) was to our knowledge one of the largest implantation studies (Jiang *et al*., 2002; Wang *et al*., 2004; Jager *et al*., 2010) ever carried out for PPy-biomaterials, and was a necessary demonstration of the preformance of PPyCS material in inducing favourable tissue reactions in bone and systemic toxicity. Furthermore, the study was one of the first in probing the erosion and degradation of chemically polymerized PPyCS *in vivo*, a subject which is currently poorly understood. Gaining more understanding of this was the fifth target of this doctoral thesis.

4. Experimental procedures

4.1 Synthesis of the test materials

4.1.1 Electropolymerization of PPyHA and PPyCS

Polymerizations on microelectrodes and large area electrodes have been conducted in two- and standard three-electrode configurations, utilizing potentiostat to deliver the constant potential (potentiostatic) or constant current (galvanostatic) for the electrochemical oxidation of Pyrrole. In all setups the inert counter electrode utilized was a platinum mesh having a geometric surface area significantly larger (3-electrode setup), or equal (2-electrode setup) to the area of the working electrode onto which the PPy was deposited. In the 3-electrode setup the potential of the working electrode was set and measured against a standard reference electrode, either Ag/AgCl in saturated KCl (+197 mV vs. standard hydrogen electrode SHE) or saturated calomel electrode (SCE) (+241 mV vs. SHE). In the 2-electrode setup the potential in the electrochemical cell is the measured difference between the counter and working electrodes.

We conducted electropolymerizations on various substrates: Titanium foil (P1), sputter-coated gold polyethylene-naphthalate film (PEN/Au), films with 50 nm Au-coating (P4), AT-cut 5MHz Au coated QCM crystals (P1), inter-digitated Au-microelectrodes on silicon (µ-Au/Si) (P1) and indium tin oxide on polyethylene terephtalate (PET/ITO) (P2). The specification of the substrates, successful polymerization conditions, experimental procedures for the characterization and the

most important experimental results based on the samples are summarized in the upper part of Table 1.

Table 1. All PPy samples studied. The various functional dopants are identified in the footnote.

Substrate	Polymerization method	Studied PPy/dopant	Scope, results and characterization methods	Reference
Electropolymerized PPy				
Titanium foil, t= 0.1 mm, A= 18 mm^2, Ti 99.6+%, activated by RCA (SC-1) (Goodfellow Cambridge Ltd)	3-electrode potentiostatic, +0.9 V vs. Ag/AgCl, 11 C/cm^2, 0.3-0.6 mA/cm^2	PPyHA[1]-CNT[2] onto PPyDBS adhesion layer	hASC attachment and viability , PPyHA layer thickness t_{PPy}>10 µm, Ti/PPyDBS/PPyHA-CNT electrodes attached to t=1mm /D10 mm PLA disk	Figure 5A [P1]
AT-cut 5MHz Au coated QCM crystals A = 1.37 cm^2 (Jiaxing Jingkong Electronic Co., Ltd., China)	3-electrode potentiostatic, +0.9 V vs. Ag/AgCl, 100 mC/cm^2, 0.2-0.4 mA/cm^2	PPyHA[1], PPyHA-CNT[2] PPyDBS (adhesion layer)	EC-QCM: swelling 4%, shear modulus 100 kPa (PPyHA), t_{PPy} = 210 nm (AFM) reversible redox activity by *in-situ* Raman spectroscopy (PPyHA-CNT), t_{PPy} = 410 nm	Figure 5B [P1]
Inter-digitated Au-microelectrodes (5 µm) on silicon, A ≈ 0.5 mm2 (VTT, Finland)	3-electrode galvanostatic, j=1-2 mA/cm^2	PPyDBS, PPyHA[1], PPyHA-CNT	EC-AFM, out-of plane nanoactuation of PPyHA by swelling 19-22% for well-adhering samples t_{PPy} = 200-400 nm	Figure 5C [P1]
Sputter-coated polyethylene-naphtalate film (PEN)/Au films (125 µm Dupont Teonex®), with 50 nm Au-coating (VTT, Finland)	2-electrode, potentiostatic, +1.0 V vs. Ag/AgCl, 300 mC/cm^2, 0.2-0.3 mA/cm^2	PPyHA[3] PPyCS[4]	Viability,attachment, proliferation and osteogenic differentiation of hASC on PPys, electrical stimulation in 2D geometry, AFM, t_{PPy} = 600-800 nm	Figure 5D [P4]
Sputtered-coated polyethylene-terephtalate (PET)/ ITO films, cat no.668559 Aldrich, 45 Ω surface resistance	2-electrode, potentiostatic, +0.9 V - 1.0 V vs. Ag/AgCl, 500 mC/cm^2, 0.1-0.15 mA/cm^2	PPyHA[5]	hASC attachment in charged films, KFPM, force mapping AFM, Raman spectroscopy t_{PPy} = 600-800 nm	Figure 5D [P3]
Chemically polymerized PPy				
PLA nonwoven fiber mesh (fiber diameter 10-20 µm and 40 µm), (TUT/Biomedical engineering)	interfacial chemical polymerization in aqueous solvent on PLA scaffold swollen by EtOH	PPyHA[3] PPyCS[4]	proliferation and osteogenic differentiation of hASC under electrical stimulation in 3D geometry, hydrolysis of PLA/PPy, impedance spectroscopy, SEM, AFM, t_{PPy} = 1-2 µm	Figure 6B [P2]
PLGA-tricalcium phosphate screw (ActivaScrew™ TCP, Bioretec, Tampere, Finland)	Interfacial chemical polymerization in mixed EtOH/water solvent	PPyCS[4]	Pre-clinical study, improved screws implanted in rabbit femur, t_{PPy} > 2 µm	Figure 6A [P5]

1) Bacterial derived HA sodium salt from *Streptococcus equi* (Fluka), M_w >300000 Da
2) Nanocyl 3151 oxidized multiwalled carbon nanotubes (Nanocyl S.A., Sambreville, Belgium)
3) Bacterial derived HA from *Streptococcus equi* (Sigma-Aldrich, 53747), M_w = 1630000 MDa
4) CS-A from bovine trachea (Sigma-Aldrich, C9819)
5) HA from human umbilical cord (Sigma, H1876)

Characteristic of electropolymerization substrates studies. Figure 5 depicts the various substates for the PPy electropolymerization. Already these substrates have significantly different characteristics in the electropolymerization of PPy. The differences in the substrates stem from several aspects: Au, Ti and ITO have a different surface chemistry, hydrophobic character, electrical conductivity, surface roughness, and geometric surface area, for example. Titanium metal surface carries a passivated electrically insulating oxide layer which must be chemically treated (e.g. RCA etching) for successful deposition of PPyHA. Properly cleaned noble metal surfaces can be readily coated without activation, but the polymerization conditions are different according to the hydrophobicity of the dopant used. We have utilized both potentiostatic and galvanostatic polymerization methods in the electropolymerizations. These methods yield significantly different rates of polymerization and characteristics of the PPy films, as highlighted by the following examples. We polymerized PPy films doped with hydrophilic polymeric dopants such as HA and CS (see figure 2) utilizing the potentiostatic method. Adherent films were successfully deposited on ITO, but virtually no PPy was deposited on the sputtered Au µ-electrodes (P1). A larger area Au could be readily coated with PPyHA, but the adhesion of the films was poor (P1 and P4). Hence, to achieve a significant deposition rate and adhesion on the Au µ-electrodes it was necessary to apply the galvanostatic polymerization method and to first deposit a more hydrophobic bridging PPy dodecyl benzene sulfonate (PPyDBS) film (P1). Subsequently, the polymerization of the HA doped and nanotube doped PPy was significantly enhanced on the PPyDBS/Au compared to the bare Au (P1).

Supporting electrolyte. The polymerization media containing HA or CS (or the corresponding sodium salt) as the electrolyte and the pyrrole monomer have low DC conductivity compared to low molecular weight organic acid salts, for example TS or DBS. Hence, the current during the polymerization of PPyHA and PPyCS is limited, typically one order or magnitude lower than for the more mobile electrolytes referred to. Another complication arises when the dopant has very high molecular weight (HA) and tends to form gel and accumulate onto the working electrode. These factors altogether slow down significantly the rate of PPy deposition on both micro- and large area electrode subtrates. The rate can be enhanced by adding a supporting electrolyte. In the supporting information submitted with Publication 3, we have addressed this issue by adding a KCl supporting electrolyte into the electropolymerization of PPyHA: potentiostatic polymerization of PPyHA (0.2 M Py and 0.2 mg/ml HA) onto 1.5 cm^2 ITO substrate without the supporting electrolyte was carried out: +900 mV vs. Ag/AgCl, current density j = 0.07 mA/cm^2, Q_{pol} = 0.5 C/cm^2. Subsequently, the same polymerization charge Q_{pol} = 0.5 C/cm^2 was applied, this time with the supporting KCl electrolyte in galvanostatic deposition (0.03 M KCl, 0.42 mA/cm^2,) and in the potentiostatic deposition (0.2 M KCl, 0.42 mA/cm^2). Cyclic voltammograms (CV) of the samples were recorded in 0.1 M KCl electrolyte. Hence, all the samples had been in contact with chloride

ions and electrochemically reduced/oxidized several times. Before elemental analyses by X-ray fluorescence (XRF) all the samples were rinsed with copious amounts of Millipore water and dried in air. All PPyHA films were slightly brown, soft and extremely hydrophilic (water contact angle >5 degrees), indicating that a significant amount of HA was present in the films. The rate of polymerization, as indicated by the rate of charge transfer *dQ/dt,* was significantly higher for the samples prepared in the presence of KCl supporting electrolyte. The chloride peak intensities were 17, 5 and 288 kc/s for samples polymerized without the supporting electrolyte, in the presence of 0.03 M KCl and in the presence of 0.2 M KCl, respectively. Although not highlighted in the manuscripts, the results indicate that the supporting KCl electrolyte may be beneficial in the polymerization of PPyHA. Chloride ions are inserted to the PPyHA at the latest during the immersion into Cl-containing electrolyte, possibly forming PPyCl. However, the hydrophilic nature of PPyHA is retained during the synthesis, and during the incubation in physiological salt solutions (saline, PBS, cell culturing medium containing serum, etc.).

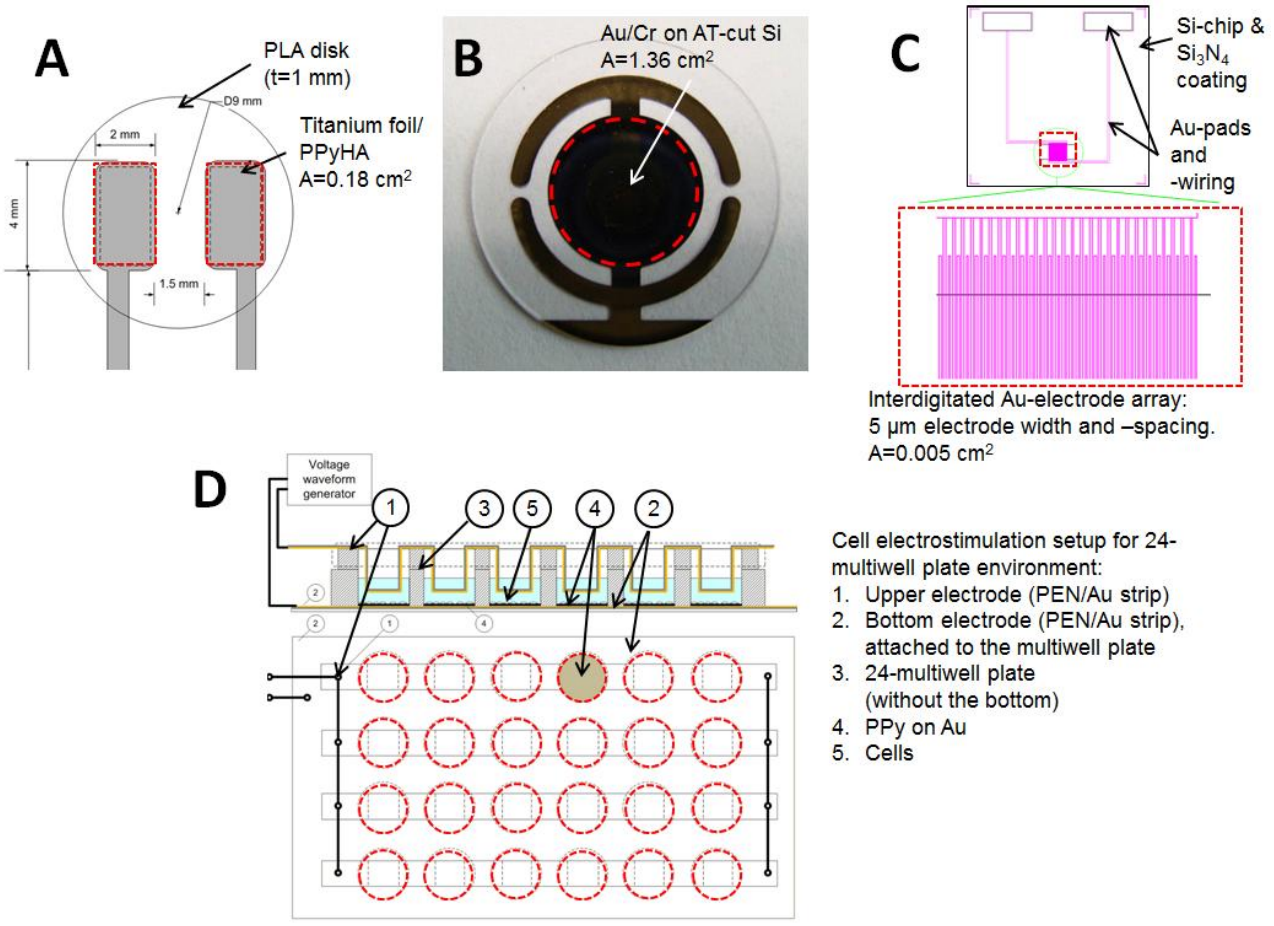

Figure 5. Substrates for the electropolymerization. The active electrode areas are marked with dashed red lines. In the electrostimulation setup (D) the sputter-coated conductive substrates (Au or ITO) were attached to bottomless multiwall plates by medical grade silicone rubber glue. PPy was deposited on the 24 circular areas simultaneously (marked #4 in the D). Platinum mesh was utilized as the (upper) counter electrode in the synthesis.

4.1.2 Chemical oxidative polymerization of PPy

PLA nonwoven scaffold. Polylactide fibers and non-woven scaffolds were supplied by Tampere University of Technology. The manufacturing of PLA (poly-96L/4D-lactide with inherent viscosity of 2.1 dl g-1, PURAC Biochem BV, Gorinchem, The Netherlands) nonwoven scaffolds is reported elsewhere (Ellä et al., 2007).

Prior to the polymerization, CS-A from bovine trachea (Sigma-Aldrich, C9819) and APS (Sigma–Aldrich) were dissolved separately in distilled water. CS and APS solutions were combined and pyrrole immediately added under vigorous stirring. The sample was placed into the polymerization bath, containing 0.036 M pyrrole, 0.1 M oxidant ammonium peroxydisulfate and 1 mg/mL chondroitin sulphate. The PLA nonwoven and the PPyCS coated scaffolds are depicted in Figure 6 A.

The non-woven scaffolds were pre-treated in ethanol before the polymerization. This was done in order to allow better absorption of the pyrrole monomer to the surface layer. The polymerization time in the non-stirrer reactor was 150 s. After the polymerization, the samples were rinsed thoroughly with water and dried in air. The samples were sterilized by gamma irradiation (BBF Sterilisationsservice GmbH, Kernen, Germany) with an irradiation dose of >25 kGy.

PLGA-β-TCP-composite screws (ActivaScrew™ TCP, Bioretec, Tampere, Finland), 2 mm in diameter and 10 mm in length were coated with black PPyCS coating (Fig. 6B). The thickness of the PPyCS coating was approximately 5 µm, with a significant variation within the screw. The screws had an x-ray positive marker made of pure β-tricalcium phosphate inserted in the tip of the screws. Ferric chloride was used as an oxidant and CS as a counter ion. First, batches of 15 screws were soaked in pyrrole (1.3 M) monomer solution in ethanol for 60 minutes, and subsequently transferred into freshly prepared $FeCl_3$ (0.5 M) aqueous solution containing 1 mg/ml CS-A. The screws were placed in a stainless steel mesh cage during the 15 min polymerization time. Magnetic stirring was applied during the polymerization. The reaction was quenched by moving the cage to distilled water. The screws were carefully rinsed with deionized water in ultrasonic path and dried in air. The surface resistance of the screws was <10 kΩ. Gamma radiation of 17.5-26 kGy (Gamma-Service Produktbestrahlung GmbH, Radeberg, Germany) was used for sterilization of the screws before their implantation in a rabbit femur.

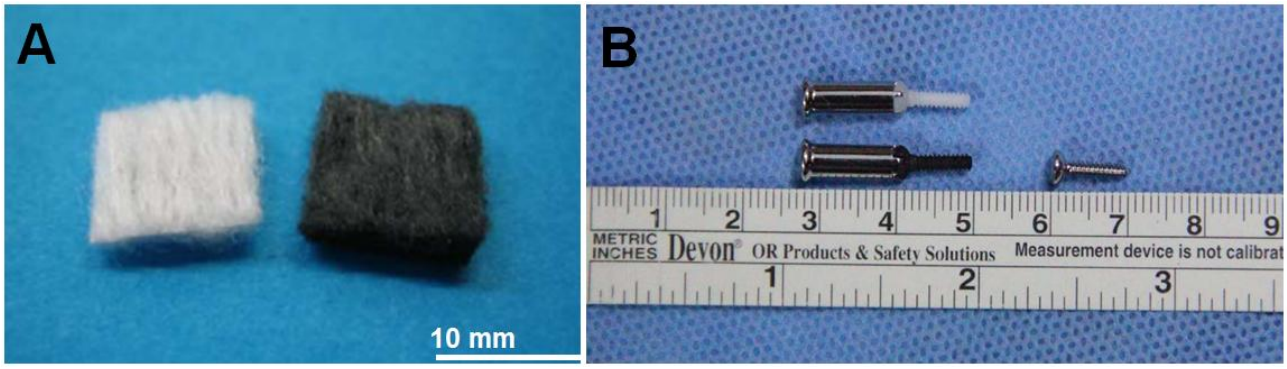

Figure 6. (A) PLA nowwoven scaffold coated with coated with the black PPyCS and (B) PLGA ActivaScrew™ TCP (Bioretec).

4.2 Fluid AFM

Surface roughness measurement. The PPyHA and PPyCS films studied in Publication 4 were polymerized onto Au/PET. The films were imaged in Dulbecco's phosphate-buffered saline (PBS; Lonza Biowhittaker, Switzerland). The imaging was done in contact mode using Park Systems XE-100 AFM (Park Systems, Suwon, Korea). Silicon nitride probes HYDRA-6R100N (Applied Nanostructures, Inc., Santa Clara, USA), with a nominal force constant 0.28 Nm^{-1} and a tip radius of curvature < 8 nm were applied. Areas of 20 x 20 μm^2 were scanned at 7 and 20 nN force set points for PPyHA and PPyCS surfaces, respectively. Images of 12 x 12 μm^2 were acquired with a scan speed of 1 Hz. Surface roughness analysis was done on the raw 512 x 512 pixel data. R_a values for a total of 10 randomly chosen 4 x 4 μm^2 sub-areas were calculated using Park Systems XEI 1.7.5 image analysis software. AFM image data (section 4.1) was 4th order plane fitted to show the nanoscale details of the PPy–HA and PPy–CS surfaces.

Surface elasticity, -adhesion and -charge - AFM force-distance curves of PPyHA films were acquired using an Asylum MPF-3D AFM in force volume mode. All measurements were done in dilute 0.005M NaCl electrolyte in an open measurement cell at room temperature. Silver wire was used as a pseudo reference electrode in those experiments with a biased AFM tip.

Characterization of the surface charge was done using biased (-200 mV) or neutral (0 mV) gold-coated silicon nitride tips OBL (Olympus Corp., Tokyo, Japan). The spring constant of the OBL cantilever was determined to be 0.020 N/m by the Sader method (Sader et al., 1999), and the cantilever sensitivity in the electrolyte was measured from the slope of the recorded force curves. Negative or zero bias voltage kept the tip-sample interaction in the repulsive regime indicating negative surface charge of PPyHA. The negative surface charge was confirmed by initial testing with both positive and negative bias on the tip, of which only the negative bias resulted in repulsive interaction. A maximum applied force of 0.7 nN was kept constant for the individual curves, which

were obtained at a scan rate of 300 nm/s. 32x32 force curve maps were collected for both the neutral (0 mV) and negatively biased (-200 mV) tip.

The surface elasticity was measured using platinum-iridium coated pyramidal silicon tips ANSCM-PC (Applied Nanostructures Inc., Santa Clara, CA, USA). A maximum applied force of 1-1.5 nN was kept constant for the individual curves, which were obtained at a scan rate of 300 nm/s. 64x64force curve maps were collected with a neutral (0 mV) tip. The spring constant of the ANSCM-PC cantilever was determined to be 0.034 N/m by the Sader method (Sader *et al*., 1999) and the cantilever sensitivity in the electrolyte was measured from the slope of the recorded force curves. The force curves were converted to force versus indentation curves and fitted with the Hertz Model (Hertz, 1882) to quantify Young's modulus. The analysis procedure was carried out using Asylum AFM Software (Igor Pro, Wavemetrics) and according to previously described methods (Higgins *et al*., 2012).

In total, 20 representative force curves taken from the nodule region of the uncharged and charged film and utilizing the -200 mV biased tip, were fitted to two simple double layer electrostatic force models, the linear model suggested by Onshima (1998) and the nonlinear model by Hull and Kitchener (1969), (see section 1.13 for details). Zero-distance was set manually and the data fitting done utilizing the nonlinear data fitting tools provided in the Origin Pro (Originlab Corporation, Northampton, MA, USA), version 8.

4.3 Kelvin force probe microscopy (KFPM)

KFPM images curves were acquired using an Asylum MPF-3D AFM. For the KFPM analysis the dried PPyHA samples were first immersed in dilute 0.005 M NaCl electrolyte. Subsequently, the samples were either charged (+200 mV vs. Ag/AgCl) or shortcut to the Ag-pseudo-reference electrode (0 mV vs. Ag). The samples were carefully rinsed to remove any salt solution and left to dry under ambient conditions.

4.4 Raman spectroscopy

In situ Raman spectroscopy. In Publication 1 the approximately 400 nm thick sample was polymerized on 1.36 cm^2 Au-coated At-cut QCM crystal. The Raman spectra of the PPyHA-CNT were measured *in situ* during electrochemical cycling of the 0.1M NaCl solution. The potential was continuously cycled between +200 mV and -1000 mV vs. Ag/AgCl at scan rate 5 mV/s. Each recording of the spectrum took 4 seconds. Therefore, each spectrum was averaged over 20 mV potential range.

The free liquid surface was covered with microscopic cover slide to minimize interference from the liquid-air surface. The spectra were measured using Horiba Jobin Yvon Labram HR micro-

Raman spectrometer (Horiba, Kyoto, Japan): 632.8 nm laser, 1200 lines/mm diffraction grating, 180 degrees scattering angle and through 50x objective lens.

De-doping of PPyHA. The same spectrometer was used in studying the de-doping of the dry PPyHA samples (Section 4.2). All samples were deposited by potentiostatic electropolymerization (Table 1) on ITO substrates, rinsed with PBS, air-dried and gamma sterilized (20 kGy radiation dose). The samples were categorized into four groups (Table 2). De-doping and Raman spectroscopy were done after subsequent transport of the samples from Finland to Australia. Group I and III were subjected to a 2 day pre-incubation period in the maintenance medium.
All Groups I-IV were immersed in PBS for 48 hours. Groups III and IV were subjected to +200 mV (vs. Ag/AgCl) electrochemical charging during the immersion in PBS for 48 h. After the 48 hour period in PBS, all samples were taken off from the the PBS, wiped dry and the Raman spectra recorded.

Table 2. Treatments and de-doping conditions before collecting Raman spectra.

Group	treatment after the electropolymerization	de-doping conditions during the test	electrochemical charging
I	pre-incubated in maintenance medium 48h	immersion in PBS 48 h	none (open circuit)
II	rinsing with PBS	immersion in PBS 48 h	none (open circuit)
III	pre-incubated in maintenance medium 48h	immersion in PBS 48 h	charging at +200 mV
IV	rinsing with PBS	immersion in PBS 48 h	charging at +200 mV

4.5 Electrospray ionization mass spectroscopy (ESI-MS)

The hydrolysis products of PPyHA-PLA fibers incubated in pure water were studied by ESI-MS [P2]. Gamma sterilized, non-coated PLA and PPyCS coated samples were hydrolyzed for 30 days at +60°C in 1.0 mL water. The water solvent was utilized because the ESI-MS method is not directly applicable for samples containing salts. The hydrolyzed samples were analyzed with a single quadrupole Perkin Elmer SQ 300-electrospray mass spectrometry (MS) system (PerkinElmer, Massachusetts, USA) in the positive ion mode. The drying gas (nitrogen) temperature was set at +175 °C and the drying gas flow rate at 8 L/min. The capillary exit voltage was varied between 60 V and 200 V to screen the onset of cracking of the PLA oligomers. The MS was operated in scan mode (mass range 200–1000) and dwell time was set at 0.1 ms. Briefly, the (hydrolysis) solution was filtered through 0.45 µm PTFE filter, 0.5 mL methanol was added to the mixture (water/MeOH 2:1 v/v) and the sample injected by syringe pump into the mass spectrometer at a flow rate of 5 µL/min.

4.6 Quartz crystal microbalance under electrochemical control (EC-QCM)

QCM technique was applied to detect the mass changes and viscoelastic properties during electrochemical cycling. The QCM probe was immersed in 0.2M NaCl solution containing Ag/AgCl reference electrode and platinum mesh counter electrode. The potential of the sample was controlled by a potentiostat. A viscoelastic model (Bahrami-Samani *et al*., 2008) was used to calculate the shear modulus and volume change of the material. The PPyHA-CNT films were electropolymerized on the Au-coated QCM crystals with an active area of 1.37 cm^2. Potentiostatic polymerization method was used (+0.9 V vs. Ag/AgCl). The deposited PPyHA-CNT and PPyHA films on the QCM crystals were characterized directly after the synthesis. SRS QCM200 (Stanford Research Systems) with AT-cut 5 MHz Au-coated crystals were used. The QCM probe was immersed in 0.2M NaCl solution containing Ag/AgCl reference electrode and platinum mesh counter electrode. The potential of the sample was controlled by BAS CV-27 potentiostat (Bioanalytical Sciences, West Lafayette, IN). The raw data signals (frequency and admittance) recorded from the QCM were converted to polymer film thickness and shear modulus using a solver program reported in a PhD Thesis (Bahrami-Samani, 2007). The density of PPyHA film was assumed constant (1.3 g/cm^3). The solver utilizes a viscoelastic material model capable of handling QCM data beyond the limitations of the well known Sauerbrey equation (Sauerbrey, 1959). Viscoelastic models are commonly applied for soft materials, such as polymeric hydrogels (Bandey *et al*., 1999). The SRS200 is equipped with a capacitance cancellation system. The CV signals and the raw data signals from the SRS QCM200 were recorded using Maclab 4/e DAQ system (AD Instruments Ltd, Dunedin, New Zealand).

4.7 Two and three dimensional cell culturing platforms

Electrical stimulation of Mesenchymal stem cells (Jha *et al*., 2011; Hwang *et al*., 2012; Kim *et al*., 2009) and hASCs (McCullen et al., 2010; Hammerick et al., 2010) have recently attracted attention due to reports of enhanced osteogenic differentiation *in vitro*. In tissue engineering this could bring new perspectives for the practical protocols of cell culture; for example, in enabling a culture condition avoiding growth factors.

In publications 4 and 2 we have built and utilized platforms for the 2- and 3-dimensional (2D) (3D) electrical stimulation of hACSs, respectively (Figure 7 A-C). The platform enabled cell stimulation condition was similar to the related previous work reported in planar (2D) geometry (McCullen et al., 2010; Hammerick et al., 2010; Kim *et al*., 2009; Tandon *et al*., 2010, 2012; Ercan and Webster, 2010) and 3D geometry utilizing dielectric substrates for cell culture (Sun *et al*., 2007; Hwang *et al*. 2012; Bolin *et al*., 2009). As distinct from previous studies, our platform utilizes electrically conductive PPy-PLA tissue engineering substrate with 3D-stimulation in multiwall plate culturing.

The top and the bottom electrodes were sputter-coated polyethylene-naphthalate (PEN) /Au films (125 µm Dupont Teonex®, with 50 nm Au-coating applied by VTT, Finland). The scaffolds were placed in custom made bottomless 24-well plates (Greiner Bio-One GmbH, Frickenhausen, Germany). The two electrodes were in galvanic contact with the cell culture medium in each well (Fig. 7A and 7B). The cell impedance in DMEM was approximately 15 Ω (see Table 2).

The single bottom electrode covering all the 24 wells was attached to the well plate with biomedical grade Silastic® Q7-4720 liquid silicone rubber. The top electrodes were bent strips of PEN/Au-film, partly extending to the cell culture medium, electronically connected in parallel (Fig. 7A and 7B, indicated by number 1). The electrode surface area was approximately 1 cm^2 for the top- and approximately 1.5 cm^2 for the bottom electrode in each well.

In the 2D stimulation the bottom electrode (Figure 7B, indicated by number 2) was coated with PPy on the areas exposed to the wells, i.e. the circular areas indicated by dashed line in Fig. 7C. Cells were attached to and stimulated on the PPy, as indicated by the 4 in Fig. 7B.

In the 3D stimulation the hASCs were attached to PPy-coated scaffolds (section 6.1), which were placed under mild compression between the Au-electrodes, as indicated by number 4 in Fig. 7C. Hence the scaffolds were in physical contact with both the top and bottom Au-electrodes.

According to impedance spectroscopy (Table 2), the low frequency impedance of a test cell (planar TiN) was significantly reduced by introducing scaffolds. This was also observed for the PLA, which is a dielectric. The reason for this could not be evidenced, but it could be hypothesized that the ionic conductivity of the electrical double layer on hydrated PLA played a role. As anticipated, the PLA-PPy scaffold induced the most significant decrease in impedance. At 10 kHz the properties of the DMEM started to dominate. However, at 10 kHz the PPy coated scaffold had significantly lower impedance compared to the medium.

ASCs were exposed to millisecond symmetric biphasic DC voltage pulses, illustrated in Figure 7D. Stimulation waveforms were generated by AFG 3010B (Tektronix Inc., Beaverton, USA) and the stimulation signal was supplied by a laboratory voltage amplifier (VTT, Finland). The amplifier system did not have charge compensation.

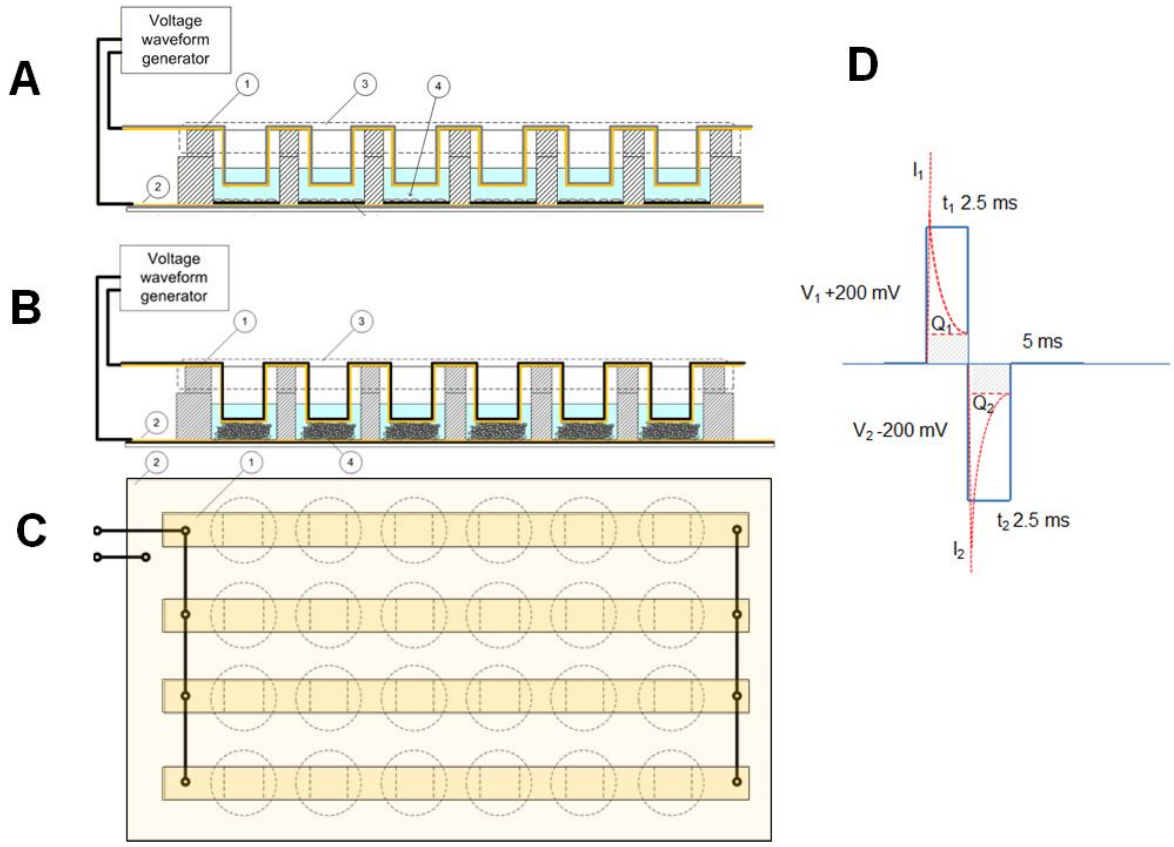

Figure 7. Platforms for (A) 2D- and (B) 3D-electrical stimulation of hACSs. The system was utilized in delivering biphasic pulsed DC voltage stimulation (D) for the cell, simultaneously in each well of the 24 multiwell plate (C). Adapted from Pelto *et al*. (2012) *Tissue Engineering A.* 19:7-8: 882–892.

Table 2. Summary of impedance spectroscopic data measured in DMEM and the corresponding constant phase element analyses. HP 4192A impedance analyser, excitation voltage sinusoidal 50 mV_{p-p}.

Sample	$\|Z\|_{cell}$ at 1 Hz (Ω)	$\|Z\|_{cell}$ at 10 kHz (Ω)	CPE capacitance (μF)	ideality coeff. η
PEN/Au/film	240000	15	2	0.97
TiN	83000	17	20	0.94
TiN/ PLA scaffold	13000	26	20	0.90
TiN/ PLA-PPy scaffold	1700	12	14	0.83

4.8 Cell culture

All the cell work was done at the University of Tampere, adult stem cells group.

For the cell study in Publication 3, the *attachment and viability* of thin PPyHA films on ITO were studied using Live/Dead staining (Invitrogen) at 3 h time points. The viable cells (green fluorescence) and dead cells (red fluorescence) were examined using a fluorescence microscope. Five representative optical images of the cells were analysed to measure the surface area of the individual cells using i-Solution Lite image acquisition and measuring software (IMT i-Solutions Inc.).

In Publication 4 the differences between various HA and CS dopants were examined, in combination with 2D electrical stimulation. For the testing, the PPy films were grown on Au-substrates (see section 3.1 for details). In Publication 2, we reported the viability and *early osteogenic differentiation* of hASCs in 3D cultures of electrically stimulated PPyCS coated with PLA nonwoven scaffolds. In both studies, the cell attachment and viability were assessed by live/dead staining (Molecular Probes, Eugene, USA).

Cell proliferation was studied with CyQuant Cell Proliferation Assay Kit (Molecular Probes). Osteogenic differentiation was assessed by alkaline phosphatase (ALP) activity, which was determined using an ALP Kit (Sigma-Aldrich).

4.9 Pre-clinical study

For the pre-clinical study reported in Publication 5, the biocompatibility and osteogenic induction of PPyCS coated bioabsorbable polymer composite bone fixation screws (ActivaScrew™ TCP, Bioretec, Tampere, Finland) were implanted into New Zealand white rabbits for a duration of 26 weeks. Uncoated bioabsorbable polymer composite screws and commercially available stainless steel cortical screws were inplanted as references.

The systemic effects were evaluated from food and water consumption, body weight, body temperature, clinical signs, blood samples, internal organs weights, and histological examination. Local effects were studied from bone tissue and surrounding soft tissue histology. New bone formation was evaluated by micro-computed tomography (μ-CT), torsion test and tetracycline labelling. Hard tissue histology was conducted from the tetracycline-labelled samples. After examining the tetracycline fluorescence lines of the slices, toluidine blue (ZiYi Chemical Ltd, Shanghai, China) was added on the slices for 15 min.

5. Results

5.1 Surface properties of PPyHA and PPyCS

Surface roughness. Figure 8 depicts contact AFM images of PPyHA (A) and PPyCS (B) and individual scan line profiles (below the AFM images, marked red and green) acquired in PBS (P4, 2014). The surface topographies are similar to the PPys reported earlier for electropolymerized films (Armes et al, 1999b, Barisci *et al*., 2000; Gelmi *et al*., 2010; Silk *et al*., 1998a, 1998b; Mabrouk, 2005; P3, 2013). Both PPyHA and PPyCS surfaces present approximately 100 nm high protruded islands breaking the otherwise uniform (R_q 25nm) surface nanotopography. The surface roughness and the film thickness of the PPyHA were in the same range as for the films studied inPublication 3 (Table 1).

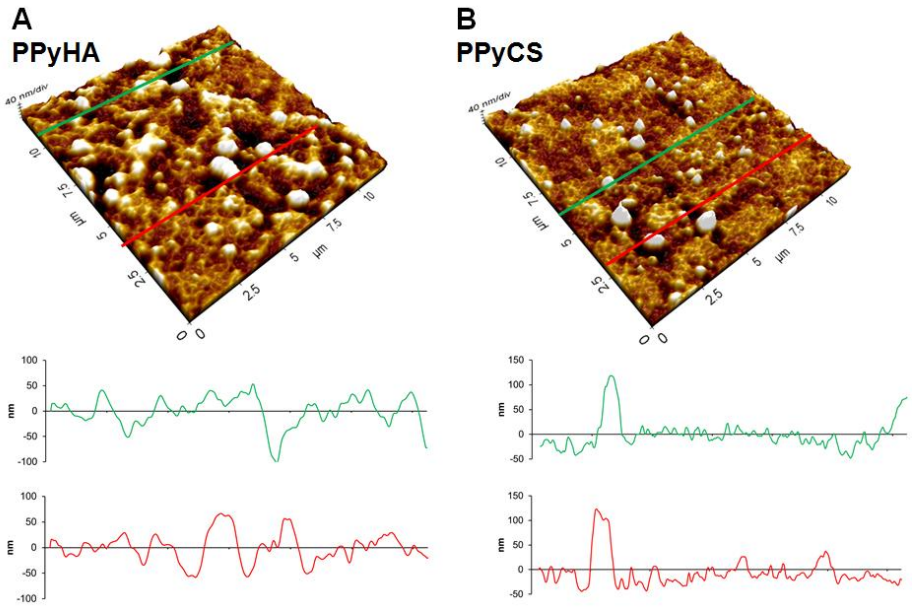

Figure 8. Contact AFM image of (A) PPyHA and (B) PPyCS surfaces in PBS. The individual scan line profiles are presented. Both surfaces have the same surface roughness (R_q=25 nm).

Surface Charge in air. Figure 9 presents the KFPM height and surface potential images of the as-grown (A and B) and the +200 mV vs. Ag/AgCl electrochemically charged (C and D) PPyHA films.

KFPM topography images (left) and surface potential maps (right) of uncharged (+0 mV) (A and B) and charged (+200 mV) (C and D) PPy-HA are presented inFigure 9. The surface roughness values of the uncharged and charged films were 8.9 nm and 9.4 nm, respectively, indicating that the surface roughness was not significantly affected by the electrochemical charging. The surface potential images in figures 9B and 9D display average variations of 4.38 mV RMS and 2.91 mV RMS for the uncharged and charged films, respectively. The surface potential image of the uncharged (+0 mV) film showed phase separation in surface potential. More negative potentials

(darker regions in Fig. 9B) correlated with the nodule structures, while areas of more positive surface potential correlated with the peripheries of the nodules (brighter regions in Fig. 3B). In contrast, the surface potential of the charged films showed a more uniform distribution of the surface potential with no clear correlation with the topography (Fig. 9D). Previous observations in the surface potential (Barisci *et al*., 2000; Semenikin *et al*., 1996), conduction current (Gelmi *et al*., 2013) and AFM phase signals (Gelmi *et al*., 2010), showing that the application of a positive electrochemical potential largely removes this phase separation, are in accordance with the observations. Previous studies and our study support the presence of more crystalline, heavily doped and electrically conductive parts of the PPyHA in the nodules, similar to organized and rigid PPys, such as PPyTS (Gelmi *et al*., 2010).

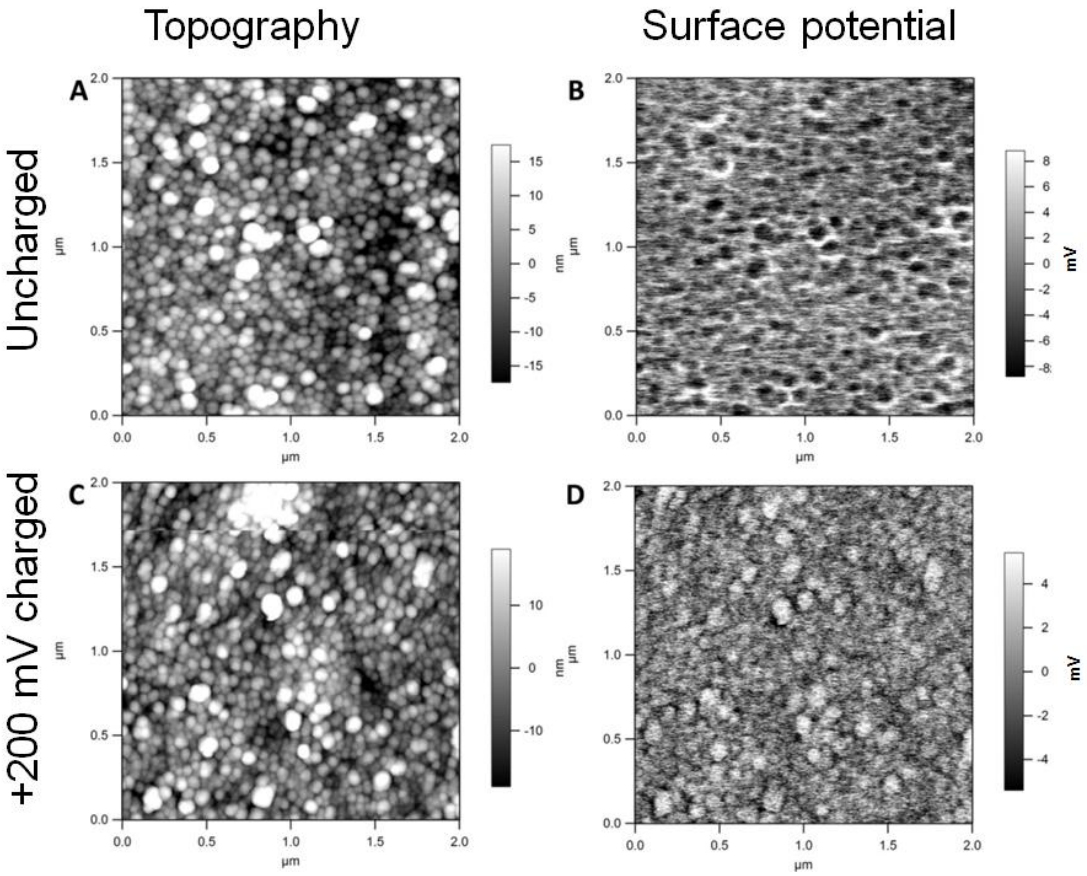

Figure 9. Kelvin force probe microscopy. (A and B) Corresponding height (8.9 nm RMS) and surface potential images (4.38 mV RMS) for the uncharged PPy-HA film. (C and D) For the same film, corresponding height (9.4 nm RMS) and surface potential images (2.91 mV RMS) after charging (+200 mV). Reprinted with permission from Pelto *et al*., *Langmuir* 29:20: 6099 – 6108. Copyright (2013) American Chemical Society.

Surface charge in fluid. Force maps for the uncharged and charged samples with no potential bias applied to the tip and obtained in 5 mM NaCl are shown in Figures 10A-D and 11A-D, respectively. For the uncharged sample, the topography image gave an RMS (average) surface

roughness of 23.7 nm (surface area, 1.23 μm^2) (Fig. 10A). Each pixel in the topography image represents a single force curve, which correlates with a specific x-y position on the film. The inset in Figure 10B shows two force curves taken on a nodule structure (position 1) and the periphery of the nodules (position 2) from the marked region (red square) in the topography image. These force curves were recorded with unbiased tip (tip potential 0 mV). Neither of the curves exhibited adhesion, but the slope of their contact regions differed (Figure 10B). The slope of the contact region in the force curves for the nodule structure (solid line) was steeper compared to the nodule periphery (dashed line), indicating that former had a higher stiffness. Figure 10C of the adhesion map, which is also overlaid on a 3-dimensional topography image in Figure 10D, showed low adhesion (RMS average, 45 pN) between the tip and polymer and no correlation with the surface topography.

In comparison, the charged sample showed the same morphology and similar RMS (average) roughness of 29.2 nm (surface area, 1.28μm^2) (Fig. 11A), indicating that the charging of the film did not have a significant effect in the surface topography. Individual force curves on the nodules (position 1, inset from the marked region in Fig. 11A) showed no adhesion (Fig. 11B, solid curve), but in this case adhesion was observed at the nodule periphery. This was clearly observed in the adhesion maps (Fig. 11C) and adhesion overlay with the topography (Fig. 11D), which showed significantly greater adhesion (RMS 634 pN) that strongly correlated with regions of only the nodule peripheries.

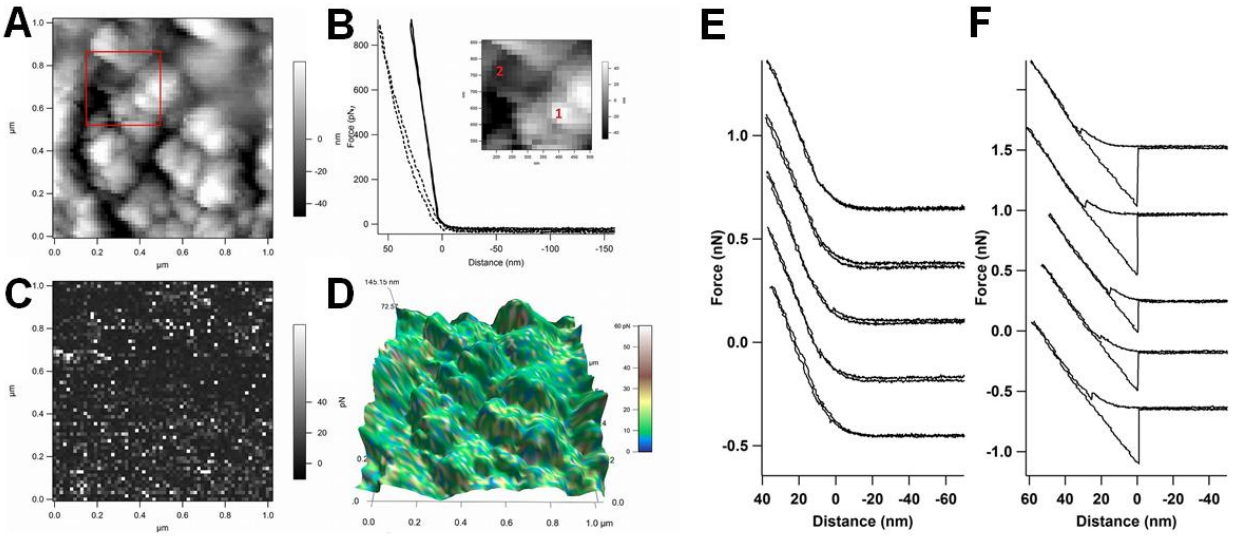

Figure 10. Uncharged Film – (A) Height image (23.7 nm RMS) obtained from the force map. (B) Representative curves taken from the different regions (inset) of the film. Curves 1 and 2 are taken from nodules and peripheries, respectively. (C) Adhesion map. (D) 3-D image of adhesion map overlaid on topography. (A-D) Tip potential 0 mV. (E) Representative approach curves and the retracting curves on the nodules. (F) The approach curves and the retraction curves on the peripheries of the nodules. Tip potential -200 mV in 0.005M NaCl (aq) electrolyte. (E and F) Tip potential -200 mV. Reprinted with permission from Pelto *et al*., *Langmuir* 29:20: 6099 – 6108. Copyright (2013) American Chemical Society.

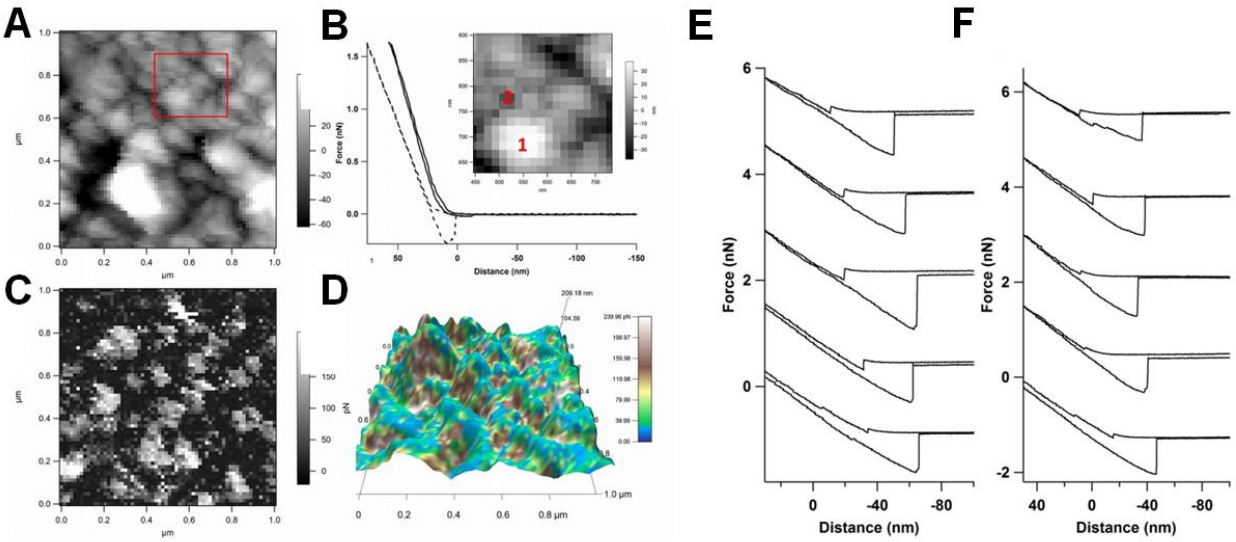

Figure 11. Charged Film – (A) Height image (29.2 nm RMS) obtained from the force map. (B) Representative curves taken from the different regions (inset) of the film. Curves 1 and 2 are taken from nodules and peripheries, respectively. (C) Adhesion map. (D) 3-D image of adhesion map overlaid on topography. (A-D) Tip potential 0 mV. (E) Representative approach curves and the retracting curves on the nodules. (F) The approach curves and the retraction curves on the peripheries of the nodules. Tip potential -200 mV in 0.005M NaCl (aq) electrolyte. (E and F) Tip potential -200 mV. Reprinted with permission from Pelto *et al*., *Langmuir* 29:20: 6099 – 6108. Copyright (2013) American Chemical Society.

Compared to the previous force maps recorded with a non-biased tip, an applied bias to the tip enabled further insight into the interaction forces, particularly electrostatic repulsion and adhesion. Figure 10E and 10F and 11E and 11F present in total 20 representative force curves for the uncharged (0 mV) and charged (+200 mV) PPy-HA surfaces, respectively, obtained from force maps taken in 5 mM NaCl with a bias of -200 mV applied to the AFM tip. A low concentration of salt was applied in order to be able to project the electrostatic interactions to long distances (the calculated Debye double layer thickness 4.3 nm) where they can be distinguished from shorter range hydration and steric forces.

Force curves were selected either from the nodules (Figure 10E and 11E) or from the peripheries of the nodules (Figure 10F and 10F). For the uncharged surfaces, a repulsive interaction upon approach and no adhesion were observed on the nodules, whereas, in contrast, an increased ‘snap-in’ or small-range attractive force upon approach and adhesion of ~ 350 pN RMS were observed in the peripheries. The observed repulsive interactions for both the nodules and their peripheries are due to electrostatic forces. We suggest that the small range attractive forces occurring only on the peripheries contribute to the observed adhesion (Fig. 10F and 11F). When the film was charged (+200 mV), small-range attractive forces upon approach and increased adhesion appeared on the nodules (Fig. 11E) and remained on the nodule peripheries. The

appearance of small-range attractive forces on the nodule areas again correlates with adhesion at these locations. Furthermore, the effect of charging on the surface potential in the KFPM images and above surface forces is clearly more pronounced at the nodule regions. Occasionally, multiple, small-range attractive forces were observed on the charged films, indicating that some of these interactions were attributable to the tip penetrating the sample surface. Indeed, the observed low elastic modulus of these films makes them susceptible to penetration by the AFM tip, which may contribute to the adhesion. The presence of these multiple 'snap-ins', however, makes the analysis somewhat more difficult due to the fact that small-range attractive forces also arise due to the break-up of the double layer repulsion and subsequent effect of the attractive (van der Waals) force experienced by the tip in the proximity of the surface. The presence of increased attractive forces and decreased electrostatic repulsion on the nodules of charged surfaces compared to uncharged ones can additionally result in increased adhesion. It is therefore possible to elucidate the fundamental surface forces that play a role in the nanoscale and molecular interactions at these polymer surfaces in liquid.

***Surface potential*.** The linear DLVO model comprising a single exponential function fitted reasonably well to the data (non-weighted χ^2, R>0.96) using the two parameter (surface potential and Debye length) model, and the fitted curves were consistent with the theoretical Debye length of the 0.005M NaCl(aq) electrolyte (4.3 nm). Long range repulsion forces of the order of 10-100 pN were present in all analysed curves and were attributable to double layer electrostatics of a slightly negatively charged surface and negatively charged AFM tip (-200 mV). For example, the quantified surface potential was in the range of -5 mV to – 50 mV for the films. Initial qualitative observations showed that the repulsive forces were weaker for the charged films compared to the uncharged ones, as expected due to the application of a positive bias (+200 mV) to these surfaces and quantitatively supported by the data fitting to the force curves. From the DLVO fitting, it was confirmed that the nodules of the charged film were significantly more positive than the nodules of the uncharged film ($p < 0.001$ at significance level of 0.05) but there was no significant difference in the estimated surface potentials of the peripheries of the uncharged and charged films ($p = 0.11$ at significance level of 0.05). When comparing differences across the polymer surfaces, the estimated surface potential of the nodules was slightly but not significantly more positive than that of the peripheries of the uncharged surfaces ($p = 0.086$ at significance level of 0.05). In contrast, the estimated surface potential of the nodules was significantly higher than that of the peripheries ($p < 0.001$ at significance level of 0.05) for the charged films.

It is noted that the nonlinear DLVO model (eq.2), which is more appropriate for higher surface potentials (> ±50 mV), did not fit the data as well as the linear model and hence showed larger error in the calculated surface potential values. The obvious drawback in applying the nonlinear model was the difficulty in setting the zero-distance to the experimental data (section 7.2). Fitting

the data to the nonlinear DLVO model systematically predicted 10 - 25 mV more negative surface potential, both on the nodules and on the peripheries. Nonetheless, the general trends were identical to the linear model.

Surface elasticity. Figure 12 depicts the AFM surface elasticity mapping of different charged PPyHA films. Asylum MPF-3D AFM system in force volume mode was applied. The elastic modulus in 64x64 pixels was overlayed on the topographic image. Calibration of the AFM probe (gold coated silicon nitride tip, OBL Olympus Corp, Tokyo Japan) was done utilizing the Sader method (Sader *et al*., 1999).

Using this setup, we examined simultaneously the effects of the charged state of PPyHA on elastic moduli, roughness, tip adhesion and correlated the AFM data with a cell attachment study (section 5.4). For the AFM experiments, the charged and uncharged samples were identically prepared, with the charged samples being subjected to the application of +200 mV versus Ag/AgCl (0.005 M NaCl) in the AFM electrochemical cell shortly before the AFM scan. Elastic modulus was derived by fitting F-D data into the Hertz contact model. The surface roughness of the films was 23.7 nm and 29.2 nm (RMS) and the elastic moduli 2.3 MPa and 5.3 MPa (RMS) for the uncharged and charged films, respectively. Thus, the surface roughness was not changed significantly by applying the charging potential. However, the charged sample had higher elastic modulus, the difference being clearly noticeable but not dramatic. The elastic moduli estimated from the AFM analysis were low compared to previously reported values for conductive polymers (30-1000 MPa) (Gelmi *et al*., 2010).

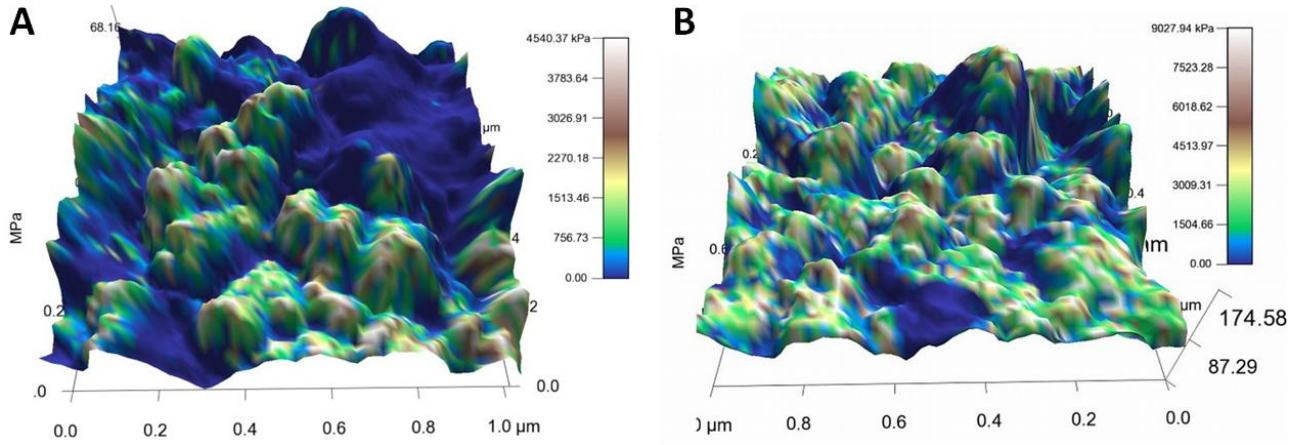

Figure 12. Surface elasticity mapping overlayed on surface topography. (A) As synthesized (B) Electrochemically charged PPyHA films on ITO. The surface roughness of the films was 23.7 nm and 29.2 nm (RMS) and the elastic moduli 2.3 MPa and 5.3 MPa (RMS) for (A) and (B), respectively. Reprinted with permission from Pelto *et al*., *Langmuir* 29:20: 6099 – 6108. Copyright (2013) American Chemical Society.

The shear modulus of PPyHA-CNT films, derived from QCM data, was reported in Publication 1. The observed frequency shift occurring during the redox cycle was approximately 60 Hz and the corresponding change in the admittance signal was 4Ω. From these figures we calculated the shear modulus (G) of the film that was estimated to be in the order of 100 kPa (elastic modulus ~250 kPa), which is higher than that of a typical hydrogel but lower than that of highly organised conducting polymers. Given the substantial differences between the materials and test conditions in publications 1 and 3, the low modulus derived by QCM is in qualitative agreement with the values derived by AFM for the PPyHA.

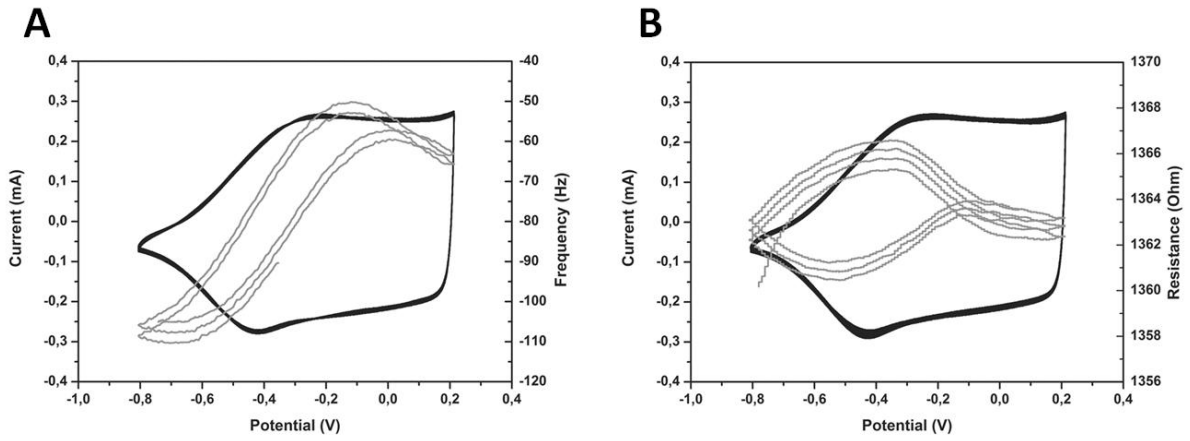

Figure 13. Electrochemical quartz crystal microbalance data for electropolymerized PPyHA-CNT film on Au coated QCM crystal. A viscoelastic model was used to calculate the shear modulus. Reprinted with permission from Pelto *et al*., *Journal of Biomedical Materials Research Part A* 93: 3:1056–1067. Copyright (2010) John Wiley and Sons.

5.2 Stability of biopolymer doped PPys

DC conductivity of the gamma sterilized samples. the conductivity of the chemically polymerized and sterilized PPyHA and PPyCS scaffolds and the electro-polymerized PPy films with gamma radiation doses 2.0-2.5 $\cdot 10^5$ Gy (P1-P5) are in agreement with the earlier results of Wolszczak *et al*. (1995). The radiation induced loss in the conductivity was 40-50%, which is in the same range with the loss observed during long term storage in air atmosphere. However, it is noteworthy that the reported loss in conductivity is sensititive to the radiation dose and dose rate (Wolszczak *et al*., 1995; Ercan *et al*., 1995), which should be carefully controlled.

De-doping and hydrolysis of PPyCS coated PLA fiber scaffold. Figure 14E shows the DC-resistance of PPyCS coated PLA nonwoven scaffolds (10-15 µm filament diameter) after ISO-15814:1999(E) standard hydrolysis test and water rinsing in each time point (1d, 2d, 7d). Conductivity has been measured from taking 20 individual PLA-PPyCS fibers into a bundle,

making electrical contact by copper electrodes and using a multimeter in 2-electrode setup for the measurement. The measurements were done on rinsed and air-dried samples.

SEM images of the sample at day 0 are shown in Figure 14A-D. The average layer thickness of PPyCS was roughly 2-3 microns (inset image in 14D). The PPyCS sample was not coated with the typically applied sputter coated Au for the SEM imaging. The PLA sample has been coated by 50 nm Au because of the heavy electric charging of insulating PLA under the SEM. The uncoated melt spun PLA fibers have a nanoscopically very smooth (R_q<30 nm by AFM) and hydrophobic surface. PPyCS coating renders the surface superhydrophilicity and nanoscopic roughness (R_q>100 nm). The PPyCS coated samples were intensely greenish-black-colored and the PPy coating had initial electrical conductivity of estimated 50 S/m. In this test the measured DC conductivity of the PLA-PPyCS nonwoven decreased almost two decades during the first 24 hours of the hydrolysis test (Figure 14E). However, as it turned out, 5-10% the original conductivity was reversible by re-doping with diluted HCl. Hence, the loss of conductivity was partly explained by de-doping in the standard test (pH 7.4).

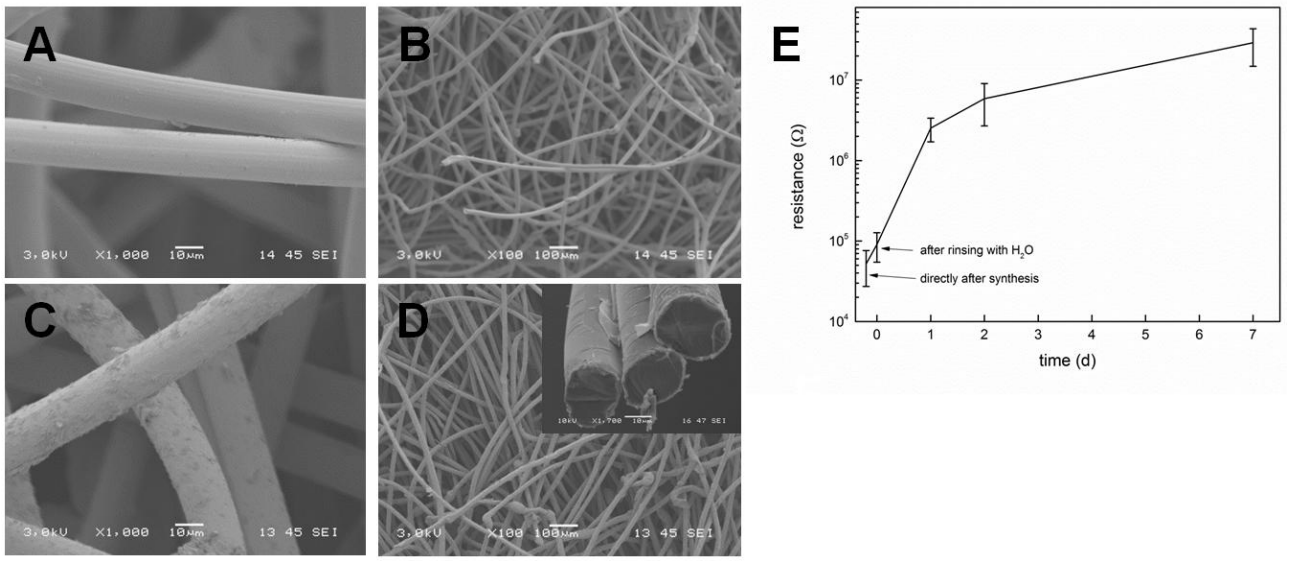

Figure 14. (A and B) SEM images of PLA fibers without sputtered gold layer. (C and D) PLA-PPyCS scaffold with 20 nm gold coating. At 3 kV acceleration voltage, the PPy-coated PLA scaffold could be readily imaged, but the electrically insulating PLA scaffold could not be imaged without a thin coating layer (typically gold or carbon) due to heavy electrostatic charging. Adapted from Pelto *et al*. (2012) *Tissue Engineering A* 19:7-8:882–892.

Figure 15 presents SEM and non-contact AFM images of the 40-50 µm thick PLA-PPyCS fibers after 0 d, 10 d and 20 d hydrolysis in the standard hydrolysis test. Significant cracking of the PPy coating has occurred already at day 3. The severity of the cracking is constantly increasing during the hydrolysis test. It has most probably occurred during the handling of the specimen, and associated with the loss of mechanical properties and/or the compromised adhesion of the PPy

layer during the incubation. At day 0 the PPy layer was very firmly adhered to the fiber. At days 6 and 10 the PPyCS layer still had morphology similar to the sample at the start of the test. However, the morphology has changed significantly by day 20. The conductivity of the sample has decreased significantly at day 20, which is evidenced by the electrostatic charging of the sample under SEM. The AFM analyses show that the surface roughness has also dropped significantly, from 120 nm (R_a) at day 0 to 30 nm (R_a) at day 20.

However, at day 20 the mechanical properties of the PPyCS fiber were at their original level (Hiltunen and Pelto, 2009). Hence, the changes observed by SEM are confined to the surface layer. The initial wetting and hydrolysis of the PLA fiber may partly explain the cracking of the PPyCS coating. The smoothening of the PPyCS is largely attributable to the changes in the highest PPy-nodules, indicated in yellow in the AFM images in Figure 15. Some dark colored PPy-particles were detected from the incubation medium during the test. However, the amounts were not significant enough to fully explain the smoothening of the fiber surface. Hence, the presumable origin of the changes is related to the re-organization and dimensional changes of PPyCS nodules during the hydrolysis test.

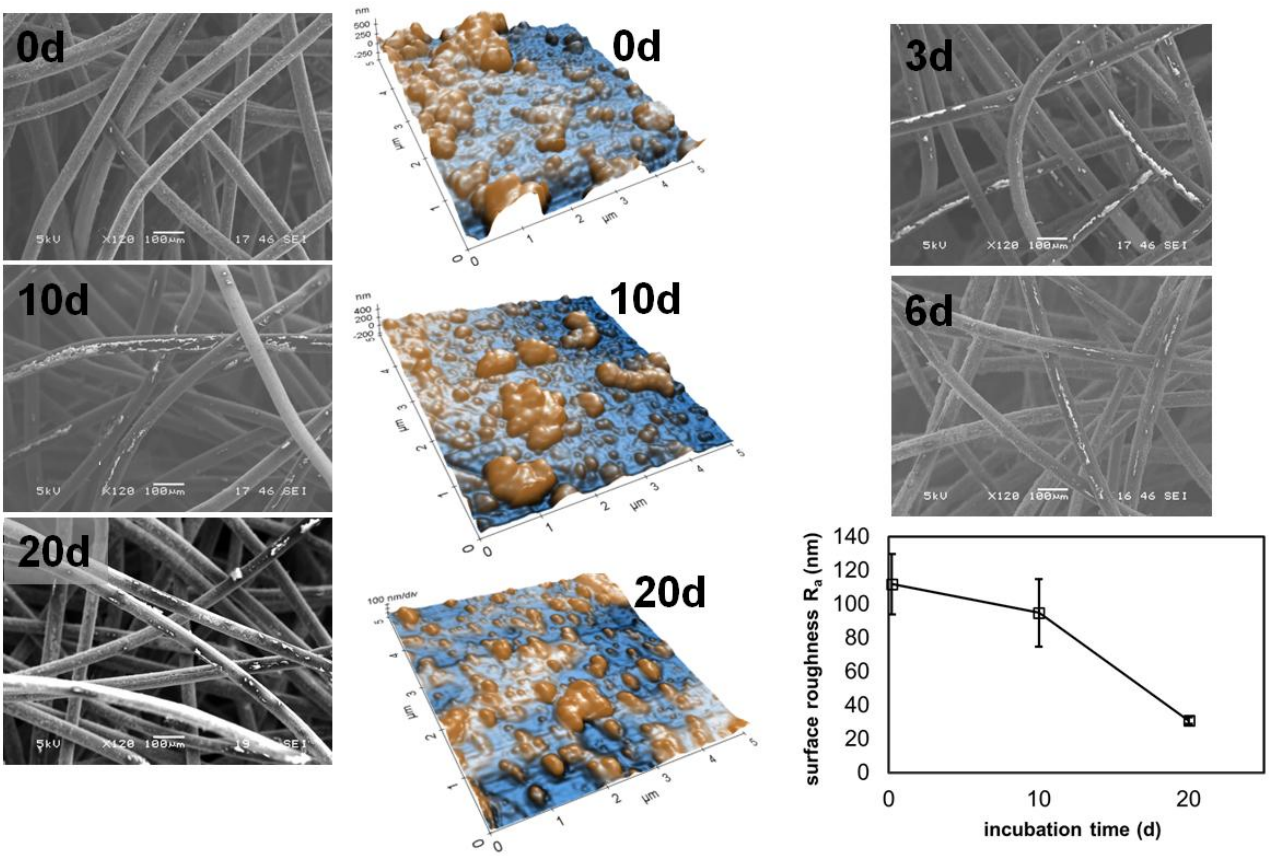

Figure 15. SEM and AFM images and surface roughness of the PLA-PPyCS fiber during the 20 day hydrolysis test. The scales of the AFM images are varied for clarity: 500 nm, 400 nm and 100

nm for the samples at 0 d, 10 d and 20 d, respectively. Adapted from Pelto *et al*. (2012) *Tissue Engineering A* 19:7-8:882–892.

The mass spectra of the PLA and PLA-PPyCS sample in the m/z ratio in the range 200-700 are shown in Figure 16. Based on the layer thickness in Figure 14D, the PLA-PPyCS sample contained an estimated 10 wt-% of the PPyCS. The spectra for the PLA are remarkably similar. Hence, the water hydrolysis of the PLA is largely unaffected by the PPyCS coating. The spectra contain peaks of PLA oligomers (2-7 mers), the highest peak representing the pentamer, and the corresponding Na- peaks (Andersson *et al*., 2010). No significant peaks associated with potential PPy or CS degradation products such as oxidized pyrrole oligomers or oligosaccharides were found in the studied m/z range. Degradation products with m/z <200 were not assessed. However, UV/VIS spectra of the hydrolysis test solutions did not indicate the presence of low molecular weight aromatic compounds (such as pyrrole, pyrrole di- or trimers, maleimide, succiimide etc.) in the water hydrolysed samples. Our data suggests that the PPy chain is at least not depolymerized or fragmented in the water hydrolysis test. More data would be required to show the stability of the PPy chain in a more complex hydrolysis test, during *in vitro* culturing in the presence of bioactive components, not to mention conditions *in vivo*.

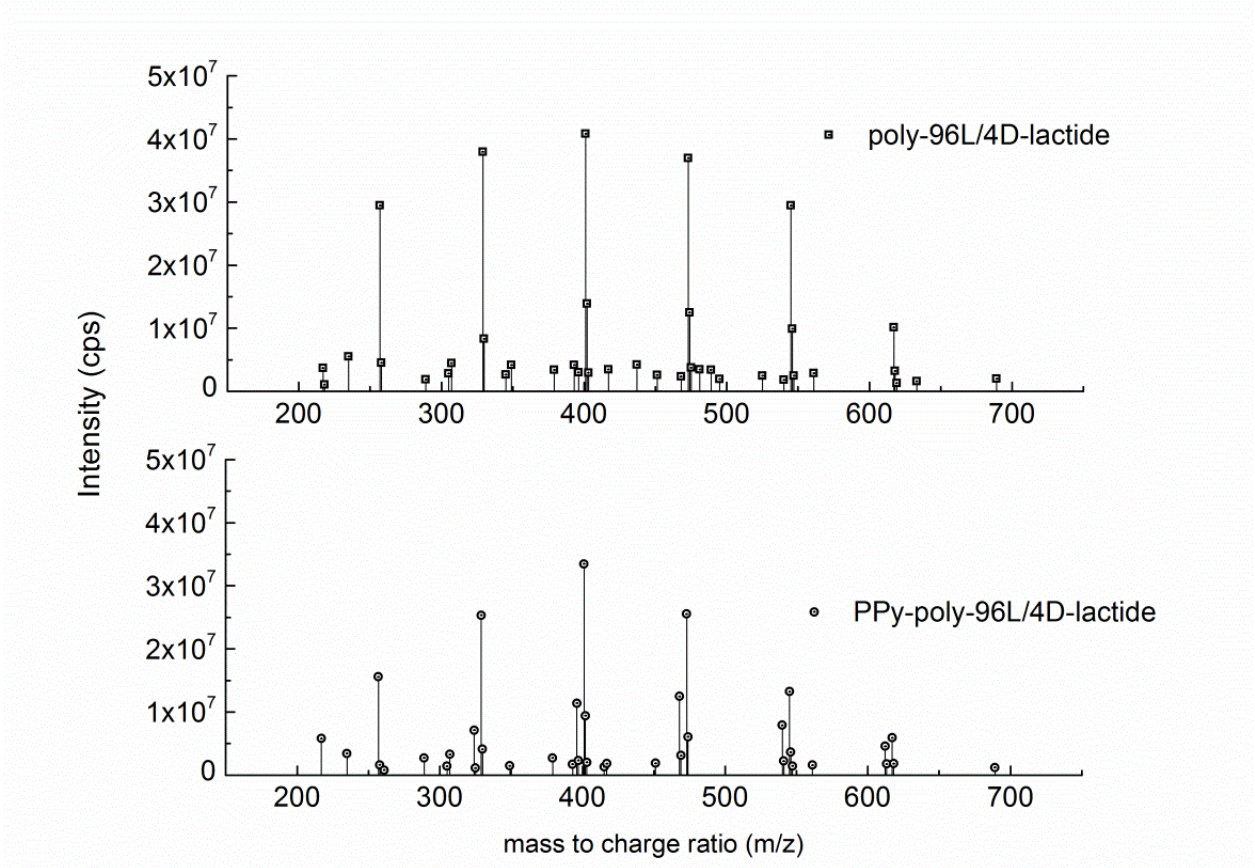

Figure 16. Mass spectra of the PLA and PLA-PPyCS hydrolysis sample. Adapted from Pelto *et al*. (2012) *Tissue Engineering A* 19:7-8:882–892.

De-doping of electropolymerized PPyHA films studied in Publication 3 was assessed by Raman spectroscopy. Figure 17 presents the Raman spectra and the peak assignment of the PPyHA samples categorized into groups (I-IV, Table 2), according to pre-incubation and charging conditions. The spectra hve been normalized by the peak at 933 cm^{-1}. The oxidation (doping) state of the PPy chain can be assessed by examining the intensities of the peaks associated with the polaron lattice, e.g. the peaks at 933 cm^{-1} (1), 988 cm^{-1} (2), 1050 cm^{-1} (3) and the position of the C=C stretching peak at 1605 cm^{-1} (10) (Santos et al., 2007).

All spectra are typical of doped PPy (Santos et al., 2007; P1, 2010). The spectral changes observed for the samples are similar the changes observed *in situ* during electrochemical cycling. Hence, they are due to the de-doping on the PPy chain. Groups III and IV (electrochemically charged during the pre-treatment/pre-incubation) show largely similar spectra, where the relative intensitities of the polaron peaks have not changed significantly. In contrast, the samples fromgroups I and II (no charging) have significantly different spectral features compared to groups III and IV, such as characteristic changes in the intensity of the peak at 988 cm^{-1}(2) and the change in position of the 1605 cm^{-1}(10) peak. These changes are attributable to the reduction of the PPy chain, i.e. the gradual change of the bipolaron (PPy^{2+}) - to polaron (PPy^{+}), and to the neutral PPy^{0} chain (Santos et al., 2007). Hence, the highly conductive bipolaron lattice can be stabilized in PBS (pH 7.4) by applying +200 mV external potential. The pre-incubation period has also contributed to the de-doping, as evidenced by the relative spectral changes in the intensities at peaks no. 1 versus 2 and no. 8 and 9 versus no. 10.

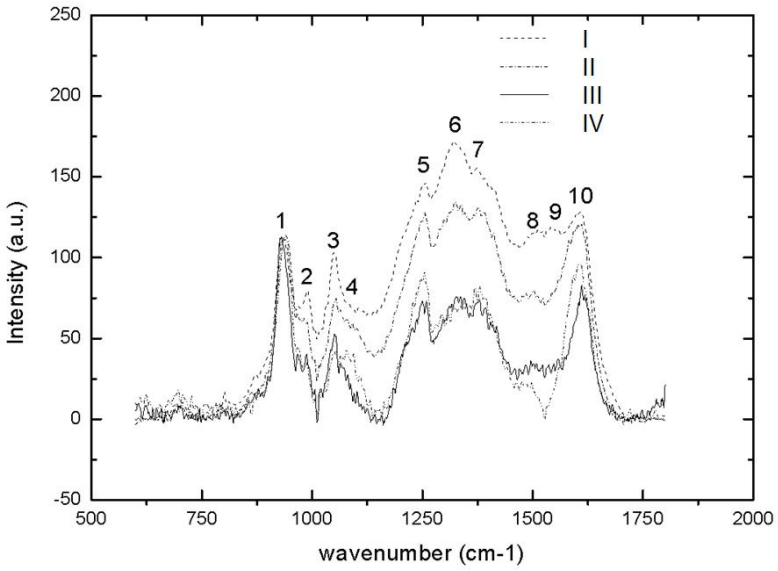

n:o of peak /assignment	cm-1
1 C-H o.o.p.b. (polaron)	933
2 CH_3 ring str.	988
3 C-H i.p.d.	1050
4 Ca-Cb str. & C-H i.p.d.	1108
5 C-H /N-H i.p.b.	1254
6 ring Ca=Cb str.	1323
7 ring Ca=Cb str.	1373
8 Unknown peak	1514
9 ring C=C str	1549
10 C=C str.	1605

Figure 17. Raman spectra and peak assignment of PPyHA films. Pre-incubation and charging during incubation can be associated with spectral changes related to de-doping.

Hydrolysis of CS in acidic polymerization medium – The viscometric studies conducted in our laboratory suggested that CS (CS-A from shark skin) was significantly affected by acid hydrolysis in an oxidative (0.1 M APS) environment mimicking the pyrrole polymerization conditions. Briefly, APS oxidant was activated by introducing isopropyl alcohol as an oxidizable reagent into solution containing 2-5 mg/ml CS in PBS. The pH of the CS solution was decreasing steadily within a few hours by the liberation of sulphuric acid. The corresponding decrease in the specific viscosity was from 0.4 to 0.2 dl/g. Omiting the dependence on the CS conformation on the pH and ionic strength of the buffered solution, this corresponds to a significant decrease in the molecular mass of the CS. (Pelto and Hiltunen, 2011).

5.3 Electro-mechanical actuation in nanometer scale

In Publication 1 we have addressed the nanoscopic bulk expansion of sub-micron thick PPyHA in physiological electrolytes. Although the biological functionality of PPyHA has been reported, the electroactivity of this material has been doubtful. For example, the electrical DC electrical conductivity was at least 1-2 orders of magnitude lower than PPyDBS (Collier et al., 2000; P3, 2013) with hydrogel like elastic properties far from the organized and densely packed PPys (P1, 2010). In order to enhance the conductivity and to increase the mechanical strength and elastic modulus, we have incorporated CNTs into the material (PPyHA-CNT).

Figure 18 shows the AFM scanning over PPyHA (A) (Q_{pol} = 40 mC/cm^2) and PPyHA-CNT (Fig. 18D) (40 mC/cm^2) grown on an interdigitated array of Au on silicon. The thicknesses of the PPyHA and PPyHA-CNT films were 220 nm and 450 nm respectively, reflecting also the different growth rates utilizing these “weak electrolyte” dopants. The HA and HA-CNT doped samples were grown onto a PPyDBS bridging layer (20 mC/cm^2), having a thickness of 150 nm, as confirmed by AFM scanning. The Au electrodes have 3 µm line width (indicated by dashed white lines) and height of 150 nm. Due to field enhancement on the edges of the Au-eletrodes, the PPy tends to grow also laterally outside the electrode area (Figure 18A and 18D). After acquiring the topography images (18A and 18D), the slow scan axis (Y) was turned off and the potential of the Au electroding cycled by potentiostat (Veeco Multimode AFM built-in system) between -0.9 V and +0.1 V vs. Ag/AgCl (scan rate 50 mV/s). Hence, the AFM was set scanning along a single line (indicated by the red line in A). The height of a single point was measured from the image showing the scanned line profile during electrochemical cycling (inset image in 18A). The height and the CV of 6 successive electrochemical cycles are shown for PPyHA (18B and 18C) and for PPyHA-CNT (18E and 18F), respectively. The dotted lines in the CVs (C and F) are the CV of the PPyDBS bridging layer.

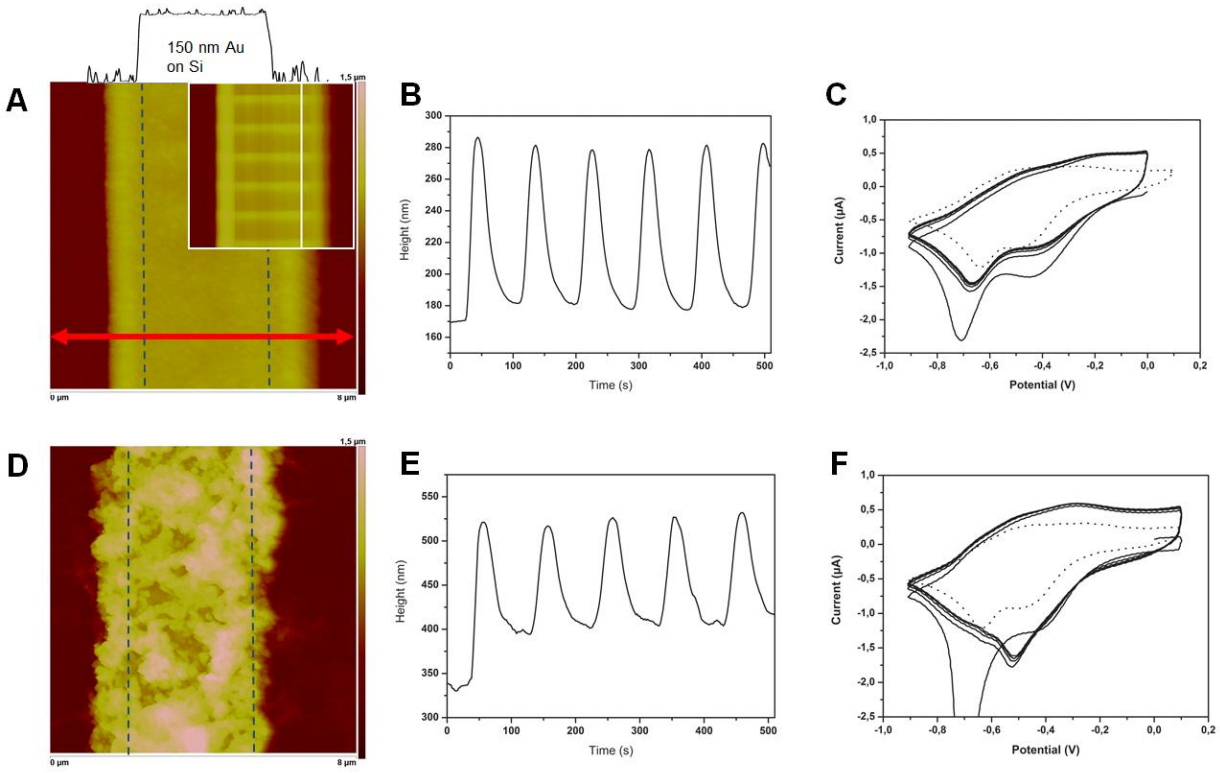

Figure 18. Bulk expansion of PPyHA (220 nm) and PPyHA-CNT (450 nm) films, grown on PPyDBS bridging layer (150 nm) probed by AFM scanning during electrochemical cycling. The multilayer materials exhibited reversible 100 nm actuation. Adapted with permission from Pelto *et al*., *Journal of Biomedical Materials Research Part A* 93:3:1056–1067. Copyright (2010) John Wiley and Sons.

Bulk expansion and the redox activity of the PPyHA and PPyHA-CNT films are clearly presented by the data. The CV show stability after the first cycle, which shows an extremely large reduction peak. The anticipated oxidation and reduction peaks of PPyHA are at -0.3 V and -0.4 V (vs. Ag/AgCl) (P1). The second reduction peaks at -0.65 V to -0.7 V (vs. Ag/AgCl) are presumably not attibutable to the PPyHA but are related to the electrochemistry of the metal substrate or the PPyDBS.

The multilayer materials show reversible 100 nm actuation. Although not shown directly here, the actuation is presumably partly due to the PPyHA and PPyHA-CNT. The estimated reversible actuations of the multilayer films are 22% and 19% for the PPyHA and PPyHA-CNT, respectively. These are lower values than measured for the 150 nm PPyDBS films of this study showing 80 nm actuation (27%), and in the preceeding studies (Smela and Gadegaard, 2001), but they are clearly in a relevant range to be applied in electromechanical stimulation devices.

5.4 Cell attachment and viability

Early cell attachment on charged PPyHA was reported for the samples investigated in Publication 3. The spreading of hASCs on non-preincubated (19A and 19B), pre-incubated (19C and 19D) and either charged (19B and 19D) or uncharged (19A and 19C) PPyHA surfaces are presented in the representative optical images (Fig. 19 A-D, top left panel). The majority of hASCs were uniformly adhered at the 3 hour time point on the surfaces of the charged samples. However, hASCs seeded on non-charged PPy-HA surfaces were unevenly spread and many cells were incompletely attached.

The combined effect of pre-incubation and charging resulted in a 215% increase of the hASC surface area compared to non-pre-incubated and non-charged control (Fig. 19E). The viability of the hASCs was not significantly affected by charging or the pre-incubation of the PPy surfaces, as indicated by live/dead images (Fig 1A-D, bottom left panel).

The main result from these observations is that the charged surfaces, even those not exposed to serum proteins for longer incubation times in cell culture medium, promoted cell adhesion more than the uncharged samples treated under the same conditions. Hence, the application of a positive bias of +200 mV was beneficial in promoting cell adhesion. A possible reason has been either increased adsorption of serum proteins (e.g. fibronectin, vitronectin) during pre-incubation, and/or immediately upon cell seeding and settling over 3 hrs, or direct electrostatic interactions with the cell membrane. The effect of pre-incubation on cell attachment was not as clear as the effect of charging, although pre-incubation seemed also to facilitate cell adhesion to the polymer.

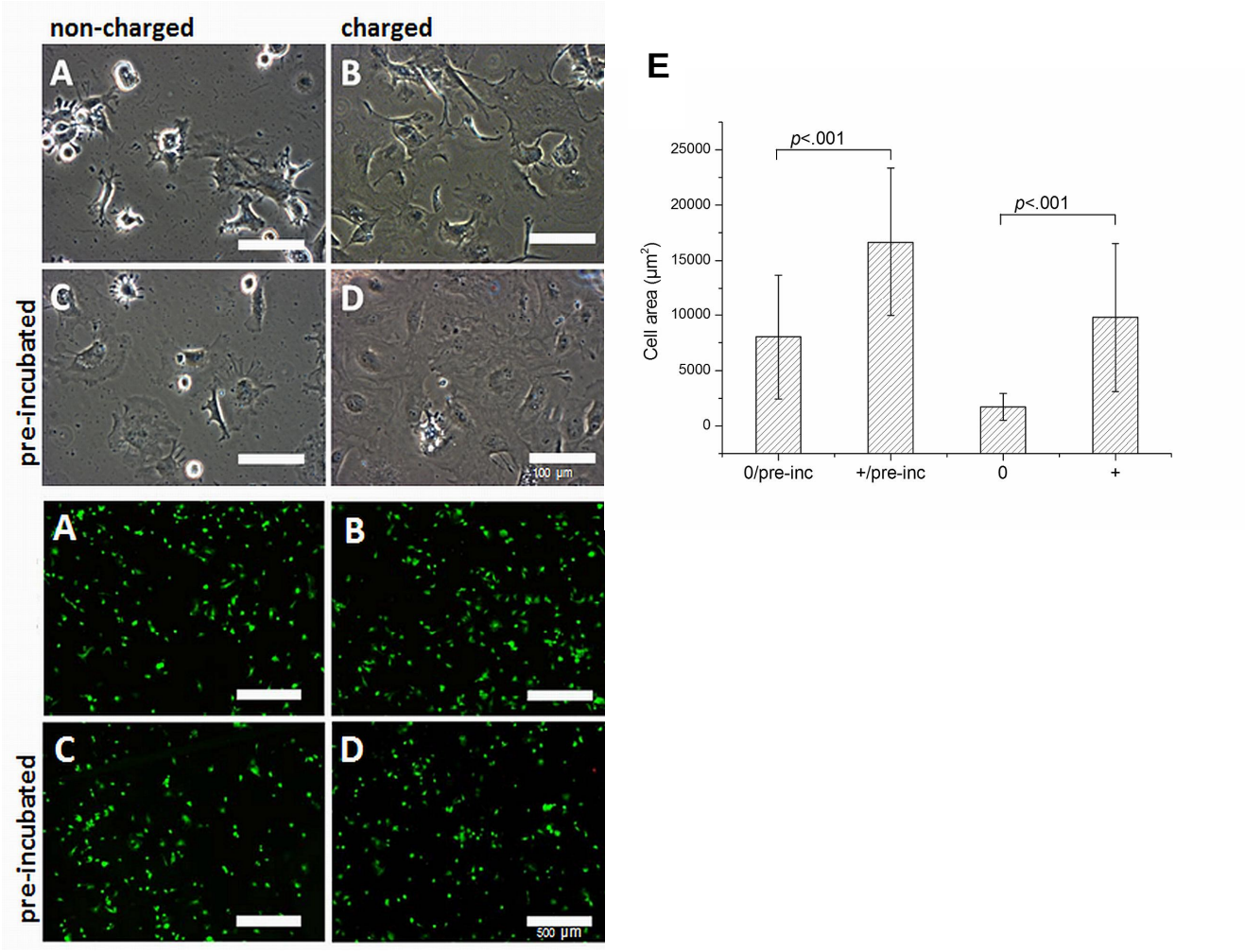

Figure 19. Left: Spreading of hASCs on non-preincubated (A and B), pre-incubated (C and D), and either charged (B and D) and uncharged (A and C) PPyHA surface at 3h. Scale bars 100 µm. Left/Bottom: corresponding live/dead images, scale bar 500 µm. **Right:** (E) Average surface area of the hASCs at 3h, measured from 5 representative optical microscope images. Reprinted with permission from Pelto *et al*., *Langmuir* 29:20:6099–6108. Copyright (2013) American Chemical Society.

Human ASC 2D culture on PPyHA and PPyCS. In Publication 4 the osteogenic induction of HA and CS dopants was evaluated for hASCs 2D cultures. This was a study preliminary to the 3D cell culturing (Publication 2) and the pre-clinical study (Publication 5). Human ASCs formed a homogenous cell monolayer on PPyCS surfaces (Figure 20 A-D), whereas, in contrast, on PPyHA the cells clustered into small spheroid structures and had poor attachment on the surface (Figure 20 E-H). On days 7 and 14, PPyCS supported hASC proliferation significantly more compared to PPyHA and the polystyrene (PS) tissue culture plate (TCP) (Figure 20 I and J). Moreover, PPyCS as well as biphasic electrical current stimulation (BEC) seemed to trigger mineralization of the matrix (data presented in P4), though a large variation of data for the ASCs derived from different patients was evident.

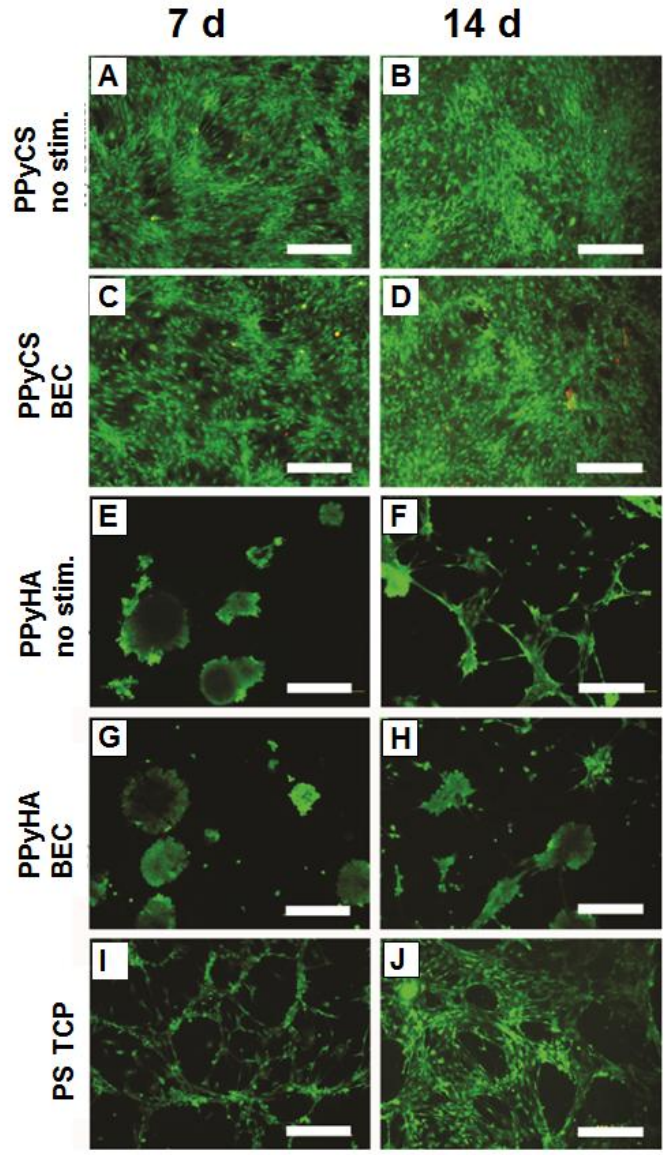

Figure 20. Live/dead images from ASCs on PPyCS (A-D), PPyHA (E-H) polymerized on Au/PET film. BEC stimulation was applied on the samples A, B, G and H. PS tissue culture plate was used as a positive control (I-J). Scale bar 500 µm. Reprinted with permission from Björninen *et al*., *Annals of Biomedical Engineering* 42:9:1889–1900. Copyright (2014) Springer.

Human ASC 3D culture on PPyCS coated PLA nonwoven scaffold. Live/dead images in Figure 21A show that the majority of hASCs were viable and spread homogenously in both PLA and PLA-PPyCS scaffolds with and without electrical stimulation (ES) on day 14. By qualitative estimation, the number of hASCs was higher in PLA-PPyCS scaffolds than in plain PLA scaffolds at all timepoints. The ES did not seem to have an effect on cell viability or cell number (Figure 21B).

ALP activity of hASCs was higher in the stimulated PLA-PPyCS scaffolds than in the PLA scaffolds at 7 and 14 days (Figure 21C). However, due to the large variation between the donors, no significant differences in the ALP activities were found between groups.

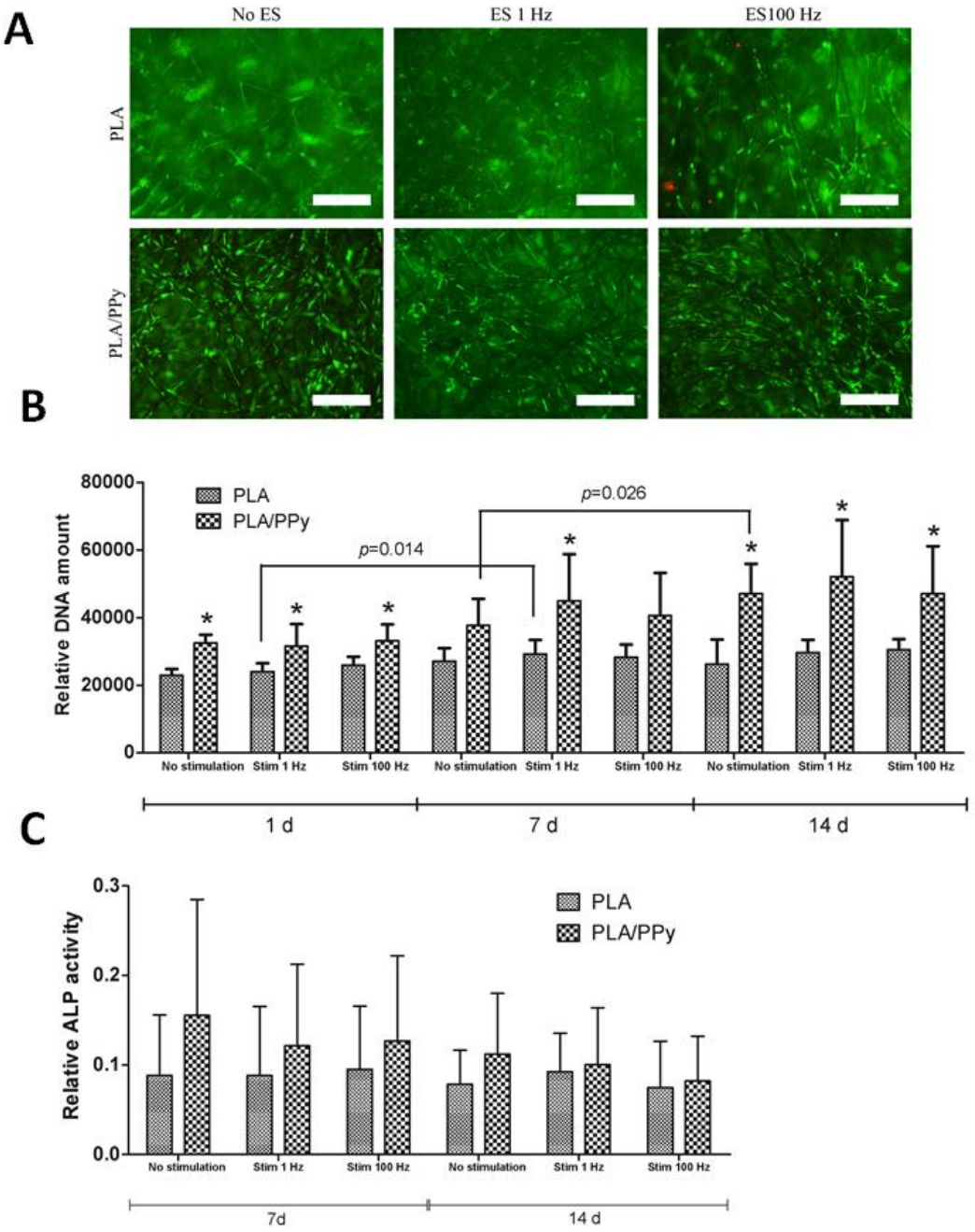

Figure 21. (A) Live/Dead images of PLA and PPyCS-PLA scaffolds with and without electrical stimulation. Scale bar 500 µm, (B) relative DNA amount and (C) relative ALP activity. Statistical significance ($p < 0.05$) between PLA and PPyCS-PLA groups at different time points is indicated by ∗. The confidence bounds (*p)* for statistical significance between time points are indicated by "⊓" -marking. Adapted from Pelto *et al*. (2012) *Tissue Engineering A* 19:7-8:882–892.

5.5 Tissue reactions

Figure 22 presents the hard tissue histology samples labelled by toluidine blue (the samples from the tetracycline labelling) in week 12. The uncoated screws and the PPyCS coated samples are depicted in A and B, respectively. New bone (NB) formation is indicated by the red arrows. Based on fluorescence from the tetracycline labelling, a significantly higher number of osteoblasts and chondroblast were present on the PPyCS coated surface. Moreover, enhanced mineralization was indicated by micro-CT imaging (reported in Publication 5).

The PPyCS coating is indicated by the black arrows in B'. According to Figure 22 (at week 12), the PPyCS is appearing as diffuse black band, suggesting disintegration and erosion. In week 26, only traces of PPyCS were found in the hard tissue histology. The cracking and erosion of the PPyCS coating was associated with the degradation of the PLGA-TCP screw. However, macrophages or other cells indicating inflammation were not found in the histology. Hence, the PPy elimination was taking place with some other mechanism, presumably by erosion as small nanoscopic particles, as suggested in previous implantation studies (Wang Z *et al*., 2007; Shi, *et al*., 2004).

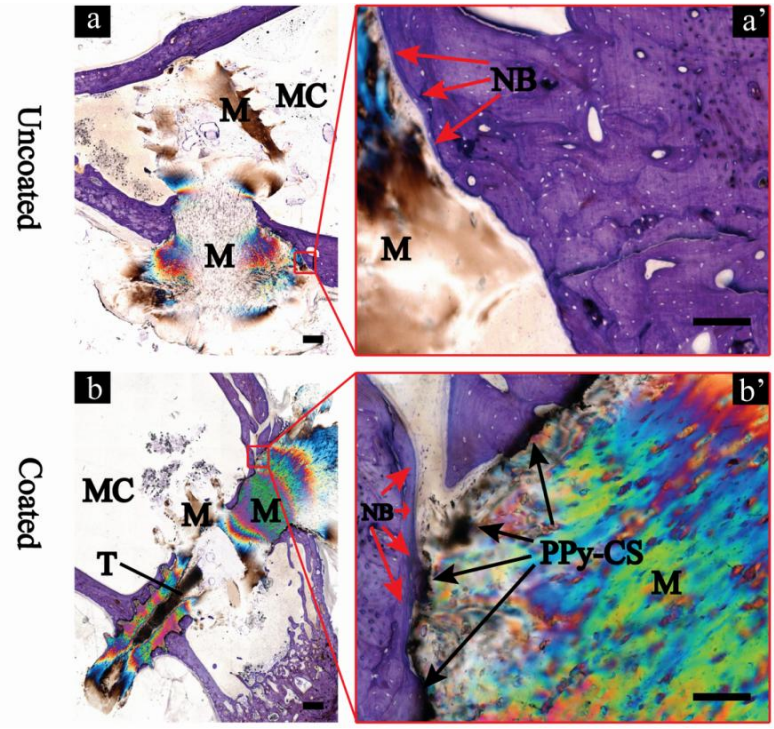

Figure 22. Toluidine blue staining 12 weeks after implantation for hard tissue samples. (a) Uncoated screw (scale bar 500 µm). (a') Magnification of the interface between the uncoated screw and bone revealed a thin detectable new bone (NB) band (scale bar 100 µm). (b) Coated screws (scale bar 500 µm). (b') Magnification of the interface between the coated screw and bone (scale bar 100 µm). NB was clearly detectable as indicated by a thick band on the surface. PPy coating appears as a black band. (MC: marrow cavity, M: PLGA and β-TCP, T: pure β-TCP).

6. Discussion

6.1 Electroactivity and the surface properties of biocompatible PPyHA and PPyHA-CNT electropolymerized films

In Publication 1 the electronic-, viscoelastic- and nanoscopic actuator properties of biopolymer HA doped PPys with and without oxidized multi-walled carbon nanotube co-dopant additive (PPyHA and PPyHA-CNT) materials were studied. Furthermore, cell attachment and viability were assessed. Bulk expansion of 22% and 19% and reversible redox activity were observed in both submicron thick PPyHA films and PPyHA-CNT films grown on Au, respectively. However, the reversible swelling, which was attributable to cation ingress during the electrochemical reduction at -0.45 V (vs. Ag/AgCl), was critically dependent on the adhesion of the film, which could be augmented by applying a hydrophilic PPyDBS bridging layer between the Au substrate and the PPyHA or the PPyHA-CNT film. The level of bulk expansion is significant but slightly lower than reported earlier for PPyDBS/Au films (Smela, 1999; Jager *et al*., 1999), but clearly applicable in electromechanical nanoactuators. The materials were superhydrophilic, with water contact angles lower than 10 degrees. Furthermore, owing to the hydrogel like properties of the HA dopant, the materials are very soft, with a shear modulus of about 100 kPa. The shear modulus of the PPyHA generated by electropolymerization was significantly lower than previously reported for PPy films (Gelmi *et al*., 2010). The discrepancy can be explained by the synthesis conditions, e.g. by the deposition potential and the properties of the high molecular weight HA dopants, which may also be reflected in the differences in the cell attachment observed in Publications 1 and 4.

CNTs render the surface of the otherwise very smooth PPyHA (R_a 8-9 nm) polymer significantly rougher (R_a 80-85 nm). AFM images clearly show that the bundle-like morphology of CNTs is manifested in the PPyHA-CNT. The CNTs are throughout covered by a uniform layer of electrically active PPyHA polymer. The electroactivity and doping of the PPy chain is evidenced by the Raman spectra of the composite (Publication 1) and the PPyHA (Figure 17). The important role of the CNTs is in enhancing the electrical conductivity of the PPyHA, particularly in the reduced state. The possible toxicity of the CNTs in long term implantable devices may be debated, but clearly they offer an efficient way of engineering the conductivity and the electroactivity of the PPyHA in electrode coatings, as later demonstrated in molecularly imprinted biosensors (Xing, *et al.*, 2012).

During the 8 days cell culture with the PPyHA-CNT films on titanium substrate, as reported in Publication 1, hASCs showed equal or better viability and proliferation compared to the reference PLA. Hence, no indications of acute toxicity were found. This result clearly showed that the HA and multi-walled and oxidized CNT co-dopants hold potential in PPy electrode coating. The cell attachment was significantly better than reported for the electropolymerized PPyHA films in Publication 4. The observed differences cannot be explanained by the single characterized

physical property of the PPyHA-CNT material of the cell culture conditions, but they are likely due to multiple factors related to the properties of the HA dopant.

Although it was not demonstrated in this thesis, a micropatterned and possibly interdigitated array of PPyHA, with or without the CNT co-dopant, could be utilized as a cell culture substrate offering a unique 2D platform for cell culture capable of microelectromechanical stimulation within approximately one volt potential window, for delivery of stimulation current, redox activated drug delivery, cell sorting, and offering cell-biosensor interphase, for example.

6.2 Hydrolytic stability of PPyCS in hASC in vitro

In Publication 2 the hydrolytic stability of PLA nonwoven scaffolds coated with chemically polymerized micrometer thick PPyCS coating was studied with a standard hydrolysis test. The physical changes of the coating were imaged by SEM and AFM and the de-doping assessed by DC conductivity of the hydrolysed samples. The appearance of the PPyCS coating reflected the surface texture of the PLA fibers, which indicates that the PPyCS had very good adhesion and was partly anchored to the PLA by a surface confined (*in situ*) polymerization. The larger PPyCS particles observed on the surface gradually disappeared on hydrolysis. This was due to the reorganization of the dopants in the PPy layer, swelling of the PLA fiber surface, or the erosion of the PPyCS particles. Indeed, the de-doping of the PPyCS was evident by decreased DC conductivity, observed already during the first days of incubation. Some evidence of chloride insertion into PPyHA was reported in the supporting information of Publication 3. Hence, it could be hypothesized that the observed changes in the PPyCS might be due to the hydrolysis and leaching of the CS dopant, associated with partial ion exchange to chloride ions. In general, the mechanical integrity of the substrate has a crucial role in macroscopic degradation, such as erosion or detachment of the coating. However, this was not the dominant factor in explaining the degradation of the PPyCS coating or the changes in its surface properties during the short hydrolysis study conducted, as the macroscopic tensile properties of the PLA fibers were not significantly changed during 20 days of incubation.

The coating process was based on a simple interfacial polymerization scheme, avoiding multiple and complex process steps, chemical crosslinking or potentially toxic click-chemistry, which is typically applied in biological activation treatments. Due to the one-pot synthetic method, it is arguable how much of the CS dopants were incorporated into the PPy, and whether the bioactivity of the CS (or HA) was affected by the syntheses. An earlier study by Collier *et al*. (2000) on electropolymerized PPyHA addressed the issue and demonstrated that the HA-binding protein was actively functioning on the PPyHA for several days during the incubation. Hydrolysis was evident, but the hydrophilic and cell binding property was maintained in the electropolymerized film. Hence, it could be anticipated that the HA and CS dopants remain bioactive, although partly hydrolysed.

This is the likely the case in the electropolymerized PPyHA and PPyCS films of Publications 1,3 and 4, and also presumed for the chemically polymerized films of publications 2 and 5 utilizing CS and HA dopants and chemical oxidant (APS).

The degradation products of PLA-PPyCS arising in pure water were analysed by ESI-MS. The hydrolysis of PLA in pure water was not significantly affected by the PPyCS coating, as evidenced by the nearly identical mass spectra of the PPyCS coated and non-coated samples. Nor could any degradation products attributable to the PPy chain or CS be identified. The spectra contained peaks attributable to the Na-adducts of lactic acid oligomers (3 to 14 monomer units), similar to the peaks described earlier by Andersson *et al*. (2010).

The performance of PPyCS coated PLA nonwoven scaffolds were evaluated in osteogenic hACS culture. Human ASCs were seeded into the scaffolds and the scaffolds incubated in osteogenic medium or in DMEM, with and without the 3D electrical stimulation delivered by Au electrodes, which were in contact with the scaffolds. The electrical stimulation using 1 Hz and 100 Hz biphasic millisecond long pulsed DC waveforms (±200 mV) was continued for 14 days. With and without the applied stimulus the PPyCS coated scaffolds significantly enhanced hASC proliferation compared to the uncoated reference PLA scaffolds. In addition, early osteogenic differentiation was consistently more enhanced in the PPyCS coated stimulated and non-stimulated scaffolds. The electrical stimulation by the two chosen, relatively low amplitude biphasic pulsed voltage millisecond long waveforms did not have a statistically significant effect on hASC proliferation or differentiation on days 1, 7 and 14. However, mineralization was significantly enhanced in the electrically stimulated group at day 7 and 14. The results of the electrical stimulation experiments had a characteristically large variability between the cell lines from the different donors. Looking at the trends, it could be argued that the electrical stimulation could have affected the early proliferative and differentiation phase. The effects may have been masked by the choice of the days for the determination of ALP activity, the amount of DNA and to the great variation between the cell lines of different donors. In conclusion, the data presented in Publication 2 supports the future potential of the electrically conductive PPyCS-coated PLA scaffolds in bone tissue engineering.

6.3 Electrical conductivity in hydrolysed PPyCS and PPyHA

In Publication 2, a significantly higher AC conductivity of the PPyCS coated scaffolds, as compared to PLA immersed in PBS, was confirmed by EIS at 24h. At 48h the conductivity was about 50% of the original (unpublished data), which is in accordance with the recent data by Serra Moreno and Panero (2012), who followed the changes in the EIS spectra of ClO_4^{-1} –ion, CS-A and heparin (Hep) doped PPys upon aging for 10 days in PBS. They also found significant differences in the stability of the PPy films according the size of the dopant and the synthesis conditions.

DC conductivity measurements on hydrolysed and air-dried PPyCS samples showed a marked decrease in conductivity during the 2 first days of incubation. Until day 10 the DC conductivity of the PPyCS had decreased about two orders of magnitude, from 100 to 1 S/m. Hence, at day 10 the conductivity had dropped to the same conductivity range reported for the ionic conductivity cell culture medium, which is 1.29 S/m for a standard medium, measured at 1 kHz frequency. It is noteworthy that the DC conductivity of ionic electrolyte solution can not be accurately measured due to the build-up of an electrical double layer, whereas in contrast the conductivity of PPy is well measurable at low frequencies down to DC, which are relevant in the BEC stimulation. The decrease in conductivity is attributable to de-doping in the pH 7.4 cell culture medium and to the de-doping during water rinsing prior to the measurements. About 5-10% of the original DC conductivity could be restored by HCl re-doping, which highlights the pH sensitivity of the conductivity.

The continuous hydration of the PPyCS films is likely to occur during the first days of incubation, which is likely reflected in the observed changes of the surface properties. Hence, it is presumable that the rate of change of the electrical properties is higher during that period. Similar trends have been reported for electropolymerized PPyCS and PPyPSS, studied by EIS (Serra Moreno and Panero, 2012), and by conductivity measurements (Fonner *et al*., 2008). In contrast to Publication 2, the cited studies found only one order of magnitude decrease in the conductivity during the 7 days of incubation. The greater extent of conductivity loss in the PPyCS coated PLA non-woven scaffold can be explained by several factors: the thin PPyCS layer is anchored to the PLA polymer, which is prone to slow swelling, dimensional changes, hydrolysis and, possibly, rupture during the incubation in PBS. Furthermore, the electrical connections between the individual fibers and between the fibers and measurement electrodes are likely to be compromised by the the hydration, rinsing and drying of the scaffolds before the DC conductity measurement. At day 20 the PPyCS coating had undergone irreversible changes, as evidenced by the electrostatic charging under SEM and confirmed by the reduced surface roughness observed in the AFM images.

6.4 The role of surface charge on early cell attachment

The AFM work reported in Publication 3 showed that the application of a relatively small potential bias potential of +200 mV to a PPyHA film on ITO has a large effect on the early attachment and spreading of hASCs. The majority of hASCs were uniformly adhered at the 3 h time point on charged sample surfaces, whereas the cells seeded on noncharged PPyHA surfaces were unevenly spread, and many cells were not well adhered. The enhancement was significant with and without a pre-incubation period in the cell culture medium containing plasma proteins. Pre-incubation alone had statistically equal significance in enhancing cell attachment. The data suggests that the attachment of hASCs to the PPyHA surface may occur directly, without specific binding to the plasma proteins, such as fibronectin, vitronectin and albumin, present on the

surface. Correlating to the data published by Molino *et al.* (2012), who found enhanced adsorption of fibronectin and bovine serum albumin onto slightly positively biased PPyDS, it can be argued that the cell attachment of hASCs does not need specific surface binding sites, but rather the suitable distribution and polarity of the surface charge in the nanoscale. Adsorption of plasma proteins, whose dimensions are in the nanoscale, is likewise enhanced by uniform positive surface charge (Lubarsky *et al.* 2005; Molino et al. 2012).

6.5 Correlation between surface charge, roughness and cell adhesion

KPFM and AFM force mapping were utilized to elucidate the effects of charging on surface properties, including the topography, modulus, surface potential, and adhesion, with the intention of correlating these properties with the hASCs cell adhesion. Charging did not have a significant effect on the topography of the studied thin PPyHA films. Charging only slightly increased the modulus but did significantly alter the surface potential and adhesion forces acting between the AFM tip and polymer. AFM force measurements with a negatively biased tip (−200 mV) showed that prior to charging of the PPyHA films, short-range attractive forces and adhesion were restricted to the nodule peripheries but appeared on the nodules and uniformly across the film upon charging. As expected, the charging of the films increased the surface potential, as shown by both KPFM and DLVO analysis of the force curves, which had the effect of also decreasing the magnitude of the electrostatic repulsion between the tip and polymer.

Hence, it looks evident that the uniformity of the surface features, such as roughness and the electrical potential/charge of the biopolymer in the nanoscopic domain are critically important factors in the first phases of the cell attachment, i.e. the attachment of adhesion proteins. Although not shown experimentally here, it can be hypothesized that the driving force for the protein adsorption is the physical size and lateral distribution of properties related of the surface features. To allow efficient adsorption, these should be matching with the the charged domains of the absorbing proteins. The chain conformation of the proteins on the ad-layer can be altered by the surface charge (Molino *et al*. 2012; Hartvig *et al*., 2011; Takahashi *et al*., 2000; Asthagiri and Lenhoff, 1997; Zhou *et al*., 2003). Analogically, the mobile proteins on the cell membrane, which also have their electrical charges distributed in the nanometer domain, may experience the surface features, but the plasticity of the cell membrane allows the integrins and other adhesion proteins to probe for attractive sites for adhesion.

In Publication 4 it was demonstrated that clustering and detachment of hASCs was promoted on PPyHA. This was not in accordance with the observations in Publication 1. Later in Publication 3 it was shown that the cell adhesion was not only dependent on the surface chemistry but also on the surface charging conditions. Hence, although not demonstrated in Publication 4, we anticipate that the hACS attachment on PPyHA could be modulated by applying an appropriate (positive) bias

potential on the PPyHA. Since the HA itself has few binding sites for adhesion proteins, the PPyHA could facilitate selective attachment of proteins and cells by the application of electrochemical charging. This could be utilized in stimulation or recording electrodes, as already demonstrated in neural probe applications by Lee and Schmidt (2010), who studied the attachment of fibroblasts and astrocytes on PPyHA, and discussed their applications in neuroprosthetic devices where the attachment of cells or the formation of high impedance tissue is highly undesirable. Another possible application area for the electronically tunable cell binding property is in cell sorting.

Future work will concentrate on gathering direct evidence of the protein organization (conformation) on nanoscopically homogenously charged surfaces. This can be utilized by examining the surface topography and charge distribution and correlating the data with organization of the protein ad-layers imaged by appropriately functionalized AFM tips. Perhaps the biopolymer doped PPy surfaces could be used as a “tunable” cell adhesion platform to study single protein adsorption or even facilitate direct cell attachment through membrane protein electrostatics with the biopolymer surface, without the help of plasma proteins.

6.6 Electrical stimulation in 2D and 3D cell cultures

In Publication 4 PPyCS and PPyHA coated 2D stimulation electrodes were applied in the electrical stimulation of hASC on 24 multi-well plates. PPyCS supported the proliferation and homogenous spreading of hASCs significantly more than PPyHA. This observation is in accordance with work reported by other investigators of HA dopant in PPy, which state that HA, although biologically active, presents very few non-specific binding sites for proteins and hence cell binding (Lee and Schmidt, 2010; Cen *et al*., 2004). The different biological responses of ASCs cultured on the two PPy surfaces may be due to different surface morphologies originating from the CS and HA dopants, as evidenced by AFM (section 5.1), or by other factors such as surface elasticity and charging, as discussed in sections 2.13 and 5.1.

Both PPyCS and PPyHA supported early osteogenic differentiation of hASCs over time. The mineralization of hASCs was significantly greater with PPyCS under electrical stimulation using 4 h a day for 14 days with a ±200 mV amplitude pulsed DC, 2.5 ms pulse width and 100 Hz pulse repetition frequency, delivering approximately 50 µA/cm^2 current density on the cells. The electrical stimulation did not show significant effects on hASC proliferation or osteogenic differentiation. This result is in contrast with the results from Hammerick *et al*., (2010) and McCullen *et al*. (2010), who reported enhanced expression of osteogenic markers in electrically stimulated hASCs. The discrepancy is likely due to the different means of delivering the stimulation current to the cells: their studies utilized very large stimulation voltages and salt bridges for electrode isolation (Hammerick *et al*., 2010) and interdigitated ITO microelectrodes (McCullen *et al*. 2010). Although giving highly promising results, their setups were designed for stimulation on a single dish cell

culture, and could not be practically used in the 24 well plate experiment of Publication 4. Stimulation of the cell using the setup described could be realized by using higher stimulation current, up to the electrochemical stability limits of Au electrode (at about +700 mV vs. SHE) in a two electrode setup. However, utilizing such large potential will likely induce significant electrode effects, even in electrochemically stable Au (Howlader *et al*., 2013).

PPyCS can be recommended over PPyHA for osteogenic coating in bone tissue engineering scaffolds for future studies. Furthermore, based on the results of Publication 3, we can anticipate that applying a positive bias voltage could be beneficial in the attachment of cells on 3D PPyHA electrically conductive scaffold, to better facilitate the osteogenic properties of HA hydrogels (JHa *et al*., 2011).

6.7 In vivo biocompatibility of PPyCS

Finally, in Publication 5 it was demonstrated in a 26 week pre-clinical study with New Zealand rabbits that PPyCS coating on implanted PLGA-TCP bone fixation screws was beneficial in promoting new bone formation and osteointegration of the implant. PPyCS coating and its erosion products did not show any increased adverse reactions locally or systematically. These results highlight the potential of PPy as a multifunctional osteogenic coating material to facilitate better bone tissue-implant interactions. In addition, none of the implants induced any systemic or local toxicity. The results suggest that PPy is biocompatible with bone tissue and is a potential coating for enhancing osteointegration in orthopedic implants. Further *in vitro* assessment of the erosion, biodegradation, and possible biological elimination pathways *in vivo* are needed to fully draw conclusions about the biostability of the PPyCS. This is still one important aspect for future studies.

7. Conclusions

In this work, utilizing electrochemical and chemical synthesis strategies, the surface properties, stability and the performance in hASCs culture were investigated for PPyHA and PPyCS. Chemically polymerized PPyCS coatings were applied in electrically stimulated 3D PLA tissue engineering scaffolds and PLGA-TCP bone fixation screws. The main conclusions and the most important findings from the studies were as follows:

I. Electropolymerized PPyHA, and the materials containing oxidized multi-walled carbon nanotubes (PPyHA-CNT) as co-dopant, both have large and reversible bulk expansion property, which could be utilized in electromechanical microactuations, such as in cell stimulation platforms for tissue engineering. The materials have high electronic conductivity and reversible redox doping, typical of the other PPys doped with inorganic acids. Both PPyHA and PPyHA-CNT are very soft, exhibit hydrogel-like elasticity and support hASC attachment.

II. Simple one-pot chemical polymerization schemes can be utilized to synthesize micrometer thick, biocompatible and electrically conductive PPyCS coatings on PLA fiber and PLGA-TCP substrates. The incorporated CS dopant renders the substrates highly hydrophilic, attractive for hASC attachment and can be utilized in bone tissue engineering and biomedical implants.

III. Early attachment of hASCs on PPyHA can be significantly enhanced by the application of a positive bias potential, which serves to improve the uniformity of the nanoscopic surface charge distribution on the surface. The significance of the effect at 3 hours time point is statistically equal to the effect of pre-incubation in osteogenic medium containing plasma proteins. In addition, the application of positive bias reduces the de-doping of PPy chain, and hence improves the stability of the electrical conductivity during the incubation in physiological environment.

The observations and conclusions of this thesis support the use of PPyCS coatings in bone tissue engineering. The electropolymerized films and also the chemically polymerized PPyHA and PPyCS coatings on bioabsorbable polymer are highly compatible with hASCs, support adhesion and can be utilized in delivering direct electrical stimulation *in vitro*. There is also future potential in designing permanently implantable scaffolds and microstimulation devices, but still further insight into the biodegradation and biological elimination of PPy *in vivo* is needed.

REFERENCES

Adey, W.R. Biological effects of electromagnetic fields (1993) *Journal of Cellular Biochemistry*, 51 (4), pp. 410-416.

Albers, W.M. (2013), private communications.

Aldissi, M., Armes, S.P. Colloidal dispersions of conducting polymers (1991) *Progress in Organic Coatings*, 19 (1), pp. 21-58.

Andersson, S.R., Hakkarainen, M., Inkinen, S., Sodergard, A., Albertsson, A.C. Polylactide stereocomplexation leads to higher hydrolytic stability but more acidic hydrolysis product pattern (2010) *Biomacromolecules* 11, pp. 1067.

Angeli, A., Alessandri, L. *Gazzetta Chimica Italiana* (1916), 46, p. 283.

Angeli, A. *Gazzetta Chimica Italiana* (1916), 46, p. 279.

Antony, M.J., Jayakannan, M. Molecular template approach for evolution of conducting polymer nanostructures: tracing the role of morphology on conductivity and solid state ordering (2010) *Journal of Physical Chemistry B*, 114 (3), pp. 1314-1324.

Armand, G., Baugh, P.J., Balazs, E.A., Phillips, G.O. Radiation protection of hyaluronic acid in the solid state (1975) *Radiation Research*, 64 (3), pp. 573-580.

Armes, S.P., Aldissi, M. Preparation and characterization of colloidal dispersions of polypyrrole using poly(2-vinyl pyridine)-based steric stabilizers (1990) *Polymer*, 31 (3), pp. 569-574.

Armes, S.P., Aldissi, M., Hawley, M., Beery, J.G., Gottesfeld, S. Morphology and structure of conducting polymers (1991) *Langmuir*, 7 (7), pp. 1447-1452.

Armes, S.P., Aldissi, M., Idzorek, G.C., Keaton, P.W., Rowton, L.J., Stradling, G.L., Collopy, M.T., McColl, D.B. Particle size distributions of polypyrrole colloids (1991) *Journal of Colloid and Interface Science*, 141 (1), pp. 119-126.

Asthagiri, D., Lenhoff, A.M. Influence of structural details in modeling electrostatically driven protein adsorption (1997) *Langmuir*, 13 (25), pp. 6761-6768.

Ates, M. A review study of (bio)sensor systems based on conducting polymers (2013) *Materials Science and Engineering C*, 33, pp. 853–1859.

Bahrami-Samani, M. PhD Thesis (2007). Dynamics of conductive polymer actuators. University of Wollongong.

Bahrami-Samani, M., Whitten P.G., Cook, C.D., Spinks, G.M. Quartz crystal microbalance study of volume changes and modulus shift in electrochemically switched polypyrrole (2008). *Thin Solid Films*, 516, pp. 2800-07.

Baker, C.K., Qiu, Y.-J., Reynolds, J.R. Electrochemically induced charge and mass transport in polypyrrole/poly(styrenesulfonate) molecular composites (1991) *Journal of Physical Chemistry*, 95 (11), pp. 4446-4452.

Balint, R.,Cassidy, N.J.,Cartmell, S.H. Conductive polymers: towards a smart biomaterial for tissue engineering (2014) *Acta Biomaterialia*, 10, S1742–7061.

Bandey, H.L., Martin, S.J., Cernosek, R.W. Hillman, A.R. Modeling the responses of thickness-shear mode resonators under various loading conditions (1999) *Analytical Chemistry*, 71, pp. 2205-2214.

Bargon, J., Baumann, R. Laser processing of electrically conducting polymers into patterns (1993) *Microelectronic Engineering*, 20 (1-2), pp. 55-72.

Barisci, J.N., Stella, R., Spinks, G.M., Wallace, G.G. Characterization of the topography and surface potential of electrodeposited conducting polymer films using atomic force and electric force microscopies (2000) Electrochimica Acta, 46 (4), pp. 519-531.

Bay, L., Jacobsen, T., Skaarup, S., West, K. Mechanism of actuation in conducting polymers: Osmotic expansion (2001) Journal of Physical Chemistry B, 105, pp. 8492-97.

Bay, L., Mogensen, N., Skaarup, S., Sommer-Larsen, P., Jørgensen, M., West, K. Polypyrrole doped with alkyl benzenesulfonates (2002) Macromolecules, 35 (25), pp. 9345-9351.

Bay, L., West, K., Skaarup, S. Pentanol as co-surfactant in polypyrrole actuators (2002) Polymer, 43 (12), pp. 3527-3532.

Berdichevsky, H. and Lo, Y Polymer microvalve based on anisotropic expansion of polypyrrole, Materials Research Society Symposium Proceedings, Materials Research Society (2004) A4.1–4.7.

Biggs M.J.P., Richards, R.G., Gadegaard, N., McMurray, R.J., Affrossman, S., Wilkinson, C.D.W., Oreffo, R.O.C., Dalby, M.J. Interactions with nanoscale topography: Adhesion quantification and signal transduction in cells of osteogenic and multipotent lineage (2009) *Journal of Biomedical Materials Research Part A*, 91A: 195-208.

Blinova, N.V., Stejskal, J., Trchová, M., Prokeš, J., Omastová, M. Polyaniline and polypyrrole: A comparative study of the preparation (2007) *European Polymer Journal*, 43 (6), pp. 2331-2341.

Bolin, M.H., Svennersten, K., Wang, X., Chronakis, I.S., Richter-Dahlfors, A., Jager, E.W.H., Berggren, M. Nano-fiber scaffold electrodes based on PEDOT for cell stimulation (2009) *Sensors and Actuators B: Chemical*, 142 (2), pp. 451-456.

Braun, D., Cherdron, H., Rehahn, M., Ritter, H., Voit, B. Polymer synthesis: theory and practice fundamentals, methods, experiments, 4th ed. Springer (2005).

Brown, T.D. Techniques for mechanical stimulation of cells in vitro: A review (2000) *Journal of Biomechanics*, 33 (1), pp. 3-14.

Butt, H.-J., Cappella, B., Kappl, M. Force measurements with the atomic force microscope: Technique, interpretation and applications (2005) *Surface Science Reports*, 59 (1-6), pp. 1-152.

Carter, D.R. Mechanical loading histories and cortical bone remodelling (1984) *Calcified Tissue International*, 36 (SUPPL. 1), pp. S19-S24.

Carvalho, R.S., Scott, J.E., Suga, D.M., Yen, E.H.K. Stimulation of signal transduction pathways in osteoblasts by mechanical strain potentiated by parathyroid hormone (1994) *Journal of Bone and Mineral Research*, 9 (7), pp. 999-1011.

Castano H., O'Rear E.A., McFetridge P.S., Sikavitsas V.I. Polypyrrole thin films formed by admicellar polymerization support the osteogenic differentiation of mesenchymal stem cells (2004) *Macromolecular Bioscience*, 4, pp. 785-94.

Cen, L., Neoh, K.G., Li, Y., Kang, E.T. Assessment of in vitro bioactivity of hyaluronic acid and sulfated hyaluronic acid functionalized electroactive polymer (2004) *Biomacromolecules*, 5 (6), pp. 2238-2246.

Chen, G.Z., Shaffer, M.S.P., Coleby, D., Dixon, G., Zhou, W., Fray, D.J., Windle, A.H. Carbon nanotube and polypyrrole composites: coating and doping (2000) *Advanced Materials*, 12 (7), pp. 522-526.

Chitta, R., D'Souza, F. Self-assembled tetrapyrrole-fullerene and tetrapyrrole-carbon nanotube donor-acceptor hybrids for light induced electron transfer applications (2008) *Journal of Materials Chemistry*, 18 (13), pp. 1440-1471.

Cho, J., Shin, K.-H., Jang, J. Micropatterning of conducting polymer tracks on plasma treated flexible substrate using vapor phase polymerization-mediated inkjet printing (2010) *Synthetic Metals*, 160 (9-10), pp. 1119-1125.

Choi, W.M., Park, O.O. Microfabrication of polypyrrole using patterned ITO substrate by the soft-imprint technique (2006) *Current Applied Physics*, 6 (4), pp. 695-699

Christensen PA, Hamnett A. In situ spectroscopic investigations of the growth, electrochemical cycling and overoxidation of polypyrrole in aqueous solution (1991) *Electrochimica Acta*, 36, pp. 1263-86.

Collier, J., Camp, J., Hudson, T., Schmidt, C. Synthesis and characterization of polypyrrole-hyaluronic acid composite biomaterials for tissue engineering applications (2000). *Journal of Biomedical Materials Reseach*, 50, pp. 574-584.

Cui, T., Liang, G., Varahramyan, K. An organic poly(3,4-ethylenedioxythiophene) field-effect transistor fabricated by spin coating and reactive ion etching (2003) *IEEE Transactions on Electron Devices*, 50 (5), pp. 1419-1422.

De Giglio, E.,Guascito, M:R:, Sabbatini L., Zambonin, G. Electropolymerization of pyrrole on titanium substrates for the future development of new biocompatible surfaces (2001) *Biomaterials* 22, pp. 2609–2616.

De Jesus, M.C., Fu, Y., Weiss, R.A. Conductive polymer blends prepared by in situ polymerization of pyrrole: A review (1997) *Polymer Engineering and Science*, 37 (12), pp. 1936-1943.

DeArmitt, C., Armes, S.P. Colloidal dispersions of surfactant-stabilized polypyrrole particles (1993) *Langmuir*, 9 (3), pp. 652-654.

Diaz, A.F., Castillo, J.I., Logan, J.A., Lee, W.-Y. Electrochemistry of conducting polypyrrole films (1981) *Journal of Electroanalytical Chemistry*, 129 (1-2), pp. 115-132.

Discher, D., Janmey, P., Wang, Y. Tissue cells feel and respond to the stiffness of their substrate (2005) *Science*, 310, pp. 1139-43.

Domke, J., Radmacher, M. Measuring the elastic properties of thin polymer films with the atomic force microscope (1998) *Langmuir*, 14 (12), pp. 3320-3325.

Dubiel, E., Martin, Y., Vermette, P. Bridging the gap between physicochemistry and interpretation prevalent in cell-surface interactions (2011) *Chemical Reviews*, 111, pp. 2900−2936.

Ellä, V., Gomes, M.E., Reis, R.L., Törmälä, P., Kellomäki, M. Studies of P(L/D)LA 96/4 non-woven scaffolds and fibres; properties, wettability and cell spreading before and after intrusive treatment methods (2007) *Journal of Materials Science: Materials in Medicine*, 18 (6), pp. 1253-1261.

Engler, A.J., Richert, L., Wong, J.Y., Picart, C., Discher, D.E. Surface probe measurements of the elasticity of sectioned tissue, thin gels and polyelectrolyte multilayer films: Correlations between substrate stiffness and cell adhesion (2004) *Surface Science*, 570 (1-2), pp. 142-154.

Engler, A.J., Sen, S., Sweeney, H.L., Discher, D.E. Matrix elasticity directs stem cell lineage specification (2006) *Cell*, 126 (4), pp. 677-689.

Ercan B, Webster T.J. The effect of biphasic electrical stimulation on osteoblast function at anodized nanotubular titanium surfaces (2010) *Biomaterials*, 31, pp. 3684-93.

Ercan, I., Günal, I., Güven, O. Conductance of polypyrole irradiated with gamma rays to low doses (1995) *Radiation Physics and Chemistry*, 46 (4-6 PART 1), pp. 813-817

Ettelaie, R., Akinshina, A., Maurer, S. Mixed protein-polysaccharide interfacial layers: Effect of polysaccharide charge distribution (2012) *Soft Matter*, 8 (29), pp. 7582-7597.

Evolution of physical and electrochemical properties of polypyrrole during extended oxidation (1992) Journal of the Electrochemical Society, 139(9),

Fonner, J.M., Forciniti, L., Nguyen, H., Byrne, J., Kou, Y.F., Syeda-Nawaz, J.. Schmidt, CE. Biocompatibility Implications of Polypyrrole Synthesis Techniques (2008) *Biomedical Materials*, 3(3), no. 034124.

Fukada, E., Yasuda, I. On the piezoelectric effect of bone (1957) *Journal of the Physical Society of Japan*, 12 (10), pp. 1158-1162.

Gaihre, B., Alici, G., Spinks, G.M., Cairney, J.M. Pushing the limits for microactuators based on electroactive polymers (2012*) Journal of Microelectromechanical Systems*, 21 (3), art. no. 6146449, pp. 574-585.

Gao, Z., Minxian Z., Beshen, C. The influence of overoxidation treatment on the permeability of polypyrrole films (1994) *Journal of Electroanalytical Chemistry*, 373, pp. 141-8.

Garner, B., Georgevich, A., Hodgson, A.J., Liu, L., Wallace, G.G. Polypyrrole-heparin composites as stimulus-responsive substrates for endothelial cell growth (1999) *Journal of Biomedical Materials Research*, 44, pp. 121-9.

Geiss, R.H., Street, G.B., Volksen, W., Economy, J. Polymer structure determination using electron diffraction techniques (1983) *IBM Journal of Research and Development*, 27 (4), pp. 321-329.

Gelmi, A., Higgins, M.J., Wallace, G.G. Attractive and repulsive interactions originating from lateral nanometer variations in surface charge/energy of hyaluronic acid and chondroitin sulfate doped polypyrrole observed using atomic force microscopy (2012) *Journal of Physical Chemistry B*, 116 (45), pp. 13498-13505.

Gelmi, A., Higgins, M.J., Wallace, G.G. Physical surface and electromechanical properties of doped polypyrrole biomaterials (2010) *Biomaterials*, 31, pp. 1974-83.

Gelmi, A., Higgins, M.J., Wallace, G.G. Quantifying fibronectin adhesion with nanoscale spatial resolution on glycosaminoglycan doped polypyrrole using atomic force microscopy (2013) *Biochimica et Biophysica Acta - General Subjects*, 1830 (9), pp. 4305-4313.

Gelmi, A., Higgins, M.J., Wallace, G.G. Resolving sub-molecular binding and electrical switching mechanisms of single proteins at electroactive conducting polymers (2013) *Small*, 9 (3), pp. 393-401.

Genies, E.M., Bidan, G., Diaz, A.F. Spectroelectrochemical study of polypyrrole films (1983) *Journal of Electroanalytical Chemistry*, 149 (1-2), pp. 101-113.

Gilmore K.J., Kita, M., Han, Y., Gelmi, A., Higgins, M.J., Moulton, S.E., Clark, G.M., Kapsa, R., Wallace, G.G. Skeletal muscle cell proliferation and differentiation on polypyrrole substrates doped with extracellular matrix components (2009) *Biomaterials*, 30, pp. 5292-304.

Gimsa, J., Habel, B., Schreiber, U., Rienen, U.V., Strauss, U., Gimsa, U. Choosing electrodes for deep brain stimulation experiments-electrochemical considerations (2005) *Journal of Neuroscience Methods*, 142 (2), pp. 251-265.

Gimsa, U., Schreiber, U., Habel, B., Flehr, J., Van Rienen, U., Gimsa, J. Matching geometry and stimulation parameters of electrodes for deep brain stimulation experiments - Numerical considerations (2006) *Journal of Neuroscience Methods*, 150 (2), pp. 212-227.

Gittens, R.A., McLachlan, T., Olivares-Navarrete, R., Cai, Y., Berner, S., Tannenbaum, R., Schwartz, Z., Sandhage, K.H., Boyan, B.D. The effects of combined micron-/submicron-scale surface roughness and nanoscale features on cell proliferation and differentiation (2011) *Biomaterials*, 32, pp. 3395-403.

Goktas, H., Ince, F.G., Iscan, A., Yildiz, I., Kurt, M., Kaya, I. The molecular structure of plasma polymerized thiophene and pyrrole thin films produced by double discharge technique (2009) *Synthetic Metals*, 159 (19-20), pp. 2001-2008.

Gregory, R.V., Kimbrell, W.C., Kuhn, H.H. Conductive textiles (1989) Synthetic Metals, 28 (1-2), pp. 823-835.

Guimard, N.K., Gomez, N., Schmidt, C.E. Conducting polymers in biomedical engineering (2007) Progress in Polymer Science (Oxford), 32 (8-9), pp. 876-921

Guimard, N.K.E., Sessler, J.L., Schmidt, C.E. Toward a biocompatible and biodegradable copolymer incorporating electroactive oligothiophene units (2009) *Macromolecules*, 42 (2), pp. 502-511.

Gumus, A., Califano, J. P., Wan, A. M. D., Huynh, J., Reinhart-King, C. A., Malliaris, G. G. Control of cell migration using a conducting polymer device (2010) *Soft Matter* 6, 5138−5142.

Gura, E., Hückel, M., Müller, P. Specific degradation of hyaluronic acid and its rheological properties (1998) *Polymer Degradation and Stability*, 59, (1–3), pp. 297–302.

Hallab, N.J., Bundy, K.J., O'Connor, K., Moses, R.L., Jacobs, J.J. Evaluation of metallic and polymeric biomaterial surface energy and surface roughness characteristics for directed cell adhesion (2001) *Tissue Engineering*, 7 (1), pp. 55-70.

Hammerick, K.E., James, A.W., Huang, Z., Prinz, F.B., Longaker, M.T. Pulsed direct current electric fields enhance osteogenesis in adipose-derived stromal cells (2010) Tissue Engineering Part A, 16, pp. 917-31.

Han, M.G., Armes, S.P. Preparation and characterization of polypyrrole-silica colloidal nanocomposites in water-methanol mixtures (2003) *Journal of Colloid and Interface Science*, 262 (2), pp. 418-427.

Harlin, A., Nousiainen, P., Puolakka, A., Pelto, J., Sarlin, J. Development of polyester and polyamide conductive fibre (2005) *Journal of Materials Science* (2005), 40 (20), pp 5365-537

Hartvig, R.A., Van De Weert, M., Østergaard, J., Jorgensen, L., Jensen, H. Protein adsorption at charged surfaces: The role of electrostatic interactions and interfacial charge regulation (2011) *Langmuir*, 27 (6), pp. 2634-2643.

Heinze, J., Frontana-Uribe, B.A., Ludwigs, S. Electrochemistry of conducting polymers-persistent models and new concepts (2010) *Chemical Reviews*, 110 (8), pp. 4724-4771.

Helenius, J., Heisenberg, C.-P., Gaub, H.E., Muller, D.J. Single-cell force spectroscopy (2008) *Journal of Cell Science*, 121 (11), pp. 1785-1791.

Hertz HJ (1882) Über die Berührung fester elastischer Körper. *J Reine Angew Math* 92:156–171.

Higgins, M., Molino, P., Yue, Z., Wallace, G. Organic conducting polymer-protein interactions (2012) *Chemistry of Materials*, 24, pp. 828-39.

Higgins, M.J., McGovern, S.T., Wallace, G.G. Visualizing dynamic actuation of ultrathin polypyrrole films (2009) *Langmuir*, 25 (6), pp. 3627-3633.

Howlader, M.M.R., Doyle, T.E., Mohtashami, S., Kish, J.R. Charge transfer and stability of implantable electrodes on flexible substrate (2013) *Sensors and Actuators, B*: Chemical, 178, pp. 132-139.

Hull, M., Kitchener, J. Interaction of spherical colloidal particles with planar surfaces (1969) *Transactional of the Faraday Society*, 65, pp. 3093-3104.

Hwang, S.J., Song, Y.M., Cho, T.H., Kim, R.Y., Lee, T.H., Kim, S.J., Seo, Y.K., Kim I.S. The implications of the response of human mesenchymal stromal cells in three-dimensional culture

to electrical stimulation for tissue regeneration (2012) *Tissue Engineering Part A*, 18, pp. 432-45.

Ikkala, O.T., Pietilä, L.-O., Passiniemi, P., Vikki, T., Österholm, H., Ahjopalo, L., Österholm, J.-E. Processible polyaniline complexes due to molecular recognition: Supramolecular structures based on hydrogen bonding and phenyl stacking (1997) *Synthetic Metals*, 84 (1-3), pp. 55-58.

Jager, E.W.H. in Iontronics: Ionic Carriers in Organic Electronic Materials and Devices (2010). Leger, J., Berggren, M., Carter, S. (eds). CRC Press, pp.141-162.

Jager, E.W.H., Immerstrand, C., Peterson, K.H., Magnusson, K.-E., Lundström, I., Inganäs, O. The cell clinic: Closable microvials for single cell studies (2002) *Biomedical Microdevices*, 4 (3), pp. 177-187.

Jager, E.W.H., Smela, E., Inganäs, O. On-chip microelectrodes for electrochemistry with movable PPy bilayer actuators as working electrodes (1999) *Sensors and actuators B*, 56, pp. 73-78.

Jang, J., Oh, J.H., Stucky, G.D. Fabrication of ultrafine conducting polymer and graphite nanoparticles (2002) *Angewandte Chemie - International Edition*, 41 (21), pp. 4016-4019.

Jha A.K., Xu, X., Duncan, R.L., Jia, X. Controlling the adhesion and differentiation of mesenchymal stem cells using hyaluronic acid-based, doubly crosslinked networks (2011) *Biomaterials*, 32, pp. 2466-78.

Jiang, X., Marois, Y., Traoré, A., Tessier, D., Dao, L.H., Guidoin, R., Zhang, Z. Tissue reaction to polypyrrole-coated polyester fabrics: An in vivo study in rats (2002) *Tissue Engineering*, 8 (4), pp. 635-647.

Jin, L., Wang, T., Feng, Z.-Q., Zhu, M., Leach, M.K., Naim, Y.I., Jiang, Q. Fabrication and characterization of a novel fluffy polypyrrole fibrous scaffold designed for 3D cell culture (2012) *Journal of Materials Chemistry*, 22 (35), pp. 18321-18326.

Kane, M.C., Lascola, R.J., Clark, E.A. Investigation on the effects of beta and gamma irradiation on conducting polymers for sensor applications (2010) *Radiation Physics and Chemistry*, 79 (12), pp. 1189–1195.

Kern, J.-M., Sauvage, J.-P. Photochemical deposition of electrically conducting polypyrrole (1989) *Journal of the Chemical Society, Chemical Communications*, (10), pp. 657-658.

Kim, I.S., Song, J.K., Song, Y.M., Cho, T.H., Lee, T.H., Lim. S.S., Kim. S.J., Hwang. S.J. Novel effect of biphasic electric current on in vitro osteogenesis and cytokine production in human mesenchymal stromal cells (2009) *Tissue Enginering Part A*, 15, pp. 2411-22.

Kim, J.K., Srinivasan, P., Kim, J.H., Choi, J.-i., Park, H.J., Byun, M.W., Lee, J.W. Structural and antioxidant properties of gamma irradiated hyaluronic acid (2008) *Food Chemistry*, 109 (4), pp. 763-770.

Kulik, B., Kruse, S. Pelto, J. High pressure phase equilibrium studies of the pyrrole–carbon dioxide binary system (2008) *The Journal of Supercritical Fluids*, 47 (2), pp.135-9.

Kumar, S.S., Hsiao, J.-H., Ling, Q.-D., Dulinska-Molak, I., Chen, G., Chang, Y., Chang, Y., Chen, Y.H., Chen, D.-C., Hsu, S.-T., Higuchi, A. The combined influence of substrate elasticity and surface-grafted molecules on the ex vivo expansion of hematopoietic stem and progenitor cells (2013) *Biomaterials*, 34 (31), pp. 7632-7644.

Kuwabata, S., Nakamura, J., Yoneyama, H. The effect of basicity of dopant anions on the conductivity of polypyrrole films (1988) *Journal of the Chemical Society, Chemical Communications*, (12), pp. 779-780.

Lee, J., Schmidt, C. Pyrrole-hyaluronic acid conjugates for decreasing cell binding to metals and conducting polymers (2010) *Acta Biomaterialia*, 6, pp. 4396-4404.

Lee, J.Y., Bashur, C.A., Goldstein, A.S., Schmidt, C.E. Polypyrrole-coated electrospun PLGA nanofibers for neural tissue applications (2009) *Biomaterials*, 30, pp. 4325–4335

Lee, K.K.C., Herman, P.R., Shoa, T., Haque, M., Madden, J.D.W., Yang, V.X.D. Microstructuring of polypyrrole by maskless direct femtosecond laser ablation (2012) *Advanced Materials*, 24 (9), pp. 1243-1246.

Lee, Y.H., Lee, J.Y., Lee, D.S. Novel conducting soluble polypyrrole composite with a polymeric co-dopant (2000) *Synthetic Metals*, 114 (3), pp. 347-353.

Li, G., Pickup, P.G. Ion transport in a chemically prepared polypyrrole/poly(styrene-4-sulfonate) composite (1999) *Journal of Physical Chemistry B*, 103 (46), pp. 10143-

Liu, A., Zhao, L., Bai, H., Zhao, H., Xing, X., Shi, G. Polypyrrole actuator with a bioadhesive surface for accumulating bacteria from physiological media (2009) *ACS Applied Materials and Interfaces*, 1 (4), pp. 951-955.

Liu, Y., Gan, Q., Baig, S., Smela, E. Improving PPy adhesion by surface roughening (2007) *Journal of Physical Chemistry C*, 111 (30), pp. 11329-11338.

Lubarsky, G.V., Browne, M.M., Mitchell, S.A., Davidson, M.R., Bradley, R.H. The influence of electrostatic forces on protein adsorption (2005) *Colloids and Surfaces B: Biointerfaces*, 44 (1), pp. 56-63.

Ludwig, T., Kirmse, R., Poole, K., Schwarz, U.S. Probing cellular microenvironments and tissue remodelling by atomic force microscopy (2008) *Pflugers Archiv - European Journal of Physiology*, 456, pp. 29–49.

Mabrouk PA. Oxidative electropolymerization of pyrrole from neat monomer solution (2005) *Synthetic Metals*, 150, pp. 101–105.

Machida, S., Miyata, S., Techagumpuch, A. Chemical synthesis of highly electrically conductive polypyrrole (1989) *Synthetic Metals*, 31 (3), pp. 311-318.

McCaig, C.D., Rajnicek, A.M., Song, B., Zhao, M. Controlling cell behavior electrically: Current views and future potential (2005) *Physiological Reviews*, 85 (3), pp. 943-978.

McCullen, S.D., McQuilling, J.P., Grossfeld, R.M., Lubischer, J.L., Clarke, L.I., Loboa, E.G. Application of low-frequency alternating current electric fields via interdigitated electrodes: effects on cellular viability, cytoplasmic calcium, and osteogenic differentiation of human adipose-derived stem cells (2010) *Tissue Engineering Part C Methods*, 16, pp. 1377-86.

McNeill, R. Siudak, J. H. Wardlaw, D. E. Weiss. Electronic Conduction in Polymers. The Chemical Structure of Polypyrrole (1963) *Australian Journal of Chemistry*, 16, pp. 1056-75.upper case here

Meng, S., Rouabhia, M. and Zhang, Z. Electrical stimulation in tissue regeneration, applied biomedical engineering (2011), Dr. Gaetano Gargiulo (Ed.), ISBN: 978-953-307-256-2, InTech, DOI: 10.5772/18874. Available from: http://www.intechopen.com/books/applied-biomedical-engineering/electrical-stimulation-in-tissue-regeneration.

Meng, S., Z. Zhang, and M. Rouabhia. Accelerated osteoblast mineralization on a conductive substrate by multiple electrical stimulation (2011) *Journal of Bone and Mineral Metabolism*, 29, pp. 535–544.

Merrill, D.R., Bikson, M., Jefferys, J.G.R. Electrical stimulation of excitable tissue: Design of efficacious and safe protocols (2005) *Journal of Neuroscience Methods*, 141 (2), pp. 171-198.

Mesimäki, K., Lindroos, B., Törnwall, J., Mauno, J., Lindqvist, C., Kontio, R., Miettinen, S., Suuronen, R. Novel maxillary reconstruction with ectopic bone formation by GMP adipose stem cells (2009) *International Journal of Oral and Maxillofacial Surgery*, 38 (3), pp. 201-209.

Mikami, T., Kitagawa, H. Biosynthesis and function of chondroitin sulfate (2013) *Biochimica et Biophysica Acta - General Subjects*, 1830 (10), pp. 4719-4733.

Miller, D.C., Thapa, A., Haberstroh, K.M., Webster, T.J. Endothelial and vascular smooth muscle cell function on poly(lactic-co-glycolic acid) with nano-structured surface features (2004) *Biomaterials*, 25 (1), pp. 53-61.

Molino, P.J., Higgins, M.J., Innis, P.C., Kapsa, R.M.I., Wallace, G.G. Fibronectin and bovine serum albumin adsorption and conformational dynamics on inherently conducting polymers: A QCM-D study (2012) *Langmuir*, 28 (22), pp. 8433-8445.

Naarman, H. (1986) *BASF Kunststoffe, Forschung und Entwicklung*, p. 40.

Naegele, D., Bittihn, R. Electrically conductive polymers as rechargeable battery electrodes (1988) *Solid State Ionics*, 28-30 (PART 2), pp. 983-989.

Nakata, Masakazu, Kise, Hideo Preparation of polypyrrole-poly(vinyl chloride) composite films by interphase oxidative polymerization (1993) *Polymer Journal*, 25 (1), pp. 91-94.

Naoi, K., Sakai, H., Ogano, S. Osaka, T. Application of electrochemically formed polypyrrole in lithium ion secondary batteries: Analysis of anion diffusion process (1987) *Journal of Power Sources*, 20 (3-4), pp. 237–242.

Newton, J.C., Knisley, S.B., Zhou, X., Pollard, A.E., Ideker, R.E. Review of mechanisms by which electrical stimulation alters the transmembrane potential (1999) *Journal of Cardiovascular Electrophysiology*, 10 (2), pp. 234-243

Nyström, G., Razaq, A., Strømme, M., Nyholm, L., Mihranyan, A. Ultrafast All-Polymer Paper-Based Batteries (2009) *Nano Letters*, 9, pp. 3635–3639.

Oh, Eung Ju; Jang, Kwan Sik; MacDiarmid, Alan G. High molecular weight soluble polypyrrole (2002) *Synthetic Metals*, 125 (3), 267-72

Ohshima, H. Electrostatic interaction between a sphere and a planar surface: Generalization of point-charge/surface image interaction to particle/surface image interaction (1998) *Journal of Colloid and Interface Science*, 198, pp. 42-52.

O'Neil, K., Shaw, B., Semenikhin, O. On the origin of mesoscopic inhomogeneity of conducting polymers (2007) *Journal of Physical Chemistry B,* 111, pp. 9253-69.

Park, D.S., Shim, Y.B., Park S.M. Degradation of electrochemically prepared polypyrrole in aqueous sulfuric acid (1993) *Journal of Electrochemical Society*, 140, p. 609

Pei, Q., Inganäs, O. Electrochemical applications of the bending beam method. Mass transport and volume changes in polypyrrole during redox (1992) *Journal of Physical Chemistry*, 96, pp. 10507-14.

Pron, A., Zagorska, M., Fabianowski, W., Raynor, J.B., Lefrant, S. Spectroscopic and morphological studies of a polypyrrole-poly(vinyl alcohol) composite (1987) *Polymer communications Guildford*, 28 (7), pp. 193-195.

Pyo, M., Bohn, C.C., Smela, E., Reynolds, J.R., Brennan, A.B. Direct strain measurement of polypyrrole actuators controlled by the polymer/gold interface (2003) *Chemistry of Materials*, 15 (4), pp. 916-922.

Ravichandran, R., Sundarrajan, S., Venugopal, J.R., Mukherjee, S., Ramakrishna, S. Applications of conducting polymers and their issues in biomedical engineering (2010) *Journal of the Royal Society Interface*, 7 (SUPPL. 5), pp. S559-S579.

Richardson, R.T., Wise, A.K., Thompson, B.C., Flynn, B.O. Atkinson, P.J. Fretwell, N.J. Fallon, J.B. Wallace, G.G. Shepherd, R.K. Clark, G.M., O'Leary, S.J. Polypyrrole-coated electrodes for the delivery of charge and neurotrophins to cochlear neurons (2009) *Biomaterials*, 30, pp. 2614-2624.

Rivers, T.J., Hudson, T.W., Schmidt, C.E. Synthesis of a novel, biodegradable electrically conducting polymer for biomedical applications (2002) *Advanced Functional Materials*, 12 (1), pp. 33-37.

Rodriquez, J., Grande, HJ, Otero, TF (1997). Polypyrroles: from basic research to technological applications, in: handbook of organic conductive molecules and polymers, ed. Nalwa, H.S., John Wiley & Sons, Vol.2, p. 415.

Rowlands, A.S., Cooper-White, J.J. Directing phenotype of vascular smooth muscle cells using electrically stimulated conducting polymer (2008) *Biomaterials*, 29 (34), pp. 4510-4520.

Rudge, A., Davey, J., Raistrick, I., Gottesfeld, S., Ferraris, J.P. Conducting polymers as active materials in electrochemical capacitors (1994) *Journal of Power Sources*, 47 (1-2), pp. 89-107.

Sader, J., Chon, J., Mulvaney, P. Calibration of rectangular atomic force microscope cantilevers (1999) *Review of Scientific Instruments*, 70, pp. 3967-69.

Sahoo, N.G., Jung, Y.C., Goo, N.S., Cho, J.W. Conducting shape memory polyurethane-polypyrrole composites for an electroactive actuator (2005) *Macromolecular Materials and Engineering,* 290 (11), pp. 1049-1055.

Salto, C., Saindon, E., Bolin, M., Kanciurzewska, A., Fahlam, M., Jager, E.D.H., Tengvall, P., Arenas, E., Berggren, M. Control of neural stem cell adhesion and density by an electronic polymer surface switch (2008) *Langmuir*, 24, pp. 14133−14138.

Santos, M.J.L., Brolo, A.G. and Girotto, E.M. Study of polaron and bipolaron states in polypyrrole by in situ Raman spectroelectrochemistry (2007) *Electrochimica Acta*, 52 (10) pp.6141-6145.

Sasso, C., Fenoll, M., Stephan, O., Beneventia, D. Use of wood derivatives as doping / dispersing agents in the preparation of polypyrrole aqueous dispersions (2008) *BioResources*, 3 (4), pp. 1187-1195.

Sasso, C., Zeno, E., Petit-Conil, M., Chaussy, D., Belgacem, M.N., Tapin-Lingua, S., Beneventi, D. Highly conducting polypyrrole/cellulose nanocomposite films with enhanced mechanical properties(2010) *Macromolecular Materials and Engineering*, 295 (10), pp. 934-941.

Sauerbrey, G. 1959. Verwendung von Schwingquarzen zur Wägung dünner Schichten und zur Mikrowägung. *Zeitung Physics*, Vol. 155, pp. 206-222.

Schlenoff, J.B., Xu, H. Evolution of physical and electrochemical properties of polypyrrole during extended oxidation (1992) *Journal of the Electrochemical Society*, 139 (9), pp. 2397-2401.

Segawa, H., Shimidzu, T., Honda, K. A novel photo-sensitized polymerization of pyrrole (1989) *Journal of the Chemical Society, Chemical Communications*, (2), pp. 132-133.

Semenikhin, O.A., Jiang, L., Iyoda, T., Hashimoto, K., Fujishima, A. Atomic force microscopy and kelvin probe force microscopy evidence of local structural inhomogeneity and nonuniform dopant distribution in conducting polybithiophene (1996) *Journal of Physical Chemistry*, 100 (48), pp. 18605-18606.

Serra Moreno, J., Panero, S. Evaluation of the interface aging process of polypyrrole-polysaccharide electrodes in a simulated physiological fluid (2012) *Electrochimica Acta*, 68, pp. 1-8.

Serra Moreno, J., Panero, S., Materazzi, S., Martinelli, A., Sabbieti, M.G., Agas, D., Materazzi, G. Polypyrrole-polysaccharide thin films characteristics: Electrosynthesis and biological properties (2009) *Journal of Biomedical Materials Research Part A*, 88A, pp. 832-40.

Serra Moreno, J., Panero, S.,Artico, M., Filippini P. Synthesis and characterization of new electroactive polypyrrole–chondroitin sulphate A substrates (2008) *Bioelectrochemistry*, 72, pp. 3–9.

Serra Moreno, J., Sabbieti, M.G., Agas, D., Marchetti, L., Panero, S. Polysaccharides immobilized in polypyrrole matrices are able to induce osteogenic differentiation in mouse

mesenchymal stem cells (2012) *Journal of Tissue Engineering and Regenerative Medicine*, 8(12), pp. 989-99.

Shang, S., Zeng, W., Tao, X. Fabrication of conducting polypyrrole/β-cyclodextrin nano- and micro-spheres using molecular template (2012) *RSC Advances*, 2, pp. 4675-4682.

Shenoy, S.L., Cohen, D., Erkey, C., Weiss, R.A. A solvent-free process for preparing conductive elastomers by an in situ polymerization of pyrrole (2002) *Industrial and Engineering Chemistry Research*, 41 (6), pp. 1484-1488.

Shenoy, S.L., Cohen, D., Weiss, R.A., Erkey, C. Supercritical carbon dioxide aided preparation of conductive polyurethane-polypyrrole composites (2004) *Journal of Supercritical Fluids*, 28 (2-3), pp. 233-239.

Shenoy, S.L., Kaya, I., Erkey, C., Weiss, R.A. Synthesis of conductive elastomeric foams by an in situ polymerization of pyrrole using supercritical carbon dioxide and ethanol cosolvents (2001) *Synthetic Metals*, 123(3), pp. 509–514.

Shi, G., Rouabhia, M., Meng, S., Zhang, Z. Electrical stimulation enhances viability of human cutaneous fibroblasts on conductive biodegradable substrates (2008) *Journal of Biomedical Materials Research - Part A*, 84 (4), pp. 1026-1037.

Shi, G., Rouabhia, M., Wang, Z., Dao, L.H., Zhang, Z. A novel electrically conductive and biodegradable composite made of polypyrrole nanoparticles and polylactide (2004) *Biomaterials*, 25 (13), pp. 2477-2488.

Shi, G., Zhang, Z., Rouabhia, M. The regulation of cell functions electrically using biodegradable polypyrrole-polylactide conductors (2008) *Biomaterials*, 29 (28), pp. 3792-3798.

Silk, T., Hong, Q., Tamm, J., Compton, R.G. AFM studies of polypyrrole film surface morphology II. Roughness characterization by the fractal dimension analysis (1998) *Synthetic Metals*, 93 (1), pp. 65-71.

Silk, T., Hong, Q., Tamm, J., Compton, R.G. AFM studies of polypyrrole film surface morphology I. The influence of film thickness and dopant nature (1998) *Synthetic Metals*, 93 (1), pp. 59-64.

Skardal, A., Mack, D., Atala, A., Sokern, S. Substrate elasticity controls cell proliferation, surface marker expression and motile phenotype in amniotic fluid-derived stem cells (2012) *Journal of the Mechanical Behavior of Biomedical Materials*, 17, pp. 307-316.

Smela, E. Microfabrication of Ppy microactuators and other conjugated polymer devices (1999) *Journal of Micromechanics and Microengineering*, 9(1), pp. 1-18.

Smela, E., Gadegaard, N. Volume change in polypyrrole studied by atomic force microscopy (2001) *Journal of Physical Chemistry B*, 105 (39), pp. 9395-9405.

Smith, A. B.; Knowles, C. J. Investigation of the relationship between conductivity and protein-binding properties of polypyrrole (1991) *Journal of Applied Polymer Science*, 43, pp. 399−403.

Spadaro, J.A. Mechanical and Electrical Interactions in Bone Remodeling (1997) *Bioelectromagnetics*, 18 (3), pp. 193-202.

Stern, R., Kogan, G., Jedrzejas, M.J. Soltes, L. The many ways to cleave hyaluronan (2007) *Biotechnology Advances*, 25, pp. 537-557.

Stevenson, M., Baylor, K., Netherton, B.L., Stecker, M.M. Electrical stimulation and electrode properties. Part 2: Pure metal electrodes (2010) *Neurodiagnostic Journal*, 50 (4), pp. 263-296.

Sun, S., Cho, M. Human fibroblast migration in three-dimensional collagen gel in response to noninvasive electrical stimulus: II. Identification of electrocoupling molecular mechanisms (2004) *Tissue Engineering*, 10 (9-10), pp. 1558-1565.

Sun, S., Liu, Y., Lipsky, S., Cho, M. Physical manipulation of calcium oscillations facilitates osteodifferentiation of human mesenchymal stem cells (2007) *FASEB Journal*, 21, pp. 1472-80.

Sun, S., Titushkin, I., Cho, M. Regulation of mesenchymal stem cell adhesion and orientation in 3D collagen scaffold by electrical stimulus (2006) *Bioelectrochemistry*, 69 (2), pp. 133-141

Sun, S., Wise, J., Cho, M. Human fibroblast migration in three-dimensional collagen gel in response to noninvasive electrical stimulus: I. Characterization of induced three-dimensional cell movement (2004) *Tissue Engineering*, 10 (9-10), pp. 1548-1557

Svennersten, K., Berggren, M., Richter-Dahlfors, A., Jager, E.W.H. Mechanical stimulation of epithelial cells using polypyrrole microactuators (2011) *Lab on a Chip - Miniaturisation for Chemistry and Biology*, 11 (19), pp. 3287-3293.

Svennersten, K., Bolin, M.H., Jager, E.W.H., Berggren, M., Richter-Dahlfors, A. Electrochemical modulation of epithelia formation using conducting polymers (2009) *Biomaterials*, 30 (31), pp. 6257-6264.

Takahashi, D., Kubota, Y., Kokai, K., Izumi, T., Hirata, M., Kokufuta, E. Effects of surface charge distribution of proteins in their complexation with polyelectrolytes in an aqueous salt-free system (2000) *Langmuir*, 16 (7), pp. 3133-3140.

Tandon, N., Cannizzaro, C., Chao, P.-H.G., Maidhof, R., Marsano, A., Au, H.T.H., Radisic, M., Vunjak-Novakovic, G. Electrical stimulation systems for cardiac tissue engineering (2009) *Nature Protocols*, 4 (2), pp. 155-173.

Tandon, N., Goh, B., Marsano, A., Chao, P.H., Montouri-Sorrentino, C., Gimble. J., Vunjak-Novakovic, G. Alignment and elongation of human adipose-derived stem cells in response to direct-current electrical stimulation (2009) *Conference Proceedings of the IEEE Engineering in Medicine and Biology Society*, 1, pp. 6517-21.

Tandon, N., Marsano, A., Maidhof, R., Numata, K., Montouri-Sorrentino, C., Cannizzaro, C., Voldman, J., Vunjak-Novakovic, G. Surface-patterned electrode bioreactor for electrical stimulation (2010) *Lab on a Chip - Miniaturisation for Chemistry and Biology*, 10 (6), pp. 692-700.

Temmer, R., Must, I., Kaasik, F., Aabloo, A., Tamm, T. Combined chemical and electrochemical synthesis methods for metal-free polypyrrole actuators (2012) *Sensors and Actuators, B: Chemical*, 166-167, pp. 411-418.

Ueno, T., Arntz, H., Flesch, S., Bargon, J. Transparent, electrically conductive composites derived from polypyrrole and poly(vinyl chloride) by vapor-phase polymerization: Effect of environment on polymerization and reaction mechanism (1988) *Journal of Macromolecular Science. Chemistry*, A25 (12), pp. 1557-1573.

Wallace, Spinks, Teasdale, 1997. Electroactive electroactive polymers – Intelligent materials systems, 1st edition. Technomic Publishing Company, Inc. ISBN No. 1-56676-437-8.

Wan, A.M.D., Brooks, D.J., Gumus, A., Fischbach, C., Malliaras, G.G. Electrical control of cell density gradients on a conducting polymer surface (2009) *Chemical Communications*, (35), pp. 5278-5280.

Wan, Y., Wang, Y., Liu, Z., Qu, X., Han, B., Bei, J., Wang, S. Adhesion and proliferation of OCT-1 osteoblast-like cells on micro- and nano-scale topography structured poly(L-lactide) (2005). *Biomaterials*, 26 (21), pp. 4453-4459

Wang, J., Bard, A. Direct atomic force microscopic determination of surface charge at the gold/electrolyte interface-the inadequacy of classical GCS theory in describing the double-layer charge distribution (2001) *Journal of Physical Chemistry B*, 105, pp. 5217-22.

Wang, X., Gu, X., Yuan, C., Chen, S., Zhang, P., Zhang, T., Yao, J., Chen, F., Chen, G. Evaluation of biocompatibility of polypyrrole in vitro and in vivo (2004) *Journal of Biomedical Materials Research - Part A*, 68 (3), pp. 411-422.

Wang, Y., Sotzing, G.A., Weiss, R.A. Preparation of conductive polypyrrole/polyurethane composite foams by in situ polymerization of pyrrole (2008) *Chemistry of Materials*, 20 (7), pp. 2574-2582.

Wang, Z., Roberge, C., Dao, L.H., Wan, Y., Shi, G., Rouabhia, M., Guidoin, R., Zhang, Z. In vivo evaluation of a novel electrically conductive polypyrrole/poly(D,L- lactide) composite and polypyrrole-coated poly(D,L-lactide-co-glycolide) membranes (2004) *Journal of Biomedical Materials Research - Part A*, 70 (1), pp. 28-38.

Warren, Leslie F., Anderson, Dennis P. Polypyrrole films from aqueous electrolytes: the effect of anions upon order (1987) *Journal of the Electrochemical Society*, 134 (1), pp. 101-105.

Wei, S., Mavinakuli, P., Wang, Q., Chen, D., Asapu, R., Mao, Y., Haldolaarachchige, N., Young, D.P., Guo, Z. Polypyrrole-titania nanocomposites derived from different oxidants (2011) *Journal of the Electrochemical Society*, 158 (11), pp. K205-K212.

Wernet, W., M. Monkenbusch and G. Wegner. On structure and properties of polypyrrole alkylsulfonates (1985) *Molecular Crystals and Liquid Crystals*, 118, pp. 193-197.

Winther-Jensen, B., Chen, J., West, K., Wallace, G. Vapor phase polymerization of pyrrole and thiophene using iron(III) sulfonates as oxidizing agents (2004) *Macromolecules*, 37 (16), pp. 5930-5935.

Wollenweber, M., Domaschke, H., Hanke, T., Boxberger, S., Schmack, G., Gliesche, K., Scharnweber, D., Worch, H. Mimicked bioartificial matrix containing chondroitin sulphate on a textile scaffold of poly(3-hydroxybutyrate) alters the differentiation of adult human mesenchymal stem cells (2006) *Tissue Engineering*, 12 (2), pp. 345-359.

Wolszczak, M.J., Kroh, J., Abdel-Hamid, M.M. Some aspects of the radiation processing of conducting polymers (1995) *Radiation Physics and Chemistry*, 45(1), pp. 71–78.

Wong, J.Y., Leach, J.B., Brown, X.Q. Balance of chemistry, topography, and mechanics at the cell-biomaterial interface: Issues and challenges for assessing the role of substrate mechanics on cell response (2004) *Surface Science*, 570 (1-2), pp. 119-133.

Wu, S., Chang, J., Wang, C., Wang, G., Ho, M. Enhancement of chondrogenesis of human adipose derived stem cells in a hyaluronan-enriched microenvironment (2010) *Biomaterials*, 31, pp. 631-40.

Wu, Y. Alici, G. Spinks, G.M. Wallace, G.G. Fast trilayer polypyrrole bending actuators for high speed applications (2006) *Synthetic Metals*, 156, pp. 1017–1022.

Xing, X., Liu, S., Yu, J., Lian, W., Huang, J. Electrochemical sensor based on molecularly imprinted film at polypyrrole-sulfonated graphene/hyaluronic acid-multiwalled carbon nanotubes modified electrode for determination of tryptamine (2012) *Biosensors and Bioelectronics*, 31 (1), pp. 277-283.

Yin, W., Li, J., Li, Y., Wu, J., Gu, T. Conducting composite film based on polypyrrole and crosslinked cellulose (2001) *Journal of Applied Polymer Science*, 80 (9), pp. 1368-1373.

Yoon, C.O., Reghu, M., Moses, D., Heeger, A.J., Cao, Y., Chen, T.-A., Wu, X., Rieke, R.D. Hopping transport in doped conducting polymers in the insulating regime near the metal-insulator boundary: polypyrrole, polyaniline and polyalkylthiophenes (1995) *Synthetic Metals*, 75 (3), pp. 229-239.

Yu, Q.-Z., Dai, Z.-W., Lan, P. Fabrication of high conductivity dual multi-porous poly (l-lactic acid)/polypyrrole composite micro/nanofiber film (2011) *Materials Science and Engineering B: Solid-State Materials for Advanced Technology*, 176 (12), pp. 913-920.

Zelikin, A.N., Lynn, D.M., Farhadi, J., Martin, I., Shastri, V., Langer, R. Erodible Conducting Polymers for Potential Biomedical Applications (2002) *Angewandte Chemie International Edition*, 41, pp. 141-4.

Zhang, X., Bai, R. Surface electric properties of polypyrrole in aqueous solutions (2003) *Langmuir*, 19, pp. 10703-09.

Zhang, Z., Rouabhia, M., Wang, Z., Roberge, C., Shi, G., Roche, P., Li, J., Dao, L.H. Electrically conductive biodegradable polymer composite for nerve regeneration: Electricity-stimulated neurite outgrowth and axon regeneration (2007) *Artificial Organs*, 31 (1), pp. 13-22.

Zhao, H., Price, W.E., Wallace, G.G. Synthesis, characterisation and transport properties of layered conducting electroactive polypyrrole membranes (1998) *Journal of Membrane Science*, 148 (2), pp. 161-172.

Zhao, L., Gwon, H.-J., Lim, Y.-M., Nho, Y.-C., Kim, S.Y. Gamma ray-induced synthesis of hyaluronic acid/chondroitin sulfate-based hydrogels for biomedical applications (2015) *Radiation Physics and Chemistry*, 106, pp. 404-412.

Zhou, D., Wang, X., Birch, L., Rayment, T., Abell, C. AFM study on protein immobilization on charged surfaces at the nanoscale: Toward the fabrication of three-dimensional protein nanostructures (2003) *Langmuir*, 19 (25), pp. 10557-10562.

Zhou, M., Heinze, J. Electropolymerization of Pyrrole and Electrochemical Study of Polypyrrole. 2. Influence of Acidity on the Formation of Polypyrrole and the Multipathway Mechanism (1999) *Journal of Physical Chemistry B*, 103 (40), pp. 8443-8450.

Zhou, M., Pagels, M., Geschke, B., Heinze, J. Electropolymerization of pyrrole and electrochemical study of polypyrrole. 5. Controlled electrochemical synthesis and solid-state transition of well-defined polypyrrole variants (2002) *Journal of Physical Chemistry B*, 106 (39), pp. 10065-10073.

Publications 1-5

Publication 1

Pelto, J., Haimi, S., Puukilainen, E., Whitten, P.O., Spinks, G.M.,
Bahrami-Samani, M., Ritala, M., Vuorinen, T.

Electroactivity and biocompatibility of polypyrrole-hyaluronic acid multi-walled carbon nanotube composite.

Journal of Biomedical Materials Research Part A. Vol. 93 (2010) No: 3, 1056 – 1067.

Electroactivity and biocompatibility of polypyrrole-hyaluronic acid multi-walled carbon nanotube composite

Jani Pelto,[1] Suvi Haimi,[2] Esa Puukilainen,[3] Philip G. Whitten,[4] Geoffrey M. Spinks,[4] Mehrdad Bahrami-Samani,[4] Mikko Ritala,[3] Tommi Vuorinen[1]

[1]*VTT Technical Research Centre of Finland, Sinitaival 6, P.O. Box 1300, 33101 Tampere, Finland*

[2]*Regea – Institute for Regenerative Medicine, University of Tampere and Tampere University Hospital, Biokatu 12, 33520 Tampere, Finland*

[3]*University of Helsinki, Laboratory of Inorganic Chemistry, Department of Chemistry, P.O. Box 55, 00014 Helsinki, Finland*

[4]*University of Wollongong, Intelligent Polymer Research Institute, Northfields Ave. NSW 2522, Wollongong, Australia*

Received 7 October 2008; revised 28 April 2009; accepted 26 June 2009
Published online 14 September 2009 in Wiley InterScience (www.interscience.wiley.com). DOI: 10.1002/jbm.a.32603

Abstract: Electroactivity of polypyrrole hyaluronic acid, electropolymerized in the presence of oxidized carbon nanotubes (PPyHA-CNT) was studied *in situ* by electrochemical atomic force microscopy (EC-AFM) in physiological electrolyte solution. *In situ* Raman spectroscopic and quartz crystal microbalance (QCM) studies were conducted on layers of the polymer grown on AT-cut 5 MHz quartz crystals. Human adipose stem cell (ASC) attachment and viability were studied by Live/Dead staining, and the proliferation was evaluated by WST-1 Cell proliferation assay for polypyrrole samples electropolymerized on titanium. According to cyclic voltammetry, the measured specific capacitance of the material on gold is roughly 20% of the reference polypyrrole dodecylbenzene sulfonate (PPyDBS). Electrochemical-QCM (EC-QCM) analysis of a 210-nm thick film reveals that the material is very soft G′∼100 kPa and swells upon reduction. EC-AFM of samples polymerized on microelectrodes show that there are areas of varying electroactivity, especially for samples without a hydrophopic backing PPyDBS layer. AFM line scans show typically 20–25% thickness change during electrochemical reduction. Raman spectroscopic analysis suggests that the material supports noticeable polaron conduction. Biocompatibility study of the PPyHA-CNT on titanium with adipose stem cells showed equal or better cell attachment, viability, and proliferation compared with the reference polylactide. © 2009 Wiley Periodicals, Inc. J Biomed Mater Res 93A: 1056–1067, 2010

Key words: polypyrrole composite; electroactive polymer; atomic force microscopy; quartz crystal microbalance; biocompatibility

INTRODUCTION

Polypyrroles form a group of electrically conductive polymeric materials gaining popularity in biological applications. Their properties, including interaction with biological systems may vary greatly depending on their chemical constituents, for example the "dopant" species. The dopants and modifiers coprecipitate with the growing conductive polymer and become an integral part of its morphology and the resultant properties. For example, anionic bulky alkyl sulfonates and organics modifiers like long alcohol cosurfactants[1] present in the syntheses are responsible for the resultant surface morphology, hydrophilicity, and electrochemical activity. Thus, polypyrroles offer great flexibility in terms of creating a designed profile of material properties and surface chemistry by employing different dopants or modifiers.

The electrical properties of polypyrroles observed at the macroscopic scale are due to the potentially very high interchain (bipolaron) p-type conduction and intrachain electronic hopping conduction along the ordered conjugated polypyrrole structures.[2] The limiting factor for the electronic charge transport is the mostly disordered phase surrounding the ordered phase. It is generally accepted that the redox switching of the conductivity that is the "doping" reactions are ultimately limited by the ionic diffusion of the electrolytes and dopants in the system. The anionic dopants and the ionic species present in the polypyrroles can be mobile or practically immobile. When immobile, the molecules are organized into the same phase with the individual conjugated polymer chains and remain there during redox cycling

Correspondence to: J. Pelto; e-mail: jani.pelto@vtt.fi

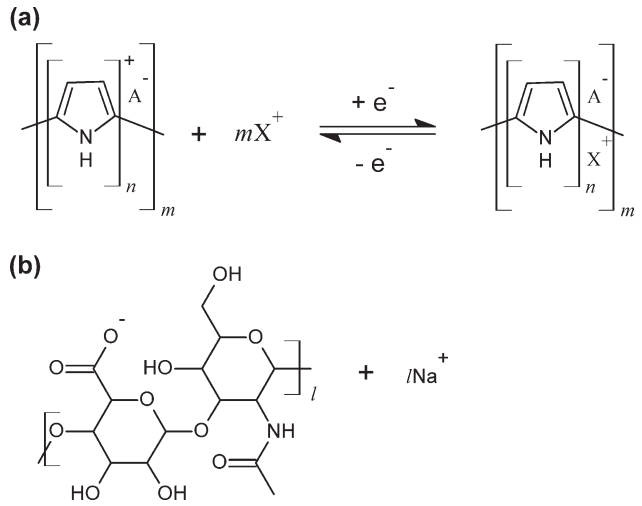

Figure 1. Polypyrrole redox reactions and the chemical structure of hyaluronic acid.

(Fig. 1). Immobile dopants are typically large anions where polymer is observed to expand upon reduction. Mobile dopants such as small anions (Cl^-, SO_4^{2-}) are free to move according to the chemical potential gradients and exchange with the ions of the surrounding electrolyte, and the polymer is observed to contract upon reduction.

The conjugated backbone of polypyrrole doped with various strong sulfonic acid anions, for example, dodecyl benzene sulfonate (DBS)[3] exhibit characteristic oxidation and reduction reactions in aqueous alkali halide electrolytes. PPyDBS reduction reaction in aqueous sodium chloride is characterized by an extremely large dimensional change[4] that is mechanical stress that can be utilized in macrosopic and microscopic electrochemical actuators.[5]

Electrical conductivity of polypyrrole is gradually increased by several orders of magnitude when the neutral PPy chain is chemically or electrochemically oxidized to form a polycation. Physically this involves increase in the number of free charge carriers due to the build-up of polaron- and bipolaron lattices. Formation of such conjugation increases the rigidity of the PPy backbone and induces structural reorganization of the material.[6] Charge neutrality requires that the excess positive charge of the polycationic PPy chain is balanced by the anions of the dopant species. Indeed, it is generally accepted that the volume change of PPyDBS is partly due to the relaxation of the polaronic polypyrrole backbone but mainly due to dopant and ion movement induced expansion of the material, accompanied by the solvation shells of the ions involved and the excess solvent driven by osmotic forces.[1] The molarity of the NaCl electrolyte can be very high in polypyrroles containing polyanionic dopants, up to several moles per liter. Therefore, the osmotic pressure of water and hence the actuation capacity is highest in diluted electrolytes for example those close to physiological molarity 0.1–0.2 *M*.[1]

Hyaluronic acid (HA), being a negatively charged polyelectrolyte is assumed to be a completely immobile dopant for PPy-matrix where the charge is balanced by the relatively free movement of Na^+ ions. It is assumed that some chloride ions must associate with some of the carboxylic acid groups of the HA in the polypyrrole and as such the material should be considered a molecular mixture of PPyHA and PPyCl.

HA is an high molecular weight polysaccharide consisting of a disaccharide D-glucuronic acid and D-*N*-acetylglucosamine. It is abundant in all vertebrates as an important constituent of the extracellular matrix (ECM). HA is constantly digested and synthesized by cells. It has structural functions due to its viscous and hydrophilic nature for example as a damper and lubricant in synovial fluid and a vital role in skin tissue repair. From the 1970's, it has been used as a therapeutic agent for treating osteoarthritis and cataract surgery. Recently, HA benzylic ester nonwoven (HYAFF 11) has gained popularity as a scaffolding material for cartilage and skin tissue engineering due to its mechanical integrity compared with crosslinked HA hydrogels.[7] HA or hyaluronan may have also important biological functions. HA plays a major role in tissue growth and remodeling as it specifically interacts with endogenous receptors regulating cellular migration, growth, and adhesion.[8] The degradation products of hyaluronan, the oligosaccharides and very low-molecular-weight hyaluronan, exhibit pro-angiogenic properties,[9,10] making the material attractive for tissue engineering applications.

The PPyHA-carbon nanotube (CNT) composite studied in this work is designed for use as an electroactive tissue engineering scaffold that promotes cell proliferation and attachment. The electroactivity enables electrical stimulation and control of the surface charge, which renders the surface selectivity in binding to proteins and cells. Electropolymerized PPyHA is a highly hydrophilic and soft material containing entrapped hyaluronic acid and having relatively low electroactivity and electrical conductivity, in the order of 10^{-3} S/cm,[11] approximately two orders of magnitude lower than polypyrroles doped with the conventional alkyl sulfonic acid dopants. Various polypyrroles doped with biologically derived polyelectrolytes (e.g., polysaccharides, proteins and oligopeptides) has been reported to be biocompatible and support cell adhesion and growth with a number of different cell types: for example human endothelial cells on polypyrrole-heparin,[12] rat pheochromocytoma (PC12) cells on polypyrrole-polystyrenesulfonate,[13] human keratinocytes with various polysaccha-

ride and protein doped polypyrroles,[14] human fibroblasts[15] and rat mesenchymal stem cells, and their differentiation toward osteoblasts *in vitro*.[16]

The embedded CNTs are intended to increase the electrical conductivity of the biopolymer doped conductive polymers, such as PPyHA. Microscopic observation shows that the CNTs also have a substantial effect on the surface morphology of the electropolymerized material, usually rendering the surface porous and more attractive to cells.[17]

Designing a CNT hybrid material, the possible cytotoxic effects of the CNTs must be taken into account, since several studies have shown carbon nanoparticles (single walled nanotubes, fullerenes etc.) express dose dependent toxicity *in vitro*. For example, necrosis of Alveolar macrophages have been reported.[18] Treatment of nanotubes with hot concentrated acids facilitates the functionalisation of the CNTs with oxygenated groups whilst removing the metal catalyst. This process renders the CNTs negatively charged such that they are more easily dispersed in weakly acidic aqueous solutions, and it also suppresses the cytotoxicity, most probably by removing the catalyst residue.[19,20,21]

Recently, atomic force microscopy (AFM) in fluids has become a standard technique for imaging soft samples like living cells in their biological environment.[22] Nondestructive imaging of soft samples is normally successful in dynamic mode where the interaction force between oscillating AFM tip and the sample surface is minimized. Fluid dynamic mode imaging is able to produce high resolution quantitative information on the samples surface profiles when the operating conditions and the AFM tip have been optimized for the sample characteristics.

Quartz crystal microbalance (QCM) is a sensitive technique measuring changes in the resonant frequency of a thickness-shear mode oscillating piezoelectric crystal when the mass density of the surface of the crystal is changed. QCM is capable of measuring mass changes as small as ng/cm^2 routinely. The technique has been applied for many years to quantitatively weigh thin films and rigid deposits on oscillating quartz crystals according to the theory developed originally by Sauerbrey[23]—that is the simplest equation relating the measured frequency shift and the deposited mass [Eq. (1)].

$$\Delta_f = -C_f \Delta m = \frac{2nf_0^2}{\sqrt{\rho_q \mu_q}} \Delta m \tag{1}$$

For AT-cut 5 MHz quartz crystal used here the coefficient equals C_f = 56.6 Hz μg^{-1} cm^2. The coefficient C_f is derived from the resonant frequency of the unloaded crystal, the harmonic mode of oscillation, and the shear modulus and density of quartz. When the change of the resonant frequency is less than 2% of the crystal frequency (i.e., Sauerbrey limit), that is the deposited mass is relatively small, it is a common approach to apply the Eq. (2) without thickness corrections or any other calibration. For thicker films, relations taking into account the acoustic impedances of both the quartz and the sample has to be used (so called Z-match method). Measuring in viscous liquid environment and having viscoelastic polymer samples, a more complex model has to be utilized.[24] This is due to the high viscoelastic damping in both the sample and the liquid medium. A more general model was presented by Bahrami-Samani et al.[25] The model links acoustic impedances and the viscoelastic effects into one equation containing frequency shift Δf and impedance (reported as a resistance ΔR) outputs from QCM studies to calculate the complex valued shear modulus G_f^* and film thickness h_F of the viscoelastic polymer body [Eq. (2)].

$$Z_m = \Delta R \frac{\sqrt{\rho_q G_q^*}}{4f_0 L_u} + j\Delta f \frac{\pi \sqrt{\rho_q G_q^*}}{f_0}$$

$$= \sqrt{\rho_q G_q^*} \left(\frac{(1+j)\sqrt{\frac{\omega \rho_l \eta_l}{2}} + j\sqrt{\rho_f G_f^*} \tan\left(\omega h_f \sqrt{\frac{\rho_f}{G_f^*}}\right)}{\sqrt{\rho_q G_q^*} + j(1+j)\sqrt{\frac{\omega \rho_l \eta_l}{2}} \tan\left(\omega h_f \sqrt{\frac{\rho_f}{G_f^*}}\right)} \right) \tag{2}$$

Equation 2 can be solved for the polymer shear modulus and layer thickness simultaneously when the imaginary part of shear moduli are set to zero at 5 MHz, which is a reasonable assumption according to Dynamical Mechanical Analysis of polypyrrole previously reported.[25]

Several studies,[26,4] have shown that polypyrrole films with large- and medium size dopants swell upon electrochemical cycling. The volumetric changes and surface roughnesses have been measured by contact mode AFM or ellipsometry and mass changes by EQCM. AFM results reported for thickness changes (z-mode) in certain polypyrrole salts for example for PPyDBS can reach as high as 30–40%.[4] The thickness expansion of a supported film (hence constrained in the plane of the film) was found to be strongly dependent on the thickness of the film studied. In Smela's study, the PPy:DBS was driven to electrochemical equilibrium (constant potential over 100 s) before the AFM line scan. A single reference was found regarding electrochemical STM measurement of the volume expansion of PPy:PSSA.[27] None of the above cited articles

reported thickness measurements in fast electrochemical switching. Moreover, the authors of this study did not find any study where the results from a single characterization technique would have been correlated to another measure. Therefore, in this study, an attempt is made to correlate the cyclic voltammetry, mass balance (EQCM), and dimensions (AFM) for a sample containing an large polyanionic HA sodium salt—the mobile ionic species being Na^+ ions and their hydration shells. The carbon nanotubes serve to increase the electrical conductivity of the composite material during the reduction phase of the PPy:HA. The CNTs have an obvious mechanical stiffening effect as well. This will presumably limit the amplitude of the observed volumetric actuation but compensate the loss of electrical conductivity in the reduced nonpolaronic polypyrrole.

EXPERIMENTAL

Electrochemical synthesis

Hyaluronic acid sodium salt (2 mg/mL) from *Strept. equi* (Fluka, M_w = 300,000 Da) was dissolved in Millipore water. Subsequently, 0.25–0.30 mg/mL of the Nanocyl 3151 oxidized multiwalled carbon nanotubes (Nanocyl AG.) were dispersed in the hyaluronic acid sodium salt solution with 30 min of intense ultrasonic agitation (100 W) by Hielscher UPS 400S. The nanotubes formed a stable fine dispersion with the HA. Pyrrole monomer (Acros organics) was vacuum distilled, stored under argon and kept in at −18°C before the experiments. The purity was considered sufficient if there was no visible discoloration of the liquid before use. In a typical synthesis, 0.2 *M* pyrrole monomer was added to the dispersion and then sonicated again in an ultrasonic bath for 15 min before the synthesis. This large amount of the monomer in the nanotube-HA dispersions clearly saturated the system, since, without strong mechanical stirring an oily pyrrole film formed on the surface above pyrrole concentration of ~0.1 *M*. The harsh ultrasonic processing evidently affected the molecular weight of the HA since the viscosity of the dispersion was greatly decreased during the processing.

Electropolymerization of PPyHA-CNT on AT-cut 5MHz Au coated QCM crystals with an active area of 1.37 cm^2 was achieved at constant potential in the range of +0.6 to +0.9 V versus Ag/AgCl. The adhesion of the PPyHA-CNT layer to gold was not very strong even when polymerizing immediately after UV-ozone cleaning. Delamination of the polypyrrole usually took place after approximately 10–20 electrochemical cycles.

Polymerization of PPyHA-CNT on inter-digitated 3 μm line width Au-microelectrodes (A = 0.5 mm^2) was successful in galvanostatic mode (j = 0.2–0.4 mA/cm^2 = 0.5–1 μA/0.005 cm^2). Two sets of samples were prepared: the first set (set A) was polymerized directly after UV-ozone cleaning of the gold surface. In some experiments, a short initial potentiostatic activation step was utilized. In another set of experiments (set B) a PPyDBS supporting layer was applied. Polymerization charge of 100 μC was consumed in the synthesis of the PPyDBS supporting layer. The additional layer rendered the sample stable for hundreds of cycles in EC testing. The polymerization charge for the PPyHA-CNT was set to 200 μC which yielded a rough polymer layer of thickness varying between 350 and 600 nm. The vertical thickness of the gold pattern on silicon substrate is approximately 160 nm. A reference sample, 200 μC PPyHA without nanotubes in the polymerization dispersion, was also synthesized.

The conductivity of the HA/CNT/pyrrole polymerization mixtures is rather low compared with more conventional systems. Therefore, the kinetics of the polymerization are quite slow. Nucleation and growth of the polymer yields solid deposits on gold only at moderate greater than +0.8 V versus Ag/AgCl potentials. Growth of the hyaluronic acid doped polymer is greatly enhanced when a polypyrrole supporting layer is applied. Therefore, to overcome the nucleation issue and the limited adhesion of the growing polymer onto gold and carbon surfaces, a thin PPyDBS adhesion layer was utilized in some of the samples. All of the electropolymerized PPyHA-CNT samples exhibited a very rough surface texture, evident from the AFM images.

Electrochemical QCM

The deposited PPyHA-CNT films on the QCM crystals were characterized immediately after the synthesis. Stanford Research Systems QCM200 with AT-cut 5 MHz Au-coated crystals were used. The QCM probe was immersed in 0.2 *M* NaCl solution containing Ag/AgCl reference electrode and platinum mesh counter electrode. The potential of the sample was controlled by a BAS CV-27 potentiostat. The CV signals and the frequency and admittance signals from the SRS QCM200 were recorded using Maclab 4/e DAQ system.

Electrochemical atomic force microscopy

Imaging with Veeco dimension 3100 system

For sample set A the tapping mode imaging in fluid was done using Veeco Dimension 3100 AFM. In-house built fluid cell (liquid volume ~ 1 mL) and silicon nitride OTR-4 cantilevers (Veeco) attached into the standard Veeco fluid cantilever holder were utilized. The potential of the sample in 0.2 *M* NaCl solution was controlled by a BAS CV-27 potentiostat. Silver pseudoreference and stainless steel counter electrode was utilized.

Imaging with Veeco multimode system

The Veeco multi-mode AFM was equipped with integrated bipotentiostat and a Veeco electrochemical cell setup. Veeco RFESP silicon cantilevers, silver pseudoreference, and platinum wire counter electrodes were used.

The AFM was scanning with the slow scan axis turned off, that is back and forth along a single 8 μm line, transverse to the long axis of the inter-digitated electrodes for

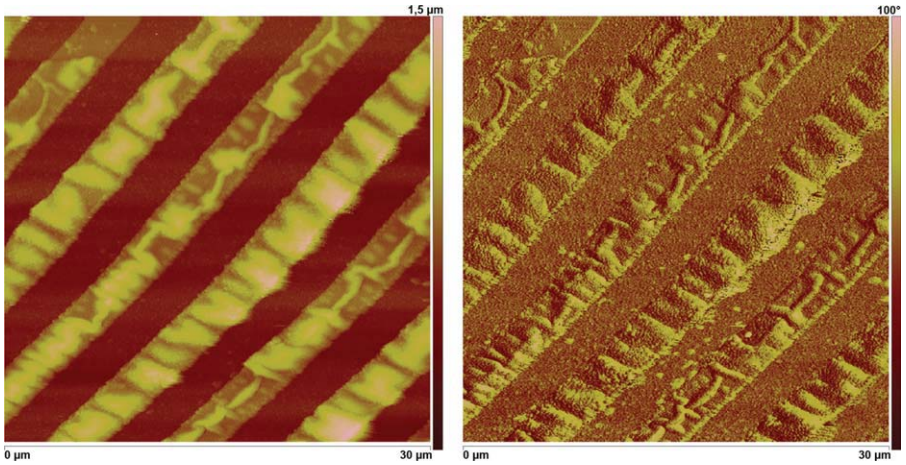

Figure 2. Morphology of the sample EC241. Height image on the left and phase image on the right (raw data). Nucleation has initiated in evenly spaced areas The granular polymer surface appears quite smooth on microscopic scale (R_a = 56 nm, R_z = 84 nm). [Color figure can be viewed in the online issue, which is available at www.interscience.wiley.com.]

six successive electrochemical cycles (+100 to −900 mV *vs.* Ag pseudoreference, 20 mV/s). The aqueous electrolyte contained 0.13 *M* NaCl and 0.02 KCl.

All of the AFM data was first order plane fitted before analysis.

Raman spectroscopy under electrochemical control

Raman spectra of electropolymerized PPyHA-CNT sample was collected at different electrochemical potentials between +200 mV and −1000 mV versus Ag/AgCl reference (with 3 KCl salt bridge). The potential of the sample was controlled by BAS CV-27 potentiostat. The Raman spectra were collected using Horiba Jobin Yvon Labram HR micro-Raman spectrometer, 632.8 nm laser, 1200 lines/mm diffraction grating and 50× objective lens. The measurement was done in 0.1 *M* NaCl solution and at a scanning rate of 5 mV/s. Each recording of a spectrum took 4 s that is the potential of the sample is an averaged spectrum over a potential range of 20 mV. The electrochemical cell (volume 1 mL) utilized was the same custom made setup used in the AFM experiments with Dimension 3100. The free liquid surface was covered with microscopic cover slide to minimize the interference from the liquid-air surface. The microscope focus point was not changed during the experiment.

Biocompatibility test

The aim of this experiment was to study the biocompatibility and specifically the adipose stem cell (ASC) viability and proliferation on the of the polypyrrole-hyaluronic acid-CNT composite material. The experiment was also set to confirm that polypyrrole studied (PPyHA-CNT) does not cause any cytotoxic effects on ASCs. The studied sam-

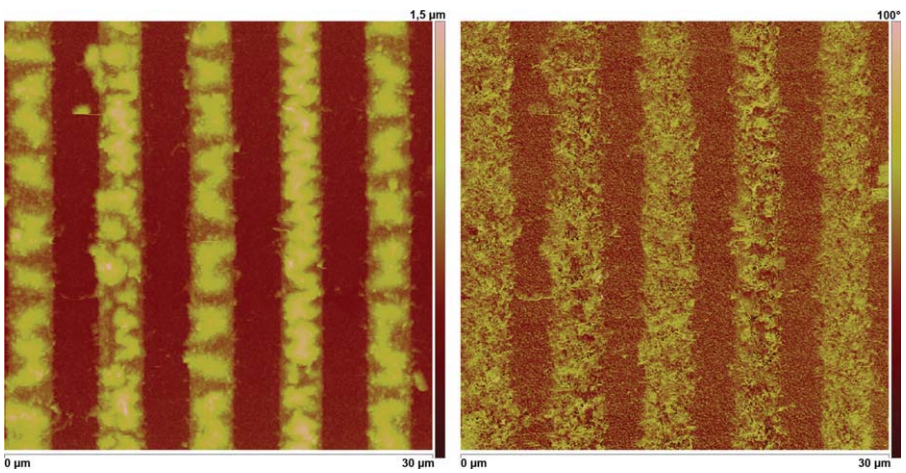

Figure 3. Morphology of the sample EC244 (reduced state). Nucleation has initiated in evenly spaced sites which combine through ribbon-like bridges, much like in the EC241 (Fig. 2). (R_a = 62 nm, R_z = 125 nm). [Color figure can be viewed in the online issue, which is available at www.interscience.wiley.com.]

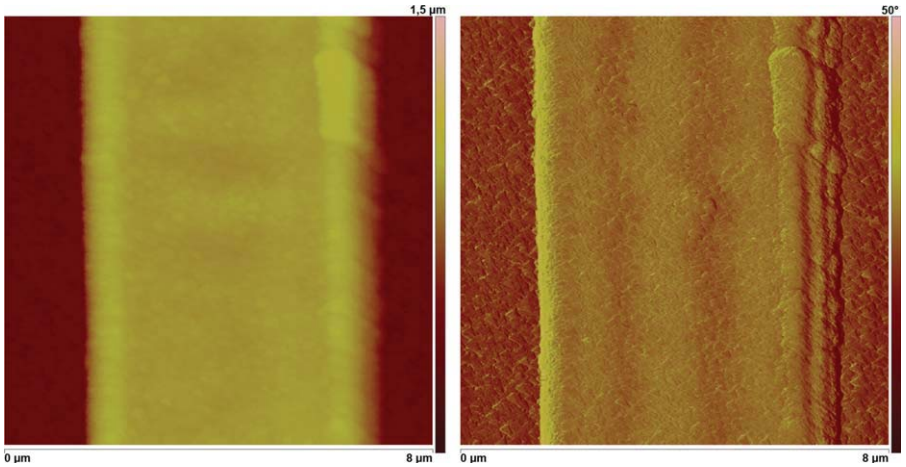

Figure 4. The tapping mode height image (left) and phase image (right) of the hyaluronic acid doped polypyrrole sample (EC875) showing the smooth morphology of the polymer. (R_a = 20 nm, R_z = 11 nm). [Color figure can be viewed in the online issue, which is available at www.interscience.wiley.com.]

ples contained electropolymerized PPyHA-CNT covering pieces of titanium foil. Two pieces (6 × 3 mm^2 × 30 µm) of the polypyrrole coated titanium were mounted on the polylactide (DL-PLA, D70/L30) disks (diameter 9 mm, thickness 1 mm), which were also used as a reference material in the biocompatibility test. ASC viability was studied in two time points; 1 and 8 days using Live/Dead staining. ASC proliferation was studied in 3 time points; 1, 4, and 8 days using WST-1 proliferation assay.

Polypyrrole-DBS adhesion layer (V_{pol} = +0.8 V *vs.* Ag/AgCl, Q_{pol} = 1 C) was first electro- polymerized on the titanium 6 × 3 mm^2 × 30 µm foil electrodes (Goodfellow UK, 99.6+% purity). PPyHA-CNT (Q_{pol} = 2 C) was polymerized subsequently onto the adhesion layer. The initially hydrophopic and smooth PPyDBS surface turned very hydrophilic and rough when coated with the PPyHA-CNT polymer. The samples (24 pcs) were rinsed with 70% ethanol and packed into a sterile D18 mm cell culture well plate for gamma sterilization and subsequent cell testing.

ASC isolation and culture

ASCs were isolated from human adipose tissue samples collected in surgical procedures from two donors (ages 50 and 46 years). The adipose tissue samples were received from the Department of Plastic Surgery, Tampere University Hospital. The adipose tissue was digested with collagenase Type I (1.5 mg/mL; Invitrogen, Paisley, UK). ASCs were expanded in T-75 polystyrene flasks (Nunc, Roskilde, Denmark) in maintenance medium consisting of DMEM/F-12 1:1 (Invitrogen), 10% FBS (Invitrogen), 1% L-glutamine (GlutaMAX I; Invitrogen) and 1% antibiotics/antimycotic (100 U/mL penicillin, 0.1 mg/mL streptomycin, and 0.25

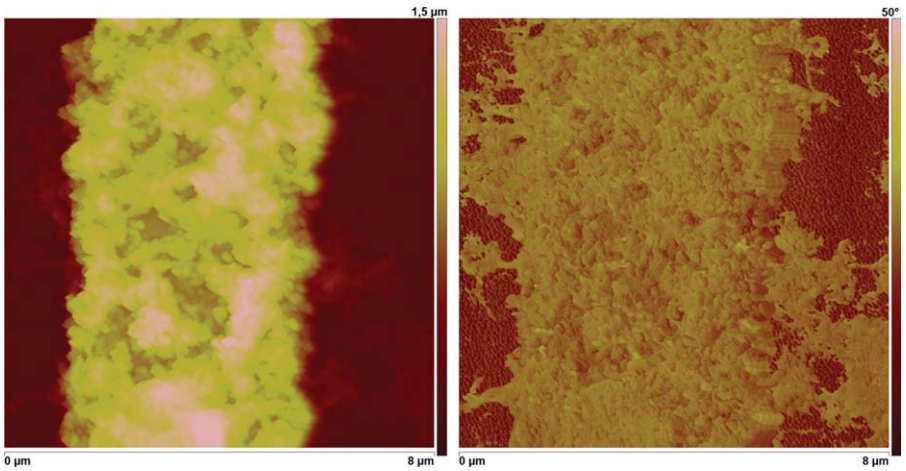

Figure 5. The tapping mode height image (left) and phase image (right) of the hyaluronic acid doped polypyrrole sample (EC878) containing carbon nanotubes and showing the rough and irregular morphology of the polymer. (R_a = 88 nm, R_z = 110 nm). [Color figure can be viewed in the online issue, which is available at www.interscience.wiley.com.]

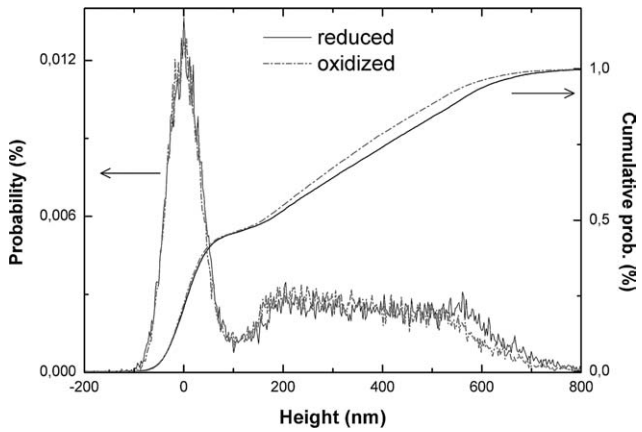

Figure 6. Bearing analysis of the PPyHA:CNT samples without backing layer.

μg/mL amphotericin B; Invitrogen). Cells of passages 5–6 were used in the experiment.

Cell seeding and culture of ASC-seeded biomaterial samples

Two patient samples were pooled together to yield enough cells for the experiment. On each sample, pretreated with maintenance medium for 24 h at 37°C, 15,000 cells in a 10 μL medium drop were seeded.

Cell attachment and viability

Cell attachment and viability was studied using Live/Dead staining. Briefly, ASC-biomaterial samples were incubated for 45 min at room temperature with a mixture of 5 μ*M* CellTracker™ green (5-chloromethylfluorescein diacetate [CMFDA]; Molecular Probes, Eugene, OR) and 2.5 μ*M* Ethidium Homodimer-1 (EH-1; Molecular Probes). The viable cells (green fluorescence) and dead cells (red fluorescence) were examined using a fluorescence microscope.

Cell proliferation

Relative proliferation of viable cells was assessed quantitatively using Premix WST-1 Cell Proliferation Assay (Takara Bio Inc, Japan) according to the manufacturer's protocol. The fluorescence was measured in a microplate reader (Victor 1420).

RESULTS

Electrochemical atomic force microscopy

Morphology of the samples

Figure 2 shows the AFM height- and phase images of PPyHA:CNT sample polymerized directly on gold microelectrode array (set A). The comparative sample shown in the Figure 3 has been polymerized otherwise similarly but with a 10 s potentiostatic activation step (+0.85 V *vs.* Ag pseudoreference) before 45 s of galvanostatic deposition. Clearly the polymerization parameters have a great effect on the kinetics and the final morphology of the product.

The AFM images show that the growth of the polypyrrole layer on Au is nucleated at several points at a time in the centerline of THE Au-electrodes. The growth continues along the centerline and the edges of the Au-electrode, leading eventually to growth between the adjacent electrode lines.

Tapping mode height and phase images of the smooth morphology of the hyaluronic acid doped polypyrrole grown on the PPyDBS adhesion layer is shown in the Figure 4. The polymer grows thicker near the edges of the electrode (5 μm line width). The surface appears rather smooth and uniform. The thickness of the polymer layer, evaluated from AFM line scans over the patterned electrode area, is approximately 450 nm.

Figure 5 shows the corresponding image for the sample containing carbon nanotubes. The polymer surface appears rough and irregular. The average thickness of the polymer is some 200 nm greater than for the reference PPyHA without CNTs. The overall appearance of is fibrillar.

In both cases the images show clearly how the polymer tends to grow laterally from the edges of the Au-electrodes. In the nanotube containing sample, the polymer grows laterally between the electrode lines, thus forming electrical shortcuts.

Activity of the samples without supporting layer (set A)

Bearing analysis of the Height data of the full images recorded and analysis of single line scans at give clear indication that both the morphology and the thickness of the polypyrrole film change upon electrochemical reduction at cathodic potential −0.8 Volts versus silver pseudoreference. The bearing analyses are presented in Figure 6. Statistically the polymer layer is on average 30–50 nm thicker in the reduced state indicating cation insertion due to the immobile anion. The thickness change is inhomogeneous, however, there are areas of apparently high electroactivity and much lower activity, which is not surprising noting the great roughness of the polymer layer. Analyses of individual line scans reveals up to 40 nm (>26%) thickness change at the extreme points.

Activity of the samples with PPyDBS supporting layer (set B)

Electrochemical AFM experiments for the sample set B were performed with Veeco multimode system.

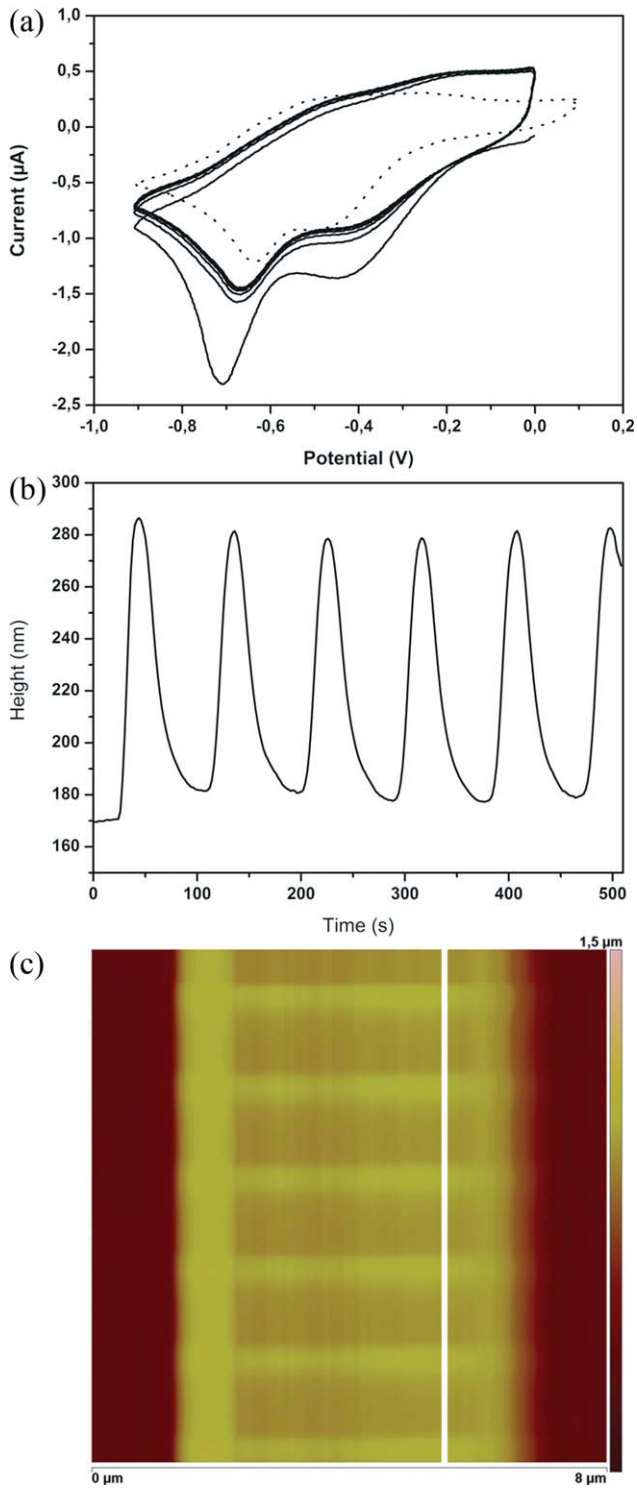

Figure 7. Electrochemical AFM of the PPyHA sample (EC875) containing a PPyDBS adhesion layer. (a) cyclic voltammetry, separately measured CV of the underlaying PPyDBS is shown by the dotted line and (b) height of a single scan line over six successive CV cycles (512 s), presented over six successive CV cycles. (c) height variation at the centreline (~100 nm). The R_a and R_z roughness values for oxidized and reduced states were $R_{a,oxidized}$ = 7 nm, $R_{z,oxidized}$ = 17 nm and $R_{a,reduced}$ = 9 nm, $R_{z,reduced}$ = 17 nm, respectively. [Color figure can be viewed in the online issue, which is available at www.interscience.wiley.com.]

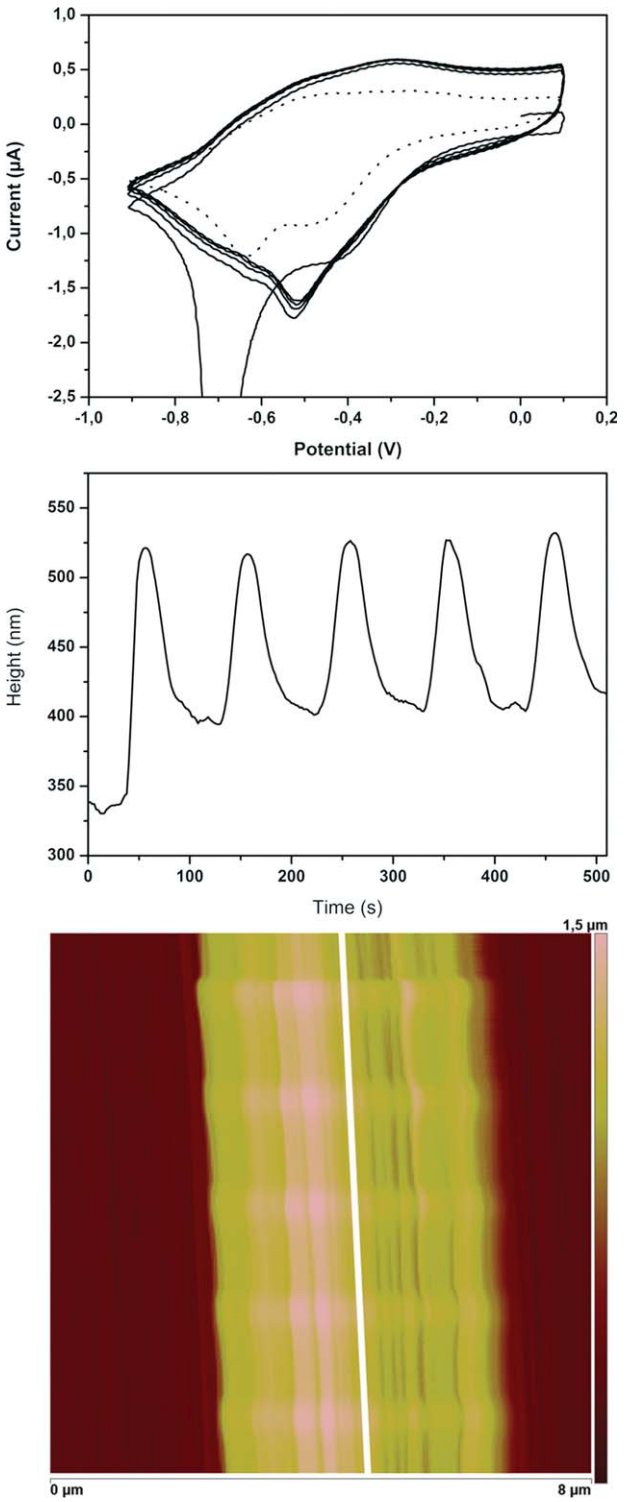

Figure 8. Electrochemical AFM data of the PPyHA-carbon nanotube sample (EC878) (a) cyclic voltammetry (separately measured CV of the underlaying PPyDBS is shown by the dotted line) (b) height of a single scan line over six successive CV cycles (512 s), presented over six successive CV cycles. (c) height variation at the centreline (~130 nm). The R_a and R_z roughness values for oxidized and reduced states were $R_{a,oxidized}$ = 80 nm, $R_{z,oxidized}$ = 214 nm and $R_{a,reduced}$ = 86 nm, $R_{z,reduced}$ = 186 nm, respectively. [Color figure can be viewed in the online issue, which is available at www.interscience.wiley.com.]

TABLE I
Summary of the Electrochemical AFM Data of Biopolymer Doped Samples with PPyDBS Underlay

Sample ID	Underlay	Biopolymer Doped Polypyrrole	Total Thickness (oxidized)	Thickness Change [%]
EC875	PPyDBS 100 μC	PPyHA 200 μC	450	22
EC878	PPyDBS 100 μC	PPyHA + MWCNT 200 μC	680 (variable)	19
EC924	PPyDBS 100 μC	–	300	27

Figure 7(a–c) presents the data from an electrochemical AFM experiment for hyaluronic acid doped polypyrrole polymerized (200 μC) on a PPyDBS adhesion layer (100 μC). This sample does not contain carbon nanotubes.

The *y*-axis in the AFM image Figure 7(b) represents the time axis during the measurement of the Height profile of a single line, perpendicular to the microelectrode array. Projection of the the data, presented in Figure 7(c) is the measured height difference (~100 nm) of one point on the scanned line 7b), presented over six successive CV cycles. The maximum height difference that is swelling is reversibly observed at the cathodic −800 mV potential. Note that the first of the six CV cycles is different and induces also the largest swelling. This phenomenon is repeated after the sample has relaxed at constant 0 mV for some minutes. The reduction charge for the sample EC875 is about 38 μC.

Figure 8(a–c) presents the corresponding electrochemical AFM data for the sample containing hyaluronic acid and multi-walled carbon nanotubes. The appearance of the sample surface is more irregular and rough (Fig. 5). The swelling occurs during reduction when the potential is less than −700 mV and is not homogeneous. At centerline [Fig. 8(c)], the swelling is about 130 nm (19%). The reduction charge for the sample EC875 is about 41 μC.

The electroactivity of the PPyDBS was studied from a layer polymerized under the same conditions (galvanostatic 10 μA, 100 μC) as the adhesion layers for the biopolymer doped samples. The reduction charge for the PPyDBS layer is about 30 μC. The CV recorded for the PPyDBS polymer is plotted to the Figures 7(a) and 8(a) with a dotted line. The maximum measured height difference for a 100 μC PPyDBS layer was 80 nm (27%). The data from EC-AFM the measurements is summarized in the following Table I.

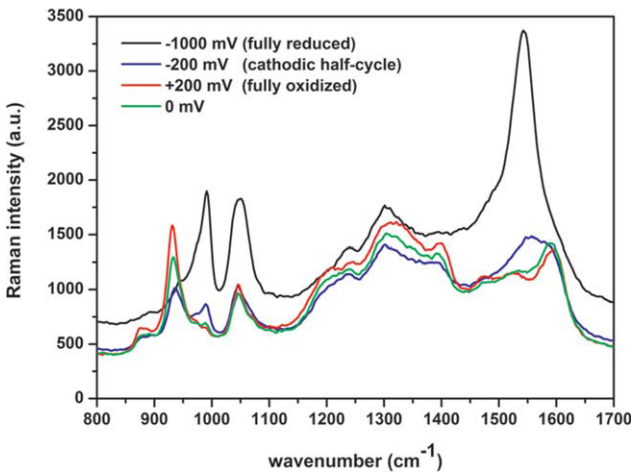

Figure 9. Raman spectra of PPyHA-CNT in different electrochemical potentials. The changes in the spectra are markers of electrochemical doping of polypyrrole conjugation. [Color figure can be viewed in the online issue, which is available at www.interscience.wiley.com.]

Raman spectroscopy under electrochemical control

Figure 9 presents the Raman spectra of electropolymerized PPyHA-CNT sample. The approximately 400-nm thick sample was polymerized on 1 cm^2 surface of a Au-coated AT-cut QCM crystal. The spectra in Figure 9 show that the relative intensities of the bipolaron- and polaron bands vary according to the potential of the sample. The bipolaron band and 930 cm^{-1} gradually strengthens in relation to the band at 990 cm^{-1} as the potential is raised from −1000 mV to about −200 V at the cathodic half-cycle. This is a marker of electrochemical doping of the polypyrrole backbone, which seems to be highest at the fully oxidized state at +200 mV. Another reversible change is observed during the cathodic half-cycle at −400 mV (not shown). These findings are direct evidence of true redox-activity of the biopolymer- and nanotube doped polypyrrole.

The overall intensity of the spectra depends slightly on the potential of the sample. This may be partly due to the dimensional changes of the polymer and the resulting slight change in the excitation laser focus point (i.e., depth of focus). This variation is in the order of 40 nm. Therefore, it is reasonable to assume that changes in the spectra are not due to compositional variation (e.g., polypyrrole/CNT ratio) in the thickness direction. The numerous polypyrrole bands are super-imposed into the CNT G- and D-bands, at 1600 and 1330 cm^{-1}, respectively. Weak absorption is observed near these particular wavenumbers only in the fully oxidized PPyHA-

TABLE II
Relevant Raman Bands for Polypyrrole and Multiwalled Carbon Nanotubes. The CNT and Polypyrrole Band are Super-imposed.*[28] and References Therein

Raman Band	Wavenumber cm^{-1} (observed)	Wavenumber cm^{-1} (Literature*)	Mode of Vibration	Note
MWCNT (super-imposed to PPy bands)	1595–1610	1600–1610	Tangential (G-band)	Characteristic to highly ordered graphene
	1330	1330	(D-band)	Disordered graphene
Polypyrrole				
Oxidized	1598	1557	Intercycle $\nu_{C=C}$	Mixed with the 1615 cm^{-1} ν_{C-C} mode
	1318	1316	ν_{C-C}	
	1245	1253	δ_{ring}	
	1047	1081	δ_{C-H} i.p.	
	932	925	δ_{C-H} o.p.	Characteristic to bipolaron species
Reduced	1545	1620	Intercycle ν_{C-C}	Mixed with the 1560 cm^{-1} $\nu_{C=C}$ mode
	1308	1310	ν_{C-C}	
	1242	1253	δ_{ring}	
	1047	1044	δ_{C-H} i.p.	
	990	990	δ_{ring}	Characteristic to neutral polypyrrole

CNT. The intensity of the numerous polypyrrole and the CNT band between 1500 and 1610 cm^{-1} increases and the "elbow" arising possibly from the MWCNT G-band seems to be shifted to lower wavenumbers upon reduction. It might indicate chemical interaction between the nanotubes and the polypyrrole chains or simply an increased intensity of the polypyrrole band at 1557 cm^{-1}, previously reported for $PPyClO_4$ by Santos et al.[28] The complex spectra and the presence of fluorescence makes it virtually meaningless to deconvolute the MWCNT bands from the composite spectrum. The relevant Raman bands are summarized in Table II.

Quartz crystal microbalance

The 20 mV/s cyclic voltammetry (CV) and frequency and resistance signals are presented in the Figure 10(a,b), respectively. The CV shows typical electrochemistry of polypyrroles. A wide reduction peak centered at −0.45 V and a oxidation wave at the cathodic half-cycle at −0.3 V can be observed. A $\Delta f \approx 60$ Hz shift in the resonant frequency (5 MHz) was observed.

Calculation of the corresponding mass change from the Sauerbray equation [Eq. (1)] yields 1.1 μg of mass deposited and released during each cycle. This mass change is attributed to migration of positively charged Na-cations, and their hydration shells as the highest mass is observed during reduction. The thickness of the sample, estimated from a more sophisticated viscoelastic QCM-model,[25] was ~210 nm. Making the crude assumption that the PPy density would remain roughly the same (e.g., 1.3 g/cm^3) during the oxidation and reduction, the 1 μg mass change implies a 4% thickness change for a con-

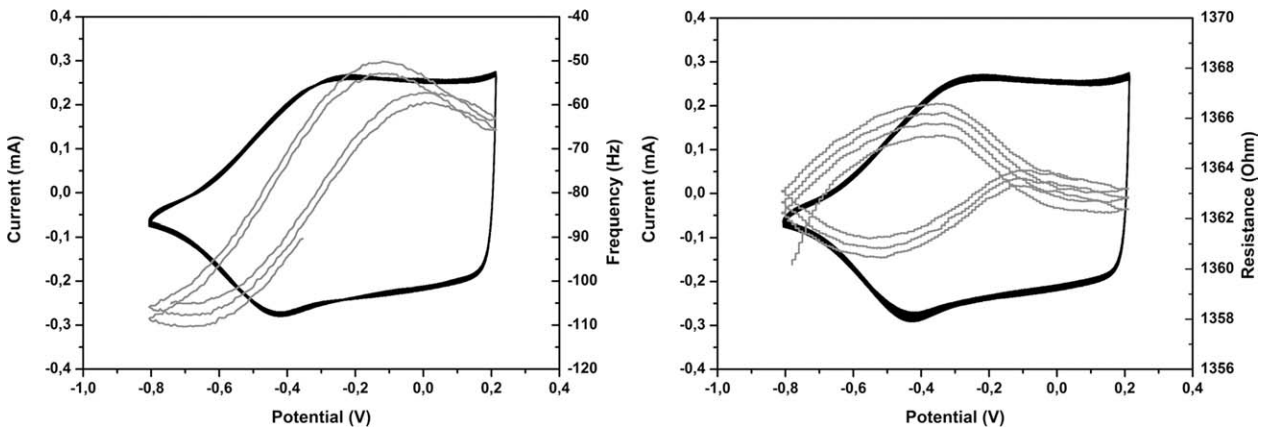

Figure 10. (a,b) Electrochemical quartz crystal microbalance data for PPyHA-CNT. The frequency signal indicates cation influx during the reduction and mixed anion/cation fluxes at higher potentials. The resistance signal indicates changes in the viscoelastic behavior of the material during the electrochemical cycle.

strained film. Hence, the approximate change in thickness predicted by QCM is almost an order of magnitude less than that measured by AFM for the same system.

The impedance to oscillation of the quartz crystal (reported as resistance R) is observed to change by only 4 Ω indicating that the viscoelastic properties of the polymer remain essentially unchanged during the cycling. Using the more sophisticated viscoelastic model recently presented[25] the shear modulus of the film was estimated to be in the order of 100 kPa. This computational result suggest that the material is very soft, possibly due to the use of the polyelectrolyte dopant. A shear modulus of 100 kPa falled within the expected range, as it was larger than that of a hydrogel but less than that of highly organized conducting polymers, that are formed at low temperatures, and often used for actuators. It should be noted that the calculated values for Δh_f and $\Delta G'$ depend on certain precalculation assumptions, for instance the loss modulus G'' is set zero by default. Therefore, the calculations are still to be treated as more indicative than the absolute values.

Cell attachment and viability

Majority of the cells seeded on PLA/PPyHA-CNT composites were attached on the polypyrrole coated part of titanium electrodes or the exposed part of the titanium connectors at day 1. The cell number was increased at day 8 compared with day 1 on PLA and PLA/polypyrrole composites.

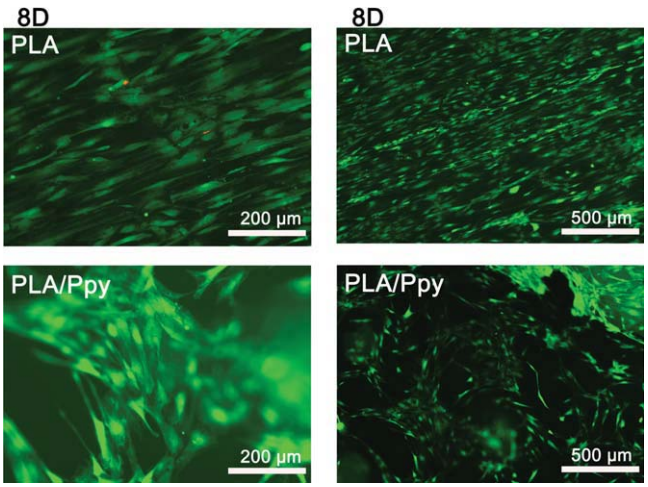

Figure 11. Representative images of viable (green fluorescence) and dead (red fluorescence) ASCs attached to surface of the samples. REF: polylactide-polypyrrole composite electrode. Scale (a) 200 µm and (b) 500 µm. [Color figure can be viewed in the online issue, which is available at www.interscience.wiley.com.]

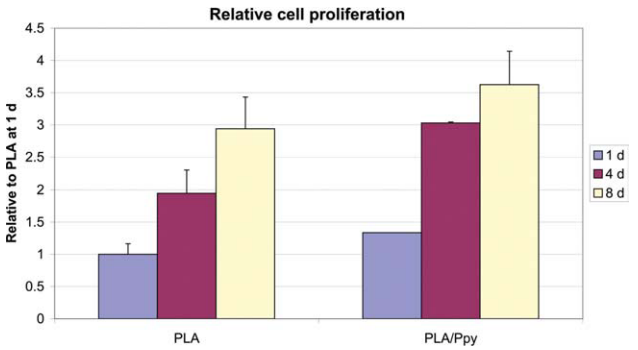

Figure 12. Relative proliferation of ASCs cultured for 1, 4, and 8 days on polylactide and polylactide-polypyrrole composite electrodes, measured with WST-1 proliferation assay. Results are expressed as mean +SD. The polypyrrole surface seemed a favorable surface for ASC viability and proliferation. [Color figure can be viewed in the online issue, which is available at www.interscience.wiley.com.]

Representative images (Fig. 11) of viable (green fluorescence) and dead (red fluorescence) ASCs attached to surface of the reference PLA and the polypyrrole sample at two magnifications (∼ ×40 and ×100). At day 8 no differences between the PLA/PPyHA-CNT composites and PLA samples were detected on the cell number or the viability of the cells (Fig. 12). Majority of the cells were viable on each sample material at 8 days.

Cell proliferation

At 1-day time point there were no differences between the sample materials (Fig. 12). At 4 and 8 days, the relative proliferation of the viable cells was higher in ASCs cultured on PLA/PPy composites compared with PLA samples. The relative cell proliferation increased in time in all sample materials. The polypyrrole coating on the titanium electrodes seemed a favorable surface for ASCs to attach and proliferate.

CONCLUSIONS

Polypyrrole hyaluronic acid electropolymerized in the presence of carbon nanotubes are electroactive in physiological electrolyte that is well recognizable redox behavior, associated polaron doping detected by *in situ* Raman spectroscopy and cation exchange.

The swelling of the polypyrrole material was attributable mainly to cation migration, in this case sodium ion transport upon the electrochemical reduction at −0.45 V versus Ag/AgCl. Quartz crystal

microbalance (4%) and fluid AFM (19–27%) studies showed that the total swelling capacity the the PPyHA-CNT material on gold electrodes is strongly affected by the adhesion of the polymer to the substrate. The material is very soft with a shear modulus G' of about 100 kPa, calculated from the QCM data. The adhesion and electroactivity of the polymer layer can be enhanced by polymerizing a more hydrophilic and strongly electroactive PPyDBS underlay. Fluid AFM imaging shows that the nanotubes render the surface of the PPyHA polymer very rough.

Biocompatibility study of the PPyHA-CNT on titanium with ASCs showed equal or better cell attachment, viability, and proliferation compared with the reference PLA. The hydrophilic nature of the polymer along the surface roughness probably contribute to the excellent biocompatibility results. The findings suggest that the polymer has potential as a cell culturing surface. Since the material is electroactive, it can be utilized in electrical and mechanical stimulation of cell for example in 3D tissue engineering scaffolds or AC microstimulation electrodes.

I would like to thank Ms. Anna-Maija Honkala for excellent technical assistance. This research was supported by the Finnish Funding Agency for Technology and Innovation (TEKES), the competitive research funding of the Pirkanmaa Hospital District.

References

1. Bay L, Jacobsen T, Skaarup S, West K. Mechanism of actuation in conducting polymers: Osmotic expansion. J Phys Chem B 2001;105:8492–8497.
2. Roth S, Bleier H, Pukacki W. Charge transport in conducting polymers. Faraday Discuss Chem Soc 1989;88:233.
3. Pei Q, Inganäs O. Electrochemical applications of the bending beam method. I. Mass transport and volume changes in polypyrrole during redox. J Phys Chem B 1992;96:10507–10514.
4. Smela E, Gadegaard N. Volume change in polypyrrole studied by atomic force microscopy. J Phys Chem B 2001; 105:9395–9405.
5. Jager EWH, Smela E, Inganäs O, Lundström I. Polypyrrole micro actuators. Synth Met 1999;102:1309–1310.
6. Otero TF, Grande H, Rodríguez J. Conformational relaxation during polypyrrole oxidation: From experiment to theory. Electrochim Acta 1996;41:1863–1869.
7. Milella E, Brescia E, Massaro C, Ramires PA, Miglietta MR, Fiori V, Aversa P. Physico-chemical properties and degradability of non-woven hyaluronan benzylic esters as tissue engineering scaffolds. Biomaterials 2002;23:1053–1063.
8. Agren U, Tolg C, Paiwand F, Paiwand SA, Turkeley SA, Harrison R. New Frontiers In Medical Sciences: Redefining Hyaluronan, Amsterdam: Elsevier Science; 2000. p 63.
9. West DC, Hampson IN, Arnold F, Kumar S. Angiogenesis induced by degradation products of hyaluronic acid. Science 1985;228:1324–1326.
10. Peattie RA, Rieke ER, Hewett EM, Fisher RJ, Shu XZ, Prestwich GD. Dual growth factor-induced angiogenesis in vivo using hyaluronan hydrogel implants. Biomaterials 2006;27: 1868–1875.
11. Collier JH, Camp JP, Hudson TW, Schmidt CE. Synthesis and characterization of polypyrrole-hyaluronic acid composite biomaterials for tissue engineering applications. J Biomed Mater Res 2000;50:574–584.
12. Garner B, Georgevich A, Hodgson AJ, Liu L, Wallace GG. Polypyrrole–heparin composites as stimulus-responsive substrates for endothelial cell growth. J Biomed Mater Res 1999; 44:121–129.
13. Schmidt CE, Shastri VR, Vacanti JP, Langer R. Stimulation of neurite outgrowth using an electrically conducting polymer. Proc Natl Acad Sci USA 1997;94:8948–8953.
14. Ateh DD, Vadgama P, Navsaria HA. Culture of human keratinocytes on polypyrrole-based conducting polymers. Tissue Eng 2006;12:645–655.
15. Serra Moreno J, Panero S, Artico M, Filippini P. Synthesis and characterization of new electroactive polypyrrole–chondroitinsulphate A substrates. Bioelectrochemistry 2008;72: 3–9.
16. Castano H, O'rear EA, Mcfetridge PS, Sikavitsas VI. Polypyrrole thin films formed by admicellar polymerization support the osteogenic differentiation of mesenchymal stem cells. Macromol Biosci 2004;4:785–794.
17. Fonner JM, Forciniti L, Nguyen H, Byrne JD, Kou Y, Syeda-Nvaz J, Schmidt CE. Biocompatibility implications of polypyrrole synthesis technigues. Biomed Mater 2008;3:1–12.
18. Jia G, Wang H, Yan L, Wang X, Pei R, Yan T, Zhao Y, Guo X. Cytotoxicity of carbon nanomaterials: Single-wall nanotube, multi-wall nanotube, and fullerene. Environ Sci Technol 2005;39:1378–1383.
19. Pulskamp K, Diabaté S, Krug HF. Carbon nanotubes show no sign of acute toxicity but induce intracellular reactive oxygen species in dependence on contaminants. Toxicol Lett 2007; 168:58–74.
20. Fenoglio I, Tomatis M, Dominique L, Muller J, Fonseca A, Nagy JB, Fubini Bice. Reactivity of carbon nanotubes: Free radical generation or scavenging activity. Free Radical Biol Med 2006;40:1227–1233.
21. Harrison BS, Atala A. Carbon nanotube applications for tissue engineering. Biomaterials 2007;28:344–353.
22. Kada G, Kienberger F, Hinterdorfer P. Atomic force microscopy in bionanotechnology. Nanotoday 2008;3:12–19.
23. Sauerbrey G. Verwendung von schwingquarzen zur wägung dünner schichten und zur mikrowägung. Ztg Phys 1959; 155:206–222.
24. Bandey HL, Martin SJ, Cernosek RW, Hillman AR. Modeling the responses of thickness-shear mode resonators under various loading conditions. Anal Chem 1999;71:2205–2214.
25. Bahrami-Samani M, Whitten PG, Cook CD, Spinks GM. Quatrz crystal microbalance study of volume changes and modulus shift in electrochemically switched polypyrrole. Thin Solid Films 2008;516:2800–2807.
26. Suarez MF, Compton RG. In situ s force microscopy study of polypyrrole synthesis and the volume changes induced by oxidation and reduction of the polymer. J Electroanal Chem 1998;462:211–221.
27. Pyo M, Kwak CH. In situ scanning tunneling microscopy study on volume change of polypyrrole/poly(styrene sulfonate). Synth Met 2005;150:133–137.
28. Santos MJL, Brolo AG, Girotto EM. Study of polaron and bipolaron states in polypyrrole by *in situ* Raman spectroelectrochemistry. Electrochim Acta 2007;52:6141–6145.

Publication 2

Pelto, J., Björninen, M., Pälli, A., Talvitie, E., Hyttinen, J., Mannerström, B., Suuronen Seppänen, R., Kellomäki, M., Miettinen, S., Haimi, S.

Novel polypyrrole-coated polylactide scaffolds enhance adipose stem cell proliferation and early osteogenic differentiation.

Tissue Engineering - Part A. Vol. 19 (2013) No: 7 - 8, 882 – 892.

TISSUE ENGINEERING: Part A
Volume 19, Numbers 7 and 8, 2013

DOI: 10.1089/ten.tea.2012.0111

Original Article

Novel Polypyrrole-Coated Polylactide Scaffolds Enhance Adipose Stem Cell Proliferation and Early Osteogenic Differentiation

Jani Pelto, MSc,[1] Miina Björninen, MSc,[2–4] Aliisa Pälli, MSc,[2–4] Elina Talvitie, MSc,[4,5] Jari Hyttinen, PhD,[4,5] Bettina Mannerström, PhD,[2–4] Riitta Suuronen Seppanen, MD, DDS,[2,4–6] Minna Kellomäki, PhD,[4,5] Susanna Miettinen, PhD,[2–4] Suvi Haimi, PhD[2–4,7]

An electrically conductive polypyrrole (PPy) doped with a bioactive agent is an emerging functional biomaterial for tissue engineering. We therefore used chondroitin sulfate (CS)-doped PPy coating to modify initially electrically insulating polylactide resulting in novel osteogenic scaffolds. *In situ* chemical oxidative polymerization was used to obtain electrically conductive PPy coating on poly-96L/4D-lactide (PLA) nonwoven scaffolds. The coated scaffolds were characterized and their electrical conductivity was evaluated in hydrolysis. The ability of the coated and conductive scaffolds to enhance proliferation and osteogenic differentiation of human adipose stem cells (hASCs) under electrical stimulation (ES) in three-dimensional (3D) geometry was compared to the noncoated PLA scaffolds. Electrical conductivity of PPy-coated PLA scaffolds (PLA-PPy) was evident at the beginning of hydrolysis, but decreased during the first week of incubation due to de-doping. PLA-PPy scaffolds enhanced hASC proliferation significantly compared to the plain PLA scaffolds at 7 and 14 days. Furthermore, the alkaline phosphatase (ALP) activity of the hASCs was generally higher in PLA-PPy seeded scaffolds, but due to patient variation, no statistical significance could be determined. ES did not have a significant effect on hASCs. This study highlights the potential of novel PPy-coated PLA scaffolds in bone tissue engineering.

Introduction

Polylactide-based polymers have been extensively used in various applications for over two decades. However, lack of bioactivity has limited their use especially in tissue engineering applications.[1,2] To overcome this problem, several approaches have been developed, such as integrating growth factors, or other bioactive agents into the polymer structure.[3,4] Another potential strategy to functionalize polylactide scaffolds could be the application of conductive polymers as a functional surface coating. Among these conductive polymers, polypyrrole (PPy) has emerged as a promising polymer group for tissue engineering due to its high biocompatibility and its good electroconductive properties.[5]

The surface roughness, hydrophilicity, and elasticity of PPys can be tailored by the choice of the dopants or surfactants used in their synthesis.[6,7] One of the most studied biopolymer dopants is chondroitin sulfate (CS), a naturally occurring ubiquitous glycosaminoglycan.[8,9] CS is found not only in the ECM, but was also discovered on the cell surfaces of most mammalian cells and reported to be involved in osteogenic processes, including development, maturation, remodeling, and repair.[10,11] CS has previously been shown to enhance bone remodeling when applied together with hydroxyapatite/collagen bone cement.[9] Due to the osteogenic potential of CS, we hypothesized that by using CS-doped PPy coating, we could stimulate the osteogenic differentiation of human adipose stem cells (hASCs), a potential mesenchymal stem cell (MSC) group in the field of skeletal tissue engineering.

In an earlier study, we already verified the good biocompatibility of PPy using hASCs.[7] The effect of PPy surfaces with or without electrical stimulation (ES) has been studied with various cell types, such as skeletal muscle cells, neurites, endothelial cells, fibroblasts, osteoblasts, and

[1]VTT Technical Research Centre of Finland, Tampere, Finland.
[2]Adult Stem Cells, Institute of Biomedical Technology, University of Tampere, Tampere, Finland.
[3]Science Centre, Pirkanmaa Hospital District, Tampere, Finland.
[4]BioMediTech, Tampere, Finland.
[5]Department of Biomedical Engineering, Tampere University of Technology, Tampere, Finland.
[6]Department of Eye, Ear, and Oral Diseases, Tampere University Hospital, Tampere, Finland.
[7]Department of Biomaterials Science and Technology, University of Twente, Enschede, Netherlands.

MSCs.[12–17] However, so far, the effects of PPy on osteogenic differentiation of human ASCs have not, to the best of our knowledge, been reported either with or without ES.

ES has been applied to a number of cell types to enhance proliferation and to direct cell differentiation, but mainly to electrically active cells, such as neurons or cardiomyoblasts.[18] Interestingly, a few recent publications have focused on the stimulation of electrically inactive MSCs, demonstrating that ES has a significant impact on ASC proliferation and differentiation.[19–21] ES has also been successfully applied via PPy for different cell types resulting in increased cell proliferation and significant changes in other cell functions.[22–24] This article is the first to report the effects of novel conductive poly-96L/4D-lactide/PPy (PLA-PPy) scaffolds and their combined effects with the ES on hASC viability, proliferation, and early osteogenic differentiation studied in a three-dimensional (3D) culture system.

Materials and Methods

Materials

Medical grade PLA with an inherent viscosity of 2.1 dL g-1 (PURAC biochembv) was used in melt spinning and scaffold manufacturing. Pyrrole monomer, ammonium peroxydisulfate oxidant (APS), and chondroitin 6-sulfate sodium salt from bovine trachea were purchased from Sigma-Aldrich. Pyrrole was distilled in a vacuum before use. Other reagents were used without any further purification. Distilled water was used in the polymerizations.

Synthesis of 3D scaffolds

Polylactide fibers and nonwoven scaffolds. PLA was extruded (GimacMicroextruder TR 12/24 B.V.O.; Gimac) and hot-drawn to 16ply multifilament fiber. The diameters of the single filaments were 10–20 μm. To manufacture the nonwoven scaffolds, the fibers were cut and carded using a manually operated drum carder (Elite Drum Carder; Louët BV). Several cards were then combined by needle punching using a James Hunter Needle Punching Machine (James Hunter Machine Co.) to obtain $10 \times 10 \times 2$ mm size scaffolds.

Chemical oxidative polymerization of PPy. The polymerization parameters were optimized to ensure optimal conductivity and uniformity of the coating; the pyrrole concentration varied between 0.03–0.3 M, the CS concentration between 0.5–2 mg/mL, the oxidant concentration between 0.01–0.1M, and the polymerization time from 30 s to 15 min in an ambient temperature. The following optimized concentrations were used for all the *in vitro* samples: [pyrrole] = 0.036 M, [APS] = 0.1 M, and [CS] = 1 mg/mL, polymerization time 150 s.

Before polymerization, CS and APS were dissolved separately in distilled water. CS and APS solutions were combined and pyrrole added immediately with vigorous stirring. The sample was placed in the polymerization bath. The nonwoven scaffolds were pretreated in ethanol before polymerization. After polymerization, the samples were rinsed thoroughly with water and dried in air. Samples were sterilized by gamma irradiation (BBF Sterilizations service GmbH) with an irradiation dose of >25 kGy.

Characterization

Hydrolysis and conductivity measurements. Gamma irradiated scaffolds were incubated in sealed plastic specimen chambers containing either a phosphate buffer solution PBS (Sörensen, pH 7.4 ± 0.2; Na_2HPO_4 0.0546 mol l-1, KH_2PO_4 0.121 mol l-1) or a maintenance medium consisting of the Dulbecco's modified Eagle's medium/Ham's Nutrient Mixture F-12 (DMEM/F-12 1:1 1 ×; Invitrogen), 10% human serum type AB (HS; PAA Laboratories GmbH), 1% L-glutamine (GlutaMAX I; Invitrogen), and 1% pen-strep (100 U/mL penicillin, 0.1 mg/mL streptomycin; Lonza) at +37°C for up to 42 days. Test conditions were set as specified in ISO-15814:1999(E) standard. The pH of the buffer solution was measured and changed every 3 days twice a week to exclude the acidic autocatalytic hydrolysis of PLA.

Directly after the synthesis and during the hydrolysis test, the direct current (DC) conductivity of air-dry scaffolds was measured using custom-made copper flat alligator clips (contact area 6 mm^2) and Fluke 189 multimeter. Non-sterilized samples were used for conductivity measurement since the electrical properties of PPy have been reported to be stable[25] with the irradiation dose used.

Electrospray ionization mass spectroscopy. Gamma-sterilized, noncoated PLA and PPy-coated samples of 10 mg were hydrolyzed for 30 days at +60°C in 1.0 mL pure water. The hydrolyzed samples were analyzed with a single quadruple Perkin Elmer SQ 300 electrospray mass spectrometry (MS) system (PerkinElmer) in the positive ion mode. The drying gas (nitrogen) temperature was set at +175°C and the drying gas flow rate at 8 L/min. The capillary exit voltage was varied between 60 and 200 V to screen the onset of cracking of the PLA oligomers. The MS was operated in a scan mode (mass range 200–1000) and dwell time was set at 0.1 ms. Briefly, the (hydrolysis) solution was filtered through 0.45-μm PTFE filter, 0.5 mL methanol was added to the mixture (water/MeOH 2:1 v/v) and the sample injected by a syringe pump into the mass spectrometer at a flow rate of 5 μL/min.

Scanning electron microscopy. Noncoated PLA and PPy-coated PLA scaffolds were imaged by JSM–6360 LV SEM (JEOL). Low 3 kV acceleration voltage was applied to prevent sample damage and to induce contrast between electrically conductive and insulating areas. For the non-coated scaffold, the imaging was first done without metallic surface coating and, subsequently, a thin 20-nm sputter-coated gold layer (SCD 050; Balzers AG).

Atomic force microscopy. The morphology of individual PLA-PPy fibers in air was imaged by noncontact mode atomic force microscopy (Park XE-100 AFM; Park Systems). Silicon probes (ACTA-905M, Applied NanoStructures, Inc.) with a nominal resonance frequency of 300 kHz and spring constant of 4 N/m were applied with a pyramidal shaped tip (radius < 10 nm) and an aluminum reflective coating. 5×5 μm^2 scans were taken with a scan rate of 0.5 Hz. The surface roughness of the hydrolyzed sample was determined from the data by Park Systems XEI image processing software (Park Systems). For the roughness data, the analyzed area size was varied to test the consistency of

the result. Roughness analysis was done on the raw data. For the presentation of the surface topography of the curved surfaces, the raw data was 0th order flattened along the fiber axes, which were parallel to the slow axis of the AFM.

Electrical stimulation

Stimulation setup. The scaffolds were placed in custom-made bottomless 24-well plates (Greiner Bio-One GmbH). The two electrodes were in galvanic contact with the cell culture medium in each well (Fig. 1A). The top and the bottom electrodes were sputter-coated polyethylene-naphthalate (PEN)/Au films (125 μm DupontTeonex®, with 50 nm Au-coating applied by VTT). The bottom electrode (PEN/Au film) was attached to the well plate with biomedical grade Silastic® Q7-4720 liquid silicone rubber. The top electrodes were bent strips of PEN/Au-film, partly extending to the cell culture medium (Fig. 1A). The four strips were connected in parallel (Fig. 1B). Hence, the individual wells were also electronically connected in parallel. The electrode surface area was approximately 1 cm^2 for the top electrode and approximately 1.5 cm^2 for the bottom electrode in each well. The distance between the top and the bottom electrodes was approximately 2 mm, matching the thickness of the scaffolds under mild (< 10 kPa) compression. Hence, the fibers of the scaffolds were in physical contact with both the top and bottom electrodes.

Human ASCs were exposed to symmetric biphasic pulsed DC voltage repeated at a frequency of 1 or 100 Hz, ES for 4 h/day. Stimulation waveforms were generated by AFG 3010B (Tektronix Inc.) and the stimulation signal supplied by a laboratory voltage amplifier (VTT). The waveforms for the 1 and 100 Hz stimulation were pulsed DC voltages 250 ms (+200 mV)/250 ms (−200 mV)/500 ms (0 mV) and 2.5 ms (+200 mV)/2.5 ms (−200 mV)/5 ms (0 mV), respectively. A schematic illustration of the voltage is presented in Figure 1C. According to cyclic voltammetry (CV), the PEN/Au-electrodes were electrochemically stable in the ±200 mV potential window (CV data not shown). The transient current generated by the pulsed DC signal was monitored for the 24-well plate assembly with Tektronix TDS 3054B oscilloscope and 100 Ω series resistor. The measured peak current into the 24-well plate assembly in series with the 100 Ω was 2 mA. The measured steady state (DC) current after the 2.5 ms and the 250 ms pulses was in the range of 40–50 μA/cm^2, corresponding to cell impedance of 5 kΩ. Such a low current level could be only roughly measured with the 100 Ω resistor and the oscilloscope. Therefore, the range of the current densities was also based on the impedance spectroscopic data recorded earlier in the DMEM.

The electrical charge of one pulse containing both the transient electrical double layer charging of the Au-electrodes (Q1, Q2 in Fig.1C) and the contribution of the ionic DC current (dashed line in Fig.1C) of the 1 and 100 Hz waveforms were estimated 28.0 and 8.2 μC, respectively. The charging conditions for the top and the bottom electrodes were not balanced electronically and the open circuit voltage of the system was not measured. A nonstimulated group was used as a control.

Impedance of the electrode, cell culture medium, and the nonwoven scaffolds. Impedance spectra of circular parallel 1 cm^2 PEN/Au-film electrodes and parallel rigid TiN-coated steel electrodes (electrode material TiN) in the DMEM were measured using an HP 4192A impedance analyzer. In the measurement a 100 Ω series resistor and excitation voltage of sinusoidal 50 mV_{p-p} was used.

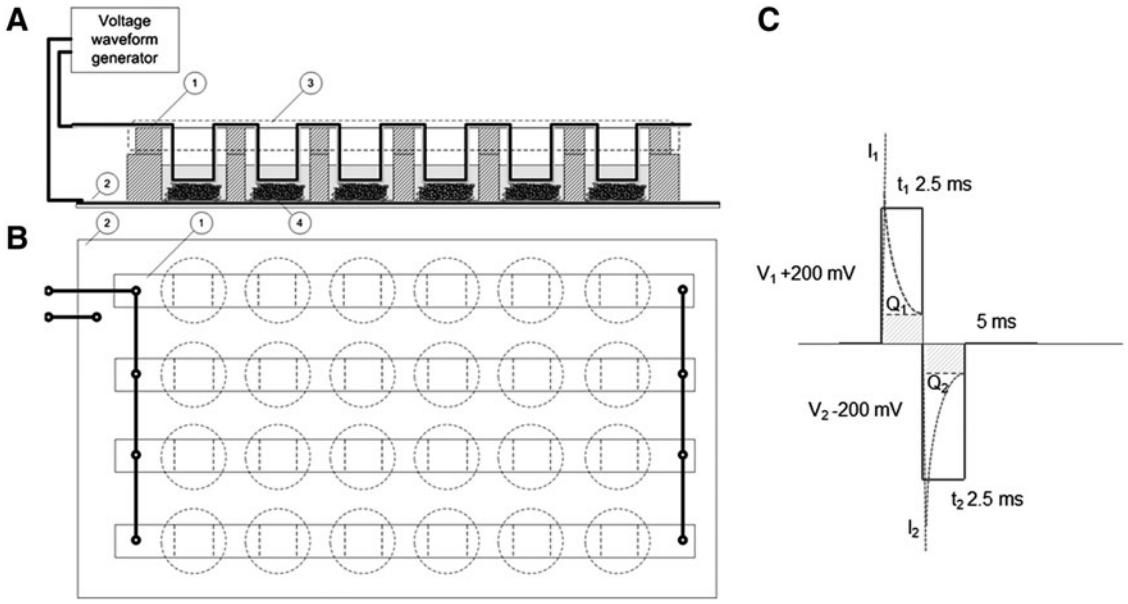

FIG. 1. **(A)** Schematic illustration of the stimulation device geometry as the side projection. Top and bottom electrodes were made of gold-coated polyethylene-naphthalate film. **(B)** The voltage waveform applied to the samples. Biphasic pulses are shown in blue color. The dashed line presents an estimation of the transient net current. Q_1 and Q_2 present both the transient electrical double layer charging of the Au-electrodes. **(C)** Schematic illustration of the stimulation device geometry as the above projection.

Subsequently, the impedance of the insulating PLA scaffold and the electrically conductive PLA-PPy scaffold was measured between the rigid TiN electrodes (OerlikonBalzersSandvik Coating). TiN electrodes were utilized as they provided an electrochemically stable, smooth, and mechanically rigid construction for the measurement cell. Constant phase element analysis (CPE) was done using the curve fitting tool provided in OriginPro 8.5.1 software (Originlab Corporation) using protocols described by Tandon et al.[26]

hASC culture

The experiments were repeated three times, each with a different human hASC line. The cells were isolated from the adipose tissue collected in surgical procedures from three females (aged 39, 43, and 79) at the Department of Plastic Surgery, Tampere University Hospital. Human ASC isolation from the tissue samples was conducted in accordance with the Ethics Committee of Pirkanmaa Hospital District, Tampere, Finland. The minced tissue samples were digested with collagenase type I (1.5 mg/mL; Invitrogen) and cell isolation was performed as previously described.[27] After primary culture in T-75 flasks, hASCs of passage 1 were harvested and analyzed by flow cytometry (FACSAria; BD Biosciences). Monoclonal antibodies against CD14-PE-Cy7, CD19-PE-Cy7, CD45RO-APC, CD49D-PE, CD73-PE, CD90-APC, CD106-PE-Cy5 (BD Biosciences Pharmingen); CD34-APC, HLA-ABC-PE, HLA-DR-PE (Immunotools GmbH Friesoythe); and CD105-PE (R&D Systems, Inc.) were used. Analysis was performed on 10,000 cells per sample, and the positive expression was defined as a level of fluorescence 99% greater than the corresponding unstained cell sample.

Cell expansion and experiments were carried out in the maintenance medium. When the ASCs reached 80% confluence, the cells were passaged. Cells of passages 4 to 5 were used for all experiments. Each scaffold was pretreated with the maintenance medium for 48 h at 37°C in custom-made 24-well plates. The scaffolds were seeded with 87,500 cells in a volume of 30 μL of the maintenance medium and the cells were allowed to attach for 3 h.

Viability. Cell attachment and viability were evaluated qualitatively using live/dead viability assay (Molecular Probes) at 7- and 14-day time points. CellTracker™ Green [5-chloromethylfluorescein diacetate (CMFDA; Molecular Probes) and ethidium homodimer-1 (EthD-1; Molecular Probes) were utilized to dye viable cells (green fluorescence) and dead cells (red fluorescence), respectively, as previously described.[7]

Proliferation and differentiation. The DNA content in the hASC-seeded scaffold constructs was measured after 1, 7, and 14 days' culture using the CyQUANT® Cell proliferation assay kit (Molecular Probes–Invitrogen) according to the manufacturer's protocol and as earlier described.[27] To uniformly extract the DNA, cells were lysed in the scaffold using 0.1% Triton X-100 followed by a freeze–thaw cycle, and then the scaffold was disrupted and the cell lysate carefully collected from the scaffolds for the analysis. The fluorescence was measured with Victor 1420 Multilabel Counter; Wallac). The quantitative alkaline phosphatase (ALP) measurement was performed at time points of 7 and 14 days according to the Sigma ALP procedure (Sigma Aldrich)[27] with minor modifications. Quantitative ALP activity results were normalized to the total amount of DNA measured from the same samples.

Statistical analysis. The statistical analyses were performed with SPSS, version 17. All assays were performed in triplicate and the data were presented as mean ± standard deviation (SD) for both quantitative analyses. The equal variance assumption was checked by the Levene's Test. All statistical analyses were performed at a significance level $p < 0.05$ using one-way analysis of variance (ANOVA) or the T-test. Bonferroni *post hoc* correction for multiple corrections was used. The effects of different culturing periods (1 day vs. 7 days vs. 14 days), scaffold materials (PLA vs. PLA-PPy), and stimulation setup (ES 1 Hz vs. ES 100 Hz vs. control) were evaluated from the combined data of the three experiments.

Results

Effect of hydrolysis on DC electrical conductivity

Incubation of the PPy-coated PLA fiber scaffolds in PBS (pH 7.4) resulted in a significant decrease in DC conductivity during the first day (Fig. 2). Directly after the synthesis the in-plane resistance of the air-dried samples was 50 ± 20 kΩ. Rinsing with deionized water increased the resistance to 90 ± 40 kΩ on day 0. At day 1, the measured resistance was 2.5 ± 0.8 MΩ and steadily increased to 29 ± 14 MΩ on day 7. According to optical microscopy, the surface of the fiber was still fully covered with the PPy coating on day 20. The DC conductivity of the hydrolyzed scaffolds could be partly restored by rinsing with a diluted hydrochloric acid (pH 2) solution and subsequent air drying. Roughly, 5%–10% of the conductivity of the hydrolyzed scaffold was restored by the acid rinse irrespective of the hydrolysis time.

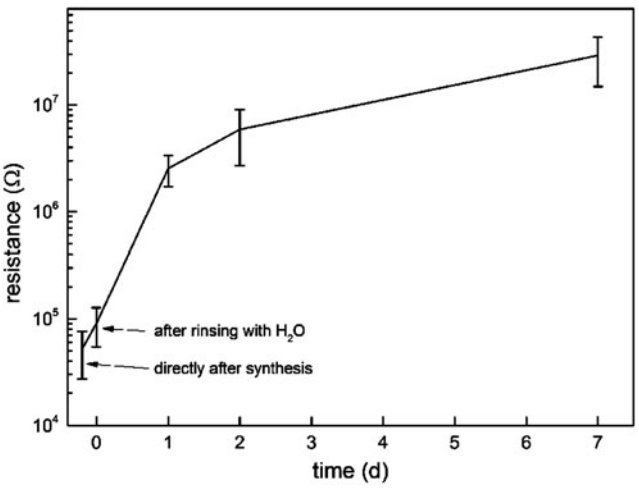

FIG. 2. Resistance of the poly-96L/4D-lactide-polypyrrole (PLA-PPy) scaffold in air ($n = 4$). The samples were rinsed with deionized and air-dried before each measurement. The conductivity of the sample remains at a level relevant for electrical stimulation for at least 2 days.

Table 1. Summary of Impedance Spectroscopic Data Measured in Dulbecco's Modified Eagle's Medium and the Corresponding Constant Phase Element Analyses

Sample	$\|Z\|_{cell}$ *at 1 Hz (Ω)*	$\|Z\|_{cell}$ *at 10 kHz (Ω)*	*CPE capacitance (μF)*	*idealitycoeff. η*
PEN/Au/film	240000	15	2	0.97
TiN	83000	17	20	0.94
TiN/PLA scaffold	13000	26	20	0.90
TiN/PLA-PPy scaffold	1700	12	14	0.83

HP 4192A impedance analyzer, excitation voltage is sinusoidal 50 mVp-p
CPE, constant phase element; PEN, polyethylene-naphthalate; PLA-PPy, poly-96L/4D-lactide-polypyrrole.

Impedance of the electrode, cell culture medium, and the nonwoven scaffolds

The results of the impedance measurement are summarized in the following Table 1.$|Z|_{cell}$ is the magnitude of cell impedance, CPE represents the capacitance of the cell, and η is a fit parameter describing the ideality of capacitance in the CPE model.[26]

According to the measured data, the PLA and the PLA-PPy scaffolds both had a significant effect on cell impedance in the DMEM. The low-frequency impedances specially were significantly lower for the cell containing the scaffolds in the DMEM (either PLA or PLA-PPy) than for the empty cell containing only the medium. As anticipated, the PLA-PPy scaffold induced the most significant decrease in cell impedance at lower frequencies. The ideality coefficient η was low (0.83) for the PLA-PPy scaffold, suggesting that the capacitive CPE model did not describe the cell impedance spectrum in this case. Contrary to expectations, the PLA scaffold also decreased the cell impedance. This was surprising since the relative permittivity of the medium (around 80) is much higher compared with the dry PLA polymer (around 3.5). The result can be explained by a marked enhancement of (low-frequency) ionic conductivity along the PLA fibers. The low-frequency impedance was three-fold higher, and the capacitance was 10-fold lower for the Au-electrodes than for the TiN electrodes.

We used impedances derived from sinusoidal test signals (2.4.2) for estimating the order of magnitude for the stimulation current during the biphasic pulses. The Ohm's law and the impedances measured at 1 Hz and 10 kHz were used for estimating the current densities in the Au-electroded stimulation 24-well setup. Theoretical current densities $I_{1,2,DC} \pm 13.3\,\mu A/cm^2$ $I_{1,2,max} \pm 16.7\,mA/cm^2$ for the DC current and the transient current were calculated, respectively. The real transient current density, which is not directly measurable using our system, was limited by the current amplifier to roughly $\pm 0.4\,mA/cm^2$. The discrepancy between the observed and the calculated values was likely due to the discrepancies between the impedance measurement and the ES setup. However, both the measured and the estimated DC and transient currents were within a physiologically relevant range, but could be considered minimally invasive for the hASCs.[28]

Electrospray ionization mass spectroscopy

The electrospray ionization-MS (ESI-MS) spectra for the PLA-PPy and PLA scaffolds were very similar (Fig. 3). The spectra contained peaks of PLA hydrolysis products[29] and the corresponding Na peaks. No significant peaks associated with potential PPy or CS degradation products, such as oxidized pyrrole oligomers or oligosaccharides, were found in the studied m/z range of 200–1000.

Scanning electron microscopy

According to scanning electron microscopy (SEM) images, the surfaces of the PPy-coated PLA fibers were covered with a conductive layer. This was clearly detected (Fig. 4, left), since the fiber scaffold did not build up any electrostatic charge under the electron beam at 3-kV acceleration voltage. The surface of the metallized (20 nm Au) PLA fibers appeared smooth in comparison to the PPy-coated fibers (Fig. 4, right).

Atomic force microscopy

Figure 5 shows representative topography and the measured surface roughness of individual PPy-PLA fibers after hydrolysis in PBS. The long axis of the fiber in each AFM was set parallel to the slow scan axis (45 degrees in the images in Fig. 5A). On day 0, the fiber surface appears extensively covered by fine nodular material individual nodules being 200 nm in diameter. This presented the typical morphology for PPys prepared by chemical polymerization. On day 10, the nodular surface morphology of the fibers was detected as on day 1. However, smoother areas and coarser (>400 nm) nodules with fine structure had appeared on day 10. On day

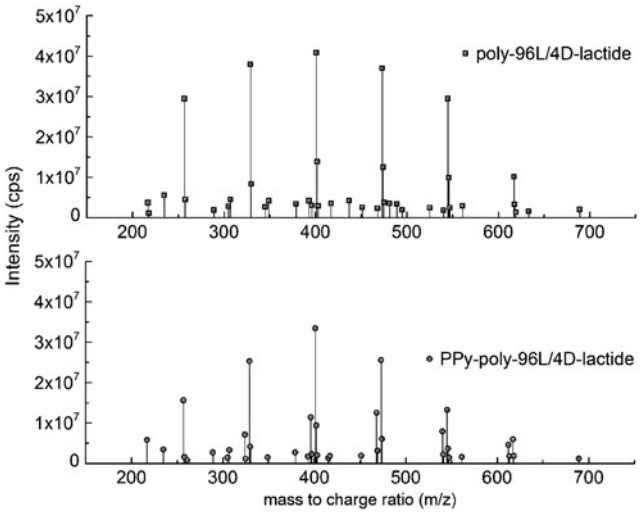

FIG. 3. Electrospray ionization-mass spectrometry spectra of the hydrolysis products from PLA-PPy and PLA scaffolds. All detectable peaks are found in the m/z range of 200–700.

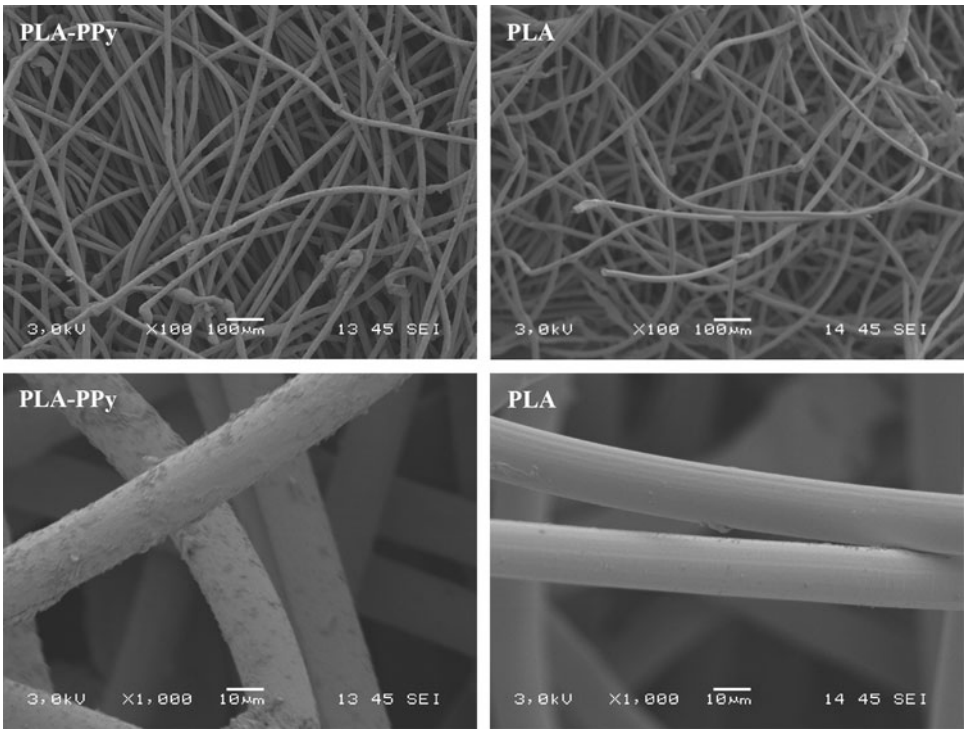

FIG. 4. Scanning electron microscopy image of PLA-PPy scaffold (left) without sputtered gold layer and PLA scaffold (right) with 20 nm gold coating. At 3-kV acceleration voltage, the PPy-coated PLA scaffold could be readily imaged, but the electrically insulating PLA scaffold could not be imaged without a thin coating layer (typically gold or carbon) due to heavy electrostatic charging.

20, the fraction of smoother areas had further increased from day 10. According to optical microscopy, the fibers were still fully covered with PPy after the 20 days in PBS. Hence, the observed changes were probably due to the changes of the PPy coating morphology and/or the hydrolysis of the PLA surface under the PPy coating.

The changes in the AFM images were reflected in the surface roughness values (Ra) derived from the images (Fig. 5B). Within 10 days, the Ra values decreased significantly from about 160 nm to less than 80 nm. The roughness analysis showed a consistency independent of how the analyzed surface area was chosen from the images ($5\times5\,\mu m^2$, $2\times2\,\mu m^2$ subareas).

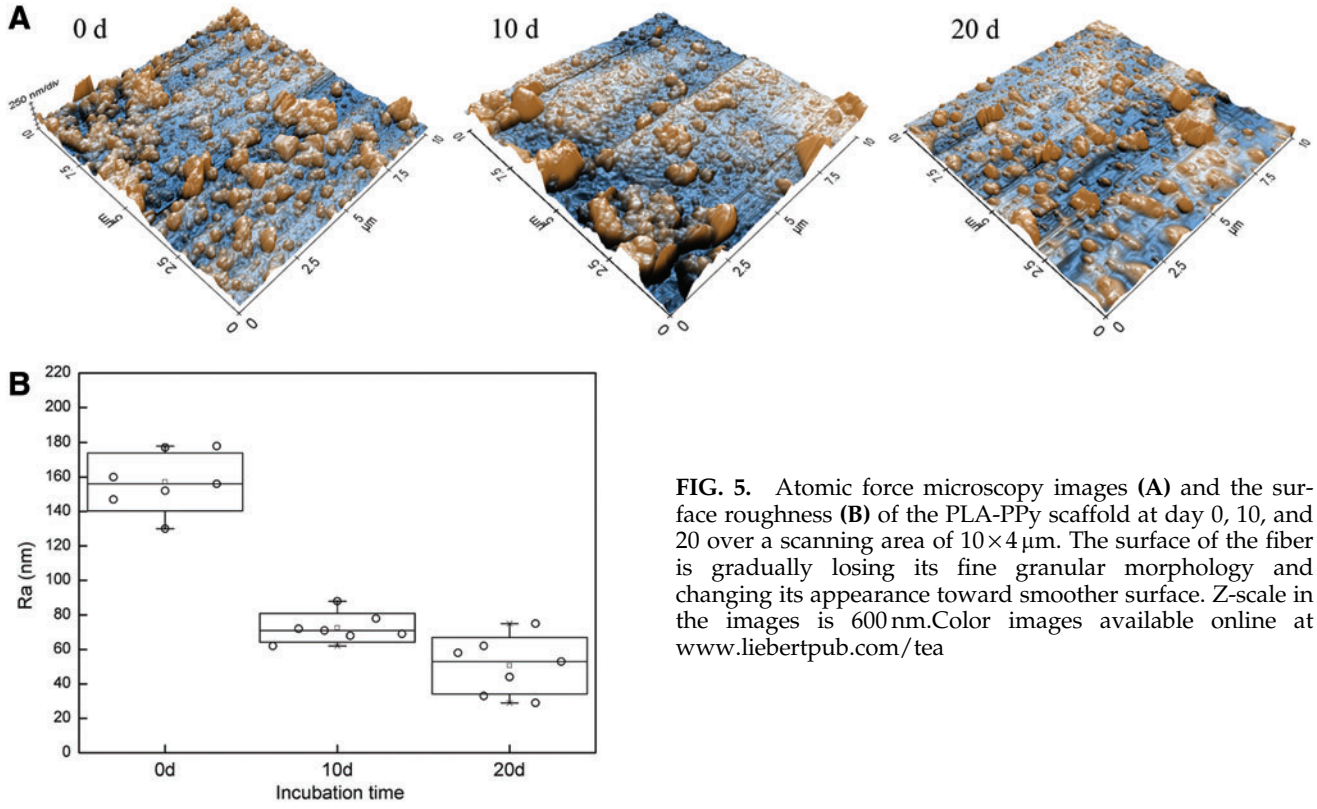

FIG. 5. Atomic force microscopy images **(A)** and the surface roughness **(B)** of the PLA-PPy scaffold at day 0, 10, and 20 over a scanning area of $10\times4\,\mu m$. The surface of the fiber is gradually losing its fine granular morphology and changing its appearance toward smoother surface. Z-scale in the images is 600 nm.Color images available online at www.liebertpub.com/tea

Cell culture

Flow cytometry. The flow cytometric analysis demonstrated that hASCs show high expression of CD105 (endoglin), CD73 (ecto 5′ nucleotidase), and CD90 (Thy-1), moderate expression (<50%>2%) of CD34 (hematopoietic progenitor and endothelial cell marker), and CD49d (integrin α4), while lacking expression (≤2%) of CD14 (monocyte and macrophage marker), CD19 (B cell marker), CD45RO (pan-leukocyte marker), CD106 (vascular cell adhesion molecule 1), and HLA-DR (HLA class II). Surface marker expression characteristics of undifferentiated ASCs from one donor cell line is presented in Figure 6. The results showed that hASCs expressed several of the specific antigens proposed by the Mesenchymal and Tissue Stem Cell Committee of the ISCT[30] defining human stem cells of mesenchymal origin. According to ISCT, CD34 should not be expressed in stem cells of mesenchymal origin; however, it showed moderate expression with high donor variation. However, varying results have been reported for CD34 on hASCs cultured in a medium supplemented with human serum[31–33] and fetal bovine serum.[31,34,35]

Viability. Live/dead staining showed that the majority of hASCs were viable and spread homogenously in both scaffold types with and without ES on day 14 (Fig. 7). By qualitative estimation, the number of hASCs was higher in PLA-PPy scaffolds than in the plain PLA scaffolds at all time points. This difference was evident on the cell seeding surface (Fig. 7) and the bottom surface of the scaffolds as well as inside the scaffolds (Supplementary Figs. S1 and S2; Supplementary Data are available online at www.liebertpub.com/tea). The ES did not seem to have any effect on cell viability or the cell number.

Proliferation and early osteogenic differentiation. The number of hASCs was assessed quantitatively using the CyQUANT proliferation method (Fig. 8), which is based on the relative absorbance values according to the amount of DNA. As demonstrated with live/dead staining, the number of hASCs was higher in PLA-PPy scaffolds at each time point compared to PLA scaffolds. This difference was statistically significant, excluding 7-day time point, in the nonstimulated and in the stimulated (100 Hz) group. In addition, the cell number in PLA scaffolds did not increase over time, whereas the cell proliferation during the 14-day culture period was detected in PLA-PPy scaffolds. Neither did the stimulation of 1 Hz nor 100 Hz show any effect on cell proliferation.

ALP analysis was performed on the same samples as used for DNA amount analysis (Fig. 9). ALP activity of hASCs was higher in PLA-PPy scaffolds in each stimulation group than in the PLA scaffolds at 7 and 14 days. One donor line did not show reliably detectable ALP activity at any of the measured time points. Therefore, data from two other repeats only are shown. The ALP activity values varied notably between the two donor lines; hence, no significant differences were detected between different scaffold types or stimulation groups.

Discussion

As our main finding, the PPy coating enhanced hASC proliferation. A similar trend was also seen in ALP activity, but no significant differences were detected. ALP activity peaked at the 7-day time point, which is typical behavior for ASCs in 3D scaffolds in the maintenance medium.[36] To the best of our knowledge, this is the first study to investigate the effect of ES on hASCs in a 3D culture system on PLA-PPy scaffolds by exploiting the conductivity properties of PPy. For the ES in the 3D culture system, we designed a custom-made stimulation setup, where multiple scaffolds could simultaneously be stimulated. Symmetric biphasic pulsed DC voltage with ±100 mV/mm pulse amplitude (2.5 ms/250 ms pulse duration and

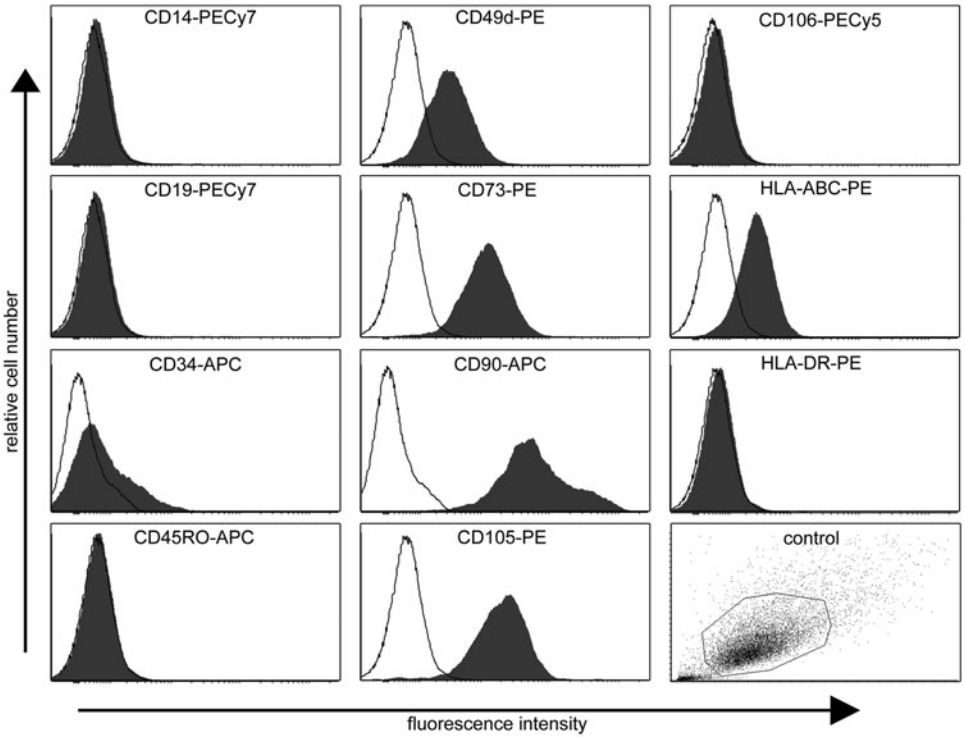

FIG. 6. Surface marker expression characteristics of undifferentiated adipose stem cells (ASCs) from one donor cell line as analyzed by flow cytometry. Relative cell number (*y*-axis) and fluorescence intensity (*x*-axis). Unstained control cells (empty histograms) and cells stained with antibody (filled histograms). Unstained control sample dot plot showing particle size and granularity (side scatter vs. forward scatter).

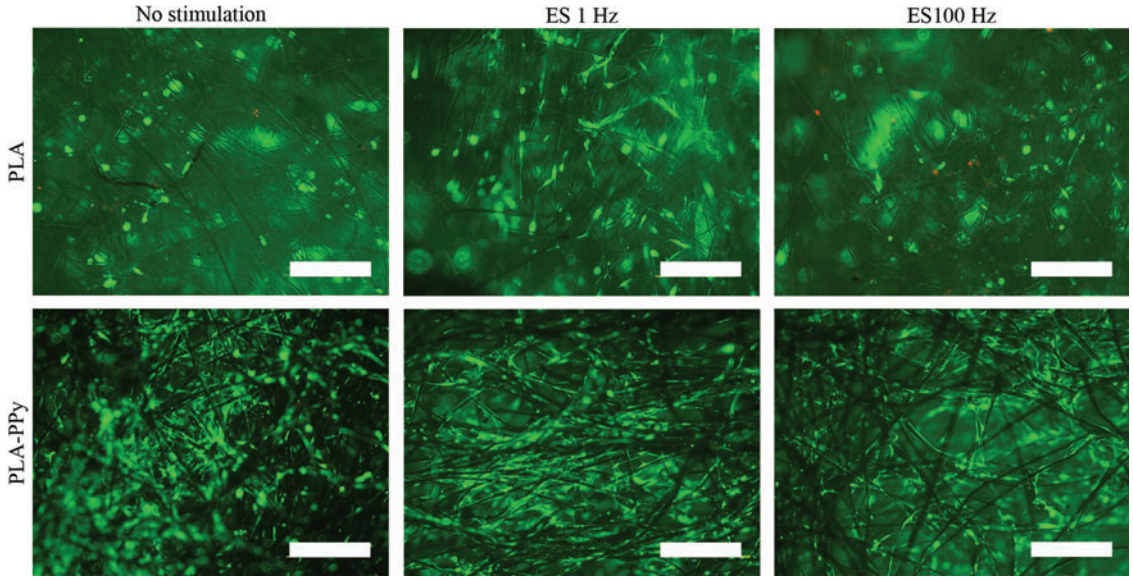

FIG. 7. Representative images of viable (green fluorescence) and dead (red fluorescence) human adipose stem cells at 14-day time point attached to PLA and PLA-PPy scaffolds visualized at top/cell seeding side of the scaffolds. Scale bar is 500 μm. Color images available online at www.liebertpub.com/tea

100 Hz/1 Hz pulse frequencies, respectively), was chosen on the basis of earlier studies demonstrating their physiological relevance, safety, and applicability to stimulating hASCs.[19,21]

ES can be considered a potential way to stimulate hASCs as it offers a means to exert similar influence on cells as, for example, growth factors, but in a safer, more inexpensive and repeatable way.[19] Nevertheless, no significant differences in early osteogenic differentiation or proliferation were detected between electrically stimulated and nonstimulated hASCs in our setup. This result was in contrast to many recent studies reporting favorable effects of ES on hASC osteogenic differentiation. McCullen et al. demonstrated hASC mineralization and differentiation toward bone tissue under ES in a 2D culture system[19] when the osteogenic medium was used (the maintenance medium supplemented with 50 mM ascorbic acid, 0.1 mM dexamethasone, and 10 mM β-glycerofosfate, while Tandon *et al.*[21] demonstrated that hASCs align and elongate in the presence of ES. Similar to our study, no differentiation medium or growth factors were used to increase the differentiation processes. As a result, they did not detect osteogenic differentiation, but rather fibroblastic or vasculogenic differentiation. As our study set out to investigate early osteogenic differentiation, it remains to be determined if differentiation into other lineages occurred.

Hammerick *et al.* used mouse ASCs and stimulated them using very similar parameters to ours. Their results on proliferation were consistent with ours since they did not detect any effect of ES on proliferation during a 10-day culture period. On the other hand, osteogenic differentiation was observed only in combination with ES and the osteogenic medium (the maintenance medium supplemented with 100 mg/mL of ascorbic acid and 10 mM β-glycerophosphate).

It should also be noted that most of the studies of using ES for stem cells have not been done in combination with electrically conductive biomaterial. PPy and ES may have synergistic effects, such as redox activity upon potential changes and bioactive molecules as dopants, which can affect also to the cell response in addition to the applied ES.[6]

The electrical impedance of the Au-electrodes in the DMEM changed significantly in the frequency range of sinusoidal (50 mV) 1–1000-Hz test signals, as confirmed by impedance spectroscopy. Indeed, the nonlinearity of the

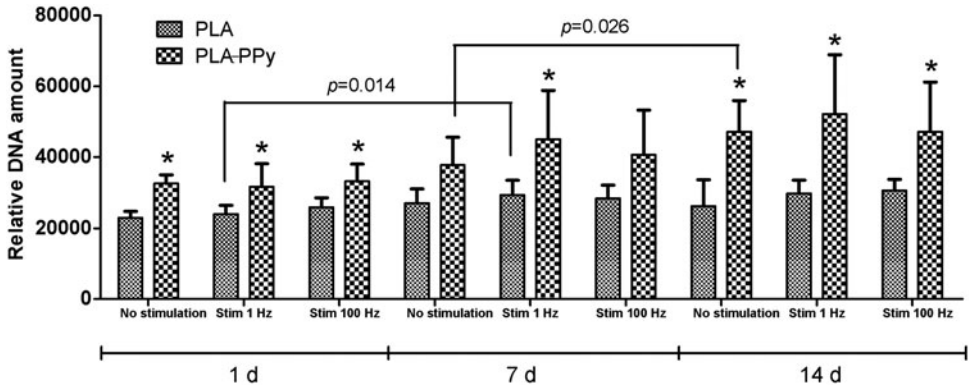

FIG. 8. Relative DNA content of human adipose stem cells cultured for 1, 7, and 14 days in PLA and PLA-PPy scaffolds. The results are expressed as mean ± SD, $n = 3$. The total number of technical samples was 9. *$p < 0.05$ with respect to the corresponding PLA scaffold.

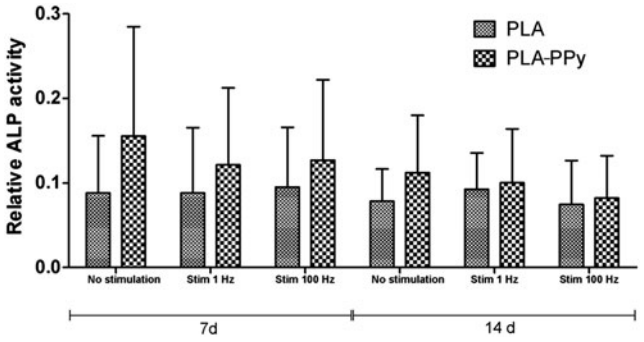

FIG. 9. Relative ALP activity of human adipose stem cells cultured for 7 and 14 days in PLA and PLA-PPy scaffolds. The results are expressed as mean ± SD, $n = 2$. The total number of technical samples was 6.

stimulation cell impedance was found to be an important factor in designing electronic stimulation setups and waveforms for stem cells. As anticipated, the electrically conductive PPy-PLA scaffold placed between the circular 1 cm^2 TiN electrodes decreased the impedance of the TiN/DMEM/TiN cell significantly, in particular, in the lower frequency range. A less significant, but a surprising decrease in cell impedance was also observed for the PLA scaffold, which is an excellent electrical insulator in air. In both cases, a possible explanation would be a marked enhancement of the conductivity of the fibers, extending to the interior of the scaffold. In the case of PLA fibers, the enhancement was likely due to increased surface ionic conductivity. For the PLA-PPy fiber, the enhancement was more easily understood since PPy is an electronic conductor both in air and in a medium. Our results suggest that an electronically conductive PPy can better deliver the stimulation currents to the cells located in the interior of the scaffold, which may have an additional effect on cell response. It is noteworthy that a significant enhancement of the electronic conductivity resulted from only 2–3 wt-% of the conductive PPy in the composite PLA-PPy fibers.

The in-plane DC resistance of air-dried PLA-PPy scaffolds was 50 kΩ on day 0. The DC conductivity of the PPy coating was roughly 10–30 S/m, based on an order of magnitude estimation of the DC conductivity of the PPy-layer and a careful extrapolation of the impedance spectroscopic data to very low frequencies. The estimated conductivity was within the range of the electronic volume conductivity reported for bulk PPy-sulfate powders prepared by APS oxidation in water.[37] Hence, the incorporation of the CS dopant did not adversely affect the electronic conductivity of PPy. The loss of DC conductivity of PPy coating was partly restored by acid doping in pH 2. Therefore, the loss of electronic conductivity was partly due to reversible de-doping of PPy chains in high pH 7.4.[6] Other mechanisms, such as PLA degradation, were also affecting the PPy coating and/or detachment, and cracking of the PPy layer. According to the impedance spectroscopy (1–10 kHz) and the DC measurements, the AC conductivity (electronic and ionic) of the PPy layer remained considerably (>2 decades) higher than the ionic conductivity of the DMEM at least on days 0–2. Although the impedance measurement cannot discriminate between the electronic conductivity and the ionic conductivity of the scaffold material, we find this a clear indication that the scaffold will enhance the stimulation current flow for periods far exceeding 2 days.

Irreversible changes were also apparent in the morphology of the fibers according to AFM topography images, which showed that the appearance of the fibers changed significantly during incubation. According to optical microscopy, the fibers were still fully covered with PPy after the 20 days in PBS. The data suggested extensive morphological changes in the thin PPy layer due to dopant ion exchange, hydration, osmotic pressure, and/or hydrolysis of the PLA surface under the PPy coating. Both factors may have affected the morphology of PPy, the local adhesion of the PPy coating, and consequently, the electronic conductivity of the coating.

Between the electrochemical potentials of the ES signals (±200 mV) used, the PPy remained in oxidized state. Thus, it is unlikely that redox chemistry had any significant effects on PPy morphology. Hydration and hydrolytic degradation of the outermost surface of the PLA may have been affected by the PPy coating and the ES, mainly due to the high ionicity of PPy. However, we found no direct evidence of such effect using SEM, AFM, and ESI-MS. This should be further studied in future.

Under the oxidative polymerization conditions, the CS was rapidly split into fragments (C4–C6) as evidenced by the viscosity measurements (data not shown). Although it was evident that the CS induced permanent hydrophilicity of the PPy coating, the role of the CS dopant in the cell response of PPy coating remained unclear. After hydrolysis in deionized water at +60°C, we did not detect pyrrole oligomers or CS fragments in the hydrolysis products of the PLA-PPy fibers by ESI-MS. It is therefore debatable if molecular fragments of the CS remained in PPy. This needs elucidation since CS fragments have well reported biological activity both *in vitro* and *in vivo*.[38,39] Nevertheless, our results showed that the effect of PPy coating on hASC response was as strong with and without ES, suggesting that the surface chemistry of PPy plays a more important role in triggering cell response than in the electrical conductivity of PPy.

According to the ESI-MS spectra, the influence of PPy coating on the hydrolysis of the PLA scaffold was negligible. According to our interpretation, the thin PPy coating was not hydrolytically degraded in water and had little effect on the hydrolytic degradation of the PLA scaffolds *in vitro*.

In conclusion, the novel PPy-coated scaffolds significantly enhanced hASC proliferation. In addition, early osteogenic differentiation was consistently more enhanced by PPy coating than by plain PLA scaffolds. This study highlights the future potential of PPy-coated PLA scaffolds seeded with hASCs in clinical bone tissue engineering applications. The ES of the relatively noninvasive biphasic pulsed voltage waveforms in 3D geometry did not have a significant effect on hASC proliferation or differentiation on days 1, 7, and 14.

Acknowledgments

The authors would like to thank Ms. Anne Rajala M.Sc, Ms. Ana Luísa Delgado Lima, and Ms. Hanna Juhola for the preparation and hydrolytic testing of the scaffolds, Ms. Anna-Maija Honkala and Ms. Minna Salomäki M.Sc for their assistance in the cell culture work. This study was financially supported by the Finnish Funding Agency for Technology

and Innovation (TEKES), the Academy of Finland and the Competitive Research Funding of Tampere University Hospital (grant 9K020).

Disclosure Statement

No competing financial interests exist.

References

1. Gloria, A., De Santis, R., and Ambrosio, L. Polymer-based composite scaffolds for tissue engineering. J Appl Biomater Biomech **8,** 57, 2010.
2. Niemelä, T., Niiranen, H., Kellomäki, M., and Törmälä, P. Self-reinforced composites of bioabsorbable polymer and bioactive glass with different bioactive glass contents. Part I: initial mechanical properties and bioactivity. Acta Biomater **1,** 235, 2005.
3. Cronin, E.M., Thurmond, F.A., Bassel-Duby, R., Williams, R.S., Wright, W.E., Nelson, K.D., and Garner, H.R. Protein-coated poly(L-lactic acid) fibers provide a substrate for differentiation of human skeletal muscle cells. J Biomed Mater Res Part A **69A,** 373, 2004.
4. Jiang, T., Khan, Y., Nair, L.S., Abdel-Fattah, W.I., and Laurencin, C.T. Functionalization of chitosan/poly(lactic acid-glycolic acid) sintered microsphere scaffolds via surface heparinization for bone tissue engineering. J Biomed Mater Res Part A **93A,** 1193, 2010.
5. Jakubiec, B., Marois, Y., Zhang, Z., Roy, R., Sigot-Luizard, M., Dugré, F.J., King, M.W., Dao, L., Laroche, G., and Guidoin, R. *In vitro* cellular response to polypyrrole-coated woven polyester fabrics: Potential benefits of electrical conductivity. J Biomed Mater Res **41,** 519, 1998.
6. Ateh, D.D., Navsaria, H.A., and Vadgama, P. Polypyrrole-based conducting polymers and interactions with biological tissues. J R Soc Interface **3,** 741, 2006.
7. Pelto, J., Haimi, S., Puukilainen, E., Whitten, P.G., Spinks, G.M., Bahrami-Samani, M., Ritala, M., and Vuorinen, T. Electroactivity and biocompatibility of polypyrrole-hyaluronic acid multi-walled carbon nanotube composite. J Biomed Mater Res Part A **93A,** 1056, 2010.
8. Du Souich, P., García, A.G., Vergés, J., and Montell, E. Immunomodulatory and anti-inflammatory effects of chondroitin sulphate. J Cell Mol Med **13,** 1451, 2009.
9. Schneiders, W., Reinstorf, A., Ruhnow, M., Rehberg, S., Heineck, J., Hinterseher, I., Biewener, A., Zwipp, H., and Rammelt, S. Effect of chondroitin sulphate on material properties and bone remodelling around hydroxyapatite/collagen composites. J Biomed Mater Res Part A **85A,** 638, 2008.
10. Manton, K.J., Haupt, L.M., Vengadasalam, K., Nurcombe, V., and Cool, S.M. Glycosaminoglycan and growth factor mediated murine calvarial cell proliferation. J Mol Histol **38,** 415, 2007.
11. Manton, K.J., Leong, D.F.M., Cool, S.M., and Nurcombe, V. Disruption of heparan and chondroitin sulfate signaling enhances mesenchymal stem cell-derived osteogenic differentiation via bone morphogenetic protein signaling pathways. Stem cells **25,** 2845, 2007.
12. Garner, B., Georgevich, A., Hodgson, A.J., Liu, L., and Wallace, G.G. Polypyrrole-heparin composites as stimulus-responsive substrates for endothelial cell growth. J Biomed Mater Res **44,** 121, 1999.
13. Gilmore, K.J., Kita, M., Han, Y., Gelmi, A., Higgins, M.J., Moulton, S.E., Clark, G.M., Kapsa, R., and Wallace, G.G. Skeletal muscle cell proliferation and differentiation on polypyrrole substrates doped with extracellular matrix components. Biomaterials **30,** 5292, 2009.
14. Richardson, R.T., Thompson, B., Moulton, S., Newbold, C., Lum, M.G., Cameron, A., Wallace, G., Kapsa, R., Clark, G., and O'Leary, S. The effect of polypyrrole with incorporated neurotrophin-3 on the promotion of neurite outgrowth from auditory neurons. Biomaterials **28,** 513, 2007.
15. Shi, G., Rouabhia, M., Meng, S., and Zhang, Z. Electrical stimulation enhances viability of human cutaneous fibroblasts on conductive biodegradable substrates. J Biomed Mater Res Part A **84A,** 1026, 2008.
16. Shi, G., Zhang, Z., and Rouabhia, M. The regulation of cell functions electrically using biodegradable polypyrrole–polylactide conductors. Biomaterials **29,** 3792, 2008.
17. Meng, S., Zhang, Z., and Rouabhia, M. Accelerated osteoblast mineralization on a conductive substrate by multiple electrical stimulation. J Bone Miner Metabol **29,** 535, 2011.
18. McCaig, C.D., Rajnicek, A.M., Song, B., and Zhao, M. Controlling cell behavior electrically: current views and future potential. Physiol Rev **85,** 943, 2005.
19. McCullen, S.D., McQuilling, J.P., Grossfeld, R.M., Lubischer, J.L., Clarke, L.I., and Loboa, E.G. Application of low-frequency alternating current electric fields via interdigitated electrodes: effects on cellular viability, cytoplasmic calcium, and osteogenic differentiation of human adipose-derived stem cells. Tissue Eng Part C Methods **16,** 1377, 2010.
20. Hammerick, K.E., James, A.W., Huang, Z., Prinz, F.B., and Longaker, M.T. Pulsed direct current electric fields enhance osteogenesis in adipose-derived stromal cells. Tissue Eng Part A **16,** 917, 2010.
21. Tandon, N., Goh, B., Marsano, A., Chao, P.H., Montouri-Sorrentino, C., Gimble, J., and Vunjak-Novakovic, G. Alignment and elongation of human adipose-derived stem cells in response to direct-current electrical stimulation. Annual International Conference of the IEEE Engineering in Medicine and Biology Society. Minneapolis, MN: IEEE Engineering in Medicine and Biology Society. 1, 6517, 2009.
22. Schmidt, C.E., Shastri, V.R., Vacanti, J.P., and Langer, R. Stimulation of neurite outgrowth using an electrically conducting polymer. Proc Natl Acad Sci U S A **94,** 8948, 1997.
23. Wong, J.Y., Langer, R., and Ingber, D.E. Electrically conducting polymers can noninvasively control the shape and growth of mammalian cells. Proc Natl Acad Sci U S A **91,** 3201, 1994.
24. Rowlands, A.S., and Cooper-White, J.J. Directing phenotype of vascular smooth muscle cells using electrically stimulated conducting polymer. Biomaterials **29,** 4510, 2008.
25. Wolszczak, M., Kroh, J., and Abdel-Hamid, M. Effects of the radiation processing of conductive polymers. Radiat Phys Chem **1,** 78, 1995.
26. Tandon, N., Cannizzaro, C., Chao, P.H., Maidhof, R., Marsano, A., Au, H.T., Radisic, M., and Vunjak-Novakovic, G. Electrical stimulation systems for cardiac tissue engineering. Nat Protoc **4,** 155, 2009.
27. Haimi, S., Moimas, L., Pirhonen, E., Lindroos, B., Huhtala, H., Räty, S., Kuokkanen, H., Sándor, G.K., Miettinen, S., and Suuronen, R. Calcium phosphate surface treatment of bioactive glass causes a delay in early osteogenic differentiation of adipose stem cells. J Biomed Mater Res Part A **91A,** 540, 2009.
28. Sun, S., Liu, Y., Lipsky, S., and Cho, M. Physical manipulation of calcium oscillations facilitates osteodiffer-

entiation of human mesenchymal stem cells. FASEB J **21,** 1472, 2007.
29. Andersson, S.R., Hakkarainen, M., Inkinen, S., Sodergard, A., and Albertsson, A.C. Polylactide stereocomplexation leads to higher hydrolytic stability but more acidic hydrolysis product pattern. Biomacromolecules **11,** 1067, 2010.
30. Dominici, M., Le Blanc, K., Mueller, I., Slaper-Cortenbach, I., Marini, F., Krause, D., Deans, R., Keating, A., Prockop, D., and Horwitz, E. Minimal criteria for defining multipotent mesenchymal stromal cells. The International Society for Cellular Therapy position statement. Cytotherapy **8,** 315, 2006.
31. Kocaoemer, A., Kern, S., Klüter, H., and Bieback, K. Human AB serum and thrombin-activated platelet-rich plasma are suitable alternatives to fetal calf serum for the expansion of mesenchymal stem cells from adipose tissue. Stem Cells **25,** 1270, 2007.
32. Lindroos, B., Boucher, S., Chase, L., Kuokkanen, H., Huhtala, H., Haataja, R., Vemuri, M., Suuronen, R., and Miettinen, S. Serum-free, xeno-free culture media maintain the proliferation rate and multipotentiality of adipose stem cells *in vitro*. Cytotherapy **11,** 958, 2009.
33. Parker, A.M., Shang, H., Khurgel, M., and Katz, A.J. Low serum and serum-free culture of multipotential human adipose stem cells. Cytotherapy **9,** 637, 2007.
34. Gronthos, S., Franklin, D.M., Leddy, H.A., Robey, P.G., Storms, R.W., and Gimble, J.M. Surface protein characterization of human adipose tissue-derived stromal cells. J Cell Physiol **189,** 54, 2001.
35. Mitchell, J.B., McIntosh, K., Zvonic, S., Garrett, S., Floyd, Z.E., Kloster, A., Di Halvorsen, Y., Storms, R.W., Goh, B., Kilroy, G., Wu, X., and Gimble, J.M. Immunophenotype of human adipose-derived cells: temporal changes in stromal-associated and stem cell-associated markers. Stem cells **24,** 376, 2006.
36. Marino, G., Rosso, F., Cafiero, G., Tortora, C., Moraci, M., Barbarisi, M., and Barbarisi, A. Beta-tricalcium phosphate 3D scaffold promote alone osteogenic differentiation of human adipose stem cells: *in vitro* study. J Mater Sci **21,** 353, 2010.
37. Blinova, N.V., Stejskal, J., Trchová, M., Prokeš, J., and Omastová, M. Polyaniline and polypyrrole: A comparative study of the preparation. Eur Poly J **43,** 2331, 2007.
38. Kang, S.K., Putnam, L., Dufour, J., Ylostalo, J., Jung, J.S., and Bunnell, B.A. Expression of telomerase extends the lifespan and enhances osteogenic differentiation of adipose tissue-derived stromal cells. Stem Cells **22,** 1356, 2004.
39. Grzesik, W.J., Frazier, C.R., Shapiro, J.R., Sponseller, P.D., Robey, P.G., and Fedarko, N.S. Age-related changes in human bone proteoglycan structure. Impact of osteogenesis imperfecta. J Biol Chem **277,** 43638, 2002.

Address correspondence to:
Suvi Haimi, PhD
Department of Biomaterials Science and Technology
University of Twente
P.O. Box 217
Enschede 7500 AE
The Netherlands

E-mail: suvi.haimi@uta.fi

Received: February 22, 2012
Accepted: October 17, 2012
Online Publication Date: January 4, 2013

Publication 3

Pelto, J., Haimi, S., Siljander, A., Miettinen, S.,
Tappura, K., Higgins, M.J., Wallace, G.G.

Surface properties and interaction forces of biopolymer-doped conductive polypyrrole surfaces by atomic force microscopy.

Langmuir. American Chemical Society . Vol. 29 (2013) No: 20, 6099 – 6108.

Langmuir

Article

pubs.acs.org/Langmuir

Surface Properties and Interaction Forces of Biopolymer-Doped Conductive Polypyrrole Surfaces by Atomic Force Microscopy

Jani M. Pelto,*[,†] Suvi P. Haimi,[‡,§] Aliisa S. Siljander,[†,§] Susanna S. Miettinen,[§] Kirsi M. Tappura,[†] Michael J. Higgins,[∥] and Gordon G. Wallace[∥]

[†]VTT Technical Research Centre of Finland, Sinitaival 6, P.O. Box 1300, 33101 Tampere, Finland

[‡]Department of Biomaterials Science and Technology, University of Twente, Enschede, P.O. Box 217, 7500 AE Enschede, The Netherlands

[§]Adult Stem Cells, Institute of Biomedical Technology, University of Tampere, Biokatu 8, FI-33014 Finland

[∥]ARC Centre of Excellence for Electromaterials Science (ACES), Intelligent Polymer Research Institute (IPRI), Australian Institute for Innovative Materials (AIIM) Facility, Innovation Campus, University of Wollongong, NSW 2522, Australia

ABSTRACT: Surface properties and electrical charges are critical factors elucidating cell interactions on biomaterial surfaces. The surface potential distribution and the nanoscopic and microscopic surface elasticity of organic polypyrrole–hyaluronic acid (PPy-HA) were studied by atomic force microscopy (AFM) in a fluid environment in order to explain the observed enhancement in the attachment of human adipose stem cells on positively charged PPy-HA films. The electrostatic force between the AFM tip and a charged PPy-HA surface, the tip–sample adhesion force, and elastic moduli were estimated from the AFM force curves, and the data were fitted to electrostatic double-layer and elastic contact models. The surface potential of the charged and dried PPy-HA films was assessed with Kelvin probe force microscopy (KPFM), and the KPFM data were correlated to the fluid AFM data. The surface charge distribution and elasticity were both found to correlate well with the nodular morphology of PPy-HA and to be sensitive to the electrochemical charging conditions. Furthermore, a significant change in the adhesion was detected when the surface was electrochemically charged positive. The results highlight the potential of positively charged PPy-HA as a coating material to enhance the stem cell response in tissue-engineering scaffolds.

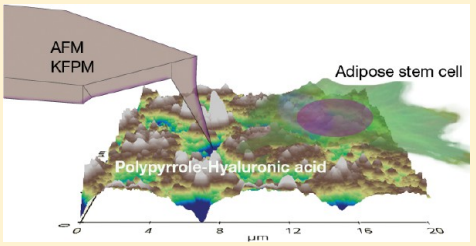

1. INTRODUCTION

Polypyrrole (PPy) is a prototype of an electroactive organic p-type semiconductor that is widely applied as a surface coating on a range of metallic conductors and insulative biomaterials such as tissue-engineering scaffolds.[1] The electroactivity of PPy stems from the property of the neutral and electrically insulating PPy^0 chains becoming positively charged (polaronic PPy+) and electronically conductive when oxidized in electrolytes. The charge of the PPy+ backbone is always compensated for by negatively charged species, called dopants, or ions from the surrounding electrolyte. Any excess surface charge of electrochemically charged polypyrrole is dependent not only on the bulk doping charge of the polymer but also on the surface chemistry in the electrolyte. Factors such as the mobility of the dopants and properties of the electrolyte solution (e.g., salt concentration and pH) are involved in the surface chemistry.[2]

We have previously reported that PPy doped with hyaluronic acid (HA) shows potential as a substrate material in supporting the growth of human adipose stem cells (hASC).[3] HA is an extracellular matrix polysaccharide that has been widely studied as a biocompatible polymeric dopant of polypyrrole. It is an extremely hydrophilic anionic polymer that renders the polymer (i.e., PPy-HA) very hydrophilic, and under certain synthesis conditions, a soft polymer with a Young's modulus in the range of megapascals can be produced. According to its charging state, PPy-HA may reversibly absorb salt and water from the surrounding electrolyte, a process that contributes to the elasticity of the polymer surface.[4] Serra Moreno et al.[5] have studied the effects of synthesis parameters of polysaccharide-doped PPy, including the effect of their surface roughness, on osteoblast adhesion and proliferation. Their findings suggest that smooth surfaces allow the best adhesion of osteoblasts on electropolymerized films. A similar PPy-HA coating has been recently designed to inhibit the unwanted adhesion of astrocytes and fibroblasts onto neural probes.[6] Cell interactions with PPy-HA-coated surfaces are likely to depend not only on the specific chemistry of the dopant type but also on other physical surfaces properties (modulus, surface potential, and morphology) that are influenced by the presence of the dopant and parameters (e.g., polymerization charge of polymer growth) used to synthesize the polymer.[7,8]

However, there are still gaps in the fundamental understanding of cell–surface interactions at the single-molecule (atomic and nanoscopic) level and on micrometer scales related

Received: March 12, 2013
Revised: April 17, 2013
Published: April 26, 2013

   dx.doi.org/10.1021/la4009366 | *Langmuir* 2013, 29, 6099–6108

to processes involving initial cell attachment, spreading, and adhesion. Therefore, the role of the interface and its various surface properties, including nanoscale and microscale surface roughness, elasticity, and electrical charges, needs further elucidation for a full understanding of cell interactions on biomaterials. This is particularly the case given the ongoing emergence of new and diverse biomaterials, including electroactive polymers that are continually under development because of their easy modification, functionalization, and doping with biological constituents (e.g., glycosaminoglycans, drugs, and proteins). Although some studies on electroactive polymers have examined the effect of their physical surface properties on cell interactions,[1,3,5,6] such as proliferation, adhesion, and differentiation, few studies in this context have been undertaken using approaches that quantify and correlate variations in nanoscale surface properties. With that said, many studies using atomic force microscopy (AFM) have shown that electroactive polymers display characteristic nanoscale lateral variations, or effective phase separations, of the modulus, surface potential, conductivity, and interaction forces that occur across the polymer surface and are related to its nanoscale morphology.[7]

Of particular interest is how these nanoscale properties are manifested under natural physiological conditions, in particular, variations in surface charge arising spontaneously on ionized chemical groups and electrical double layers at surfaces immersed in physiological fluid. Electrical double layer forces, strong van der Waals interactions, and steric forces are present in colloidal aqueous systems, including biological interfaces. Hence, the physical interactions among the continuum of biomaterial surfaces, plasma proteins, and surface receptors of living cells are clearly attributable to their electrostatic charges and/or hydrated polymers on their surfaces.[9] Lubarsky et al.[10] have shown that electrical double layer forces drive human serum albumin adsorption more efficiently onto nonoxidized and less negatively charged tissue culture polystyrene plates in phosphate-buffered saline (PBS). According to a recent review (Dubiel, Martin, and Vermette[9]), the importance of the electrostatic double layer forces in adhesion proteins and cell adhesion has been well stated in recent studies.

Surface charges measured with different analytical techniques are quite different. Atomic force microscopy (AFM) measurements in fluid yield "effective" nanoscopic information on the surface charge/potential based on the Gouy−Chapman−Stern (GCS) treatment of the diffuse electrical double layer, whereas electrokinetic measurements yield information about the averaged surface zeta potential, which by definition are different quantities. Both of these parameters have been used to describe the attachment of charged biopolymers and cells on biomaterials, but neither can be directly deduced from the electrochemical (bulk or surface) charge injected into the biomaterial and/or the properties of the physiological electrolyte. Because there is no universally applicable theory available linking the electrochemical charge and the effective surface charge and potential, they must be determined using some probing technique, such as AFM.[11] Hence, the role of the surface charge in the adhesion of biopolymers in biological environments, in particular, for electroactive polymers on the nanoscale, has remained difficult to quantify directly, and their effects on biological interactions are unclear.

The significance of gaining an improved understanding of nanoscale surface forces is evident from the mechanisms of cell attachment and spreading that require the initial adsorption of ECM proteins followed by the application of piconewton or even nanonewton forces to the substrate via focal adhesion complexes, all of which are also influenced by the elastic response of the substrate.[12,13] Emerging evidence suggests that the mechanochemical response originating from the cell−substrate interactions is specific to the cell phenotype, the understanding of which has already been utilized to great effect in the differentiation and sorting of cell types[12] and could also be applied to electroactive polymers through the modulation of redox surface properties.

In this study, we have utilized Kelvin force probe microscopy (KFPM) and AFM to elucidate nanoscopic lateral variations in the roughness, elasticity, and surface charge across the surface of PPy-HA substrates as a function of the redox state of the polymer. In particular, we attempt to relate these variations in surface properties, in addition to the surfaces forces operating in fluid, to observed differences in human adipose stem cell (hASC) adhesion and spreading on thin, potentiostatically electropolymerized, charged PPy-HA surfaces.

2. MATERIALS AND METHODS

2.1. Polypyrrole−Hyaluronic Acid Synthesis. Polypyrrole samples were electropolymerized onto indium tin oxide (ITO) substrates (surface resistance 40 Ω/square, Sigma-Aldrich, St. Louis, MO) using a potentiostat (Parstat 261A, EG&G, Oak Ridge, TN). Another set of samples for the electrical characterization was grown on Au-Mylar (rf-sputtered 50 nm Au, VTT, Finland) films. For the electropolymerization, 0.2 M distilled pyrrole (Sigma) was dissolved in a 1 mg/mL solution of HA extracted from human umbilical cords (Sigma). Constant potential +1.0 V versus Ag/AgCl was applied to the working electrode substrate. A platinum counter electrode was used. The polymerization was continued until a polymerization charge of 0.5 C/cm^2 had been consumed. At this point, the PPy-HA film thicknesses were 600−800 nm, as confirmed by AFM.

After the synthesis, the PPy-HA samples were rinsed with deionized water and dried in air. Samples grown on ITO substrates were gamma sterilized (20 kGy radiation dose) before cell seeding or before the 2 day preincubation period in the maintenance medium consisting of DMEM/F-12 1:1 (Invitrogen, Paisley, U.K.), 10% FBS (Invitrogen), 1% L-glutamine (GlutaMAX I, Invitrogen), and 1% penstrep (100 U/mL penicillin, 0.1 mg/mL streptomycin, Invitrogen). Corresponding PPy-HA films grown on Au-Mylar were used in the electrical characterization.

2.2. Electrochemical Charging. We examined the effect of the charged state of PPy-HA on hASCs adhesion. For charged samples, the PPy-HA films were electrochemically charged by applying the +200 mV versus Ag/AgCl reference directly before seeding hASCs and during the cell culturing period (Table 1). For uncharged samples (defined as samples where +200 mV was not applied), the as-synthesized films were connected to a reference +0 mV electrode. Therefore, both groups of samples were set to a potential during cell culturing. For the AFM experiments, the charged and uncharged samples were identically prepared, with the charged samples being subjected to the application of +200 mV versus Ag/AgCl (0.005 M

Table 1. PPy-HA Samples Were Categorized in Four Groups According to the Pretreatment and Charging Conditions

abbreviation	pretreatment prior to ASC seeding and charging	electrochemical charging
0/preinc	preincubated in maintenance medium 48h	set to 0 mV
+/preinc	preincubated in maintenance medium 48h	oxidized at +200 mV
0	rinsing with PBS	set to 0 mV
+	rinsing with PBS	oxidized at +200 mV

dx.doi.org/10.1021/la4009366 | Langmuir 2013, 29, 6099−6108

NaCl) in the AFM electrochemical cell shortly before the AFM scan. The sample potential was controlled using an EDAQ EA161 potentiostat and a platinum wire counter electrode immersed into the AFM electrochemical cell. During the AFM scan, the sample potential was not controlled.

2.3. Cell Culture. *2.3.1. Human Adipose Stem Cells.* Human ASCs were isolated from the adipose tissue samples of subcutis collected from surgical procedures from two females (ages 45 and 50), kindly provided by the Department of Plastic Surgery, Tampere University Hospital. Isolation of hASCs from the tissue samples was conducted in accordance with the Ethics Committee of Pirkanmaa Hospital District, Tampere, Finland (R03058). The adipose tissue was digested with collagenase type I (1.5 mg/mL, Invitrogen). Human ASCs were expanded in T-75 polystyrene flasks (Nunc, Roskilde, Denmark) in a maintenance medium. Cells of passages 5−7 were used in the experiments. Cells were seeded onto each PPy-HA sample in a medium volume of 1 mL, with 25 000 cells per sample, and cultured for up to 3 h.

The hASCs of passages 2−3 were harvested and analyzed by flow cytometry (FACSAria, BD Biosciences, Erembodegem, Belgium). Monoclonal antibodies against CD9-PE, CD10-PECy7, CD13-PE, CD29-APC, CD49d-PE, CD90-APC, CD106-PE-Cy5, CD146-PE, and CD166-PE (BD Biosciences); CD45-FITC (Miltenyi Biotech, Bergisch Gladbach, Germany); CD31-FITC, CD34-APC, CD44-FITC, and HLA-ABC-PE (Immunotools GmbH Friesoythe, Germany); and CD105-PE (R&D Systems Inc., Minneapolis, MN, USA) were used. Analysis was performed on 10 000 cells per sample, and unstained cell samples were used to compensate for the background autofluorescence levels. The flow cytometric analysis on hASCs demonstrated an expression for markers substantiating the mesenchymal origin of cells and showing a low or lack of expression of markers, suggesting a hematopoietic and angiogenic origin of the cells. The characterization data comply with the existing results on hASCs.[14−16]

2.3.2. Cell Attachment and Viability. Cell attachment and viability were studied using live/dead staining (Invitrogen) according to the manufacturer's protocol at the 3 h time point. The viable cells (green fluorescence) and dead cells (red fluorescence) were examined using a fluorescence microscope. For AFM visualization, similarly treated samples as for live/dead staining were fixed before imaging. After the 3 h culturing period, cell-seeded samples were washed with DPBS and fixed with 5% glutaraldehyde-fixative in 0.1 M phosphate buffer (pH 7.4) for 48 h. Glutaraldehyde cell fixation (5%) is a standard cell fixation method that we have used in our previous studies with human adipose stem cells for morphology imaging.[17,18] Fixative was replaced by Dulbecco's phosphate-buffered saline (DPBS), where samples were stored until imaging. Three to five representative optical images of the cells, selected from different areas of each PPy-HA sample, were analyzed to measure the surface area of the individual cells (n = 26) using i-Solution Lite image acquisition and measuring software (IMT i-Solutions Inc.).

2.4. Characterization of the Polypyrrole Films. *2.4.1. Kelvin Force Probe Microscopy.* For the KFPM analysis, the dried samples were first immersed in a dilute 0.005 M NaCl electrolyte. Subsequently, the samples were either charged (+200 mV vs Ag/AgCl) or shortcut to the Ag-pseudoreference electrode (0 mV vs Ag). The samples were carefully rinsed to remove any salt solution and left to dry under ambient conditions. The surface charge distribution of the PPy-HA samples in air was measured using an Asylum MPF-3D AFM in standard Kelvin force probe mode. Olympus OMCL-AC240TM probes with a platinum coating, a cantilever spring constant of ∼2 N/m, and a resonance frequency of 70 kHz were used for imaging at a scan rate of 0.5 Hz. The topography of the sample area was acquired in ac mode while simultaneously recording the surface potential of the polymer films. Relative differences in the surface potential across the films were obtained.

2.4.2. AFM Force Spectroscopy. AFM force−distance curves were acquired using an Asylum MPF-3D AFM in force volume mode. The measurements were made in dilute 0.005 M NaCl electrolyte in an open measurement cell at room temperature. Silver wire was used as a pseudoreference electrode in those experiments with a biased AFM tip.

The characterization of the surface charge was carried out using biased (−200 mV) or neutral (0 mV) gold-coated silicon nitride tips OBL (Olympus Corp, Tokyo, Japan). The spring constant of the OBL cantilever was determined to be 0.020 N/m by the Sader method,[19] and the cantilever sensitivity in the electrolyte was measured from the slope of the recorded force curves. The low concentration of salt (0.005M) was applied in order to be able to project the electrostatic interactions to long distances where they can be distinguished from hydration and steric forces. Negative or zero bias voltage kept the tip−sample interaction in the repulsive regime, indicating the negative surface charge of PPy-HA. The negative surface charge was confirmed by initial testing with both positive and negative bias on the tip, of which only the negative bias resulted in a repulsive interaction. A maximum applied force of 0.7 nN was kept constant for the individual curves, which were obtained at a scan rate of 300 nm/s. Force curve maps (32 × 32) were collected for both the neutral (0 mV) and negatively biased (−200 mV) tip. To elucidate the effect of electrostatic double-layer forces on the tip−sample interaction under physiological conditions qualitatively, the force curve data was fitted to two simple DLVO models.[20,21] The DLVO fitting gave estimates on the range of the repulsion forces for comparison with the theoretically calculated double layer. In addition, the polarity and relative magnitude of the excess surface charge density (surface potential) could be estimated.

The surface elasticity was measured using ANSCM-PC platinum−iridium-coated pyramidal silicon tips (Applied Nanostructures Inc., Santa Clara, CA, USA). A maximum applied force of 1−1.5 nN was kept constant for the individual curves, which were obtained at a scan rate of 300 nm/s. Force curve maps (64 × 64) were collected with a neutral (0 mV) tip. The spring constant of the ANSCM-PC cantilever was determined to be 0.034 N/m by the Sader method,[19] and the cantilever sensitivity in the electrolyte was measured from the slope of the recorded force curves. The force curves were converted to force versus indentation curves and fitted with the Hertz model to quantify the Young's modulus. The analysis procedure was carried out using the Asylum AFM Software (Igor Pro, Wavemetrics) according to previously described methods.[7]

2.5. Statistical Analyses. Statistical analyses were performed using Origin Pro (Originlab Corporation, Northampton, MA, USA), version 8. The statistical significance of the cell spreading data was assessed using the student's t test and ANOVA at a significance level of 0.01. Levene's test for equal variance and Bonferroni's post hoc correction and test for equal means were used with ANOVA.

The significance of the possible variation in the surface potential derived from the AFM force spectroscopy data was assessed by the student's t test at a significance level of 0.05.

3. RESULTS AND DISCUSSION

3.1. Cell Attachment and Viability. The spreading of hASCs on nonpreincubated (1A and B), preincubated (1C and D), and either charged (1B and D) or uncharged (1A and C) PPy-HA surfaces are presented in the representative optical images (Figure 1A−D, left panel). The majority of hASCs were uniformly adhered at the 3 h time point on charged sample surfaces. However, hASCs seeded on noncharged PPy-HA surfaces were unevenly spread, and many cells were incompletely attached.

Analyzing the average cell areas showed that both the preincubation and charging influenced the cell spreading significantly (Figure 2): student's t test statistics for equal means between preincubated groups (+/preinc) versus (0/preinc) gave $p < 0.001$, between nonpreincubated groups (+) versus (0) $p < 0.001$, and between groups (+/preinc) and (0) $p < 0.001$. The effect of the preincubation and the charging compared in the groups (0/preinc) versus (+) were not

dx.doi.org/10.1021/la4009366 | Langmuir 2013, 29, 6099−6108

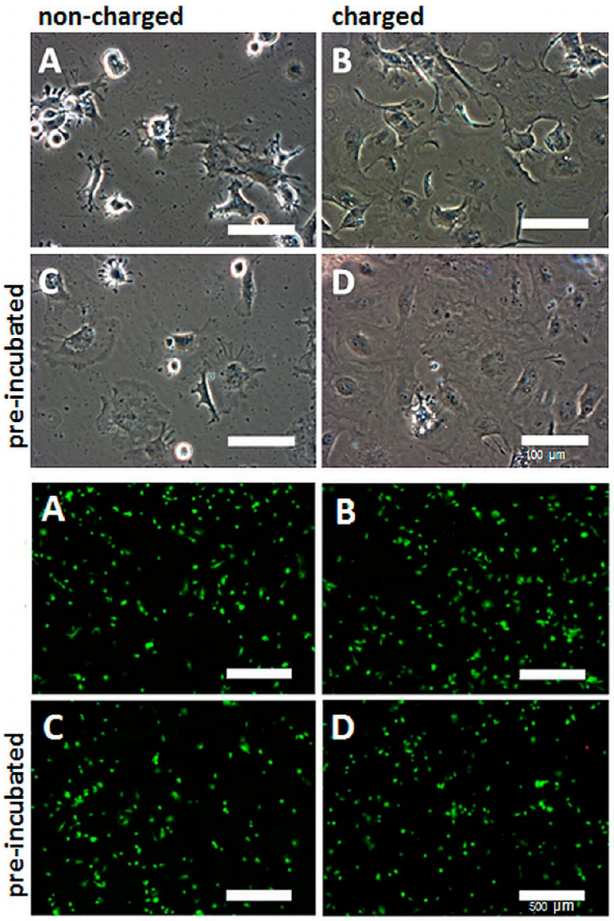

Figure 1. (Top) Spreading of hASCs on nonpreincubated (A and B), preincubated (C and D), and either the charged (B and D) or uncharged (A and C) PPy-HA surface at 3 h. Scale bars are 100 μm. (Bottom) Corresponding live/dead images with a scale bar of 500 μm.

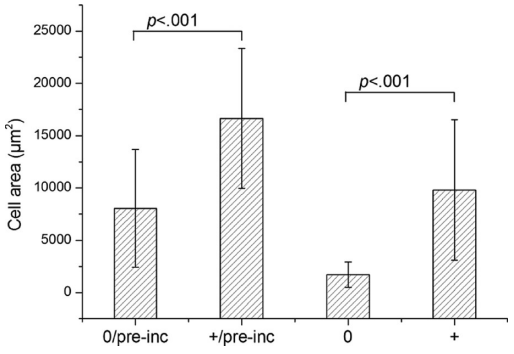

Figure 2. Average surface area of the hASCs at 3 h, as measured from three to five representative optical microscope images per group (n = 26 in each group). According to the t-test and ANOVA, the differences in cell areas were very significantly (at a level of 0.01) different (p < 0.001) within the preincubated and the PBS rinsed groups but not between the (0/preinc) and (+) groups.

statistically significant (p = 0.28). Qualitatively, the charged (+200 mV) PPy-HA samples supported hASC attachment and spreading notably more than the noncharged (0 mV) samples.

Levene's test indicated significantly different variances $F(3,135)$ = 28.8, p < 0.001. According to one-way ANOVA, the average cell areas were significantly different between the groups $F(3135)$ = 55.1, p < 0.001. The Bonferroni test indicated that the difference between groups (0/preinc) and (+) was not significant at a level of 0.01, which was consistent with the result of the pairwise t test.

In summary, the combined effect of preincubation and charging resulted in a 215% increase in the hASC surface area compared to nonpreincubated and noncharged control. The viability of the hASCs was not significantly affected by charging or the preincubation of the PPy surfaces, as indicated by live/dead images (Figure 1A–D, right panel).

Therefore, the main finding from these observations is that the charged surfaces, even those not exposed to serum proteins for longer incubation times in the media, promoted cell adhesion to a greater extent than uncharged samples treated under the same conditions. This suggest that the application of a positive bias of +200 mV was beneficial in promoting cell adhesion, which may have occurred by increased adsorption of serum proteins (e.g., fibronectin, vitronectin) either during preincubation and/or immediately upon cell seeding and settling over 3 h or through direct electrostatic interactions with the cell membrane.[22] The effect of preincubation on cell attachment was not as clear as the effect of charging, although preincubation also seemed to facilitate cell adhesion to the polymer.

3.2. Characterization of the Surface Charge. *3.2.1. Kelvin Force Probe Microscopy.* AFM topography images (left) and their corresponding surface potential maps (right) of uncharged (+0 mV) (Figure 3A,B) and charged (+200 mV) (Figure 3C,D) PPy-HA obtained from KFPM are presented in Figure 3. The root-mean-square (rms) (average) roughness values of the uncharged and charged PPy-HA were 8.9 and 9.4 nm, respectively, indicating that the surface roughness was not significantly affected by the electrochemical charging. These roughness values, along with the geometric area of the images, also equate to comparable surface area values of 4.52 μm^2 (uncharged) and 4.57 μm^2 (charged). The surface potential images in Figure 3B,D display relative (not absolute) changes in the surface potential across the uncharged and charged films, with average variations of 4.38 mV rms and 2.91 mV rms, respectively. As evident in the surface potential images, the uncharged (+0 mV) films showed phase separation in the surface potential where more negative potentials (darker regions in Figure 3B) correlated with the nodule structures whereas areas of more positive surface potential correlated with the peripheries of the nodules (brighter regions in Figure 3B). In contrast, the surface potential of the charged films showed a more uniform distribution of the surface potential with no clear correlation with the topography (Figure 3D). In some cases, it did appear that the larger nodules showed a more positive potential than the surrounding areas. These observations were also confirmed in previous studies using KPFM,[23] conductive AFM,[24] and recently AFM phase imaging.[7,25] Previous observations in the surface potential, conduction current, and AFM phase signals showing that the application of a positive electrochemical potential largely removes this phase separation are in accordance with the observations of this study. Many of these studies, as well as ours here, support the presence of more crystalline, heavily doped, and electrically conductive parts of the PPy-HA in the nodules. In this study, we also applied a positive bias to the PPy-HA films with a moderate oxidizing potential (+200 mV vs Ag) in the presence of a dilute saline electrolyte to avoid overoxidation of the polaronic PPy+ chain and the accumulation of excess salt on the PPy-HA surface upon drying. It is likely that charge compensation by sodium

dx.doi.org/10.1021/la4009366 | Langmuir 2013, 29, 6099–6108

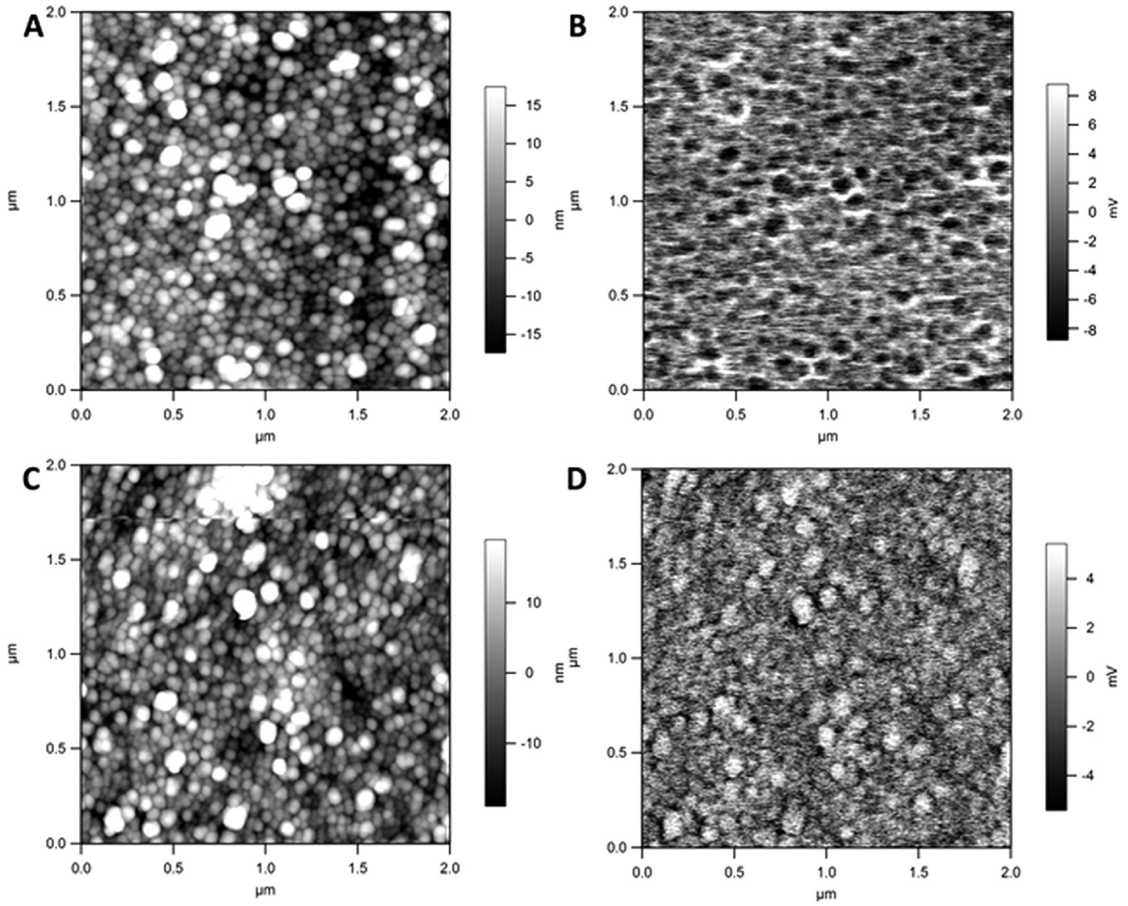

Figure 3. Kelvin force probe microscopy. (A and B) Corresponding height (8.9 nm rms) and surface potential images (4.38 mV rms) for the uncharged PPy-HA film. (C and D) For the same film, the corresponding height (9.4 nm rms) and surface potential images (2.91 mV rms) after charging (+200 mV).

and chloride ions in the dilute electrolyte would have occurred immediately; therefore, the extent and role of the negatively charged HA molecules remained unclear in the PPy. We have learned from our previous X-ray fluorescence elemental analysis (unpublished data) that a significant number of chloride ions remain in the PPy-HA films after being rinsed with water. However, the PPy-HA surface remained extremely hydrophilic, implying that the surface exposed to the electrolyte contains significant amounts of HA fragments and/or polymers. Nevertheless, it is possible that that ion exchange between the chloride ions and acid groups of the HA were at least partially responsible for the structural and electrical reorganization observed in this study and the preceding studies.[7,22−25]

3.2.2. AFM Force Mapping. Force maps for the uncharged and charged samples with no potential bias applied to the tip and obtained in 5 mM NaCl are shown in Figures 4 and 5, respectively. For the uncharged sample, the topography image gave an rms (average) surface roughness of 23.7 nm (surface area, 1.23 μm^2) (Figure 4A). As each pixel in the topography image represents a single force curve, we were able to correlate the latter with specific $x-y$ positions on the film. The inset in Figure 4B shows two force curves taken on a nodule structure (position 1) and the periphery of the nodules (position 2) from the marked region (red square) in the topography image. Neither of the curves exhibited adhesion, but the slope of their contact regions differed (Figure 4B). The slope of the contact region in the force curves for the nodule structure (solid line) was steeper compared to the nodule periphery (dashed line), indicating that the former had a higher stiffness. Variation in both the adhesion and stiffness properties, extracted from the force curves, could be further assessed as a function of the morphology by plotting these two parameters as function of the $x-y$ coordinates to display adhesion (Figure 4C,D) and Young's modulus (Figure 4E,F) maps. Figure 4C of the adhesion map, which is also overlaid on a 3D topography image in Figure 4D, showed low adhesion (rms average = 45 pN) between the tip and polymer and no correlation with the surface topography. A higher modulus (lighter areas) was observed at the nodule structures compared to their peripheries (Figure 4E,F), indicating a phase separation in the stiffness of the film. The rms (average) values of Young's modulus estimated from the AFM analysis gave a value of 2.3 MPa, which is very low compared to previously measured Young's modulus values for electroactive polymers.[7] In comparison, the charged sample showed the same morphology and a similar rms (average) roughness of 29.2 nm (surface area, 1.28 μm^2) (Figure 5A), indicating that the charging of the film did not have a significant effect on the surface topography. Individual force curves on the nodules (position 1, inset from the marked region in Figure 5A) showed no adhesion (Figure 5B, solid curve), but in this case, adhesion was observed at the nodule periphery. This was clearly observed in the adhesion maps (Figure 5C) and the adhesion overlay with the topography (Figure 5D), which showed significantly greater adhesion (rms 634 pN) that strongly correlated with regions of only the nodule peripheries. The charged surface had a slightly higher

dx.doi.org/10.1021/la4009366 | *Langmuir* 2013, 29, 6099−6108

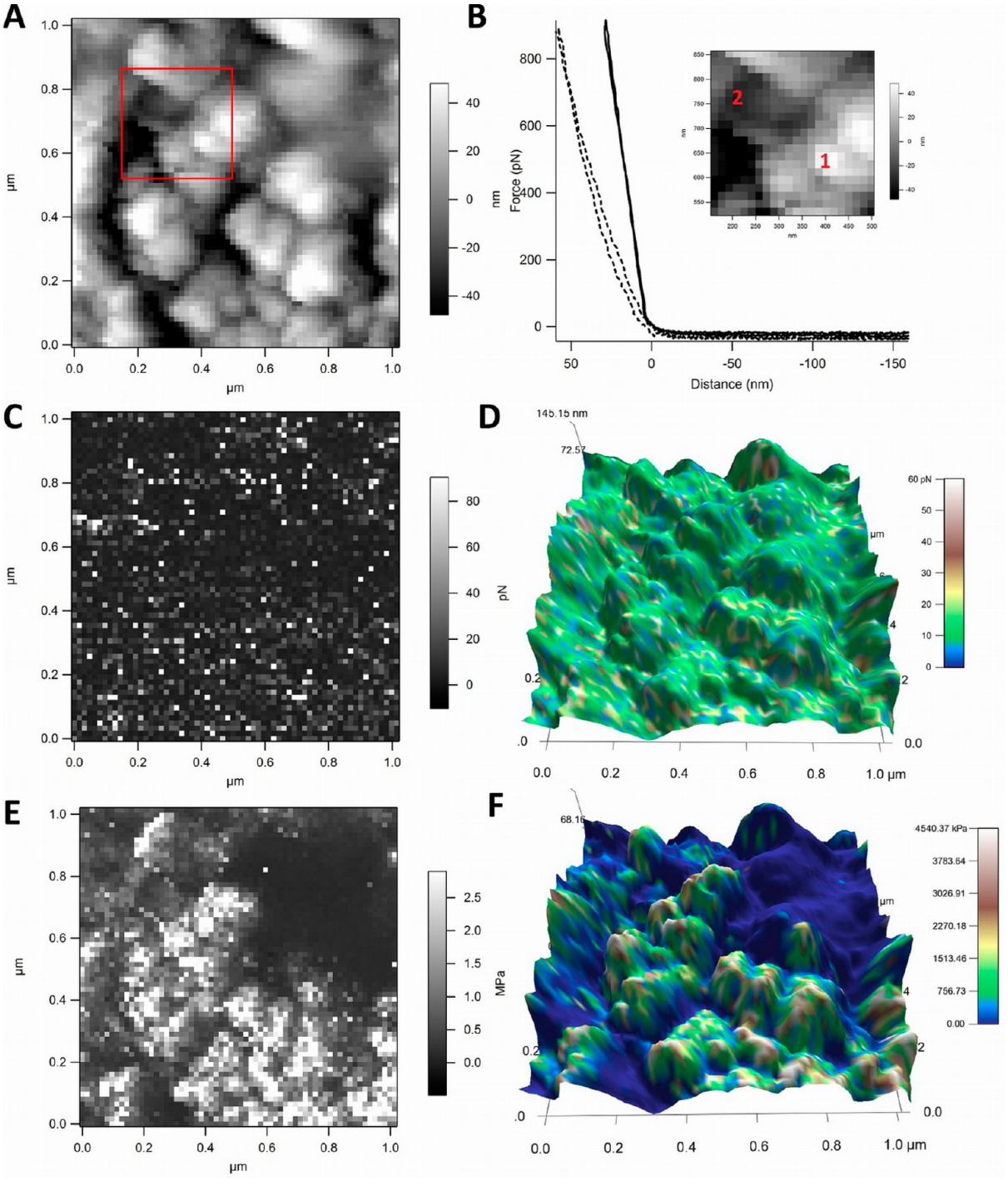

Figure 4. Uncharged film. (A) Height image (23.7 nm rms) obtained from the force map. (B) Representative curves taken from the different regions (inset) of the film. Curves 1 and 2 are taken from nodules and peripheries, respectively. (C) Adhesion map. (D) Three-dimensional image of adhesion overlaid on topography. (E) Modulus map (2.3 MPa rms). (F) Three-dimensional image of modulus overlaid on topography. Tip potential 0 mV.

Young's modulus (rms average, 5.5 MPa) than the uncharged surface though both of the surfaces showed that the nodule regions (rms average 5.4 MPa) were stiffer than their peripheries (rms average 2.3 MPa). See Figures 5E,F and 4E,F.

Although the increase in the modulus for the charged samples was not significant, the oxidation−reduction cycling of conducting polymers has previously been shown to induce significant changes in the stiffness of PPy films.[3,4,7,26] It has been well stated in the literature that both the osmotic pressure mediated by the water of hydration and the ion concentration gradients of the electrolyte salt and/or inherent stiffness change of the polypyrrole chains in response to doping are relevant factors explaining the observed changes in the elasticity in PPy doped with sulfonic acids.[26] For PPy-HA in aqueous NaCl electrolyte, the exchange of both Na^+ and Cl^- ions (and their water of hydration), driven by the Donnan potentials of the ions, is likely to occur.[26] However, we did not observe a significant change in Young's modulus attributable to an excess

dx.doi.org/10.1021/la4009366 | *Langmuir* 2013, 29, 6099−6108

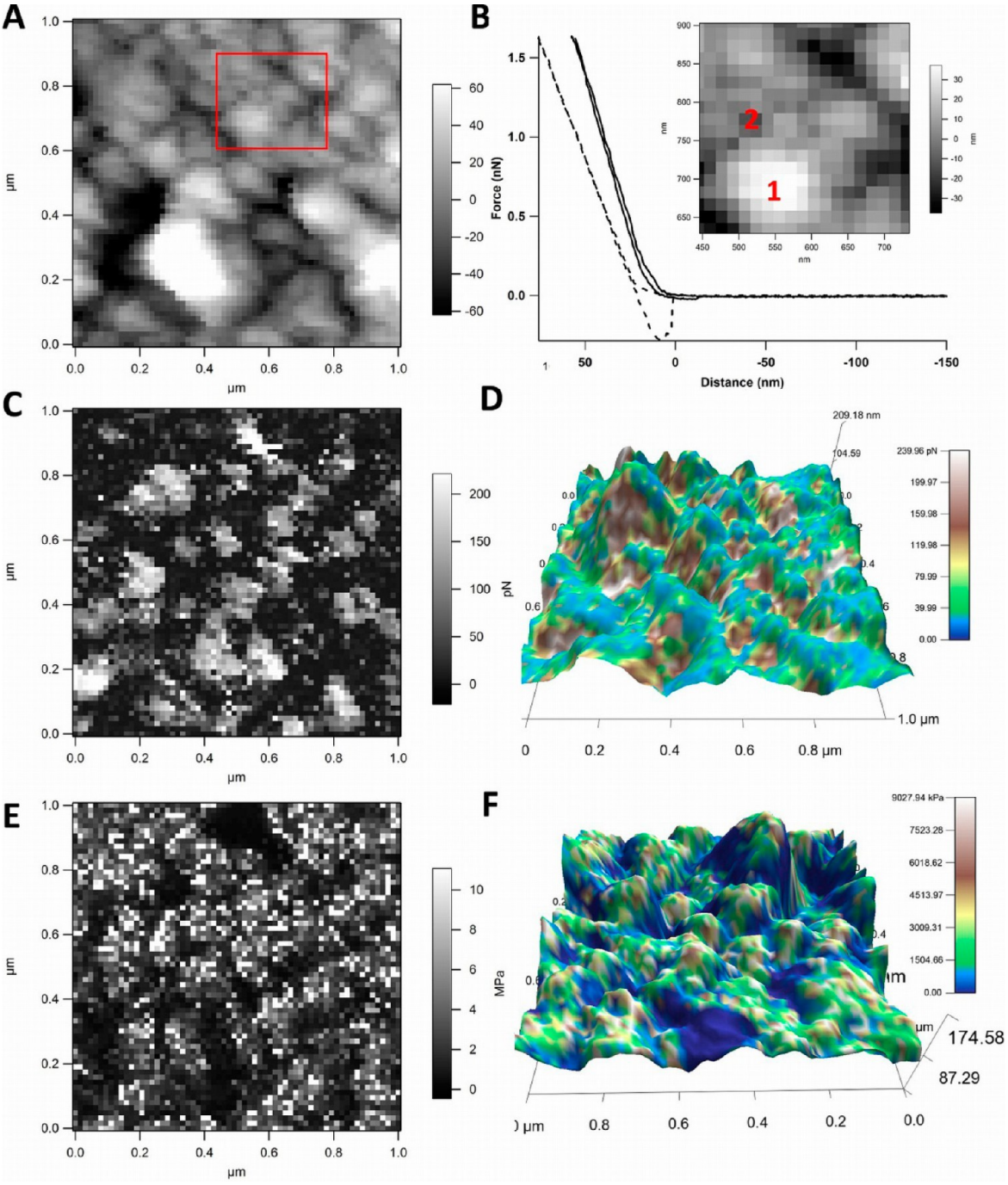

Figure 5. Charged film (+200 mV). (A) Height image (29.2 nm rms) obtained from the force map. (B) Representative curves taken from the different regions (inset) of the film. Curves 1 and 2 are taken from nodules and peripheries, respectively. (C) Adhesion map (634 pN rms). (D) Three-dimensional image of adhesion overlaid on topography. (E) Modulus map (5.3 MPa rms). (F) Three-dimensional image of modulus overlaid on topography. Tip potential 0 mV.

concentration of Na^+ (or Cl^-) ions within PPy-HA upon charging. Interestingly, Young's modulus values measured for PPy-HA in this study are two orders of magnitude lower than previously reported values. For example, the incorporation of HA into PPy was qualitatively shown to result in rougher and more brittle films when compared to PPy-PSS films,[1] whereas Gelmi et al.[7] obtained values of 600−700 MPa in phosphate-buffered saline using similar AFM approaches. The large variation in the reported Young's moduli is attributable to the different polymerization methods and reagents, especially the origin and molecular weight of the HA. The thickness of the PPy-HA films in this study was significantly greater than in the previous studies.[1,5,7,25] The typical Young's moduli of conducting polymers, including PPy and commonly applied poly(3,4-ethylenedioxythiophene) (PEDOT), on the order of several hundred MPa to a few GPa remain one caveat in their use as biomaterials because there is often a modulus mismatch between the polymer and much softer target tissue (e.g., nerve and muscle). Therefore, our particularly low modulus values (2−5 MPa) are representative of more mechanically compatible conducting polymers with values that are even lower than for PPy doped with poly(methoxy aniline sulfonate) (PMAS) (30

dx.doi.org/10.1021/la4009366 | *Langmuir* 2013, 29, 6099−6108

MPa), whereby PMAS introduces hydrogel-like properties and a high water content (>90%). An important conclusion that could be drawn from the above force maps is that the charging of the films did not have a significant effect on the topography and Young's modulus but clearly increased the adhesion, specifically at the nodules, between the AFM tip and polymer. By excluding the topography and Young's modulus, we suggest that the interactions (e.g., electrostatic forces) and surface properties related to increased adhesion on the charged films are likely to be responsible for increased cell spreading and adhesion on these films, as observed in Table 1 and Figure 1.

Compared to the previous force maps, an applied bias to the tip enabled further investigation of the interaction forces, particularly electrostatic and adhesion, by providing a known surface potential at the AFM tip that could be controlled externally. Figures 6 and 7 present a total of 20 representative

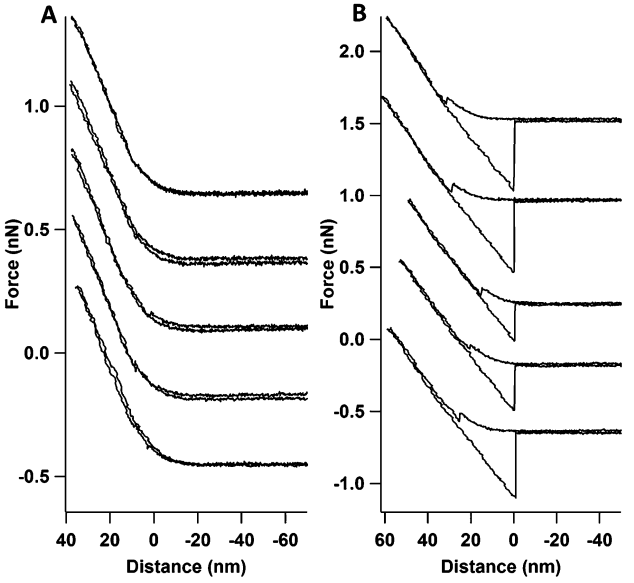

Figure 6. Force−distance curves for an uncharged (0 mV) PPy-HA film. (A) Approach curve and retracting curve on the nodules. (B) Approach curve and retraction curve on the peripheries of the nodules. Tip potential −200 mV in 0.005 M NaCl(aq) electrolyte.

force curves for the uncharged (0 mV) and charged (+200 mV) PPy-HA surfaces, respectively, obtained from force maps taken in 5 mM NaCl with a bias of −200 mV applied to the AFM tip. Force curves were selected either from the nodules (Figures 6A and 7A) or from the peripheries of the nodules (Figures 6B and 7B). For the uncharged surfaces, a repulsive interaction upon approach and no adhesion were observed on the nodules, whereas in contrast, an increased "snap-in" or small-range attractive force upon the approach and adhesion of ∼350 pN rms were observed in the peripheries (Figure 6A,B). In particular, we show below that the observed repulsive interactions for both the nodules and their peripheries are due to electrostatic forces and suggest that the small-range attractive forces occurring only on the peripheries contribute to the observed adhesion (Figure 6B). When the film was charged (+200 mV), small-range attractive forces upon approach and increased adhesion appeared on the nodules and remained on the nodule peripheries (Figure 7). The appearance of small-range attractive forces on the nodule areas again correlates with adhesion at these locations. Furthermore, the effect of charging

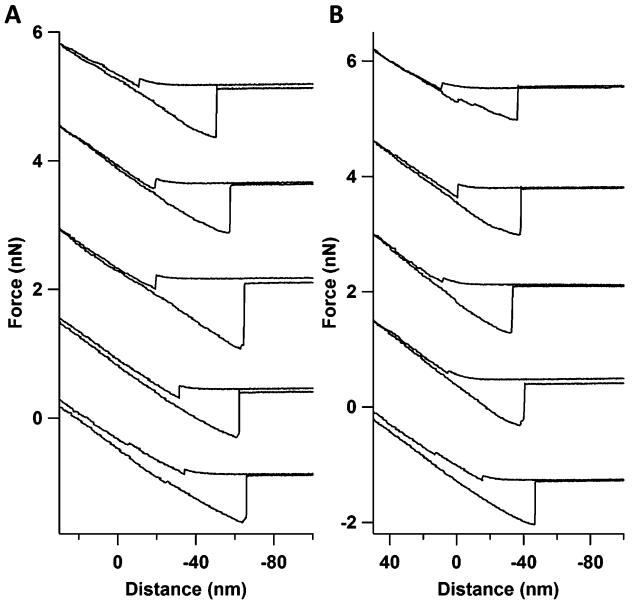

Figure 7. Force−distance curves for a charged (+200 mV) PPy-HA film. (A) Approach curve and retracting curve on the nodules. (B) Approach curve and retraction curve on the peripheries of the nodules. Tip potential −200 mV in 0.005 M NaCl(aq) electrolyte.

on the surface potential in the KFPM images and the above surface forces is clearly more pronounced in the nodule regions. Occasionally multiple small-range attractive forces were observed on the charged films, indicating that some of these interactions were attributable to the tip penetrating the sample surface. Indeed, the observed low elastic modulus of these films makes them susceptible to penetration by the AFM tip, which may contribute to the adhesion. The presence of these multiple snap-ins, however, makes the analysis somewhat more difficult because of the fact that small-range attractive forces also arise as a result of the break-up of the double-layer repulsion and the subsequent effect of the attractive (van der Waals) force experienced by the tip in the proximity of the surface. The presence of increased attractive forces and decreased electrostatic repulsion on the nodules of charged surfaces compared to the uncharged can additionally result in increased adhesion. It is therefore possible to elucidate the fundamental surface forces that play a role in the nanoscale and molecular interactions at these polymer surfaces in liquid.

Individual force curves were fitted to DLVO models to assess the relative magnitude of the excess surface charges and potentials. In total, eight force curves per sample were analyzed, including fitting comparisons between force curves taken on the nodules and peripheries, for both uncharged and charged films. The significance of the possible variation in the surface potentials between the samples was assessed by the student's *t* test at a level of significance of 0.05. The linear DLVO model comprising a single-exponential function fitted reasonably well to the data (nonweighted χ^2, $R > 0.96$) using the two-parameter (surface potential and Debye length) model, and the fitted curves were consistent with the theoretical Debye length of the 0.005 M NaCl(aq) electrolyte (4.3 nm). Figure 8 shows representative examples of the fitting for force curves taken from the nodule regions of the uncharged (Figure 8A) and charged surfaces (Figure 8B). Long-range repulsion forces on the order of 10−100 pN were present in all analyzed curves and attributable to double-layer electrostatics of a slightly negatively

dx.doi.org/10.1021/la4009366 | *Langmuir* 2013, 29, 6099−6108

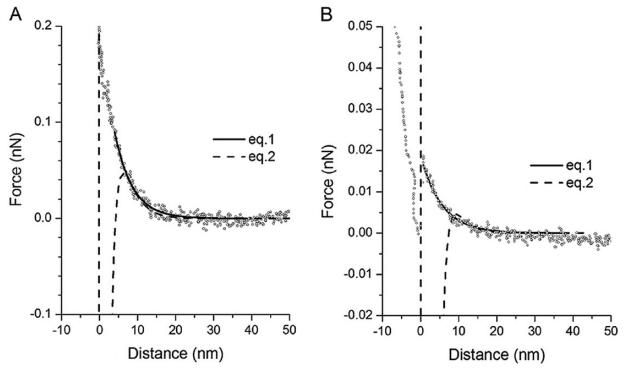

Figure 8. Typical approach curves and data fitting to simple exponential model according to Ohshima[20] (eq 1, solid line) and a nonlinear model according to Hull and Kitchener[21] (eq 2, dashed line). (A) Uncharged PPy-HA and (B) charged PPy-HA films. Tip potential −200 mV in 0.005 M NaCl(aq) electrolyte.

charged surface and negatively charged AFM tip (−200 mV). For example, the quantified surface potential was in the range of −5 to −50 mV for the films. Initial qualitative observations showed that the repulsive forces were weaker for the charged films than for the uncharged films, as expected because of the application of a positive bias (+200 mV) to these surfaces and are quantitatively supported by the data fitting to the force curves. From the DLVO fitting, it was confirmed that the nodules of the charged film were significantly more positive than the nodules of the uncharged film ($p < .001$ at a significance level of 0.05), but there was no significant difference in the estimated surface potentials of the peripheries of the uncharged and charged films ($p = 0.11$ at a significance level of 0.05). When comparing differences across the polymer surfaces, the estimated surface potentials of the nodules were slightly but not significantly more positive than that of the peripheries of the uncharged surfaces ($p = 0.086$ at a significance level of 0.05). In contrast, the estimated surface potential of the nodules was significantly higher than that of the peripheries ($p < .001$ at a significance level of 0.05) for the charged films.

It is noted that the nonlinear DLVO model (eq 2, Figure 8A), which is more appropriate for larger surface potentials, did not fit the data as well as the linear model and hence showed a larger error in the calculated surface potential values. The nonlinear model also estimated shorter Debye lengths (3.0 nm) that were not consistent with expected theoretical values (4.3 nm). The weakness of the nonlinear model may be due to its greater sensitivity to error in defining the zero distance (contact region) from the force curve recorded for soft materials such as the compliant PPy-HA films. Fitting the data to the nonlinear DLVO model (eq 2, Figure 8A) systematically predicted a 10−25 mV more negative surface potential, both on the nodules and on the peripheries. Nonetheless, the general trends were identical to the linear model.

4. CONCLUSIONS

This work highlighted that the application of a relatively small potential bias of +200 mV to a PPy-HA film may have a large effect on the early attachment and spreading of hASCs. The majority of hASCs were uniformly adhered at the 3 h time point on charged sample surfaces; however, cells seeded on noncharged PPy-HA surfaces were unevenly spread, and many cells were not well adhered. The enhancement was significant with and without a preincubation period in the cell culture medium containing plasma proteins. Preincubation alone had statistically equal significance in enhancing cell attachment. By using KPFM and AFM force mapping, it was possible to investigate the effects of charging on surface properties, including the topography, modulus, surface potential, and adhesion, with the intention of correlating these properties with the hASCs cell adhesion. As it turned out, charging did not have a significant effect on topography and only slightly increased the modulus but did significantly alter the surface potential and adhesion forces acting between the AFM tip and polymer. AFM force measurements with a negatively biased tip (−200 mV) showed that prior to charging of the PPy-HA films short-range attractive forces and adhesion were restricted to the nodule peripheries but appeared on the nodules and uniformly across the film upon charging. The exact reason for such changes to occur only at the nodules is unclear, though these regions are known to be more highly doped and conductive. As expected, the charging of the films increased the surface potential, as shown by both KPFM and DLVO analysis of the force curves, which had the effect of also decreasing the magnitude of the electrostatic repulsion between the tip and polymer. These changes in the interaction potential profile, namely, the decreased repulsion and increased short-range attraction and adhesion, give insight into the nature of the interaction forces that may play a role in promoting cell adhesion. Future work will concentrate on imaging the surface interactions of the PPy-HA surface with an AFM tip functionalized with plasma proteins and systematically adjusting the salt concentration and pH to investigate further the double-force electrostatics.

AUTHOR INFORMATION

Corresponding Author

*E-mail: Jani.Pelto@vtt.fi. Tel: +358 207223571. Fax: +358 207223498.

Author Contributions

This manuscript was written through the contributions of all authors. All authors have given approval to the final version of the manuscript.

Notes

The authors declare no competing financial interest.

ACKNOWLEDGMENTS

The support of this work by The Finnish Funding Agency for Technology and Innovation (TEKES) is gratefully acknowledged. This work has been supported by the Australian Research Council under the Australian Research Fellowship and DP110104359 (M.J.H.) and ARC Federation Fellowship (G.G.W.). We also greatly acknowledge the Australian National Fabrication Facility (ANFF) for providing atomic force microscopy instrumentation. We thank Miss Anne Rajala and Miss Leena Jaatinen for the preparation of the samples.

ABBREVIATIONS

DMEM, Dulbecco's modified Eagle's medium; DPBS, Dulbecco's phosphate-buffered saline; FACS, fluorescence-activated cell sorting; CD, cluster of differentiation (e.g., CD10-PECy7, CD10 transmembrane protein, fluorescence labeled with R-phycoerythrin cyanine-7 conjugate)

REFERENCES

(1) Collier, J.; Camp, J.; Hudson, T.; Schmidt, C. Synthesis and characterization of polypyrrole-hyaluronic acid composite biomaterials for tissue engineering applications. *J. Biomed. Mater. Res.* **2000**, *50*, 574−584.

(2) Zhang, X.; Bai, R. Surface electric properties of polypyrrole in aqueous solutions. *Langmuir* **2003**, *19*, 10703−10709.

(3) Pelto, J.; Haimi, S.; Puukilainen, E.; Whitten, P.; Spinks, G.; Bahrami-Samani, M.; Ritala, M.; Vuorinen, T. Electroactivity and biocompatibility of polypyrrole hyaluronic acid multi-walled carbon nanotube composite. *J. Biomed. Mater. Res. A* **2010**, *93*, 1056−1067.

(4) Pei, Q.; Inganäs, O. Electrochemical applications of the bending beam method. Mass transport and volume changes in polypyrrole during redox. *J. Phys. Chem.* **1992**, *96*, 10507−10514.

(5) Serra Moreno, J.; Panero, S.; Materazzi, S.; Martinelli, A.; Sabbieti, M.; Agas, D.; Materazzi, G. Polypyrrole-polysaccharide thin films characteristics: electrosynthesis and biological properties. *J. Biomed. Mater. Res. A* **2009**, *88*, 832−840.

(6) Lee, J.; Schmidt, C. Pyrrole-hyaluronic acid conjugates for decreasing cell binding to metals and conducting polymers. *Acta Biomater.* **2010**, *6*, 4396−4404.

(7) Gelmi, A.; Higgins, M.; Wallace, G. Physical surface and electromechanical properties of doped polypyrrole biomaterials. *Biomaterials* **2010**, *31*, 1974−1983.

(8) Gilmore, K.; Kita, M.; Han, Y.; Gelmi, A.; Higgins, M.; Moulton, S. E.; Clark, G. M.; Kapsa, R.; Wallace, G. G. Skeletal muscle cell proliferation and differentiation on polypyrrole substrates doped with extracellular matrix components. *Biomaterials* **2009**, *30*, 5292−5304.

(9) Dubiel, E.; Martin, Y.; Vermette, P. Bridging the gap between physicochemistry and interpretation prevalent in cell-surface interactions. *Chem. Rev.* **2011**, *111*, 2900−2936.

(10) Lubarsky, G.; Browne, M.; Mitchell, S.; Davidson, M.; Bradley, R. The influence of electrostatic forces on protein adsorption. *Colloids Surf., B* **2005**, *44*, 56−63.

(11) Wang, J.; Bard, A. Direct atomic force microscopic determination of surface charge at the gold/electrolyte interface-the inadequacy of classical GCS theory in describing the double-layer charge distribution. *J. Phys. Chem. B* **2001**, *105*, 5217−5222.

(12) Discher, D.; Janmey, P.; Wang, Y. Tissue cells feel and respond to the stiffness of their substrate. *Science* **2005**, *310*, 1139−1143.

(13) De Santis, G.; Lennon, A.; Boschetti, F.; Verhegghe, B.; Verdonck, P.; Prendergast, P. How can cells sense the elasticity of a substrate? An analysis using a cell tensegrity model. *Eur. Cells Mater.* **2011**, *22*, 202−213.

(14) Gimble, J.; Guilak, F. Adipose-derived adult stem cells: Isolation, characterization, and differentiation potential. *Cytotherapy* **2003**, *5*, 362−369.

(15) Gronthos, S.; Franklin, D.; Leddy, H.; Robey, P.; Storms, R.; Gimble, J. Surface protein characterization of human adipose tissue-derived stromal cells. *J. Cell Physiol.* **2001**, *189*, 54−63.

(16) Lindroos, B.; Boucher, S.; Chase, L.; Kuokkanen, H.; Huhtala, H.; Haataja, R.; Vemuri, M.; Suuronen, R.; Miettinen, S. Serum-free, xeno-free culture media maintain the proliferation rate and multipotentiality of adipose stem cells in vitro. *Cytotherapy* **2009**, *11*, 958−972.

(17) Haimi, S.; Pirhonen, E.; Moimas, L.; Lindroos, B.; Huhtala, H.; Räty, S.; Kuokkanen, H.; Sándor, G. K.; Miettinen, S.; Suuronen, R. Calcium phosphate surface treatment of bioactive glass causes a delay in early osteogenic differentiation of adipose stem cells. *J. Biomed. Mater. Res., Part A* **2009**, *91*, 540−547.

(18) Haimi, S.; Suuriniemi, N.; Haaparanta, A.-M.; Ellä, V.; Lindroos, B.; Huhtala, H.; Räty, S.; Kuokkanen, H.; Sándor, G. K.; Kellomäki, M.; Miettinen, S.; Suuronen, R. Growth and osteogenic differentiation of adipose stem cells on PLA/bioactive glass and PLA/β-TCP scaffolds. *Tissue Eng. Part A* **2009**, *15*, 1473−1480.

(19) Sader, J.; Chon, J.; Mulvaney, P. Calibration of rectangular atomic force microscope cantilevers. *Rev. Sci. Instrum.* **1999**, *70*, 3967−3969.

(20) Ohshima, H. Electrostatic interaction between a sphere and a planar surface: generalization of point-charge/surface image interaction to particle/surface image interaction. *J. Colloid Interface Sci.* **1998**, *198*, 42−52.

(21) Hull, M.; Kitchener, J. Interaction of spherical colloidal particles with planar surfaces. *Trans. Faraday Soc.* **1969**, *65*, 3093−3104.

(22) Higgins, M.; Molino, P.; Yue, Z.; Wallace, G. Organic conducting polymer-protein interactions. *Chem. Mater.* **2012**, *24*, 828−839.

(23) Barisci, J.; Stella, R.; Spinks, G.; Wallace, G. Characterization of the topography and surface potential of electrodeposited conducting polymer films using atomic force and electric force microscopies. *Electrochim. Acta* **2000**, *46*, 519−531.

(24) O'Neil, K.; Shaw, B.; Semenikhin, O. On the origin of mesoscopic inhomogeneity of conducting polymers. *J. Phys. Chem. B* **2007**, *111*, 9253−9269.

(25) Gelmi, A.; Higgins, M.; Wallace, G. Attractive and repulsive interactions originating from lateral nanometer variations in surface charge/energy of hyaluronic acid and chondroitin sulfate doped polypyrrole observed using atomic force microscopy. *J. Phys. Chem. B* **2012**, *116*, 13498−13505.

(26) Bay, L.; Jacobsen, T.; Skaarup, S.; West, K. Mechanism of actuation in conducting polymers: osmotic expansion. *J. Phys. Chem. B* **2001**, *105*, 8492−8497.

Publication 4

Björninen, M., Siljander, A., Pelto, J., Hyttinen, J.,
Kellomäki, M., Miettinen, S., Seppänen, R., Haimi, S.

Comparison of Chondroitin Sulfate and Hyaluronic Acid Doped Conductive Polypyrrole Films for Adipose Stem Cells.

Annals of Biomedical Engineering. Vol. 42 (2014) No: 9, 1889 - 1900.

Annals of Biomedical Engineering (© 2014)
DOI: 10.1007/s10439-014-1023-7

BMES BIOMEDICAL ENGINEERING SOCIETY™ www.bmes.org

Comparison of Chondroitin Sulfate and Hyaluronic Acid Doped Conductive Polypyrrole Films for Adipose Stem Cells

MIINA BJÖRNINEN,[1,2,3] ALIISA SILJANDER,[1,2,3] JANI PELTO,[4] JARI HYTTINEN,[3,5] MINNA KELLOMÄKI,[3,5] SUSANNA MIETTINEN,[1,2,3] RIITTA SEPPÄNEN,[1,3,5,6] and SUVI HAIMI[1,2,3,7]

[1]Adult Stem Cells, Institute of Biomedical Technology, University of Tampere, Biokatu 8, 33014 Tampere, Finland; [2]Science Centre, Pirkanmaa Hospital District, P.O. BOX 2000, 33521 Tampere, Finland; [3]BioMediTech, Biokatu 10, 33520 Tampere, Finland; [4]VTT Technical Research Centre of Finland, Sinitaival 6, P.O. Box 1300, 33101 Tampere, Finland; [5]Department of Biomedical Engineering, Department of Electronics and Communications Engineering, Tampere University of Technology, P.O. 692, 33101 Tampere, Finland; [6]Department of Eye, Ear, and Oral Diseases, Tampere University Hospital, Division 3, P.O. Box 2000, 33521 Tampere, Finland; and [7]Department of Biomaterials Science and Technology, University of Twente, P.O. Box 217, 7500, AEEnschede, The Netherlands

(Received 7 January 2014; accepted 29 April 2014)

Associate Editor Kent Leach oversaw the review of this article.

Abstract—Polypyrrole (PPy) is a conductive polymer that has aroused interest due to its biocompatibility with several cell types and high tailorability as an electroconductive scaffold coating. This study compares the effect of hyaluronic acid (HA) and chondroitin sulfate (CS) doped PPy films on human adipose stem cells (hASCs) under electrical stimulation. The PPy films were synthetized electrochemically. The surface morphology of PPy–HA and PPy–CS was characterized by an atomic force microscope. A pulsed biphasic electric current (BEC) was applied *via* PPy films non-stimulated samples acting as controls. Viability, attachment, proliferation and osteogenic differentiation of hASCs were evaluated by live/dead staining, DNA content, Alkaline phosphatase activity and mineralization assays. Human ASCs grew as a homogenous cell sheet on PPy–CS surfaces, whereas on PPy–HA cells clustered into small spherical structures. PPy–CS supported hASC proliferation significantly better than PPy–HA at the 7 day time point. Both substrates equally triggered early osteogenic differentiation of hASCs, although mineralization was significantly induced on PPy–CS compared to PPy–HA under BEC. These differences may be due to different surface morphologies originating from the CS and HA dopants. Our results suggest that PPy–CS in particular is a potential osteogenic scaffold coating for bone tissue engineering.

Keywords—Mesenchymal stem cells, Osteogenic, Electrical stimulation, Polysaccharide.

Address correspondence to Suvi Haimi, Adult Stem Cells, Institute of Biomedical Technology, University of Tampere, Biokatu 8, 33014 Tampere, Finland. Electronic mail: suvi.haimi@uta.fi

ABBREVIATIONS

BEC	Biphasic electric current
ES	Electrical stimulation
hASC	Human adipose stem cells
PPy–CS	Chondroitin sulfate doped polypyrrole
PPy–HA	Hyaluronic acid doped polypyrrole
PS	Polystyrene cell culture plate

INTRODUCTION

Conducting polymers are an arising interest in the field of tissue engineering as they can deliver electrochemical as well as electromechanical stimulation to cells. From those polypyrrole (PPy) and poly(3,4-ethylenedioxythiophene) (PEDOT) are the most investigated for biomedical applications owing to their good biocompatibility *in vivo* and *in vitro*.[8] PPy is intensively investigated for bone[9,37,38,46] and neural applications[41,50] due to its easy modification with bioactive agents in ambient conditions and highly adjustable properties, such as surface charge and topography[17,18,44,46] whereas PEDOT studies concentrate more on neural electrodes and nerve grafts[1–5,13,20,21,35,42] mostly owing to PEDOT's higher electrical conductivity and stability compared to PPy.[8] In addition to bone and neural tissue engineering, PPy has so far been studied as bioactive coatings to improve osseointegration,[11] in biosensors,[7] drug delivery systems[50] and actuators.[34] Regards to the comprehensive research supporting

Published online: 14 May 2014

PPy's use in bone tissue engineering, we chose PPy and evaluated the effects of the two most potential bioactive dopants, hyaluronic acid (HA) and chondroitin sulfate (CS) in the PPy films.

In electrochemical polymerization of PPy, charged biomolecules, such as negatively charged glycosaminoglycans (GAGs), can be incorporated into the structure by doping when PPy is electrochemically polymerized by oxidation. Dopants play an important role in mediating the electric charges between the PPy chains.[23] In addition, the surface topography and mechanical properties of PPy can also widely be altered by the choice of dopant.[17,18]

CS and HA are GAGs commonly found in the extracellular matrices (ECMs) of most animal tissues. CS is a major proteoglycan component in organic matrix of the bone and is involved in the mineralization of the bone tissue whereas HA takes part in various cellular processes, such as ECM organization and metabolism.[43] Both GAGs are reported to support osteogenic differentiation of mesenchymal stem cells (MSCs) in scaffold structures *in vitro*.[28,53]

As regards integrating HA and CS into PPy surfaces, HA doped PPy (PPy–HA) has been studied with mouse bone marrow derived MSCs resulting in promoted osteogenic differentiation[46] and with MC3T3-E1 osteoblasts confirming cell differentiation on the surface.[45] In addition, we recently were the first to report an excellent attachment, proliferation and early osteogenic differentiation of hASCs on chemically synthetized PPy–CS coating in non-woven polylactide fiber scaffolds.[38] As both biomolecules are potential dopants for PPy coating in osteogenic applications, a systematic comparison is required to understand their benefits and differences with human MSCs.

Inherent electrical currents and fields are essential in terms of the growth and remodeling of bone tissue. This was first demonstrated by Fukada and Yasuda, who reported bone formation under tension when positive charge was dominating, and the opposite in case of a negative charge and compression.[15] This remark led to the development of electrical stimulation (ES) devices for treating severe bone defects.[22]

Even though ES has been acknowledged as a bone treatment method for several decades, the exploitation of ES to MSCs in bone tissue engineering has been studied only recently.[25,26,31,36] These studies have shown that various types of ES can be applied to improve osteogenic differentiation and proliferation of MSCs, yet no specific parameters for the efficient differentiation of MSC towards mature osteoblasts have so far been identified. In addition, most of the above mentioned studies exploited inert conductive substrates; hence a conductive coating with bioactive molecules and topographical cues may yield interesting synergy mimicking the natural environment in the bone tissue more closely. We therefore wanted to evaluate hASC spreading, proliferation and osteogenic differentiation on PPy surfaces under ES with our novel ES device developed in-house. To the best to our knowledge, this is the first paper to systematically compare HA and CS doped PPy coatings for hASCs.

MATERIALS AND METHODS

Polypyrrole Synthesis

Pyrrole (Sigma-Aldrich, St. Louis, USA) of 0.07 mL and 1 mg of HA from Streptococcus equi (Sigma-Aldrich) or CS A from bovine trachea (Sigma-Aldrich) were added per 1 mL of water. PPy–HA and PPy–CS films were grown electrochemically on a sputter-coated polyethylene-naphthalate film (PEN)/Au films (125 μm Dupont Teonex®), with 50 nm Au-coating (VTT Technical Research Center of Finland) as a working electrode, platinum mesh as a counter electrode and Ag/AgCl as a reference electrode. Constant potential of 1.0 V was applied to the films until 300 mC cm^{-2} polymerization charge had passed the cell. The stimulation plates and plate covers were sterilized by gamma irradiation (BBF Sterilisationsservice GmbH, Kernen, Germany) with an irradiation dose of >25 kGy that has not been reported to significantly alter the conductivity of the films.[12,54]

Surface Characterization of Polypyrrole Film

The surface morphology and roughness (R_a) values of the PPy films were characterized by an atomic force microscope (AFM; Park Systems XE-100, Korea) in both dry and wet conditions due to the significant water absorption and hence swelling phenomenon of wet PPy films in physiological conditions.[39,48] PPy–HA and PPy–CS films were incubated for 4 days in osteogenic medium (OM) containing 250 mM ascorbic acid 2-phosphate (Sigma-Aldrich), 5 nM dexamethasone (Sigma-Aldrich) and 10 mM *b*-glycerofosfate (Sigma-Aldrich) supplemented to maintenance medium consisting of Modified Eagle Medium/Ham's Nutrient mixture F-12 (DMEM/F-12 1:1 Invitogen), 10% fetal bovine serum (FBS; Invitrogen), 1% L-glutamine (GlutaMAX I; Invitrogen) and 1% antibiotics/antimycotic (100 U mL^{-1} penicillin, 0.1 mg mL^{-1} streptomycin; Invitrogen).

To distinguish the swelling effect from the typical polysaccharide doped PPy nodular morphology,[17,18,39,45,47] and in order to image the nanoscopic details of the soft films,[17,38] dried samples were analyzed using non-contact AFM (Park Systems XE-100)

in air using silicon probe ACTA-905M (Applied NanoStructures, Inc.) with a nominal resonance frequency of 300 kHz, spring constant 40 N m^{-1} and tip radius <10 nm. Images of 5×5 μm^2 were acquired with a scan rate of 0.5 Hz. Prior to imaging, the sample surfaces were carefully rinsed with deionized water and dried in ambient air.

The films pre-incubated in OM were imaged in Dulbecco's phosphate-buffered saline (PBS; Lonza Biowhittaker, Switzerland) using a contact mode AFM. Silicon nitride probes HYDRA-6R100N (Applied Nanostructures, Inc., Santa Clara, USA), with a nominal force constant 0.28 N m^{-1} and a tip radius of curvature <8 nm were applied. Areas of 20×20 μm^2 were scanned at 7 and 20 nN force set points for PPy–HA and PPy–CS surfaces respectively. Images of 12×12 μm^2 were acquired with the scan speed of 1 Hz.

R_a value analysis of the raw 512×512 pixel data was conducted. R_a values for 10 randomly chosen 4×4 μm^2 subareas were calculated using Park Systems XEI 1.7.5 image analysis software. AFM image data was 4th order plane fitted to show the nanoscale details of the PPy–HA and PPy–CS surfaces.

Characterization of Electrical Properties of the Films

Electrochemical impedance spectroscopy (EIS) and cyclic voltammetry measurements were taken from 1 cm^2 of doped PPy films on gold Mylar that was acting as working electrode. Platinum mesh acted as counter electrode and Ag/AgCl (3.0 M NaCl) as reference electrode. Impedance measurements were recorded by using CH 660D Electrochemical Analyzer/Workstation (CH Instruments, Austin, USA). Impedance spectra were obtained from 100 mHz to 100 kHz using an AC amplitude of ± 200 mV. All EIS measurements were performed at their resting potential ranging from $+70$ to $+195$ mV vs. the reference electrode to prevent destruction in the films. Average impedance and the standard deviation at 10 and 100 Hz were calculated from three samples per film type.

Cyclic voltammetry of the films was recorded in PBS by CH 660D Electrochemical Analyzer/Workstation in similar electrode setup as impedance recordings. Measurements were performed at the scan rate of 50 mV s^{-1} within the range of -0.6 to 0.5 V.

After the cell culture experiments, the through plane electrical conductivity of PPy films was monitored in air using a simple two-wire test setup (Fluke 170 multimeter, Washington, USA). The top and bottom electrodes applied were a round Au contact electrode (contact area of 16 mm^2) and the PEN/Au film, respectively.

Isolation and Culture of Human Adipose Stem Cells

The adipose tissue was obtained from tissue harvests from surgical procedures on three female donors with an average age of 54 ± 12 years in the Department of Plastic Surgery, Tampere University Hospital. The tissue harvesting and the use of hASCs were conducted in accordance with the Ethics Committee of the Pirkanmaa Hospital District (R03058). The hASC isolation method was presented earlier by Haimi *et al.*[24]. Briefly, the samples from adipose tissue were digested with collagenase type I (1.5 mg (ml; Invitrogen, California, USA). After centrifugation and filtration, the isolated hASCs were maintained and expanded in T-75 cm^2 polystyrene flask (Nunc, Roskilde, Denmark). The experiments were repeated three times, each time using different donors.

Before the cell seeding, PPy–CS and PPy–HA films were rinsed with PBS and pre-treated with maintenance medium at 37 °C for 48 h. PPy–CS and PPy–HA coated plates were cell seeded at passage 3 with a density of 16000 cells cm^{-2}. Cells were allowed to attach for 24 h before initiation of ES. On the first day of stimulation the maintenance medium was replaced by OM and medium was changed twice a week.

Flow Cytometric Surface Marker Expression Analysis

Cells were characterized by a fluorescence-activated cell sorter (FACSAria; BD Biosciences, Erembodegem, Belgium) at passage 1 after primary culture in T-75 flasks. This was described earlier by Lindroos *et al.*[33]. Monoclonal antibodies were used against the following surface markers: CD14, CD19, CD49d-PE, CD90-APC, CD106-PECy5 (BD Biosciences); CD45-FITC (Miltenyi Biotech, Bergisch Gladbach, Germany); CD34-APC, HLAABC-PE, HLA-DR-PE (Immunotools GmbH, Friesoythe, Germany) and CD105-PE (R&D Systems Inc., MN, USA). Analysis was performed on 10,000 cells per sample and unstained cell samples were used to compensate the background autofluorescence levels.

Biphasic Electrical Stimulation of Human Adipose Stem Cells

The stimulation plate assembly was earlier described by Pelto *et al.*[39] As an exception to the previous setup, PPy film was polymerized on the bottom electrode. ES was performed in a cell culturing incubator (37 °C, 5% CO_2). Samples were stimulated for 4 h a day for 14 days with a biphasic electric current (BEC) of ± 0.2 V amplitude, 2.5 ms pulse width and 100 Hz pulse repetition frequency. Non-stimulated samples acted as controls in each film type. The shortest vertical distance

between the top (Fig. 1: 1) and the bottom (Fig. 1: 2) electrodes immersed in each well was 2 mm. The measured steady state direct current after the 2.5 ms pulses was in the range of 40–50 μA cm^{-2}, corresponding to a cell impedance of 5 kΩ. The direction of the current was perpendicular to the PPy films.

Cell Attachment and Viability

Cell attachment and viability were evaluated qualitatively using live/dead staining (Molecular Probes, Eugene, USA). Cells were incubated in PBS-based dye solution containing 0.5 μM of CellTracker^{TM} Green (5-chloromethylfluorescein diacetate, CMFDA; Molecular Probes) and Ethidium homodimer-1 (EthD-1; Molecular Probes) at room temperature for 45 min. Samples were examined with a fluorescence microscope (Olympus IX51, Olympus Finland PLC, Vantaa, Finland). Standard polystyrene (PS) culturing plates (Nunc, Roskilde, Denmark) served as a positive control for the cell viability and morphology evaluation.

Cell Proliferation

Cell proliferation was studied with CyQuant® Cell Proliferation Assay Kit (Molecular Probes). The experiment was performed according to the manufacturer's protocol. Briefly, on the day of the analysis, samples were carefully washed with PBS and cells were suspended in 0.1% Triton-X 100 buffer (Sigma-Aldrich) in PBS and stored at −70 °C until analysis. After thawing, 20 μl of three parallel samples was mixed with CyQuant® GR dye and lysis buffer. The fluorescence was measured with a microplate reader (Victor 1420 Multilabel Counter, Wallac, Turku, Finland) at 480/520 nm.

Osteogenic Differentiation

Alkaline phosphatase (ALP) activity was determined using an ALP Kit (Sigma-Aldrich) according to the manufacturer's protocol. The ALP activity was determined from the same Triton-X 100 lysates as in the cell proliferation assay. The samples were incubated with 50% alkaline buffer solution (2-amino-2-methyl-1-propanol, 1.5 mol L^{-1}, pH 10.3; Sigma-Aldrich) and 50% of stock substrate solution (*p*-nitrophenyl phosphate; Sigma-Aldrich) at 37°C for exactly 15 min. To stop the reaction 1.0 mol L^{-1} sodium hydroxide was added. The intensity of the color was measured at 405 nm using a microplate reader (Victor 1420).

The mineralization of the ECM was studied with Alizarin Red staining. Samples were rinsed with PBS and fixed in ice cold 70% ethanol (Altia Corporation, Helsinki, Finland) for 60 min at room temperature. Samples were then rinsed with distilled water before the addition of 2% Alizarin Red solution (pH 4.2; Sigma-Aldrich) for 5 min. After incubation, samples were rinsed three times with distilled water and once with 70% ethanol. Samples were then incubated in cetylpyridium chloride (Sigma-Aldrich) for 3 hours. Supernatant was pipetted in triplicate on a 96-well plate (Nunc, Roskilde, Denmark) and absorbance measured at 544 nm using a microplate reader (Victor 1420).

Statistical Analysis

The statistical analyses of R_a values, DNA content, ALP activity and mineralization were performed with SPSS, version 19. R_a values of the films were analyzed with Student's *t* test and the equal variance assumption was checked by Levene's Test. A one way analysis of variance (ANOVA) with Bonferroni *post hoc* correction was used to determine the effect of the PPy coating and ES on DNA content, ALP activity and mineralization. The effect of culture duration on proliferation and ALP activity was analyzed using Student's *t* test for independent samples. The cell culture experiments were repeated three times with three par-

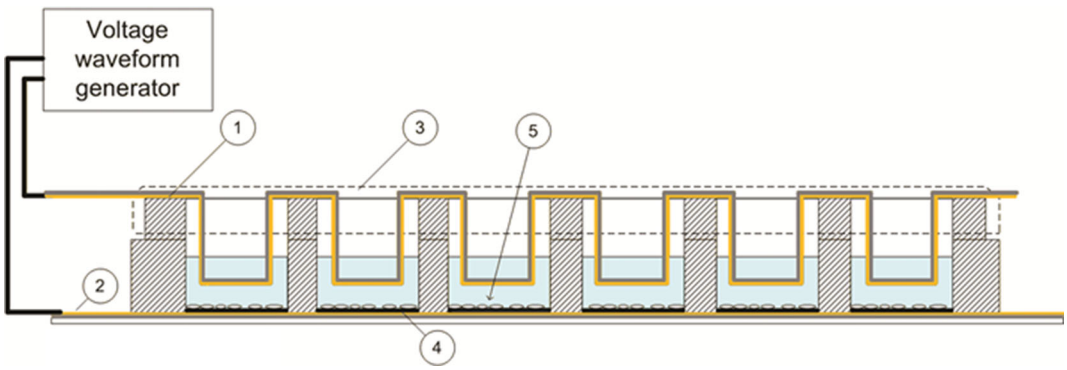

FIGURE 1. (a) Schematic illustration of the stimulation device geometry side projection. Top (1) and bottom (2) electrodes were made of gold coated PEN film. Cells were seeded to the bottom electrode (4) coated with PPy layer.

allel samples, each repetition using a different hASC donor. The data from the three experiments were combined and presented as mean ± standard deviation (SD) and the results were considered statistically significant when $p < 0.05$.

RESULTS

Surface Characterization of Polypyrrole Film

The measured R_a values of the wet and the dry PPy films are presented in Table 1. PPy–HA films had significantly higher R_a values than PPy–CS in PBS, whereas dry PPy–HA film had significantly lower R_a values when measured with non-contact AFM in air.

The non-contact AFM data (Figs. 2a and 2b) show the nanoscopic details of the dry PPy–CS (Fig. 2a) and PPy–HA (Fig. 2b) films. PPy–CS surface texture (Fig. 2a) consisted mainly of nodules, sized 40–50 nm in diameter and 5–10 nm in measurable height, which were organized into a porous web. The surface texture of PPy–HA (Fig. 2b) consisted of larger nodules, 150–160 nm in diameter and 30–35 nm in height. In both films, protrusions were sparsely distributed. The protrusions in the PPy–CS and PPy–HA films were similar in size, 500 nm in diameter and 100 nm in high. The nanoscopic texture was only observed in the dry samples and was not resolvable by AFM in PBS.

Imaging in PBS (contact mode) revealed a strongly undulating morphology of both films consisting of uniformly spread small 800–1000 nm nodules (Figs. 2c and 2d) and sparsely spread 4–10 μm circular protrusions covered with nodules (not visible in the flattened image data in Fig. 2).The nodules were typically of 100–150 and 200–300 nm in height for the PPy–HA (Fig. 2d) and PPy–CS (Fig. 2c) respectively. It is noteworthy that the hills caused by the undulating morphology as well as the protrusions were significantly higher than the nodules, typically 400–500 and 600–800 nm for the PPy–CS and PPy–HA films respectively. The protrusions in the PPy–CS were circular whereas those in PPy–HA were more oval. Hence the R_a values obtained from the AFM in PBS based on raw imaged data were not only representative of the nodules' height and shape but of the height of the protrusions.

Electrical Properties of the Films

The impedance of PPy–HA and PPy–CS films did not vary significantly yet PPy–CS showed slightly higher impedance values at 10 and 100 Hz (Table 1). Both films showed similar trend in the impedance spectra (Fig. 3). Both films showed well-defined voltammetric profiles though PPy–CS had slightly higher electrochemical activity and doping level compared to PPy–HA, as evidenced by the integrated surface areas covered by the respective voltammograms (Fig. 4). The conductivity of the films was confirmed to be in similar 10^{-3} S cm^{-1} levels as before the experiment when measured in air (data not shown).

Flow Cytometric Surface Marker Expression Analysis

Surface marker expression of hASCs was characterized by flow cytometric analysis. The cells used in this study expressed the surface markers CD73, CD90 and CD105 as shown in Table 2. Moderate expression was expressed by CD34, CD49d, HLA-ABC and HLA-DR whereas no expression was detected in CD14, CD19, CD45 and CD106. According to the results, hASCs expressed several of the specific antigens that verify the mesenchymal origin of hASCs.[33]

Cell Attachment and Viability

Cell attachment and viability were determined by live/dead staining which revealed extensive clustering of hASCs on PPy–HA surfaces as shown in Figs. 5e, 5f, 5g and 5h. In contrast, hASCs on PPy–CS were homogenously spread already after 1 week of culture (Figs. 5a, 5b, 5c, and 5d). This homogenous monolayer of hASCs was only evident on PPy–CS, since hASCs cultured on PS (Fig. 5i and 5j) were also sparsely spread on day 7. The increase in cell number over time was most obvious on PS, which had decid-

TABLE 1. R_a values of non-contact AFM data of air-dried PPy films and contact mode AFM of wet films in PBS as well as impedance at 100 Hz frequency.

Sample	R_a in air (nm)	R_a in PBS (nm)	Impedance at 10 Hz in PBS (Ω)	Impedance at 100 Hz in PBS (Ω)
PPy–CS	14 ± 0.8	320 ± 28	54 ± 13	45 ± 6
PPy–HA	8.6 ± 0.2	420 ± 40	51 ± 6	45 ± 2

R_a values were calculated from 10 successive measurements over randomly selected 4 × 4 μm^2 sub-areas. The differences between PPy–CS and PPy–HA were significant in both wet and dry films.

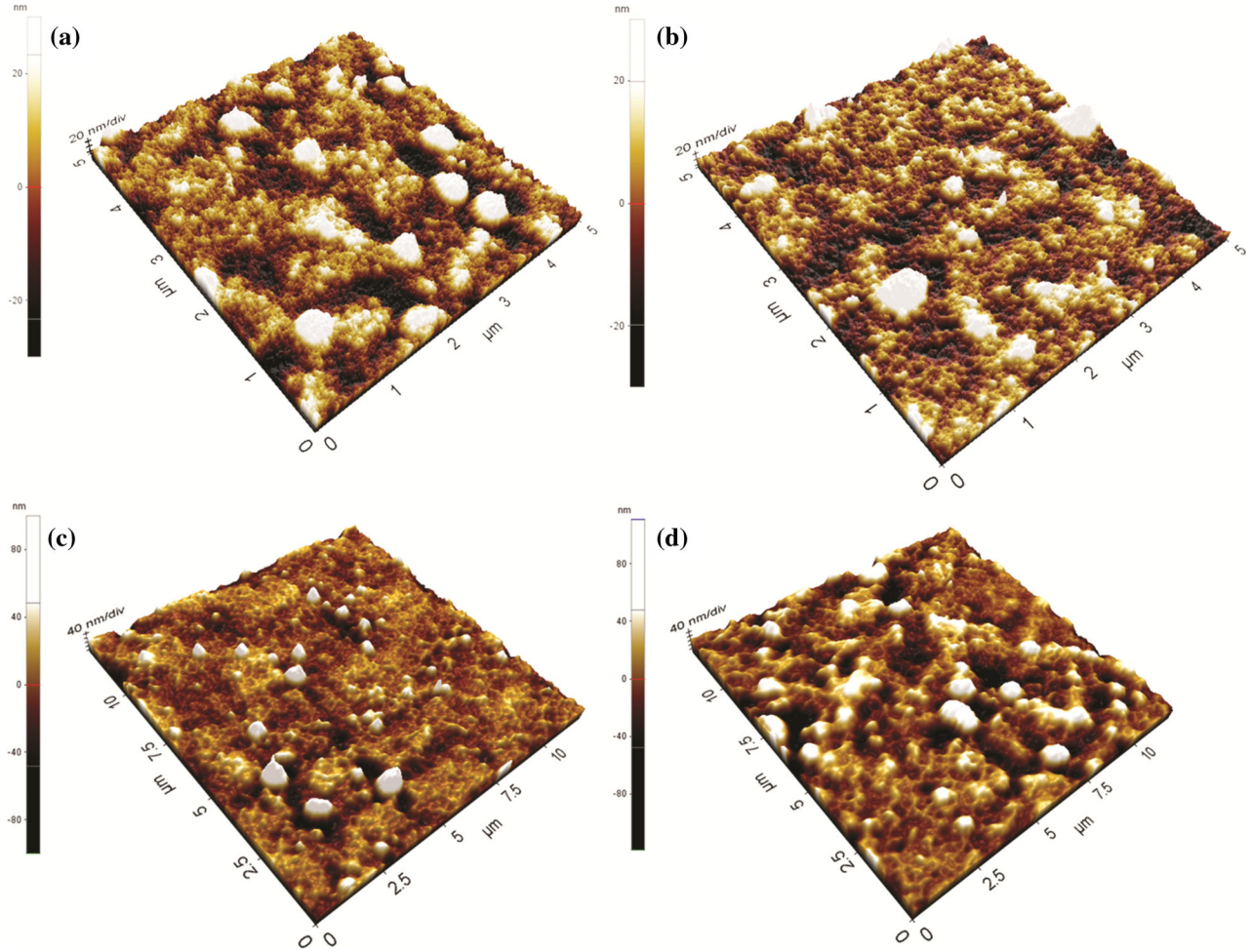

FIGURE 2. Surface topography of dry PPy–CS (a) and PPy–HA (b) films imaged using non-contact AFM in air. The sparsely distributed protrusions are seen as white areas. Scanned area is 5 × 5 μm and Z-scale 20 nm/division. (c) Surface topography images of wet PPy–CS and (d) PPy–HA films imaged with contact AFM in PBS. 800–1000 nm nodules are seen as white areas. Scanned area is 12 × 12 μm and Z-scales of the images are 40 nm/division.

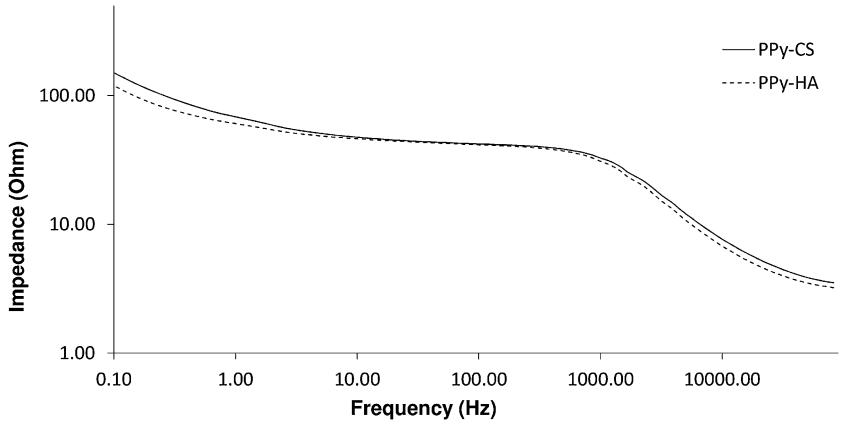

FIGURE 3. Impedance spectra for PPy films recorded in PBS.

edly fewer cells than PPy–CS at both time points. As regards BEC, no notable differences in cell number were seen between the control and stimulated group with neither of the dopants. The majority of the cells were viable on both PPy films at both time points in all experimental groups.

Cell Proliferation

Cell proliferation was evaluated quantitatively by measuring the total DNA content (Fig. 6). In the control group, the cell number on PPy–CS was significantly higher than PPy–HA on day 7. The increase in cell number on PPy–CS followed a similar trend at both time points under BEC compared with PPy–HA. However, no further significant differences were found. Consistently with the live/dead staining, no significant differences in cell number were found between the control and the stimulation group. The cell number increased significantly over time with both PPy–CS and PPy–HA without stimulation. In the stimulated group, only PPy–CS showed a significantly increasing cell number.

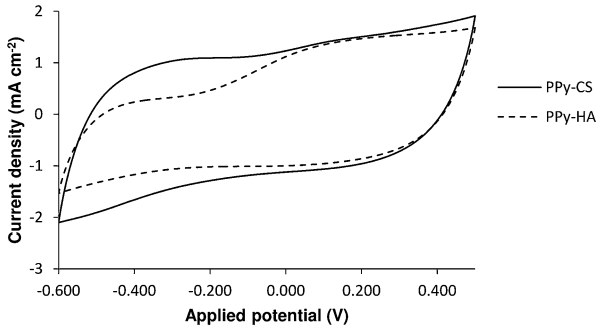

FIGURE 4. Cyclic voltammogram of PPy–CS and PPy–HA in PBS.

Osteogenic Differentiation

Both PPy–HA and PPy–CS supported hASC early osteogenic differentiation (Fig. 7) and no significant differences were detected between these two different material groups. However, ALP activity increased significantly over time only in the PPy–CS with and without stimulation. No significant differences between BEC and control groups were detected.

Under BEC, PPy–CS triggered significantly higher mineralization compared to PPy–HA (Fig. 8), whereas in the control group no significant differences were detected. Consistently with proliferation and ALP activity, no significant differences were found between BEC and the control group. One donor line did not show reliably detectable mineralization at the 14 day time point, therefore only data from two other repetitions are shown.

DISCUSSION

It has recently been reported that nanoscopic roughness in combination with microscale roughness are essential for the adhesion, proliferation and osteogenic differentiation of cells of mesenchymal origin.[19] Moreover, strong cell–ECM interactions enhanced by specific surface characteristics have an important role in osteogenic commitment among MSCs,[14] whereas proliferation is required for effective occupation of the scaffold.

As a main finding, our results demonstrate that CS was a superior dopant to HA by triggering significantly higher proliferation of hASCs after 1 week of culture. Both PPy films supported early osteogenic differentiation of hASCs yet PPy–CS showed significantly higher mineralization than PPy–HA in the stimulation group. Importantly, hASCs cultured on PPy–CS showed typical MSC morphology and already formed a homogenous monolayer on the PPy–CS film by day 7, whereas PPy–HA triggered clustering of the cells

TABLE 2. Surface marker expression of the undifferentiated hASCs after primary culture in maintenance medium.

Surface protein	Antigen	Mean	SD	Expression
CD14	Serum lipopolysaccharide binding protein	1.7	0.8	Negative
CD19	B lymphocyte-lineage differentiation antigen	0.9	0.4	Negative
CD34	Sialomucin-like adhesion molecule	9.3	8.75	Moderate expression
CD45	Leukocyte common antigen	1.1	0.3	Negative
CD49d	Integrin a2, VLA-4	11	13	Moderate expression
CD73	Ecto-50-nucleotidase	91.2	12.7	Positive
CD90	Thy-1 (T cell surface glycoprotein)	99	0.3	Positive
CD105	SH-2, endoglin	85.3	12.1	Positive
CD106	VCAM-1 (vascular cell adhesion molecule)	0.7	0.3	Negative
HLA-ABC	Major histocompatibility class I antigens	9.2	7.0	Moderate expression
HLA-DR	Major histocompatibility class II antigens	7.0	0.4	Moderate expression

Data presented as mean ± SD obtained from the three different hASC donors.

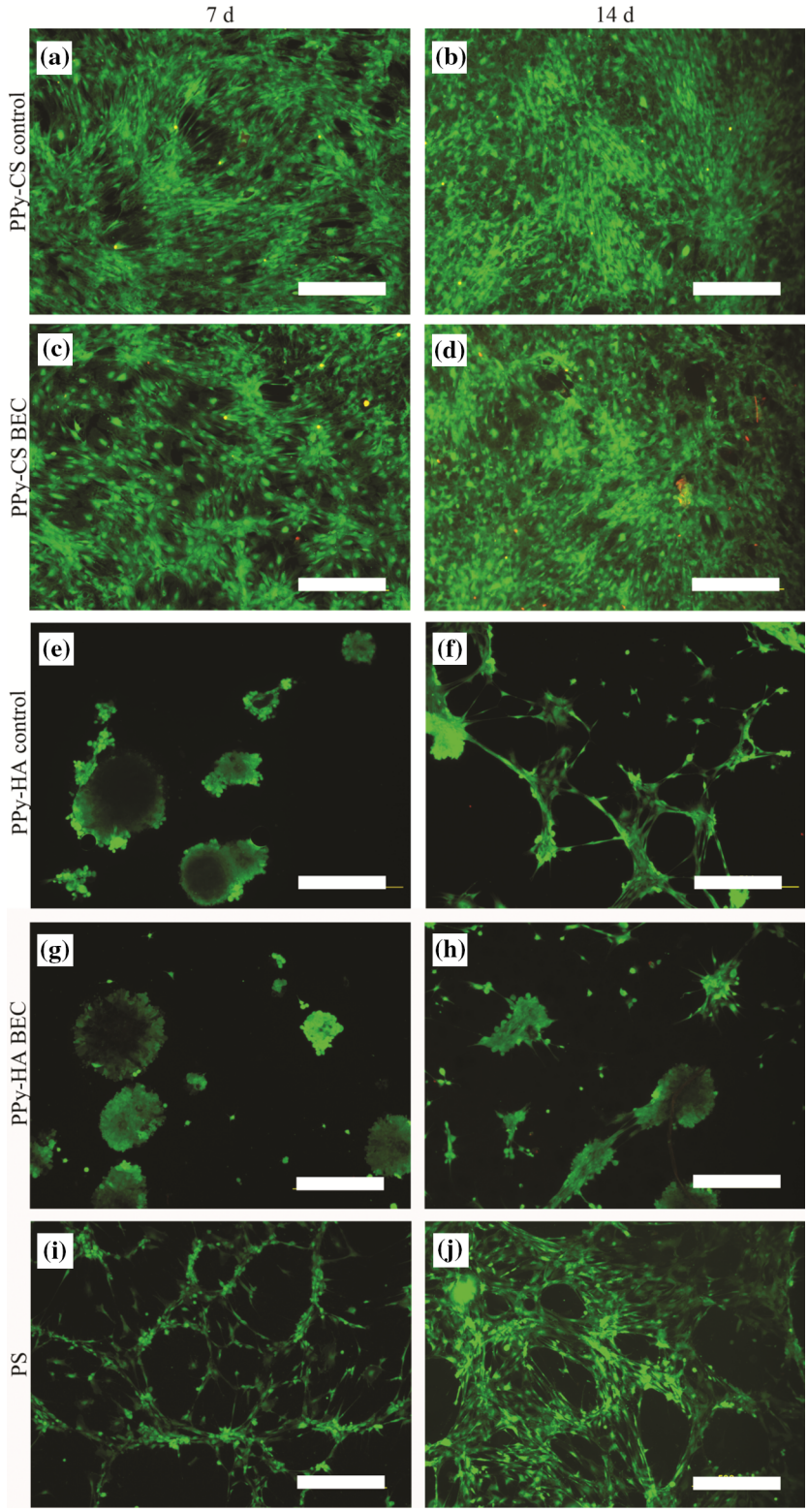

FIGURE 5. Live/dead images of hASCs on PPy–CS controls (a, b) and BEC stimulated group (c, d), PPy–HA controls (e, f) and BEC stimulated group (g, h) and PS (i, j) on days 7 and 14. Scale bar is 500 μm.

leading to detachment from the film. Aggregation of cells is an undesired effect in osteogenic applications and more characteristic of chondrogenic differentiation as it is one of the earliest signs of chondrogenesis. This suggests that PPy–HA could be a potential scaffold coating candidate for chondrogenic applications.[55]

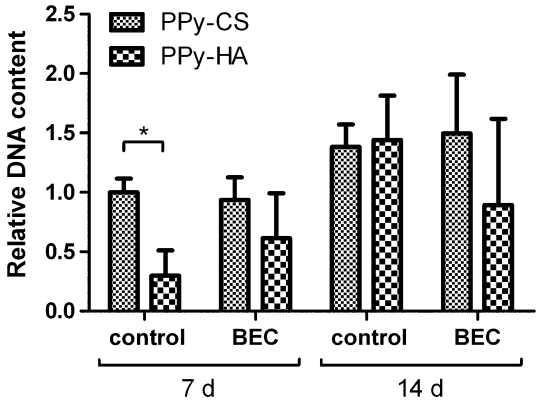

FIGURE 6. Relative DNA content of hASCs cultured for 7 and 14 days on PPy–CS and PPy–HA substrates with and without BEC. PPy–CS had significantly higher DNA content than did PPy–HA in control. The cell number increased significantly over time in the control group, on both PPy–CS and PPy–HA samples. In the stimulated group, only PPy–CS showed significantly increasing cell number. The results are expressed as mean ± SD and *$p < 0.05$.

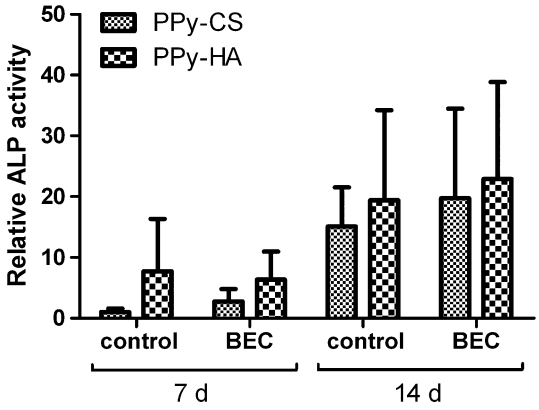

FIGURE 7. Relative ALP activity of hASCs cultured for 7 and 14 days on PPy CS and PPy–HA substrates with and without BEC. ALP activity increased significantly over time on PPy–CS control and BEC group. The results are expressed as mean ± SD.

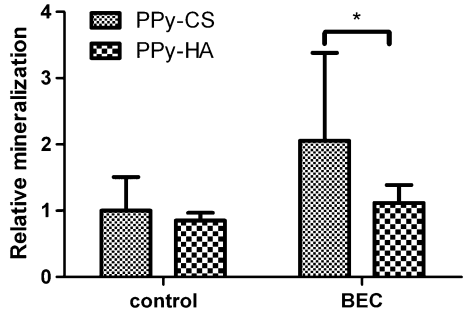

FIGURE 8. Relative ECM mineralization of hASCs cultured for 14 days on PPy CS and PPy–HA substrates with and without BEC. PPy–CS had significantly higher mineralization under BEC compared to PPy–HA. The results are expressed as mean ± SD and *$p < 0.05$.

As both dopants are commonly used macromolecules in bone tissue engineering, the reason why PPy–HA caused clustering of hASC most probably lies in the physical surface properties, such as the morphology, hydrophilicity and elasticity of the PPy–HA surface. Even though the non-uniform microscopic morphology was present in both PPy–CS and PPy–HA wet films, the swollen protrusions were significantly higher in the PPy–HA, consequently reflecting the measured R_a values in contact mode imaging. Similar differences between PPy–HA and PPy–CS morphology have also been reported by Gelmi *et al.*[17] In addition, Gilmore *et al.* compared thin and thick PPy films, formed by different polymerization charges, and examined various dopants. They concluded that PPy–HA did not support myoblast adhesion or differentiation and the elevated R_a values were one of the parameters correlating with the poor performance of PPy–HA. Greater surface thickness of PPy–HA compared to other films, such as PPy–CS, was deduced to lead to the development of greater nodules.[18] Moreover, smooth surface morphology polymerized with low current densities (100–700 μA cm^{-2}) was demonstrated to be the key parameter for MC3T3-E1 osteoblast adhesion on PPy–HA surfaces, whereas those polymerized with higher current densities (~1 mA cm^{-2}) exhibited more irregular surface and did not ensure good cell adhesion.[45] The current density in our study stayed under 700 μA cm^{-2} implying that surface roughness should be within suitable ranges in means of cell adhesion during the ES.

The optimal AFM imaging conditions in PBS for the PPy–CS (force setpoint 20 nN) and PPy–HA (7 nN) films were different from those measured in air, indicating that PPy–HA was softer than PPy–CS in wet state. This was also supported by the occasional adhesion of the AFM tip to the PPy–HA surface. Comparison of AFM images in wet and dry state also showed that both PPy–CS and PPy–HA films absorbed significant amounts of PBS, resulting in swelling, large dimensional changes and softening of the films to hydrogel-like materials. Earlier studies with similar films have estimated the swelling percent to be 11–25%.[39,46,48] In contrast, Gelmi *et al.* did not detect any significant swelling of the PPy–HA and PPy–CS films.[17] Furthermore, the nanoscopic textures of the dry samples were significantly different from those of the wet samples. The characteristic nodular nanomorphology was detected for both PPy films in PBS consistent with earlier reports on PPy–CS and PPy–HA.[17,18,47]

Hills caused by undulating morphology may result from the local detachment of the material from its metallic substrate, which has been previously observed for electropolymerized PPy–HA films on Au microelectrodes upon repeated electrochemical cycling.

However, the characteristic pattern of the microscopic circular protrusions has not been observed on microelectrodes of other substrates.[39]

Regarding electrical properties of the films, the choice of dopant did not pose drastically different impedance either at 10 or at 100 Hz, yet the decrease in impedance was more evident for PPy–CS from 10 to 100 Hz. In contrast to our study, Gilmore *et al.* has earlier compared impedance of electrochemically grown thick PPy–HA and PPy–CS films reporting substantially higher impedance for PPy–HA at 10 Hz.[18] Cyclic voltammetry showed slightly higher electrical activity and doping level of PPy–CS. Higher acidic strength of dopants has been shown to enhance charge carrier (bipolaron) formation in the PPy chains, hence, the stronger acidity of the sulfonic acid groups in CS compared to less acidic carboxylic acid groups in HA could potentially yield higher doping ratio in PPy–CS.[32]

The selected parameters of the ES in our study were based on earlier study with ASCs in osteogenic applications.[25] According to Hammerick *et al.*, ALP activity increased in mouse ASCs in response to pulsed electric field stimulation. We chose a pulsed BEC waveform since it is expected to prevent the accumulation of charged proteins and keep the pH of media at steady levels.[31] In addition to our present work, only one study has examined the effect of a combination of PPy and ES on osteogenic differentiation for conducting a study with SAOS-2 cells.[37] Interestingly, mineralization in our study was significantly higher in PPy–CS compared to PPy–HA in BEC group whereas no differences were detected in control group. Mineralization slightly increased in both groups, being more substantial in PPy–CS, yet not significant. This could suggest synergistic effects of PPy–CS and BEC. The reason why no significant effect of ES on ALP activity could be detected in our study is not clear. One possible reason might be donor variation in means of osteogenic differentiation, which has been reported with MSCs exposed to dexamethasone.[6] In our study, one patient had clearly higher ALP activity than the two others on day 14 (data not shown). In addition, the standard deviation of the stimulated groups was, in general, slightly higher than in the control groups, which may have prevented the detection of some differences between the groups. The reason for greater deviation could be attributable to synergy between BEC and PPy coating, such as overoxidation of PPy during high electrochemical potentials that leads to the loss of conductivity,[10] and de-doping or ion exchange between medium and PPy.[16,27] Moreover, several factors, such as protein deposition from the culture medium and their interactions with redox reactions of the PPy surface[27] or local detachment of PPy film may have affected on the homogenicity of the electrical field. To minimize the bias, three parallel samples were used in all of the assays in every patient lineage. Despite the slight increase in mineralization under BEC, more systematic screening of BEC parameters is needed to find an effective ES pattern for ASCs.

Even though PPy is considered biocompatible by several *in vivo* studies, the longest implantation period has only been six months,[29,40,51,52] PPy is not inherently biodegradable which may pose challenges in its use in tissue engineering. It may be possible that PPy coatings do not fully erode during their use of time and therefore it needs further evaluation of the long term effects in the body. What comes to the inevitable erosion products, PPy nanoparticles have shown to be less cytotoxic compared to silver or TiO_2 nanoparticles that are common wear products of orthopedic implants.[30,49]

CONCLUSION

PPy–CS supported the proliferation and homogenous spreading of hASCs significantly more than PPy–HA. Both PPy–CS and PPy–HA supported early osteogenic differentiation of hASCs over time but mineralization of hASCs was significantly greater with PPy–CS under BEC. PPy–HA is not recommended for osteogenic applications as it promotes the clustering and detachment of hASCs. This is most probably due to different surface properties since PPy–HA had a significantly rougher and softer surface than did PPy–CS in wet conditions. BEC stimulation showed no significant effects on hASC proliferation or osteogenic differentiation. This is the first study to report on the suitability of PPy–CS for bone tissue engineering applications.

ACKNOWLEDGMENTS

The authors would like to thank Ms. Anne Rajala M.Sc, Ms. Ana Luísa Delgado Lima, and Ms. Hanna Juhola for the preparation and of the scaffolds, Ms. Anna-Maija Honkala, Ms. Minna Salomäki M.Sc and Ms Miia Juntunen for their assistance in the cell culture work. This study was financially supported by the Finnish Funding Agency for Technology and Innovation (TEKES), the Academy of Finland and the Competitive Research Funding of Tampere University Hospital (Grant 9K020).

REFERENCES

[1]Abidian, M. R., J. M. Corey, D. R. Kipke, and D. C. Martin. Conducting-polymer nanotubes improve electrical properties, mechanical adhesion, neural attachment, and

neurite outgrowth of neural electrodes. *Small* 6:421–429, 2010.
[2]Abidian, M. R., E. D. Daneshvar, B. M. Egeland, D. R. Kipke, P. S. Cederna, and M. G. Urbanchek. Hybrid conducting polymer–hydrogel conduits for axonal growth and neural tissue engineering. *Adv. Healthc. Mater.* 1:762–767, 2012.
[3]Abidian, M. R., D.-H. Kim, and D. C. Martin. Conducting-polymer nanotubes for controlled drug release. *Adv. Mater.* 18:405–409, 2006.
[4]Abidian, M. R., K. A. Ludwig, T. C. Marzullo, D. C. Martin, and D. R. Kipke. Interfacing conducting polymer nanotubes with the central nervous system: chronic neural recording using poly(3,4-ethylenedioxythiophene) nanotubes. *Adv. Mater.* 21:3764–3770, 2009.
[5]Abidian, M. R., and D. C. Martin. Multifunctional nanobiomaterials for neural interfaces. *Adv. Funct. Mater.* 19:573–585, 2009.
[6]Alm, J. J., T. J. Heino, T. A. Hentunen, H. K. Vaananen, and H. T. Aro. Transient 100 nM dexamethasone treatment reduces inter- and intraindividual variations in osteoblastic differentiation of bone marrow-derived human mesenchymal stem cells. *Tissue Eng. Part C* 18:658–666, 2012.
[7]Ates, M. A review study of (bio)sensor systems based on conducting polymers. *Mater. Sci. Eng. C* 33:1853–1859, 2013.
[8]Balint, R., N. J. Cassidy, and S. H. Cartmell. Conductive polymers: towards a smart biomaterial for tissue engineering. *Acta Biomater.* 10:S1742–7061, 2014.
[9]Castano, H., E. A. O'Rear, P. S. McFetridge, and V. I. Sikavitsas. Polypyrrole thin films formed by admicellar polymerization support the osteogenic differentiation of mesenchymal stem cells. *Macromol. Biosci.* 4:785–794, 2004.
[10]Christensen, P. A., and A. Hamnett. In situ spectroscopic investigations of the growth, electrochemical cycling and overoxidation of polypyrrole in aqueous solution. *Electrochim. Acta* 36:1263–1286, 1991.
[11]De Giglio, E., M. R. Guascito, L. Sabbatini, and G. Zambonin. Electropolymerization of pyrrole on titanium substrates for the future development of new biocompatible surfaces. *Biomaterials* 22:2609–2616, 2001.
[12]Ercan, I., I. Günal, and O. Güven. Conductance of polypyrole irradiated with gamma rays to low doses. *Radiat. Phys. Chem.* 46:813–817, 1995.
[13]Esrafilzadeh, D., J. M. Razal, S. E. Moulton, E. M. Stewart, and G. G. Wallace. Multifunctional conducting fibres with electrically controlled release of ciprofloxacin. *J. Controlled Release* 169:313–320, 2013.
[14]Frith, J. E., R. J. Mills, J. E. Hudson, and J. J. Cooper-White. Tailored integrin-extracellular matrix interactions to direct human mesenchymal stem cell differentiation. *Stem Cells Dev.* 21:2442–2456, 2012.
[15]Fukada, E., and I. Yasuda. Piezoelectric effects in collagen. *Jpn. J. Appl. Phys.* 3:117–121, 1964.
[16]Gandhi, M. R., P. Murray, G. M. Spinks, and G. G. Wallace. Mechanism of electromechanical actuation in polypyrrole. *Synth. Met.* 73:247–256, 1995.
[17]Gelmi, A., M. J. Higgins, and G. G. Wallace. Physical surface and electromechanical properties of doped polypyrrole biomaterials. *Biomaterials* 31:1974–1983, 2010.
[18]Gilmore, K. J., M. Kita, Y. Han, A. Gelmi, M. J. Higgins, S. E. Moulton, G. M. Clark, R. Kapsa, and G. G. Wallace. Skeletal muscle cell proliferation and differentiation on polypyrrole substrates doped with extracellular matrix components. *Biomaterials* 30:5292–5304, 2009.
[19]Gittens, R. A., T. McLachlan, R. Olivares-Navarrete, Y. Cai, S. Berner, R. Tannenbaum, Z. Schwartz, K. H. Sandhage, and B. D. Boyan. The effects of combined micron-/submicron-scale surface roughness and nanoscale features on cell proliferation and differentiation. *Biomaterials* 32:3395–3403, 2011.
[20]Green, R. A., N. H. Lovell, and L. A. Poole-Warren. Cell attachment functionality of bioactive conducting polymers for neural interfaces. *Biomaterials* 30:3637–3644, 2009.
[21]Green, R. A., P. B. Matteucci, R. T. Hassarati, B. Giraud, C. W. Dodds, S. Chen, P. J. Byrnes-Preston, G. J. Suaning, L. A. Poole-Warren, and N. H. Lovell. Performance of conducting polymer electrodes for stimulating neuroprosthetics. *J. Neural Eng.* 10(1):016009, 2013; (Epub 2013 Jan 3).
[22]Griffin, M., and A. Bayat. Electrical stimulation in bone healing: critical analysis by evaluating levels of evidence. *Eplasty* 11:e34, 2011.
[23]Guimard, N. K., N. Gomez, and C. E. Schmidt. Conducting polymers in biomedical engineering. *Prog. Polym. Sci.* 32:876–921, 2007.
[24]Haimi, S., L. Moimas, E. Pirhonen, B. Lindroos, H. Huhtala, S. Räty, H. Kuokkanen, G. K. Sándor, S. Miettinen, and R. Suuronen. Calcium phosphate surface treatment of bioactive glass causes a delay in early osteogenic differentiation of adipose stem cells. *J. Biomed. Mater. Res. Part A* 91A:540–547, 2009.
[25]Hammerick, K. E., A. W. James, Z. Huang, F. B. Prinz, and M. T. Longaker. Pulsed direct current electric fields enhance osteogenesis in adipose-derived stromal cells. *Tissue Eng. Part A* 16:917–931, 2010.
[26]Hess, R., A. Jaeschke, H. Neubert, V. Hintze, S. Moeller, M. Schnabelrauch, H. Wiesmann, D. A. Hart, and D. Scharnweber. Synergistic effect of defined artificial extracellular matrices and pulsed electric fields on osteogenic differentiation of human MSCs. *Biomaterials* 33:8975–8985, 2012.
[27]Higgins, M. J., P. J. Molino, Z. Yue, and G. G. Wallace. Organic conducting polymer–protein interactions. *Chem. Mater.* 24:828, 2012.
[28]Jha, A. K., X. Xu, R. L. Duncan, and X. Jia. Controlling the adhesion and differentiation of mesenchymal stem cells using hyaluronic acid-based, doubly crosslinked networks. *Biomaterials* 32:2466–2478, 2011.
[29]Jiang, X., Y. Marois, A. Traore, D. Tessier, L. H. Dao, R. Guidoin, and Z. Zhang. Tissue reaction to polypyrrole-coated polyester fabrics: an *in vivo* study in rats. *Tissue Eng.* 8:635–647, 2002.
[30]Kim, S., W. Oh, Y. S. Jeong, J. Hong, B. Cho, J. Hahn, and J. Jang. Cytotoxicity of, and innate immune response to, size-controlled polypyrrole nanoparticles in mammalian cells. *Biomaterials* 32:2342–2350, 2011.
[31]Kim, I. S., J. K. Song, Y. M. Song, T. H. Cho, T. H. Lee, S. S. Lim, S. J. Kim, and S. J. Hwang. Novel effect of biphasic electric current on *in vitro* osteogenesis and cytokine production in human mesenchymal stromal cells. *Tissue Eng. Part A* 15:2411–2422, 2009.
[32]Kuwabata, S., J. Nakamura, and H. Yoneyama. The effect of basicity of dopant anions on the conductivity of polypyrrole films. *J. Chem. Soc. Chem. Commun.* 779–780, 1988.
[33]Lindroos, B., S. Boucher, L. Chase, H. Kuokkanen, H. Huhtala, R. Haataja, M. Vemuri, R. Suuronen, and S.

Miettinen. Serum-free, xeno-free culture media maintain the proliferation rate and multipotentiality of adipose stem cells *in vitro*. *Cytotherapy* 11:958–972, 2009.
[34]Liu, A., L. Zhao, H. Bai, H. Zhao, X. Xing, and G. Shi. Polypyrrole actuator with a bioadhesive surface for accumulating bacteria from physiological media. *ACS Appl. Mater. Interfaces* 1:951–955, 2009.
[35]Ludwig, K. A., J. D. Uram, J. Yang, D. C. Martin, and D. R. Kipke. Chronic neural recordings using silicon microelectrode arrays electrochemically deposited with a poly(3,4-ethylenedioxythiophene) (PEDOT) film. *J. Neural Eng.* 3:59–70, 2006.
[36]McCullen, S. D., J. P. McQuilling, R. M. Grossfeld, J. L. Lubischer, L. I. Clarke, and E. G. Loboa. Application of low-frequency alternating current electric fields *via* interdigitated electrodes: effects on cellular viability, cytoplasmic calcium, and osteogenic differentiation of human adipose-derived stem cells. *Tissue Eng. Part C* 16:1377–1386, 2010.
[37]Meng, S., Z. Zhang, and M. Rouabhia. Accelerated osteoblast mineralization on a conductive substrate by multiple electrical stimulation. *J. Bone Miner. Metab.* 29:535–544, 2011.
[38]Pelto, J., M. Bjorninen, A. Palli, E. Talvitie, J. Hyttinen, B. Mannerstrom, R. Suuronen Seppanen, M. Kellomaki, S. Miettinen, and S. Haimi. Novel polypyrrole-coated polylactide scaffolds enhance adipose stem cell proliferation and early osteogenic differentiation. *Tissue Eng. Part A* 19:882–892, 2013.
[39]Pelto, J., S. Haimi, E. Puukilainen, P. G. Whitten, G. M. Spinks, M. Bahrami-Samani, M. Ritala, and T. Vuorinen. Electroactivity and biocompatibility of polypyrrole-hyaluronic acid multi-walled carbon nanotube composite. *J. Biomed. Mater. Res. Part A* 93A:1056–1067, 2010.
[40]Ramanaviciene, A., A. Kausaite, S. Tautkus, and A. Ramanavicius. Biocompatibility of polypyrrole particles: an *invivo* study in mice. *J. Pharm. Pharmacol.* 59:311–315, 2007.
[41]Richardson, R. T., A. K. Wise, B. C. Thompson, B. O. Flynn, P. J. Atkinson, N. J. Fretwell, J. B. Fallon, G. G. Wallace, R. K. Shepherd, G. M. Clark, and S. J. O'Leary. Polypyrrole-coated electrodes for the delivery of charge and neurotrophins to cochlear neurons. *Biomaterials* 30:2614–2624, 2009.
[42]Richardson-Burns, S. M., J. L. Hendricks, B. Foster, L. K. Povlich, D. Kim, and D. C. Martin. Polymerization of the conducting polymer poly(3,4-ethylenedioxythiophene) (PEDOT) around living neural cells. *Biomaterials* 28:1539–1552, 2007.
[43]Salbach, J., T. D. Rachner, M. Rauner, U. Hempel, U. Anderegg, S. Franz, J. C. Simon, and L. C. Hofbauer. Regenerative potential of glycosaminoglycans for skin and bone. *J. Mol. Med. (Berl)* 90:625–635, 2012.
[44]Serra Moreno, J., S. Panero, M. Artico, and P. Filippini. Synthesis and characterization of new electroactive polypyrrole–chondroitin sulphate A substrates. *Bioelectrochemistry* 72:3–9, 2008.
[45]Serra Moreno, J., S. Panero, S. Materazzi, A. Martinelli, M. G. Sabbieti, D. Agas, and G. Materazzi. Polypyrrole-polysaccharide thin films characteristics: electrosynthesis and biological properties. *J. Biomed. Mater. Res. Part A* 88A:832–840, 2009.
[46]Serra Moreno, J., M. G. Sabbieti, D. Agas, L. Marchetti, and S. Panero. Polysaccharides immobilized in polypyrrole matrices are able to induce osteogenic differentiation in mouse mesenchymal stem cells. Med: J. Tissue Eng. Regen., 2012.
[47]Silk, T., Q. Hong, J. Tamm, and R. G. Compton. AFM studies of polypyrrole film surface morphology II. Roughness characterization by the fractal dimension analysis. *Synth. Met.* 93:65–71, 1998.
[48]Smela, E., and N. Gadegaard. Volume change in polypyrrole studied by atomic force microscopy. *J. Phys. Chem. B* 105:9395–9405, 2001.
[49]St. Pierre, C. A., M. Chan, Y. Iwakura, D. C. Ayers, E. A. Kurt-Jones, and R. W. Finberg. Periprosthetic osteolysis: characterizing the innate immune response to titanium wear-particles. *J. Orthop. Res.* 28:1418–1424, 2010.
[50]Thompson, B. C., S. E. Moulton, R. T. Richardson, and G. G. Wallace. Effect of the dopant anion in polypyrrole on nerve growth and release of a neurotrophic protein. *Biomaterials* 32:3822–3831, 2011.
[51]Wang, X., X. Gu, C. Yuan, S. Chen, P. Zhang, T. Zhang, J. Yao, F. Chen, and G. Chen. Evaluation of biocompatibility of polypyrrole *in vitro* and *in vivo*. *J. Biomed. Mater. Res. Part A* 68A:411–422, 2004.
[52]Wang, Z., C. Roberge, L. H. Dao, Y. Wan, G. Shi, M. Rouabhia, R. Guidoin, and Z. Zhang. *In vivo* evaluation of a novel electrically conductive polypyrrole/poly(D,L-lactide) composite and polypyrrole-coated poly(D,L-lactide-*co*-glycolide) membranes. *J. Biomed. Mater. Res. Part A* 70A:28–38, 2004.
[53]Wollenweber, M., H. Domaschke, T. Hanke, S. Boxberger, G. Schmack, K. Gliesche, D. Scharnweber, and H. Worch. Mimicked bioartificial matrix containing chondroitin sulphate on a textile scaffold of poly(3-hydroxybutyrate) alters the differentiation of adult human mesenchymal stem cells. *Tissue Eng.* 12:345–359, 2006.
[54]Wolszczak, M., J. Kroh, and M. M. Abdel-Hamid. Some aspects of the radiation processing of conducting polymers. *Radiat. Phys. Chem.* 45:71–78, 1995.
[55]Wu, S., J. Chang, C. Wang, G. Wang, and M. Ho. Enhancement of chondrogenesis of human adipose derived stem cells in a hyaluronan-enriched microenvironment. *Biomaterials* 31:631–640, 2010.

Publication 5

Zhao, M-D., Björninen, M., Cao, L., Wang H-R., Pelto J., Hyttinen J.,
Jiang Y-Q., Kellomäki M., Miettinen S., Haimi S., Dong J.

Polypyrrole coating enhances new bone formation on polylactic/glycolic acid -β-tricalcium phosphate screws in rabbits. Polypyrrole coating enhances new bone formation on polylactic/glycolic acid -β-tricalcium phosphate screws in rabbits.

Submitted to Tissue Engineering – Part A.

.

Polypyrrole coating on poly-(lactide/glycolide)-β-tricalcium phosphate screws enhances new bone formation in rabbits

Ming-Dong Zhao[a,b,△], Miina Björninen [c,d△], Lu Cao[a,△], Hui-Ren Wang[a], Jani Pelto[e], Xiang-Qian Li[a], Jari Hyttinen[c], Yun-Qi Jiang[a], Minna Kellomäki[c], Susanna Miettinen[c,d], George K. Sándor[c,g] Suvi Haimi[c,d,f*], Jian Dong[a,*]

[a] *Department of Orthopaedic Surgery, Zhongshan Hospital, Fudan University, Shanghai 200032, China;*

[b] *Department of Orthopaedic Surgery, Jinshan Hospital, Fudan University, Shanghai 201508, China*

[c] *Adult Stem Cell Group, Institute of Biosciences and Medical Technology (BioMediTech), Biokatu, Tampere, Finland*

[d] *Science Center, Tampere University Hospital, Tampere, Finland,*

[e] *VTT Technical Research Centre of Finland, Sinitaival 6, P.O. Box 1300, 33101 Tampere, Finland,*

[f] *Department of Biomaterials Science and Technology, University of Twente, Enschede, P.O. Box 217 7500 AE Enschede.*

[g] *Tissue Engineering and Oral and Maxillofacial Surgery, Medical Research Center, University of Oulu, Oulu University Hospital, Oulu, Finland*

Corresponding authors: Jian Dong, Email: dong.jian@zs-hospital.sh.cn, and Haimi Suvi, E-mail: suvi.haimi@uta.fi

[△] *Equal contribution*

Abstract

Polypyrrole (PPy) has gained interest as an implant material due to its multifunctional properties and its high compatibility with several cell and tissue types. For the first time, the biocompatibility and osteogenic induction of PPy coating, incorporated with chondroitin sulfate (CS), were studied in vivo by implanting PPy-coated bioabsorbable polymer composite bone fixation screws into New Zealand white rabbits. Uncoated bioabsorbable polymer composite screws and commercially available stainless steel cortical screws were used as reference implants. The rabbits were euthanized 12 and 26 weeks after the implantation. The systemic effects were evaluated from food and water consumption, body weight, body temperature, clinical signs, blood samples, internal organs weights, and histological examination. Local effects were studied from bone tissue and surrounding soft tissue histology. New bone formation was evaluated by micro-computed tomography, tetracycline labelling and torsion tests.

The coated screws induced significantly more bone formation than the uncoated screws. In addition, none of the implants induced any systemic or local toxicity. The results suggest that PPy is biocompatible with bone tissue and is a potential coating for enhancing osteointegration in orthopedic implants.

Keywords: Polypyrrole (PPy); Absorbable screw; Biocompatibility; In vivo; Osteointegration.

Introduction

Poly-(lactide/glycolide) copolymers (PLGA) are widely used as bioabsorbable polymers in bone fracture fixations due to biocompatibility, non-toxicity and simple processability (Tian *et al.*, 2012). However, common disadvantages of polylactide and its copolymers as a bone implant material are their non-polar and hydrophobic surface properties, which limit cell attachment on the implant surface (Ajiro *et al.*, 2012; Wang *et al.*, 2005). Several surface modification methods have been tested for overcoming this problem, including incorporation of growth factors and mixing polymers with osteoconductive calcium phosphates (Son *et al.*, 2011; Zhang *et al.*, 2009; Zhou *et al.*, 2012). These methods may contribute to distinct properties, such as enhancement of osteointegration in the case of calcium phosphates (Zhou *et al.*, 2012), but they face limitations when highly controllable multifunctionality is desired.

Polypyrrole (PPy) is a promising polymer coating for medical implant materials due to its multifunctional properties, such as controlled drug delivery, biocompatibility and relatively high electrical conductivity (De Giglio *et al.*, 2001). It is the most frequently investigated conductive polymer due to its easy synthesis, good tunability of the surface properties and long-term ambient stability (Shi *et al.*, 2004). Furthermore, PPy incorporated with a variety of biomolecules has been investigated in several osteogenic applications in vitro (Castano *et al.*, 2004; Meng *et al.*, 2013; Meng *et al.*, 2011; Pelto *et al.*, 2013; Serra *et al.*, 2012; Zhang *et al.*, 2013). Among these studies, Pelto et al. studied a chemically polymerized PPy coating on fibrous non-woven polylactide scaffolds seeded with human mesenchymal stem cells (MSCs); they reported enhanced early osteogenic differentiation on the PPy-coated scaffolds (Pelto *et al.*, 2013). In addition to MSCs, PPy has also proven to be compatible with many other cell types such as endothelial cells, PC-12 cells and osteoblasts (De Giglio *et al.*, 2000; Garner *et al.*, 1999; Pelto *et al.*, 2013; Schmidt *et al.*, 1997).

The in vitro and in vivo biocompatibility of PPy, in both chemically and electrochemically synthetized forms, has been investigated in depth by Wang et al (Wang X. *et al.*, 2004). When a PPy coated silicone tube was applied to bridge the gap of the transected sciatic nerve of rat, they observed only a mild inflammatory reaction 6 months postoperatively. The PPy extraction solution was found to possess neither acute nor subacute toxicity, which further suggested the high biocompatibility of PPy with nerve tissue. Furthermore, PPy has been demonstrated to have a high in vivo compatibility with several other tissue types, such as the hypodermis of rats, guinea pig brain, and mice peritoneum (Cui *et al.*, 2003; Jiang *et al.*, 2002; Ramanaviciene *et al.*, 2007; Wang X. *et al.*, 2004). PPy-coated polyester fabrics have been reported to show a similar or milder inflammation in comparison to non-coated fabrics when implanted into the backs of rats (Jiang *et al.*, 2002). Moreover, no significant inflammation was detected in another study where PPy/hyaluronic acid and PPy/polystyrene sulfonate composite was implanted into subcutaneous pouches in rats for 6 weeks (Collier *et al.*, 2000). PPy has also shown its potential as a

blood-contacting material without adverse effects on hemolysis or coagulation (Zhang *et al.*, 2001).

Despite the several in vivo compatibility studies and the proven osteogenic potential of PPy in vitro, the influence and compatibility of PPy in bone tissue in vivo had not been shown before. We therefore investigated the in vivo biocompatibility and new bone formation of the PPy coating on bioabsorbable bone fixation composite screws of poly-(lactide/glycolide) copolymer (PLGA) and β-tricalcium phosphate (TCP).

Materials and methods

Polypyrrole coating

Pyrrole monomer, ferric chloride hexahydrate ($FeCl_3$) and chondroitin 6-sulfate A sodium salt (CS) from bovine tracheae were purchased from Sigma-Aldrich (St. Louis, USA). Pyrrole was distilled for purity in a vacuum before use. Other reagents were used without any further purification. Distilled water and ethanol (Altia Oyj, Rajamäki, Finland) were used in the polymerizations. PPy was oxidatively polymerized on PLGA-β-TCP-composite screws (ActivaScrew™ TCP, Bioretec, Tampere, Finland) consisting of 85:15 PLGA mixed with 10 wt% of β-TCP. The screws were 2 mm in diameter and 10 mm in length (Fig. 1). The PLGA-β-TCP-composite screws had an x-ray positive marker made of β-TCP inserted into the tip of the screws. $FeCl_3$ was used as an oxidant and CS as a counter ion to introduce hydrophilicity to the coating. First, the screws were soaked in pyrrole monomer solution in ethanol (1.3 mol/l, 67 min soaking time) and then transferred into a freshly prepared $FeCl_3$ aqueous solution (0.5 mol/l, 15 min polymerization time) containing 1 mg/ml CS. The coated screws were then carefully rinsed with deionized water in an ultrasonic bath and air-dried. Gamma irradiation of 17.5–26 kGy (by a commercial supplier) was used for the sterilization of the coated and uncoated bioabsorbable screws. The stainless steel screws (Synthes 211.010, diameter 2.0 mm, length 10 mm) were sterilized by autoclaving at 121 °C.

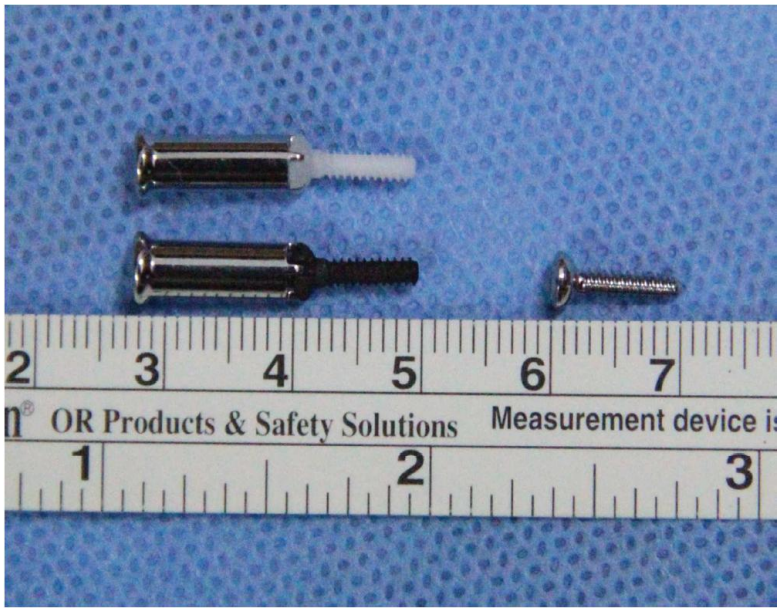

Fig. 1. *The coated (black), uncoated (white) bioabsorbable screws and a steel screw, which were implanted into the rabbits' femurs and tibiae. The screws are 2 mm in diameter and 10 mm in length.*

Implantation

The animal experiments were authorized by the Animal Ethics Committee of the Zhongshan Hospital, Fudan University, China [SYXK(2008)-039]. The studies were conducted on 17 female New Zealand white rabbits with a mean weight of 3.1 ± 0.1kg. The rabbit was the smallest possible animal model for conducting the study according to the standard ISO 10993-6 for biocompatibility studies for bone implants.

The animals were randomly separated into 2 groups. In the coated group, 3 rabbits had 3 PPy coated screws implanted in the left leg (n=18). The right leg was left intact in the group euthanized 12 weeks postoperatively, whereas the rabbits euthanized 26 weeks postoperatively had steel screws implanted in the right leg in similar manner to the left leg. In the control group, uncoated screws were implanted in the left leg (n=18) in a similar manner to coated screws and 3 steel screws were implanted in the right leg (n=36) as a reference for foreign body reaction. For torsion tests, 5 rabbits were operated on, implanting 3 PPy coated screws in the left leg (n=15) leg and 3 uncoated screws in the right leg (n=15).

The surgery was performed under sedation and general anesthesia with diazepam (2 mg/kg, SunRise Pharma, Shanghai, China) and ketamine (40 mg/kg, GuTian Pharma, Fujian, China) by intramuscular injection (i.m.). NaCl (0.9 %) (HuaLu Pharma, Shandong, China) was applied to the eyes to prevent drying. Anesthesia was maintained by administrating 40 mg/kg ketamine by i.m.

Two mini-incisions were made on the medial side of the distal femur, exposing

the distal femur and the upper tibia. The implant hole was drilled with a 1.5 mm drill bit to a depth of 10 mm and slightly countersunk (2.0 mm) to fit the head of the screw flush with the bone surface. The holes were tapped (2.0 mm) and the screws were inserted (Fig. 2). One screw was implanted into the distal femur and 2 screws into the proximal tibia. The wound was closed with non-absorbable surgical sutures (Ping'An Medical Equipment CO. Ltd, Huai'an, China) by suturing in 2 layers after saline (HuaLu Pharma, Shandong, China) irrigation. Penicillin (130,000 U/kg, HuaBei Pharma, Hebei, China) was used as an antibiotic by i.m. intraoperatively and on the first postoperative day to prevent infection. For analgesia, animals were dosed with a subcutaneous injection of buprenorphine hydrochloride (0.03 mg/kg, Drug Research Pharma, Tianjin, China) once a day for 3 days after the operation.

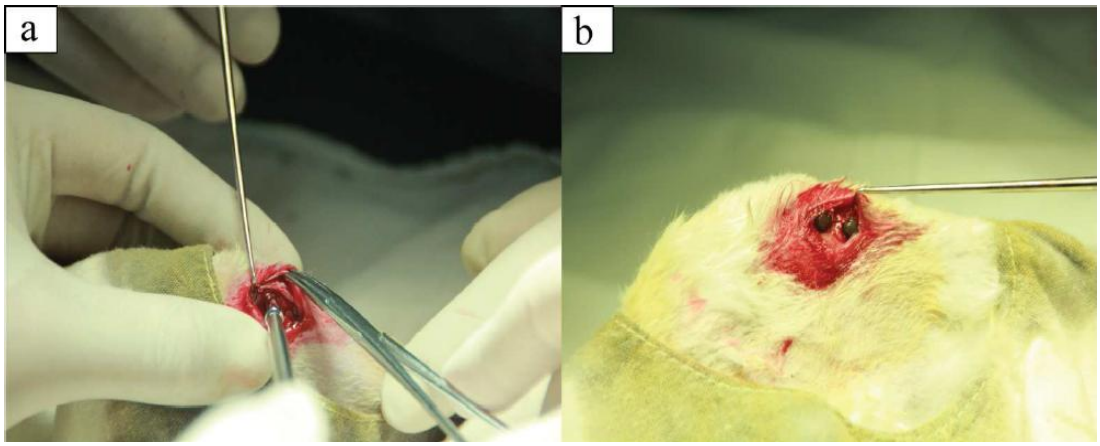

Fig. 2. *Implantation of two coated screws through one mini-incision in the upper tibia (a: turning screws into the tibia with a screwdriver, b: two screws in the tibia).*

To monitor the correct placement of the implants, postoperative radiographs of both hind legs were taken in the medio-lateral projections (49 kV, 5.0 mA, 33 ms, digital X-ray machine, Siemens, Germany) 8 weeks postoperatively. The animals were euthanized 12 and 26 weeks postoperatively with an overdose of ketamine hydrochloride (GuTian Pharma, Fujian, China). For tetracycline fluorescence detection, tetracycline (30 mg/kg, Sigma, USA) was injected intramuscularly 8 and 1 days before euthanasia.

Clinical signs

The rabbit's appearance, behavior and food and water consumption were observed twice daily on weekdays and once daily on weekends. Implantation sites were examined for the first 5 days postoperatively and weekly throughout the study. Body temperature and weight were measured prior to the implantation as well as 48 hours and 2, 4, 12 and 26 weeks postoperatively.

Hematology and clinical chemistry

For subchronic toxicity testing of the coated screws, hematology and clinical chemistry were performed prior to the implantation as well as 48 hours, and 2, 4, 12 and 26 weeks postoperatively. The blood samples were drawn from the central auricular artery under anesthesia without overnight deprivation of food. The hematological analyses were performed on an automatic hemocyte analyzer (XS-1000i and CA1500, Sysmex，Japan) and chemical analyses on a biochemical automatic analyzer (P800/ P2400, Roche, Switzerland) at Labway Clinical Laboratory Limited (Shanghai, China).

Organ examination

Organs were weighed immediately after dissection to avoid drying and subsequently false low values. For bilateral organs, the left and right organs were weighed together. Subchronic toxicity was examined from organ weights, macroscopic examinations during necropsy, and histology of the internal organs. All the organ samples were fixed in 10 % neutral buffered formalin (XingYinHe Chemical Ltd, Hubei, China) and the samples were dehydrated and embedded in paraffin (FangZheng Chemical Ltd, Sichuan, China). Paraffin blocks were cut into thin sections of 5 μm in thickness and stained with Hematoxylin and Eosin (Vaijayanthimala *et al.*, 2012). Histological evaluation was performed under an optical microscope (Axio Imager M1, Zeiss, Jena, Germany) with AxioVision SE64 software (Zeiss, Jena, Germany).

Soft tissue examination

Soft tissue of 3 mm thickness around the head of the screws (uncoated, coated and steel screws) was selected for routine histology. The soft tissue samples were processed in the same manner as the organ samples. The coated and uncoated screw samples were evaluated semi-quantitatively, including the quantitative comparison of inflammation polymorphonuclear cells, lymphocytes, plasma cells, macrophages and giant cells, as well as qualitative comparison of the extent of necrosis, neovascularization, fibrosis and fatty infiltrate.

Torsion test

To characterize the attachment strength of the bone to the screws, torsion tests (Iijima *et al.*, 2008) were performed on the day of euthanasia. Adherent soft tissue and newly formed bone tissue were carefully dissected around the screw head. The front tooth structure of metal rod was locked with the screw head. A hexagonal screwdriver linked to the sensor of a digital torque meter (HDP-5, Tuojing Measuring Instrument Limited Co, Shanghai, China) was then used to rotate the screws in order to capture the peak value of the torsion force (F_{max}, Nm) during the course of screw's loosening. The longitudinal axis of a hexagonal screwdriver was aligned with the metal rod's fixed direction. According to the manufacturer's guideline, the absorbable screws start to degrade after 16 weeks, hence the torsion test was carried out 12 weeks after implantation.

Micro-CT examination

The bone specimens with the implanted screws were harvested and bony tissue surrounding the coated and uncoated screws in the rabbit's femur and tibia was scanned non-destructively by micro-CT (μCT-80, Scanco Medical AG, Zurich, Switzerland at the 12-week time point; Inveon PET/CT, Siemens AG, Munich, Germany at the 26-week time point). As the diameter of the screw was 2 mm, a circular area with a diameter of 2.2 mm was selected for scanning the screw and its surrounding tissue. A similar scan was repeated with a 2.0 mm diameter and deducted from the first area. The relative amount of mineralized tissue (including new and old bone tissue) was calculated from the residual area. At the 12-week time point, the micro-CT (μCT-80) images were recorded on a 1024 × 1024 charge-coupled device detector, with the pixel size set to 20 μm. 3D histomorphometric analysis, including the measurements of total volume and mineral density of the implants, was performed automatically with the FEA software (Scanco Medical AG, Zurich, Switzerland). The samples at the 26-week time point were recorded on a 1888 × 2048 charge-coupled device detector with an effective pixel size of 9.5 μm. The images were analyzed with Inveon Research Workplace software (Siemens AG, Munich, Germany). The images were segmented using a nominal threshold value of 220 at both time points.

Tetracycline labelling

The bone specimens including implants were harvested to observe the bone formation around the coated and uncoated screws. The bone samples were dehydrated in acetone for 1 month and embedded in methyl methacrylate (MMA) (Suicheng Chemical Ltd, Guangzhou, China) without decalcification. Subsequently, the MMA blocks were cut into 200 μm slices with the EXAKT cutting system (E300CP, Norderstedt, Germany) and polished to a thickness of 20 μm. Distances between the 2 tetracycline fluorescence lines were measured under a microscope (Axio Imager M1, Zeiss, Jena, Germany) with AxioVision SE64 software (Zeiss, Jena, Germany).

Hard tissue examination

Hard tissue histology was conducted from the tetracycline-labelled samples. After examining the tetracycline fluorescence lines of the slices, toluidine blue (ZiYi Chemical Ltd, Shanghai, China) (Deng *et al.*, 2008) was added on the slices for 15 min. Subsequently, coverslips were mounted for 2 days at room temperature. The slices were analyzed under an optical microscope (Axio Imager M1). The number of osteoblasts and chondroblasts at the bone-implant contact (BIC) was counted under the microscope (Di Iorio *et al.*, 2006).

Statistical analysis

The statistical analyses were performed with SPSS version 17 (SPSS, Chicago, IL). One-way analysis of variance (ANOVA) with Fisher's Least Significant Difference (LSD) was used for analyzing blood samples. Student's T test was used to compare the mean values of the coated and uncoated group within the time points for the

torsion test, micro-CT, tetracycline labelling hard tissue histology, weight and temperature. All quantitative data is presented as mean ± standard error of mean (SEM) and $p < 0.05$ was considered statistically significant.

Results

Postoperative examination

All rabbits recovered uneventfully after surgery with the exception of 1 decubitus ulcer and 1 slight dehiscence of the surgical wound 3 weeks postoperatively. Radiography showed that the X-ray markers of the biodegradable screws were visible and correctly positioned (Fig. 3.).

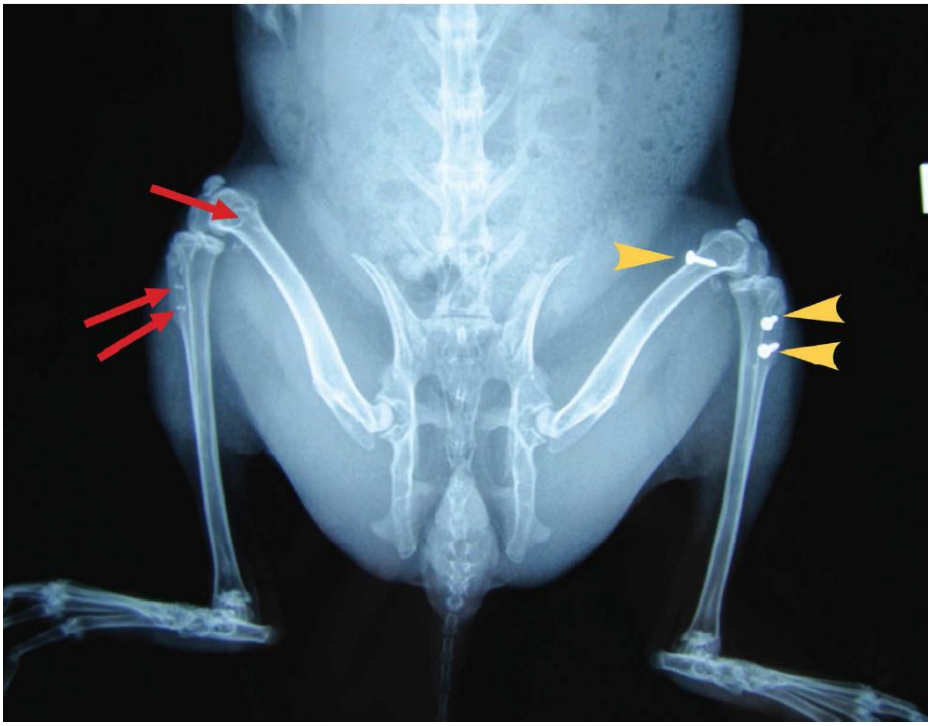

Fig. 3. *Radiographs of one rabbit 8 weeks postoperatively. The red arrows show the β-TCP marker in the bone, the yellow arrows point at the steel screws.*

Hematology and clinical chemistry

The monocyte and platelet count and blood urea nitrogen were significantly higher in the uncoated group compared to coated group 2 weeks postoperatively. Furthermore, the white blood cell count and platelet count were significantly higher in the uncoated group than in coated group 12 weeks postoperatively. No significant differences between the coated and uncoated group were found at any other time points. When the blood samples taken prior to surgery were used as a baseline, the values in the

uncoated group did not vary significantly. However, in the coated group creatinine values per weight were significantly higher 2 and 4 weeks after the surgery (79.67 ± 3.71 μmol/l and 92.23 ± 5.24 μmol/l respectively), yet still within normal ranges (26.5-115 μmol/l; Giessler *et al.*, 2007); the values recovered to baseline level after 12 weeks. At the 26-week time point, there were no statistically significant differences between the coated and uncoated groups.

Organ examination

Macroscopic and microscopic examination of the organs during the necropsy revealed that there were no significant differences in weights and histology between the 2 groups at the 12- and 26-week time points.

Soft tissue examination

All the heads of the coated, uncoated and steel screws were covered by a new callus that was greater in size at the 26-week time point than at the 12-week time point. Only slight hematoma, edema or encapsulation were found in the soft tissue around the 3 implantation sites that did not show obvious differences in macroscopic examination at the 12- and 26-week time points. Semi-quantitative evaluation also showed no differences among the 3 screw types (data not shown) at the 12-week time point. However at the 26-week time point, the irritation level, relative to the corresponding steel screws, was found to be higher in the uncoated screws compared to the coated.

Torsion test

Torsional forces were captured from all of the samples during the course of screws' rotation even though 5 coated screws and 2 uncoated screws broke during the mechanical testing. A significantly higher torsional peak value was measured for the coated screws when compared to the uncoated screws (Fig. 4) at the 12-week time point.

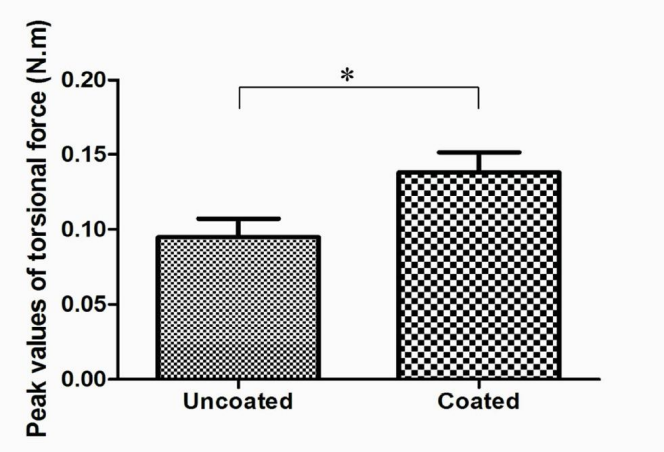

Fig. 4. *The peak values of the torsion force of the coated screws were significantly higher than those of the uncoated screws at 12-week time point. (*) Significant difference ($p < 0.05$).*

Micro-CT evaluation

Micro-CT measurements taken 12 and 26 weeks postoperatively revealed a significantly greater amount of mineralized tissue in the coated samples than in uncoated ones (Fig. 5). Representative images from each group are shown in Fig. 5a. The cylinder shaped β-TCP marker of the bioabsorbable screw shown in the images is surrounded by PLGA-β-TCP composite. Due to the selected micro-CT parameters PLGA-β-TCP composite is not apparent in the figures. Mineralized areas were evident in the surrounding tissue in most of the samples.

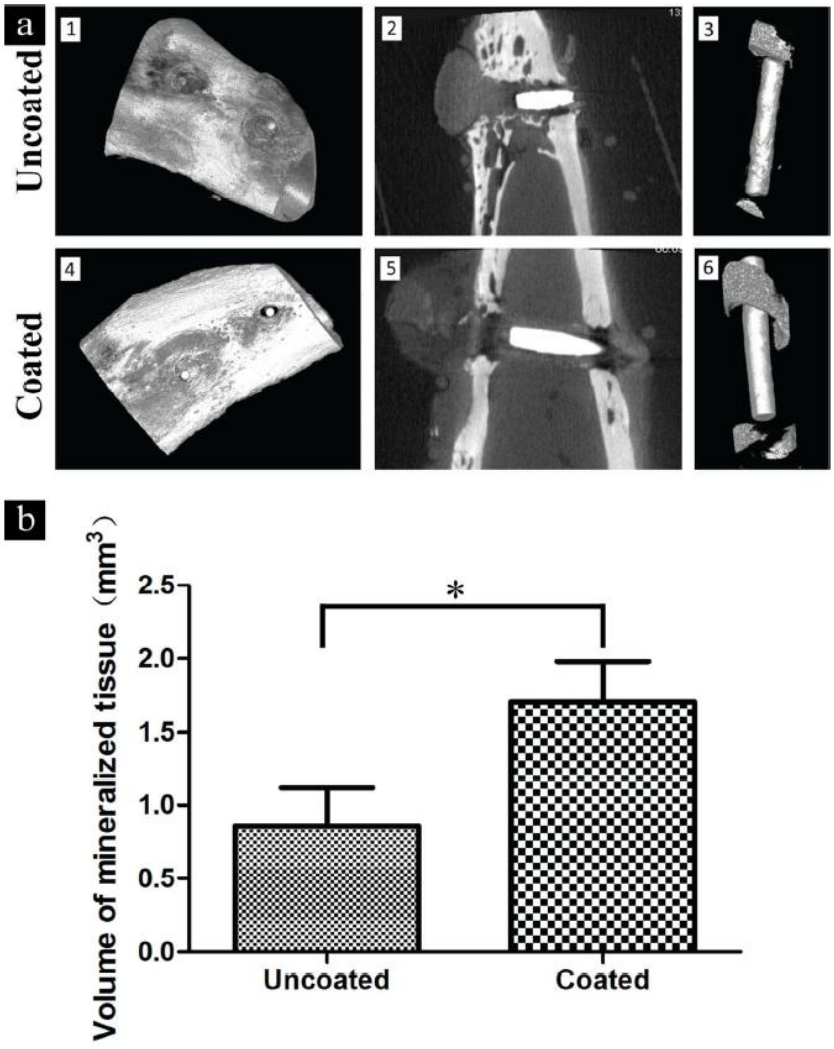

Fig. 5. *Micro-CT measurements of the implant areas. (a) Representative 3D images of the absorbable implants harvested 26 weeks postoperatively. (a1 and a4) Screw heads facing towards the viewer. (a2 and a5) Side projections of the screws. (a3 and a6) Representative images of the micro-CT measurement area around the screws (b) Quantitative micro-CT analysis revealed that the bone volume of the coated screws was significantly higher than that of the uncoated screws at the 26-week time point. (*) Significant difference ($p < 0.05$).*

Tetracycline fluorescence measurement

Coated samples (Fig. 6b, Fig. 7b) showed a significantly longer distance between the 2 tetracycline lines than the uncoated samples (Fig. 6a, 7a) as presented in Fig. 6c and 7c at the 12- and 26-week time points, respectively. This reflects the significantly greater new bone formation rate of the coated samples.

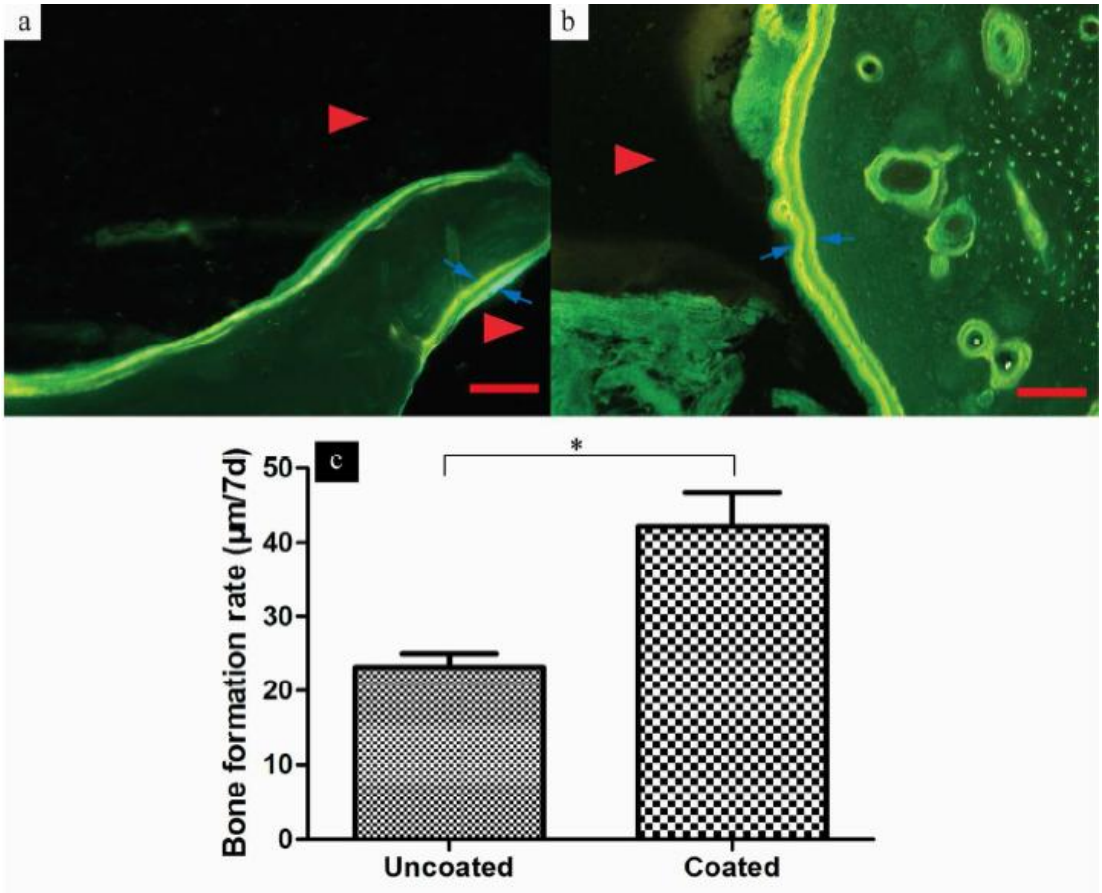

Fig. 6. *Tetracycline fluorescence measurement between two yellow bands (blue arrows) evaluating the new bone formation rate at 12-week time point. (a) Uncoated group (►: part of an uncoated screw); (b) Coated group (►: part of a coated screw). Scale bar 100µm; (c) Quantitative analysis revealed that the new bone formation rate of the coated screws was significantly higher than that of the uncoated screws at 12-week time point. (*) Significant difference ($p < 0.05$).*

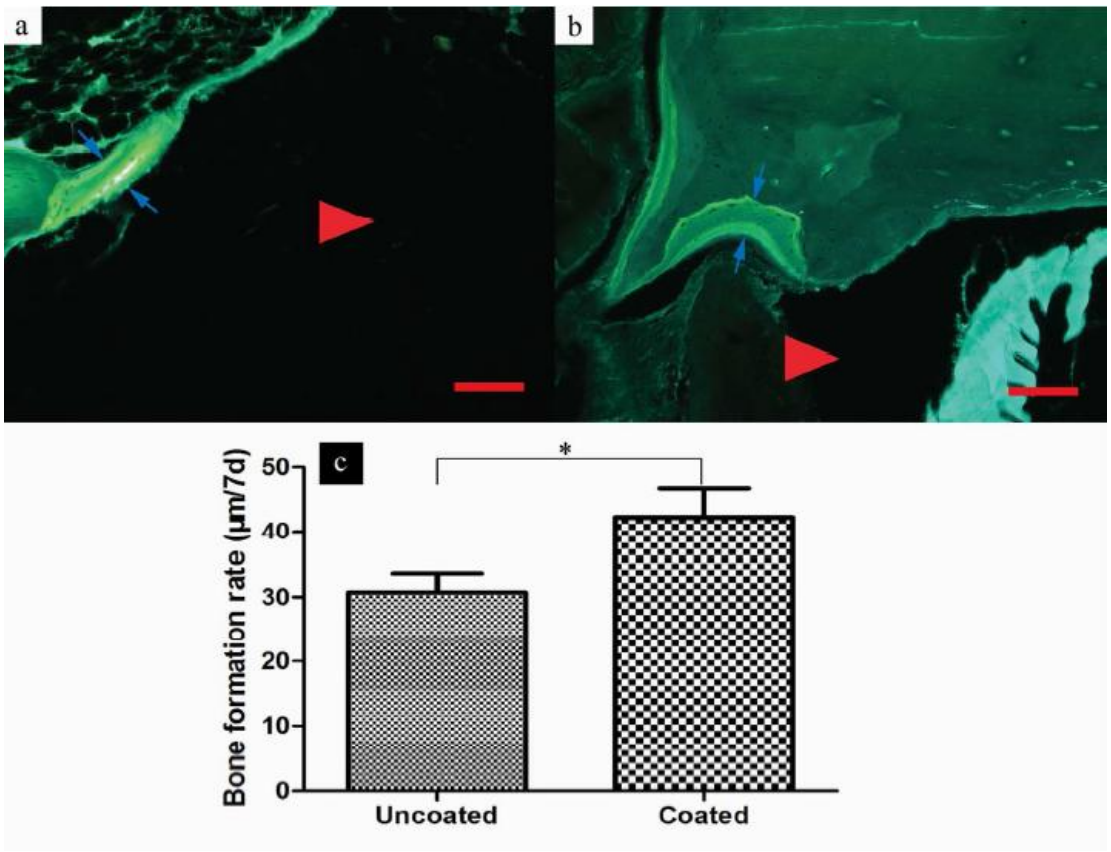

Fig. 7. *Tetracycline fluorescence measurement between two yellow bands (blue arrows) evaluating the new bone formation rate at 26-week time point. (a) Uncoated group (►: part of an uncoated screw); (b) Coated group (►: part of a coated screw). Scale bar 100µm; (c) Quantitative analysis revealed that the new bone formation rate of the coated screws was significantly higher than that of the uncoated screws at 26-week time point. (*) Significant difference ($p < 0.05$).*

Hard tissue histological evaluation

At the 12-week time point, the coated samples (Fig. 8b) showed a darker blue band, indicating a greater amount of new bone compared to the uncoated samples (Fig. 8a). Furthermore, the total number of osteoblasts and chondroblasts at the BIC in the coated group was significantly higher than that in the uncoated group (Fig. 8c.). The parts of the coated and uncoated screws in the marrow cavity were expanded and degraded, while the parts contacting the bone tissues showed good integrity. The expansion had most probably occurred during the sample fixation step with acetone. The solvent was therefore changed to formaldehyde for the 26-weeks samples and no swelling of the screws was observed at that time point. Some fibrotic tissue was apparent under the screw threads, which resulted from the compression irritation of the tissue during the implantation. The BIC showed no inflammation in the coated and

uncoated group at either of the time points. However, at the 12-week time point, the BIC of the uncoated group was larger than that of the coated group, as demonstrated by a white band seen in the uncoated samples. In the coated group at the 12-week time point, dark bands were found at the BIC, which resulted from PPy stained by toluidine blue.

At the 26-week time point, woven bone was found in greater amounts in the coated sample groups than in the uncoated sample groups (Fig. 9), which was demonstrated by a significantly greater number of osteoblasts and chondroblasts (Fig. 9c.). However, the blue band indicating new bone was now similar in the coated and uncoated samples. Small traces of PPy were apparent in the coated samples yet the amount of PPy was notably lower at the 26-week time point than at the 12 week time point. The area of the PLGA-β-TCP composite in both coated and uncoated samples was substantially smaller than those observed at the 12-week time point, and new bone tissue appeared in close proximity to the β-TCP marker.

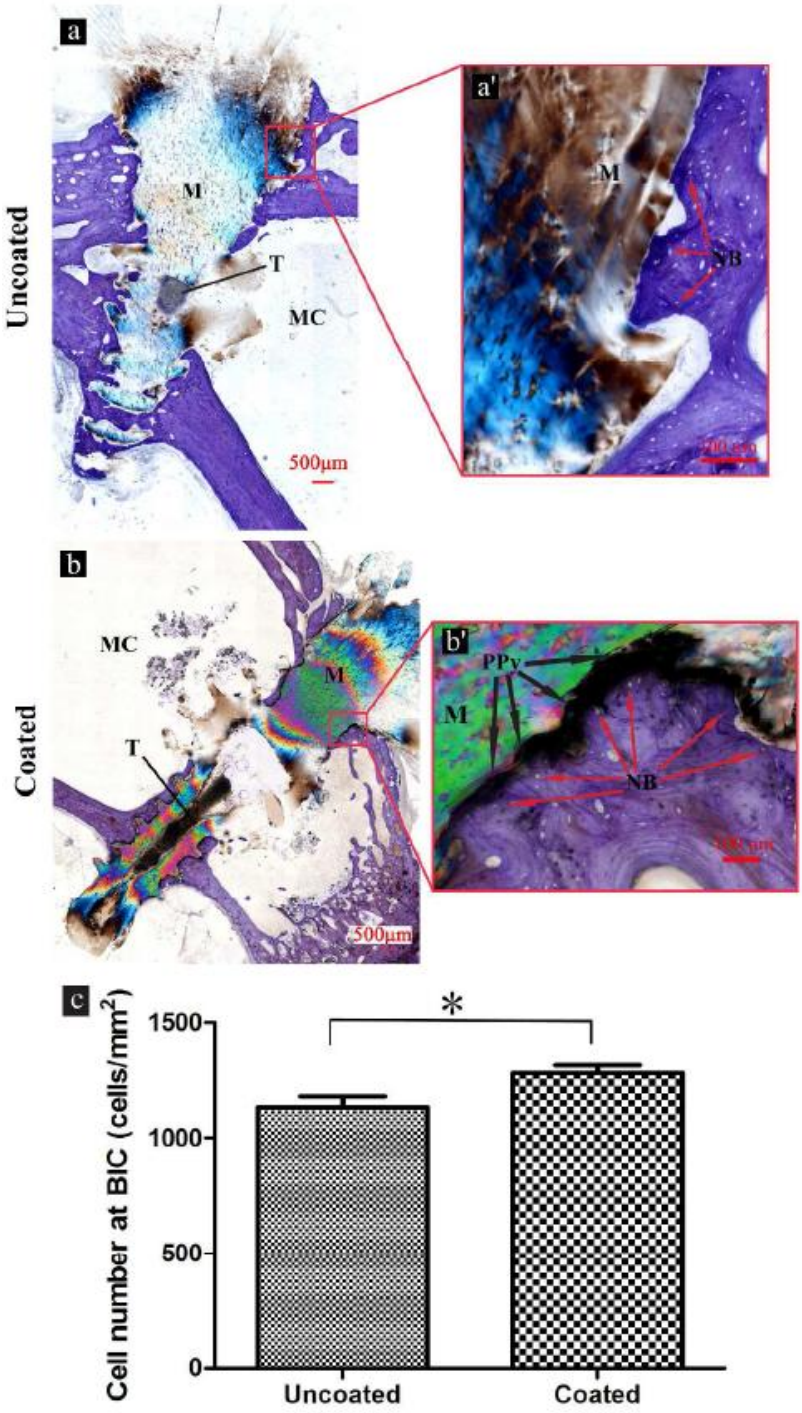

Fig. 8. *Toluidine blue staining 12 weeks after implantation for hard tissue samples. (a) Uncoated screw (scale bar 500 μm). (a') The magnification of the interface between the uncoated screw and bone revealed a thin detectable new bone (NB) band (scale bar 100 μm). (b) Coated screws (scale bar 500 μm). (b') The magnification of the interface between the coated screw and bone (scale bar 100 μm). NB was clearly detectable as indicated by a thick band on the surface. PPy coating appears as a black band. (MC: marrow cavity, M: PLGA and β-TCP, T: pure β-TCP). (c) The total number of osteoblasts and chondroblasts at the BIC in coated group was significantly higher than that in the uncoated group. (*) Significant difference ($p<0.05$).*

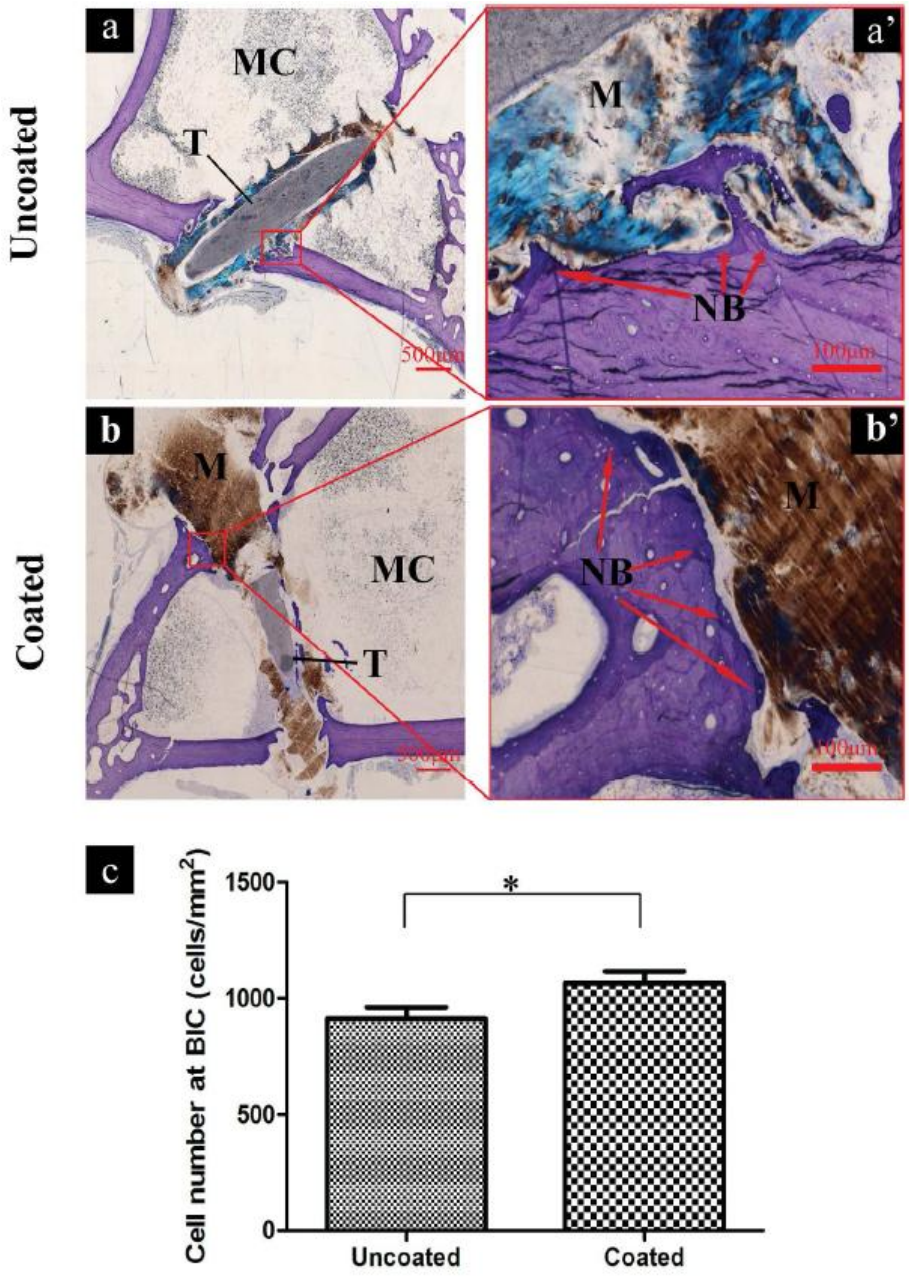

Fig. 9. *Toluidine blue staining 26 weeks after implantation for hard tissue samples. (a) Uncoated screw (scale bar 500 μm). (a') The magnification of the interface between the uncoated screw and bone revealed a thin detectable new bone (NB) band (scale bar 100 μm). (b) coated screws (scale bar 500 μm). (b') The magnification of the interface between the coated screw and bone (scale bar 100 μm). NB was clearly detectable as indicated by a thick band on the surface. PPy coating appears as a black band. (MC: marrow cavity, M: PLGA and β-TCP, T: pure β-TCP). (c) The total number of osteoblasts and chondroblasts at the BIC in the coated group was significantly higher than that in the uncoated group. (*) Significant difference ($p < 0.05$).*

Discussion

In orthopedic surgery, loosening of the implant is the most common cause of failure in internal fixation (Cordova *et al.*, 2014; Scioscia *et al.*, 2001). Therefore many coating methods have been used to enhance the bonding between bone and the surface of an orthopedic implant to improve its osteointegration (Bosco *et al.*, 2013; Browne Gregson, 2000; Chen *et al.*, 2006; De Giglio *et al.*, 2007; De Giglio *et al.*, 2001; Edlund *et al.*, 2008; Somayaji *et al.*, 2010). Of these coatings, PPy could provide an interesting approach due to its multifunctional properties. For instance, PPy could facilitate exploitation of electrical stimulation in controlled drug delivery (De Giglio *et al.*, 2001; Sirivisoot *et al.*, 2011). As PPy has previously shown a good biocompatibility with several tissues (Meng *et al.*, 2013; Meng *et al.*, 2011; Pelto *et al.*, 2013; Serra *et al.*, 2012) and has excellent cellular attachment properties in vitro (Pelto *et al.*, 2013), we hypothesized that PPy may augment the attachment of the implant in bone tissue, thereby improving new bone formation.

In the present study, systemic toxicity, biocompatibility and osteogenicity of the PPy coating was studied for the first time in vivo. As our main finding, PPy coating significantly promoted new bone formation when compared to the uncoated screws. This was consistently demonstrated by tetracycline labelling and supported by micro-CT and torsion tests. In addition, hard tissue histology showed more new bone tissue and higher number of osteoblasts and chondroblasts around the coated screws compared to the uncoated screws at both time points. At the 12-week time point, the BIC of the coated samples was narrower implying better attachment of the coated screws to the bone tissue compared to the uncoated screws (Fig. 9). At the 26-week time point, the differences between the coated and uncoated samples were less apparent as both screw types had new bone formation at the β-TCP marker surface.

In the torsion tests, the coated screws required significantly greater torsional force to be loosened from the surrounding bone. Five coated screws broke during the torsion tests whereas this occurred only twice with the uncoated screws. This could indicate a stronger attachment of coated screws to bone tissue, their faster degradation rate, or that the coating process had compromised the strength of the screws. The stage of degradation of both screw types at the 12-week time point showed a similar pattern according to the histology. However, this needs to be elucidated in the future with adequate methods. In our recent study we showed that PPy induces MSC proliferation and early osteogenic differentiation over polylactide in vitro. Moreover, we have also shown that surface roughness of PPy coating plays a major role in cell attachment and osteogenic response of MSCs to the PPy substrate. Therefore, the enhanced tissue response of coated screws may be explained be due to more favorable surface roughness and hydrophilic properties of PPy coating for surrounding cell response.

The rates of the new bone formation with the PLGA-β-TCP screws were in similar ranges as in earlier studies with polylactide-based bioabsorbable bone fixation

devices where bone formation was reported to occur between 6 and 12 weeks after implantation in bone tissue (Felix *et al.*, 2011; Saikku-Backstrom *et al.*, 2001). As expected, the bulk degradation of the screws in our study did not occur at the 12-week time point. According to the manufacturer of the PLGA-β-TCP screws, the shear strength of the screws remains at the initial level for 16 weeks and drops to 35% at 26 weeks.

Hard tissue histology at the 12-week time point showed a clear band of PPy stained by toluidine blue around the implants suggesting that it was still consistently distributed around implant and therefore played a key role in tissue attachment. At the 26-week time point, only small traces of PPy were found in the hard tissue histology as the degradation of the inner lying PLGA-β-TCP matrix had caused it to crack and erode. Macrophages did not seem to play a role in PPy elimination at this stage, as none was apparent in the histological samples. PPy is not inherently degradable but its ability to erode may contribute to its final elimination from the body (Shi *et al.*, 2004; Wang Z. *et al.*, 2004). Small water-soluble PPy chains (1700–3200 Da) have been reported to be excreted by renal clearance (Zelikin *et al.*, 2002). While the creatinine values in the coated group were elevated 2 and 4 weeks after surgery compared to the uncoated group, the increased creatinine values were still within normal levels. This suggests that the PPy coating started to erode 2 weeks after implantation. The creatinine levels recovered to baseline level 12 weeks postoperatively, showing no further statistical differences and indicating that the major erosion occurred between 12 and 26 week time points did not affect renal function.

PPy did not induce acute, subacute or subchronic toxicity and proved to be compatible with bone tissue. No inflammatory cells or allergic reactions were found around the coated and uncoated screws in the hard tissue histology (Fig. 8 and 9). No abnormal findings in terms of hematoma, edema or encapsulation in any of the samples were found on macroscopic observation. In addition, the histological soft tissue samples around the screw heads showed no abnormal reactions either in the number of polymorphonuclear cells and macrophages or in the amount of necrosis and fatty infiltrate. The PPy coating even seemed to lower the level of irritation of the absorbable screw according to the semi-quantitative evaluation. This finding is supported by earlier studies conducted on various tissue types (Collier *et al.*, 2000; Jiang *et al.*, 2002; Ramanaviciene *et al.*, 2007; Wang X. *et al.*, 2004). Moreover, PPy did not show any systemic effect according to hematology and clinical chemistry. Significant differences found between the uncoated and coated group were within normal ranges when compared to the values measured prior to surgery.

Even though several studies have reported the high biocompatibility of PPy, slight adverse reactions have also been reported (Castano *et al.*, 2004; Ferraz *et al.*, 2012; Kim *et al.*, 2011; Vaitkuviene *et al.*, 2013). For instance, different concentrations of PPy monomer used in polymerization can drastically alter cellular events as a higher PPy concentration during admicellar polymerization has been

reported to inhibit MSC attachment. It was suggested that the negative effect on cell attachment in that study was due to an unfavorable thickness and hence a changed surface roughness of the PPy layer, and not due to toxic components leaching from the polymer (Castano *et al.*, 2004). Thin PPy layers have been reported to result in a better cell attachment in studies conducted in vitro and in vivo (Castano *et al.*, 2004; Shi *et al.*, 2004; Wang Z. *et al.*, 2004). PPy nanoparticles may also induce slight adverse reactions on cells. This has been reported to be highly dependable on particle size (Kim *et al.*, 2011; Vaitkuviene *et al.*, 2013). Moreover, the aging of the PPy has been suggested to have a negative effect on its biocompatibility with nanocellulose-PPy composites, which showed evidence of cytotoxicity in several conditions after 4 weeks of storage (Ferraz *et al.*, 2012). The coated screws in our study were stored in appropriate sterile packages for 10 months at ambient temperature before implantation, and the PPy did not show signs of increased cytotoxicity when compared to uncoated screws. Nevertheless, longer-term effects of the coating require evaluation in the future studies.

Conclusion

The PPy coating on PLGA-β-TCP screws significantly enhanced new bone formation during the 26-week implantation period and significantly facilitated the attachment of the screws in bone tissue up to 12 weeks postoperatively. Moreover, the PPy coating and its erosion products did not show any increased adverse reactions locally or systematically. These results highlight the potential of PPy as a multifunctional osteogenic coating material to facilitate better bone tissue-implant interactions.

Acknowledgements

The authors wish to express their appreciation to Bioretec Ltd. for providing the bioabsorbable polymer composite bone fixation screws for this study; Deng Lianfu (Prof, PhD) and Jorma Pajamäki (MD, PhD) for consultation in bone tissue histology, and Tuija Annala (MSc) for consultation in the experiment configuration. This work was carried out with the financial support of the Shanghai International Science and Technology Partnership Program (11540702700), the Natural Science Foundation of China (81372002), the Finnish Funding Agency for Technology and Innovation (TEKES), the Academy of Finland, the City of Tampere Science Foundation, and the Competitive Research Funding of Tampere University Hospital (grants 9K020 and 9N042).

References

Ajiro H, Takahashi Y, Akashi M, Fujiwara T (2012) Polylactide block copolymers using trimethylene carbonate with methoxyethoxy side groups for dual modification of hydrophilicity and biodegradability. Macromol Biosci **12:** 1315-1320.

Bosco R, Edreira ERU, Wolke JGC, Leeuwenburgh SCG, van den Beucken JJJP, Jansen JA (2013) Instructive coatings for biological guidance of bone implants. Surface and Coatings Technology **233:** 91-98.

Browne M, Gregson PJ (2000) Effect of mechanical surface pretreatment on metal ion release. Biomaterials **21:** 385-392.

Castano H, O'Rear EA, McFetridge PS, Sikavitsas VI (2004) Polypyrrole thin films formed by admicellar polymerization support the osteogenic differentiation of mesenchymal stem cells. Macromol Biosci **4:** 785-794.

Chen Y, Mak AFT, Wang M, Li J, Wong MS (2006) PLLA scaffolds with biomimetic apatite coating and biomimetic apatite/collagen composite coating to enhance osteoblast-like cells attachment and activity. Surface and Coatings Technology **201:** 575-580.

Collier JH, Camp JP, Hudson TW, Schmidt CE (2000) Synthesis and characterization of polypyrrole-hyaluronic acid composite biomaterials for tissue engineering applications. J Biomed Mater Res **50:** 574-584.

Cordova LA, Stresing V, Gobin B, Rosset P, Passuti N, Gouin F, Trichet V, Layrolle P, Heymann D (2014) Orthopaedic implant failure: aseptic implant loosening--the contribution and future challenges of mouse models in translational research. Clin Sci (Lond) **127:** 277-293.

Cui X, Wiler J, Dzaman M, Altschuler RA, Martin DC (2003) In vivo studies of polypyrrole/peptide coated neural probes. Biomaterials **24:** 777-787.

De Giglio E, Cometa S, Calvano CD, Sabbatini L, Zambonin PG, Colucci S, Benedetto AD, Colaianni G (2007) A new titanium biofunctionalized interface based on poly(pyrrole-3-acetic acid) coating: proliferation of osteoblast-like cells and future perspectives. J Mater Sci Mater Med **18:** 1781-1789.

De Giglio E, Guascito MR, Sabbatin L, Zambonin G (2001) Electropolymerization of pyrrole on titanium substrates for the future development of new biocompatible surfaces. Biomaterials **22:** 2609-2616.

De Giglio E, Sabbatini L, Colucci S, Zambonin G (2000) Synthesis, analytical characterization, and osteoblast adhesion properties on RGD-grafted polypyrrole coatings on titanium substrates. J Biomater Sci Polym Ed **11:** 1073-1083.

Deng F, Ling J, Ma J, Liu C, Zhang W (2008) Stimulation of intramembranous bone repair in rats by ghrelin. Exp Physiol **93:** 872-879.

Di Iorio E, Barbaro V, Ferrari S, Ortolani C, De Luca M, Pellegrini G (2006) Q-FIHC: quantification of fluorescence immunohistochemistry to analyse p63 isoforms and cell cycle phases in human limbal stem cells. Microsc Res Tech **69:** 983-991.

Edlund U, Danmark S, Albertsson AC (2008) A strategy for the covalent functionalization of resorbable polymers with heparin and osteoinductive growth factor. Biomacromolecules **9:** 901-905.

Felix LR, Leeuwenburgh SC, Wolke JG, Jansen JA (2011) Bone response to fast-degrading, injectable calcium phosphate cements containing PLGA microparticles. Biomaterials **32:** 8839-8847.

Ferraz N, Stromme M, Fellstrom B, Pradhan S, Nyholm L, Mihranyan A (2012) In vitro and in vivo toxicity of rinsed and aged nanocellulose-polypyrrole composites. J Biomed Mater Res A **100:** 2128-2138.

Garner B, Georgevich A, Hodgson AJ, Liu L, Wallace GG (1999) Polypyrrole-heparin composites as stimulus-responsive substrates for endothelial cell growth. J Biomed Mater Res **44:** 121-129.

Giessler GA, Gades NM, Friedrich PF, Bishop AT (2007) Severe tacrolimus toxicity in rabbits. Exp Clin Transplant **5:** 590-595.

Iijima M, Muguruma T, Brantley WA, Okayama M, Yuasa T, Mizoguchi I (2008) Torsional properties and microstructures of miniscrew implants. Am J Orthod Dentofacial Orthop **134:** 331-333, 333-334.

Jiang X, Marois Y, Traore A, Tessier D, Dao LH, Guidoin R, Zhang Z (2002) Tissue reaction to polypyrrole-coated polyester fabrics: an in vivo study in rats. Tissue Eng **8:** 635-647.

Kallrot M, Edlund U, Albertsson AC (2007) Covalent grafting of poly(L-lactide) to tune the in vitro degradation rate. Biomacromolecules **8:** 2492-2496.

Kim S, Oh WK, Jeong YS, Hong JY, Cho BR, Hahn JS, Jang J (2011) Cytotoxicity of, and innate immune response to, size-controlled polypyrrole nanoparticles in mammalian cells. Biomaterials **32:** 2342-2350.

Meng S, Rouabhia M, Zhang Z (2013) Electrical stimulation modulates osteoblast proliferation and bone protein production through heparin-bioactivated conductive scaffolds. Bioelectromagnetics **34:** 189-199.

Meng S, Zhang Z, Rouabhia M (2011) Accelerated osteoblast mineralization on a conductive substrate by multiple electrical stimulation. J Bone Miner Metab **29:** 535-544.

Pelto J, Bjorninen M, Palli A, Talvitie E, Hyttinen J, Mannerstrom B, Suuronen SR, Kellomaki M, Miettinen S, Haimi S (2013) Novel polypyrrole-coated polylactide scaffolds enhance adipose stem cell proliferation and early osteogenic differentiation. Tissue Eng Part A **19:** 882-892.

Ramanaviciene A, Kausaite A, Tautkus S, Ramanavicius A (2007) Biocompatibility of polypyrrole particles: an in-vivo study in mice. J Pharm Pharmacol **59:** 311-315.

Saikku-Backstrom A, Tulamo RM, Raiha JE, Kellomaki M, Toivonen T, Tormala P, Rokkanen P (2001) Intramedullary fixation of cortical bone osteotomies with absorbable self-reinforced fibrillated poly-96L/4D-lactide (SR-PLA96) rods in rabbits. Biomaterials **22:** 33-43.

Schmidt CE, Shastri VR, Vacanti JP, Langer R (1997) Stimulation of neurite outgrowth using an electrically conducting polymer. Proc Natl Acad Sci U S A **94:** 8948-8953.

Scioscia TN, Giffin JR, Allen CR, Harner CD (2001) Potential complication of bioabsorbable

screw fixation for osteochondritis dissecans of the knee. Arthroscopy **17:** E7.

Serra MJ, Sabbieti MG, Agas D, Marchetti L, Panero S (2012) Polysaccharides immobilized in polypyrrole matrices are able to induce osteogenic differentiation in mouse mesenchymal stem cells. J Tissue Eng Regen Med.

Shi G, Rouabhia M, Wang Z, Dao LH, Zhang Z (2004) A novel electrically conductive and biodegradable composite made of polypyrrole nanoparticles and polylactide. Biomaterials **25:** 2477-2488.

Sirivisoot S, Pareta R, Webster TJ (2011) Electrically controlled drug release from nanostructured polypyrrole coated on titanium. Nanotechnology **22:** 85101.

Somayaji SN, Huet YM, Gruber HE, Hudson MC (2010) UV-killed Staphylococcus aureus enhances adhesion and differentiation of osteoblasts on bone-associated biomaterials. J Biomed Mater Res A **95:** 574-579.

Son JS, Kim SG, Oh JS, Appleford M, Oh S, Ong JL, Lee KB (2011) Hydroxyapatite/polylactide biphasic combination scaffold loaded with dexamethasone for bone regeneration. J Biomed Mater Res A **99:** 638-647.

Tian H, Tang Z, Zhuang X, Chen X, Jing X (2012) Biodegradable synthetic polymers: Preparation, functionalization and biomedical application. Progress in Polymer Science **37:** 237-280.

Vaijayanthimala V, Cheng PY, Yeh SH, Liu KK, Hsiao CH, Chao JI, Chang HC (2012) The long-term stability and biocompatibility of fluorescent nanodiamond as an in vivo contrast agent. Biomaterials **33:** 7794-7802.

Vaitkuviene A, Kaseta V, Voronovic J, Ramanauskaite G, Biziuleviciene G, Ramanaviciene A, Ramanavicius A (2013) Evaluation of cytotoxicity of polypyrrole nanoparticles synthesized by oxidative polymerization. J Hazard Mater **250-251:** 167-174.

Wang S, Cui W, Bei J (2005) Bulk and surface modifications of polylactide. Anal Bioanal Chem **381:** 547-556.

Wang X, Gu X, Yuan C, Chen S, Zhang P, Zhang T, Yao J, Chen F, Chen G. (2004) Evaluation of biocompatibility of polypyrrole in vitro and in vivo. J Biomed Mater Res A **68:** 411-422.

Wang Z, Roberge C, Dao LH, Wan Y, Shi G, Rouabhia M, Guidoin R, Zhang Z. (2004) In vivo evaluation of a novel electrically conductive polypyrrole/poly(D,L-lactide) composite and polypyrrole-coated poly(D,L-lactide-co-glycolide) membranes. J Biomed Mater Res A **70:** 28-38.

Zelikin AN, Lynn DM, Farhadi J, Martin I, Shastri V, Langer R (2002) Erodible conducting polymers for potential biomedical applications. Angew Chem Int Ed Engl **41:** 141-144.

Zhang J, Neoh KG, Hu X, Kang ET, Wang W (2013) Combined effects of direct current stimulation and immobilized BMP-2 for enhancement of osteogenesis. Biotechnol Bioeng **110:** 1466-1475.

Zhang P, Hong Z, Yu T, Chen X, Jing X (2009) In vivo mineralization and osteogenesis of nanocomposite scaffold of poly(lactide-co-glycolide) and hydroxyapatite surface-grafted with

poly(L-lactide). Biomaterials **30:** 58-70.

Zhang Z, Roy R, Dugre FJ, Tessier D, Dao LH (2001) In vitro biocompatibility study of electrically conductive polypyrrole-coated polyester fabrics. J Biomed Mater Res **57:** 63-71.

Zhou H, Lawrence JG, Bhaduri SB (2012) Fabrication aspects of PLA-CaP/PLGA-CaP composites for orthopedic applications: a review. Acta Biomater **8:** 1999-2016.

Tampereen teknillinen yliopisto
PL 527
33101 Tampere

Tampere University of Technology
P.O.B. 527
FI-33101 Tampere, Finland

ISBN 978-952-15-3543-7
ISSN 1459-2045